UNIVERSITÀ DEGLI STUDI DI MILANO

DEPARTMENT OF PHYSICS

PhD School in Physics, Astrophysics and Applied Physics
Cycle XXXIV

Comprehensive investigation of light neutron-rich nuclei to test modern nuclear theoretical models

Disciplinary Scientific Sector FIS/04

Supervisor: **Prof.ssa Silvia LEONI**
Co-Supervisor: **Prof.ssa Angela BRACCO**

Director of the School: **Prof. Matteo PARIS**

PhD thesis of:
Sara ZILIANI

Academic Year 2021-2022

Referees of the thesis:

Ph.D. Alessia Francesca DI PIETRO
Laboratori Nazionali del Sud (INFN), Italy

Ph.D. Gheorghe Iulian STEFAN
CNRS - Centre national de la recherche scientifique, Orsay, France

Commission of the final examination:

External Members:
Prof. Riccardo RAABE
University of KU Leuven, Belgium

Prof. Peter REITER
University of Cologne, Germany

Internal Member:
Prof.ssa Silvia LEONI
Università degli Studi di Milano, Italy

Final examination:

13th December 2021

Università degli Studi di Milano, Dipartimento di Fisica, Milano, Italy

To my hyper specific oddball

Cover illustration:

"Nucleus" Acrylic on Canvas by Shawn McNulty © 2007

Internal illustrations:

Sara Ziliani

Design:

Sara Ziliani
Annalisa Varri

MIUR subjects:

FIS/04 - Fisica Nucleare e Subnucleare

PACS:

29.30.Kv - X- and γ-ray spectroscopy
29.30.Ep - Charged-particle spectroscopy
29.40.-n - Radiation detectors
21.60.-n - Nuclear structure models and methods

Contents

Introduction

A variety of nuclear structure models, from phenomenological to first-principles approaches, is presently available, with the common goal of describing nuclear properties in systems that span from the stable nuclei in the valley of stability, to exotic ones that approach the proton and neutron drip lines. Validating and testing these theoretical models is crucial to gain accuracy and predictive power in describing nuclear structure observables. In this context, light nuclei, especially those on the neutron-rich side of the valley of stability, represent a fertile ground to look for new experimental evidence, which can be exploited to benchmark theoretical approaches. The motivation for the work presented in this Thesis is to provide an experimental investigation of light-neutron rich nuclei (in the region that goes from B to O), with state-of-the-art experimental techniques and detection systems, in order to collect novel information to be compared with the most advanced theoretical predictions currently available.

Atomic nuclei display a two-fold nature: on one side, starting from the ground state and moving up in excitation energy, they feature well-localised bound states below the particle-emission thresholds, on the other side, above particle-emission threshold, they display resonant-like unbound states in the continuum. Resonances lying close to particle-emission thresholds link the bound and unbound realms. The research activity described in this work has been developed on three levels, each associated to a different research line, that mirror the above-mentioned characteristic of the nucleus. In fact, the first line of research aims at the investigation of bound states in neutron-rich C, N and O isotopes, the second focuses on near-threshold resonances (^{11}B as a specific case), and the third on stretched unbound states in the continuum of ^{13}C, ^{14}N and ^{16}O. Altogether, a rather comprehensive body of experimental information will be discussed and confronted with some of the most advanced theoretical interpretations currently available for describing light atomic nuclei, such as *ab initio* approaches and Shell Model including the coupling to the continuum.

The present Thesis consists of four Parts, for a total of twelve Chapters, and it is structured as follows. In Part I, a brief theoretical introduction to state-of-the-art nuclear structure models (Shell-Model, Cluster-model and *ab initio* calculations) will be provided in Chapter 1. We will also contextualise the role of light neutron-rich systems in validating

modern nuclear theoretical calculations. The fundamental concept of the nucleus as an open quantum system will be introduced, and we will focus the attention on the relevance of the studies of near-threshold states, and "stretched states". Chapter 2 will give an overall illustration of the experimental techniques employed in this work (gamma and charged-particle spectroscopy), while details on the specific methods considered will be given afterwards, in the corresponding Chapters and Sections.

Part II is devoted to the study of bound states in neutron-rich C, N and O isotopes. In particular, we will present gamma-spectroscopy studies performed with the AGATA - PARIS - VAMOS multi-array detection system in an experiment performed at the Grand Accélérateur National d'Ions Lourds (GANIL), France, in July 2017 (spokepersons: S. Leoni, B. Fornal, M. Ciemała). In Chapter 3, we will introduce the case of the lifetime measurement of the 2_2^+ state in ^{16}C and ^{20}O, as one of the first examples in which electromagnetic observables in light neutron-rich nuclei have been used to validate first-principles nuclear structure calculations and pin down the role of three-body forces. We will then address the physics cases of ^{14}C and ^{18}N, whose study will be the main topic of Part II. In Chapter 4, the experiment and the detection system employed for the investigation of the above-mentioned physics case will be described. In particular, details on the deep-inelastic reaction mechanism employed and the basic features of each of the three arrays (AGATA, PARIS and VAMOS++) composing the experimental apparatus will be illustrated. Chapter 5 concerns the complete data analysis of the experiment, focusing in particular on a novel development of the Doppler-Shift Attenuation Method (DSAM), to measure nuclear excited-states lifetimes of the order of tens-to-hundreds femtoseconds, in the case of dissipative reaction mechanisms. The validation of the novel technique will be discussed in connection with known lifetimes in ^{17}O and ^{19}O, and its application will be presented in the case of excited states in ^{17}N and ^{14}C. The relevance of the AGATA performance in this kind of analysis will be also underlined. Finally, the high-resolution gamma spectroscopy of ^{18}N will be illustrated, leading to a full spectroscopy of negative-parity bound states, discussed in comparison with large-scale Shell-Model calculations.

Part III deals with the study of near-threshold resonance states. It will focus on the investigation of the existence of a near-threshold state in ^{11}B, in an experiment realised at Laboratori Nazionali di Legnaro (LNL) in February/March 2021 (spokeperson: S. Ziliani), employing gamma-particle coincidence measurements with the GALILEO + GALTRACE set-up. In Chapter 6, we will address the ^{11}B physics case: the existence of a near-threshold resonance around 11.4 MeV, in the vicinity of the proton-emission threshold, could explain a very rare phenomenon, namely the β^--delayed proton emission from ^{11}Be. This is a hot topic, that in the last few years arose the interest of both experimental and theoretical investigations. In Chapter 7, we will make a digression on the technical development of the GALTRACE silicon pixel-type telescope detector array, which represent a large fraction of this Thesis work. Details on the detectors and electronics will be presented and the performance of the system will be addressed in the context of a test experiment, performed at LNL in July 2019 (spokespersons: S. Leoni and B. Fornal), with an early version of the GALTRACE array, employed as an ancillary of the GALILEO gamma-ray spectrometer. In Chapter 8, we will present the experiment in which the ^{11}B nucleus was populated in a ^{6}Li+^{6}Li fusion/evaporation reaction, via the

evaporation of a single proton from the ^{12}C compound nucleus. The data analysis of the experiment will be presented in Chapter 9. In particular, we will discuss the GALILEO and GALTRACE data pre-processing, and we will illustrate the technique employed to extract a limit for the existence of a gamma transition of ~ 9.3 MeV, depopulating the hypothetical resonance of interest. Such a gamma transition, predicted by Shell-Model Embedded in the Continuum (SMEC) calculations to be possible with a branching ratio of 3×10^{-3}, with respect to the dominant proton emission, has been excluded with a high probability.

In Part IV, highly-lying resonances of a particular type of single-particle excitations, *i.e.*, M4 stretched resonance states, will be discussed, focusing on the case of ^{14}N and ^{16}O. Such excitations are the objective of a dedicated research program undertaken at the Cyclotron Centre Bronowice (CCB), in Kraków, Poland. Understanding the features of these rather simple resonances, would be a valuable test bench for theoretical models, such as the Gamow Shell Model (GSM), which enables calculations for states embedded in the continuum. In Chapter 10, we will recall the available information on M4 stretched states in $1p$-shell nuclei: very limited knowledge has been reported in literature, so far, about the M4 states decay. In the same Chapter, we will briefly describe the first pilot experiment of the CCB research program, in which the decay of an M4 stretched state at 21.47 MeV in ^{13}C has been studied with gamma-particle coincidences and satisfactorily compared to GSM predictions. We will then present the specific physics cases of ^{14}N and ^{16}O, where a number of M4 stretched states have been identified in previous inelastic scattering experiments with electrons, protons and pions. ^{16}O is a particularly important case, as, for this system, information on the decay of the M4 states of interest has been reported in literature, and it will serve as a test case to validate the experimental technique. In Chapter 11, we will describe the experiment performed at CCB to study ^{14}N with proton inelastic scattering (spokepersons: S. Ziliani and N. Cieplicka-Oryńczak), employing an experimental apparatus composed of the charged-particle CsI triple telescopes of KRATTA, to detect the scattered protons, coupled to four $LaBr_3$(Ce) and two PARIS clusters for the measurement of gamma rays. The 135-MeV proton beam impinged on a $Li^{14}NH_2$ lithium amide target, which was discovered to be polluted with ^{16}O, therefore ^{14}N and ^{16}O nuclei were investigated within the same experiment. Finally, in Chapter 12, the analysis of the CCB experiment will be addressed. A detailed description of the data preparation and of the experimental technique employed will be given, together with the results obtained. In particular, for ^{16}O the results are in good agreement with previous experimental investigations, thus allowing a validation of the present experimental approach. In the case of ^{14}N, only a qualitative study has been performed, which will serve as a starting point for a new experiment that will be realised at CCB with a new target, free of oxygen contamination.

A substantial fraction of Part II and Chapter 7 has appeared as peer-reviewed publications in scientific journals; the relevant articles with the list of co-authors are mentioned in the List of publications. Variations have been made in the presentation of previously published content, to maintain consistency of style and structure throughout the Thesis.

Part I

Context and methods

Chapter 1

Theoretical introduction

The number of known nuclides has grown by more than a factor of ten over the last 85 years, resulting in nearly 4000 currently known isotopes out of 118 elements. Moreover, beyond 7000 nuclei are predicted to exist in the Universe, a substantial number of them being still unknown to science and waiting to be discovered. Figure 1.1 illustrates the considerable progress in discovering new nuclei occurred between 1935 and 2015 [1]. The introduction of new reaction mechanisms, together with the progress undergone

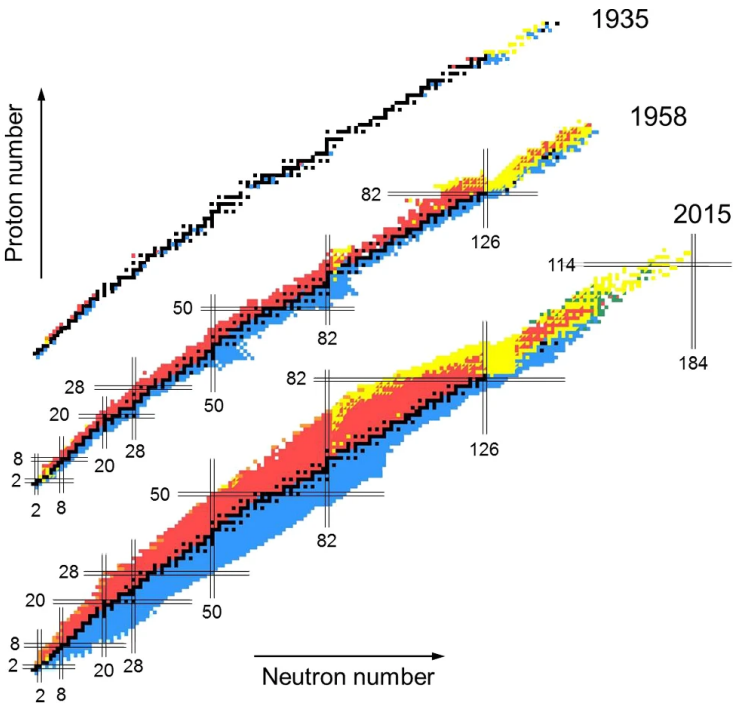

Figure 1.1: The nuclide chart evolution over 80 years, from 1935 to 2015. The first Karlsruhe Chart of Nuclides appeared in 1958 and reported up to 1500 isotopes of 102 elements. From the 327 isotopes of 92 elements recorded in 1935, the chart reached over 4000 nuclei from 118 elements in 2015. Figure reprinted from Ref. [1] [a]

[a] Licensed under the CC BY 4.0 License [2]

by experimental techniques and devices for production, separation and identification of reaction residues was at the basis of this advancement. Such an effort in discovering new nuclei has its roots in a better comprehension and characterisation of the nuclear force.

In fact, a unified description of all the nuclei present in the Universe or produced in laboratories is one of the main purposes and challenges of nuclear physics. To achieve this, highly-advanced nuclear structure models have been developed in the last decades. Many phenomenological and *ab initio* models have been introduced to describe nuclei in various areas of the nuclear chart. Up to now, no "universal" nuclear theory has been reached: different approaches are applied depending on the dimension (number of nucleons A) of the system. Figure 1.2 shows the regions of application for the three major theoretical frameworks, namely *ab initio* calculations, Configuration Interaction (CI) models (*e.g.*, interacting Shell Model), and Density Functional Theory (DFT). These theoretical approaches overlap in some regions and need to be linked and validated.

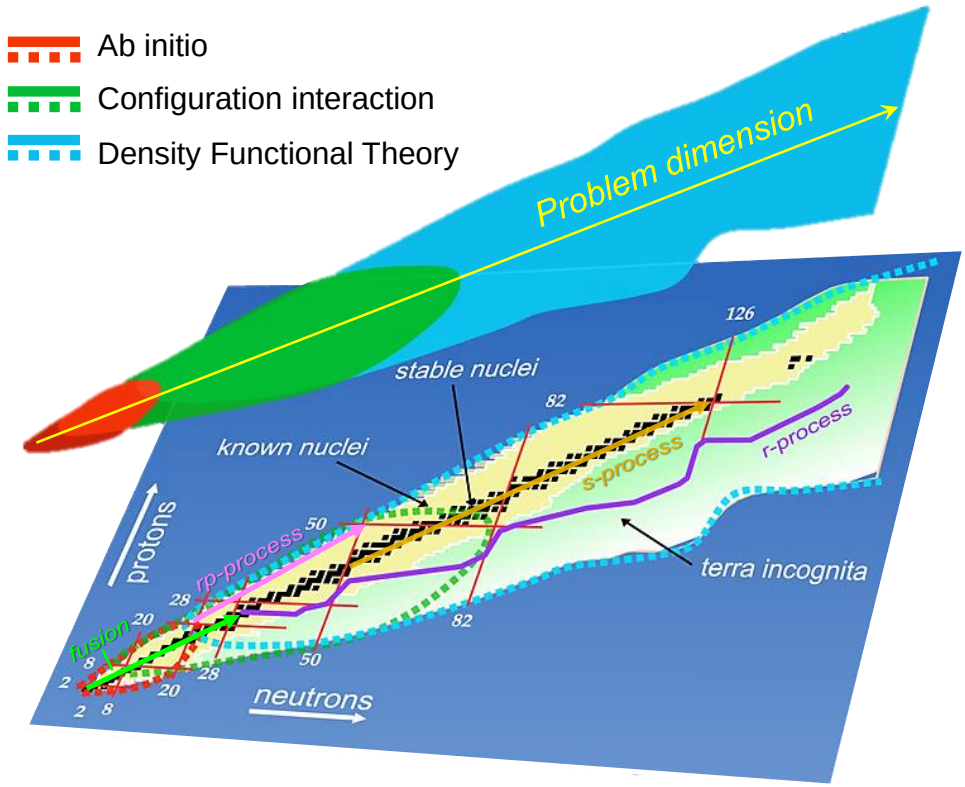

Figure 1.2: Schematic view of the chart of nuclides with the ranges of applicability of different theoretical frameworks, depending on the dimension of the problem [3]. *Ab initio* calculations are mainly considered in the treatment of light systems, while Configuration Interaction (CI) is suitable to describe light-to-medium mass nuclei. Density-Functional Theory (DFT) application ranges from intermediate up to heavy systems: light nuclei are not usually treated in such a framework.

In this context, light nuclei, for example those in the region between lithium and

fluorine, play a key role in benchmarking these sophisticated theoretical models. In fact, the study of these systems, and in particular their neutron-rich isotopes, via high-precision gamma spectroscopy or combined gamma-particle coincidence measurements, can provide unique observables sensitive to the details of the nuclear structure.

In this chapter, we will firstly give a brief overview on the nucleus as an open quantum system in Section 1.1, a fundamental concept to contextualise the work of this Thesis. Secondly, we will introduce a number of theoretical techniques useful for the interpretation of the experimental work presented afterwards. Finally, in Section 1.5, we will give an insight into the role of light nuclei in benchmarking modern nuclear theoretical models, which is the leading idea behind the experimental work reported in this Thesis.

1.1 The atomic nucleus: an open quantum system

Atomic nuclei display a dual behaviour: below particle-emission thresholds there are bound states, described by well-localised wave functions, while above the thresholds, where one or more particles can be emitted from the nucleus, resonant-like unbound states appear, as exemplified in Figure 1.3. Resonances can be depicted as specific energy regions at which the probability of the absorption of a particle (proton or neutron) in a scattering process is enhanced. This results, from an experimental point of view, in the appearance of peaks of varying widths in the cross section. In between the two opposite conditions of bound and unbound states, weakly bound systems, like halo configurations, represent an intermediate behaviour. These systems are characterised again by localised wave functions, but more extended, as less energy is required to remove one or more particles from the system.

In standard Shell Model (SM) formulation (see Section 1.2), the nucleons occupy bound single-particle orbits in an infinite potential [4]. Therefore, they are isolated from the continuum, in a closed quantum system. This approach is successful in describing bound states, but cannot account for particle-emission thresholds, decay channels and resonance states, which are instead characteristic features of open quantum systems. These features can be described by few-body techniques, which involve conglomerates of nucleons as degrees of freedom (see Section 1.3). Anyhow, these models cannot provide a full description of the nuclei bound states, because they are missing the microscopic degrees of freedom associated to the single nucleons. In this context, many innovative techniques have been developed recently, to connect the two disjoint approaches.

In this Thesis, we will concentrate on both bound states (Part II) and unbound states (Part IV and Part III) in light neutron-rich nuclei (see also Section 1.5), in order to test state-of-the-art theoretical models, that are introduced in the following.

1.2 The Shell model

The Shell Model is the nuclear analogue of the atomic theory that describes the structure of the atom, considering the electrons occupying diffuse shells in the space surrounding the positively-charged nucleus. The atomic model cannot be directly extended to the nuclear territory, as in the atomic case the potential is supplied by the external Coulomb

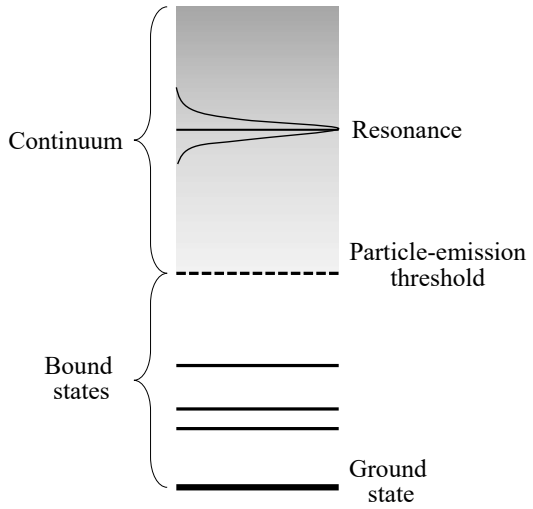

Figure 1.3: Sketch of a generic atomic nucleus level scheme structure.

field of the nucleus, while protons and neutrons move in an effective potential that they themselves create. The second major difference is that the numbers associated to shell closures (magic numbers), and consequently to particularly stable configurations, are different in the two cases, and the introduction of a distinct potential alone cannot account for this discrepancy. The solution to the prediction of magic numbers was independently found in 1949 by Haxel, Jensen and Suess [5], and by Goeppert-Mayer [6]. They showed that the inclusion of a spin-orbit coupling could give the proper separation of the subshells, as schematically shown in Figure 1.4.

Nowadays, the SM, which is a phenomenological approach, is still a valuable technique to address nuclear structure studies. New interactions, Hamiltonians and large-scale model spaces have been introduced, to extend the calculations outside the valley of stability, towards the proton and neutron drip lines. Recent SM calculations, based on an Hamiltonian developed from a monopole-based universal interaction [7], will be considered in Part II to investigate the structure of ^{18}N.

In addition, a great effort has been recently made to extend this model to include the continuum and describe open quantum systems. This extension led to the development of Gamow Shell Model (GSM) and Shell Model Embedded in the Continuum (SMEC), of which we will give here a brief overview.

1.2.1 Gamow Shell Model

As already mentioned in Section 1.1, the nucleus behaves as an open quantum system. To extend the standard SM formulation to open quantum systems, back in 1969, the so-called Continuum Shell Model (CSM) was introduced by Mahaux and Weidenmüller in Ref. [8]. In the original CSM, the Schroedinger equation is solved with an ansatz containing both bound and unbound states [9], considering a finite-depth potential to generate the single-particle basis and the radial wave functions. Only single-nucleon scattering states are

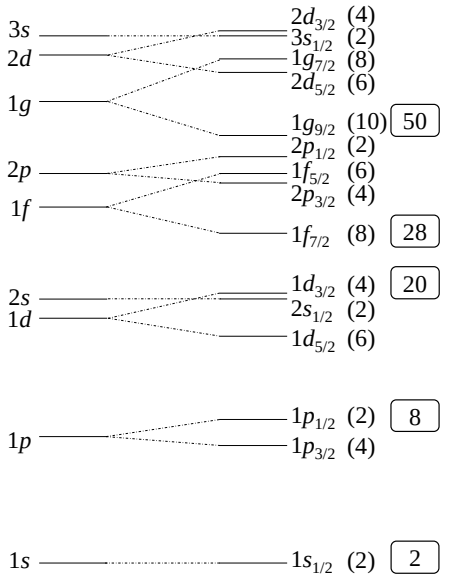

Figure 1.4: Partial nuclear SM level scheme, without (left) and with (right) spin-orbit coupling. The numbers in the boxes on the right indicate the shell closures (magic numbers).

taken into account, and the total function space is divided into two orthogonal subspaces: the Q subspace of discrete states and the P subspace of scattering states. However, in this kind of approach, variations of the radial wave functions and corrections to the effective nucleon–nucleon interaction due to the coupling to the continuum are not considered [10].

An extension of the CSM, that provides an accurate treatment of the many-body correlations and the coupling to the resonant and non-resonant continuum, is the so-called Gamow Shell Model (GSM) [11]. GSM is a complex-energy CSM implementation, formulated in the complex-k momentum plane, based on the Berggren ensemble. If CSM relied on a kind of artificial separation between bound/resonant and non-resonant scattering states, GSM, instead, treats all the states on the same footing.

1.2.2 Shell Model Embedded in the Continuum

When moving away from the valley of stability, a more realistic description of the bound-states subspace is needed. CSM cannot provide this kind of accuracy, due to the restricted space of configurations generated with the finite-depth potential. In this context, the so-called Shell Model Embedded in the Continuum (SMEC), introduces the realistic SM to generate the A-particle (A being the mass number) wave functions [10, 12].

In SMEC, as in CSM, only single-particle resonances are treated. The equations to be solved are the same as in CSM [13], but with the difference that the starting point is a realistic SM calculation and the coupling to the continuum is added in a second step. In addition, the ingredients needed to solve these equations are modified on the basis of the nucleus considered.

1.3 Cluster models and collective phenomena

Nuclear matter displays a quantum-liquid structure, where nucleons behave as independent particles in a mean field, resulting in shell structures, as explained in Section 1.2. However, a second nature coexist with this feature in nuclear systems: finite nuclei can behave like molecules composed of conglomerates of protons and neutrons, called clusters [14, 15], like in Figure 1.5. Clusters, were thought to play a relevant role in nuclear structure, especially in light nuclei, since the very beginning of nuclear physics. Nowadays, we are aware that the clustering phenomenon is influential not only in defining the properties of both ground and excited states in N=Z nuclei [14], but also of states close in excitation energy to particle-emission thresholds, where collective phenomena become dominant [16–18].

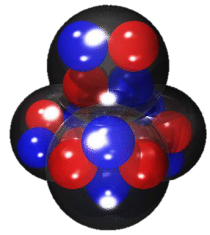

Figure 1.5: Schematic representation of ^{16}O alpha-cluster structure.

Historically, α clusters were the first to be investigated, owing to the high binding energy and stability of the alpha particle, which makes it a natural cluster. Back in 1968 Ikeda *et al.* [19] suggested a threshold picture of cluster states in Z=N nuclei, which means that states close to α-decay thresholds have a well-developed α-cluster structure. The α formation as a stable subunit within the nucleus and the arising of collective states in the vicinity of emission thresholds were at the origin of the Ikeda diagram [19]. In the diagram, α-conjugate nuclei, *i.e.*, nuclei that can be decomposed into alpha subunits, are presented in an excitation energy vs. mass number plot, with their α-cluster structures close to the associated decay thresholds [16]. Moreover, when other valence particles (protons and neutrons) are added to these systems, they can be shared by the α-particle cores, in a process analogous to the exchange of electrons in atomic molecules, and a variety of molecular structures arise in these cases [20–22].

The first models developed in the '30s to describe nuclear clustering assumed a geometric arrangement of pre-existing clusters within the nucleus, that moved in an effective interaction [15]. The ground and excited states were then described in terms of different geometrical configurations of the clusters. This assumption is a valid starting point to derive an approximate solution of the many-body Schroedinger equation and a the natural basis for the characterisation of collective continuum states [23]. However, such a picture is incompatible with the Shell Model framework.

The dualism between shell-model and cluster-model descripions was overcome via the introduction of theoretical calculations that described the nucleus as an A-body system, without assuming neither the presence of a mean field nor pre-existing clusters.

This kind of approach could take into account both single-particle shell structure and cluster correlations on an equal footing. Even so, the clustering assumed in the geometrical α-particle models could be deduced from these techniques [15]. In parallel, a great effort had been made in developing realistic nucleon-nucleon interactions, some of them based on more fundamental assumptions, such as Effective Field Theory (see Section 1.4).

Having a detailed description of clustering phenomena and cluster models is beyond the scope of this work. An extensive review on these topics can be found in Ref. [15, 16]. However, in Section 1.5.2 we will address the case of collective phenomena in close proximity to particle-emission thresholds in light nuclei within the recently proposed SMEC framework, already presented in Section 1.2.2.

1.4 *Ab initio* models

A great deal of research has been undertaken to provide a unified description of the atomic nucleus with a bottom-up approach, *i.e.*, from first principles, to compensate for the limitations of phenomenology, especially far away from the valley of stability. This kind of approaches, called *ab initio*, have seen an exponential growth during the past decade, in which they passed from describing only few light stable nuclei in 2010 to reach nuclei with Z=40 and N=50 between 2016 and 2018, and pushing to proton and neutron drip lines in 2020 [24].

Ab initio methods aim at solving a non-relativistic many-nucleon Schroedinger equation with the inter-nucleons interaction as the only input [25]. This is a challenge, due to the complex nature of the nuclear force, which arises from the underlying Quantum Chromodynamics (QCD), the fundamental theory of the strong force between quarks and gluons. The strong-force coupling is small enough at high energies to allow perturbative expansions. However, it becomes large in the low-energy region relevant for nuclear structure and dynamics, making QCD non-perturbative in this regime. A possible solution is to introduce the framework of effective field theoy (EFT) [26], for which the quark degrees of freedom are frozen and pions mediate the effective strong force between non-fundamental particles, *i.e.* the nucleons, which are considered as degrees of freedom. As outlined by Weinberg in its seminal paper [27], it is possible to construct general effective Lagrangians, consistent with the symmetries of QCD, and in particular the broken chiral symmetry. In chiral EFT, nuclear forces are given by a systematic expansion of two-nucleon (NN), three-nucleon (NNN), and many-nucleon interactions that include pion exchanges and contact terms.

We will give a brief introduction to a selection of *ab-initio* models, that will be recalled to interpret experimental results in this work.

1.4.1 No-Core Shell Model

In the No-Core Shell Model (NCSM) [28], a system of A point-like non-relativistic nucleons that interact by realistic two- (NN) or two- plus three-nucleon (NN+NNN) interactions are considered. All the nucleons are treated as active, *i.e.* there is no inert core, like in standard shell-model calculations. An harmonic oscillator (HO) basis is used,

truncated by a chosen maximal total HO energy of the A-nucleon system. This basis allows the use of single-nucleon coordinates and the second-quantisation representation without violating the translational invariance of the system. As a result of the basis truncation, a renormalisation procedure is adopted, to take into account short-range correlations. This procedure results in softened effective interactions, that act among all A nucleons and preserve the symmetries of the initial or "bare" NN+NNN interactions.

1.4.2 Many-Body Perturbation Theory

The Many-Body Perturbation Theory (MBPT) is a quantum field theory aimed at resolving many-body problems, with the aim of second quantization and Green functions. It relies on the partitioning of a given Hamiltonian H in an unperturbed part H_0 plus a perturbation H_1,

$$H = H_0 + H_1 \tag{1.1}$$

that allows an expansion of the eigenvalues and eigenstates in powers of H_1, usually starting from a mean-field solution. This method has been successfully used together with interactions built with the chiral EFT, and a recent review with a detailed description of the MBPT implementations can be found in Ref. [29].

1.4.3 Valence-Space In-Medium Similarity Renormalisation Group

Similarity Renormalisation Group (SRG) methods were introduced independently in the context of condensed matter and light-front quantum field theories, by Wegner [30] and by Glazek and Wilson [31]. These techniques aim at simplifying the Hamiltonian through continuous unitary transformations, in order to decouple low- and high-momentum regimes, suppressing off-diagonal matrix elements. SRG can be carried out in free space, with the advantage that it does not require to be implemented for each different nucleus. However, it does not allow to handle NNN or higher-body interactions. A valid alternative consists in performing SRG evolutions directly in the A-body system of interest, from which the name In-Medium SRG (IMSRG) [32]. This approach has the advantage of describing three- to A-body operators using two-body tools and operators normal ordering, and it is non-perturbative. IMSRG has been further developed decoupling core, valence and beyond-valence states, and introducing the solution of the eigenvalue problem in the valence space with shell-model codes and an improved operator basis. This last implementation of the method is called Valence-Space IMSRG (VS-IMSRG) [33].

1.5 The role of light nuclei: from bound to unbound states

Light-nuclei structure properties can be accessed by both state-of-the-art *ab initio* and large-scale shell model calculations [7, 34–36], as shown in Figure 1.2, while DFT calculations are not suitable to describe this kind of systems. For all these approaches, the common goal is to describe nuclear interactions and nuclear properties in systems that go from the stable nuclei of the valley of stability to those exotic systems that lie close to the drip lines. For intermediate-mass and heavy elements, the known isotopes lie far away

from the predicted neutron drip line (see Figure 1.2), but in the case of light systems this boundary has been reached [37–42]. Therefore, light nuclei, especially the neutron-rich ones, represent a particularly fertile ground to investigate nuclear properties and test nuclear structure theoretical models predictions, which need experimental validation to reach sufficient accuracy in the description of nuclear structure observables, such as level ordering, decay branchings, and so on. In addition, these systems are the only ones accessible by *ab initio* calculations mainly due to computational capabilities, although great improvements and extensions of these methods took place in the last ten years [24].

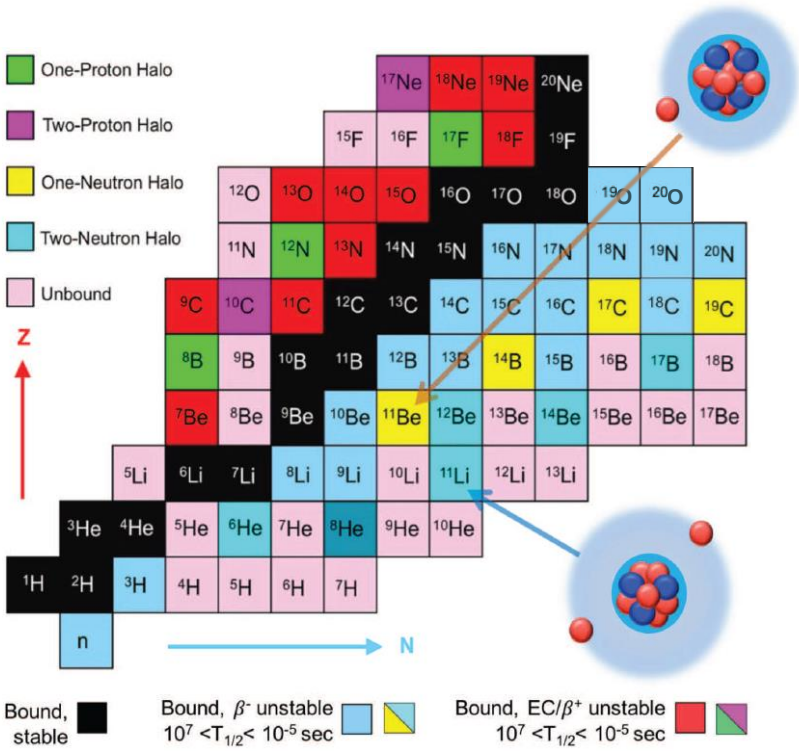

Figure 1.6: Light region of the nuclear chart, with details on the general ground-state properties of the isotopes displayed. Figure reprinted by permission from Springer Nature: Ref. [43], Copyright 2018.

Figure 1.6 displays the light sector of the nuclear landscape, with nuclei up to nearly $A = 20$. Just by looking at this Z vs. N map, one can have a feeling of the wide range of characteristics that occur even when a limited number of nucleons is considered [43]: a significant part of the light nuclei shown are either unstable or unbound, and their properties range from the well-known stable nuclei, to halo systems, up to unbound nuclei beyond the drip lines. In addition to these very general features, this region of the nuclear chart is particularly rich with a variety of phenomena, from clustering [14, 15], to the appearance of three-body forces effects in the nuclear interaction [44, 45]. Moreover, the structure of light neutron-rich nuclei has a significant impact in nuclear astrophysics

[46–50]. For example, these light systems can be considered to extend reaction networks usually involving only heavier systems in the modelling of processes of astrophysical interest [46]. In particular, this is the case of the *r* process, which is at the basis of the production of heavy elements [51] (see Figure 1.2 for the approximative *r*-process path).

The work of the present Thesis is placed in this context, with the leading idea of presenting a comprehensive experimental investigation of light neutron-rich nuclei, looking for new observables, which can be used to test modern nuclear theoretical models. To achieve this, we will explore the nucleus intended as an open quantum system, starting from the simpler case of bound states, passing then to the investigation of unbound states near particle-emission thresholds, which are the link between bound and continuum realms, and finally we will study resonances in the continuum, well above the particle-emission thresholds. In the following, we will provide some details regarding these three (bound, near-threshold, and unbound) regions of interest with examples in the case of light nuclei of B, C, N and O, in connection to theoretical calculations.

1.5.1 Bound states

The investigation of bound states in neutron-rich light nuclei can shed light on the details of the nucleon-nucleon interaction. The three body term of the nuclear force, for example, plays an important role in these light systems. The effects of NNN forces are amplified and testable in neutron-rich nuclei, a remarkable example being the anomaly in the oxygen isotopic chain neutron drip line location, which is observed in correspondence to ^{24}O, closer to the valley of stability than expected. This anomaly can be explained within the SM approach when three-nucleon forces are introduced [36].

Recent *ab initio* calculations indicated the strong sensitivity of the bound excited states lifetimes to the features of the nuclear interaction. NCSM and MBPT approaches (described in Sections 1.4.1 and 1.4.2, respectively) were employed to calculate electromagnetic transition probabilities between excited states in neutron-rich carbon [44] and oxygen [45] isotopes, respectively. Rather low sensitivity to the details of the nuclear force were observed in the case of the $2^+_1 \rightarrow 0^+$ transitions in even-even isotopes, while observables related to higher-lying excitations, especially the 2^+_2 states, exhibited high sensitivity. In particular, the state lifetimes appeared to be largely depending to the inclusion of three-body terms in the interaction considered. Table 1.1 summarises the lifetimes deduced from the theoretical transition probabilities of the first and second 2^+ states in ^{16,18}C and ^{20,22}O neutron-rich isotopes, obtained including two-body terms only (NN) or two-body plus three-body (NN+NNN) interactions. The lifetimes of the 2^+_1 states are not significantly influenced by the introduction of NNN forces, while the ones of the 2^+_2 states can vary nearly up to a factor 3. More recently, the most advanced VS-IMSRG *ab initio* method (see Section 1.4.3) was employed to calculate the lifetime of the 2^+_2 state in ^{20}O [52] (see Table 1.1), improving MBPT estimates. A shorter lifetime was still confirmed with respect to the case of NN terms only.

Being able to access this information on the lifetimes of bound excited states is a crucial point to test *ab initio* calculations. This, in fact, was the aim of the experiment of Ref. [52], that will be presented in Part II, in which the lifetime of the second 2^+ state in ^{16}C and

Table 1.1: Lifetimes (τ) of the first and second 2^+ states in ^{16,18}C and ^{20,22}O from the *ab initio* calculations, using NCSM for the C isotopes and MBPT for the O ones, with NN and NN+NNN interactions. In the case of ^{20}O, predictions for the lifetime of the 2^+_2 state is also given from the VS-IMSRG *ab initio* approach. The literature experimental lifetimes (τ_{exp}) are quoted in the last column [53]. In blue bold are reported the lifetimes measured in the experiment of Ref. [52] (see also Section 3.1).

Nucleus	Excited state	τ [ps]		τ_{exp} [ps]
		NN	NN+NNN	
^{16}C	2^+_1	24	24	$11.4^{+1.2}_{-1.9}$
	2^+_2	0.23	0.08	**<0.18**
^{18}C	2^+_1	19.4	20	22.4(35)
	2^+_2	2.2	1.1	<4.6
^{20}O	2^+_1	10.3	11.7	10.5(4)
	2^+_2	0.32	0.20 (MBPT) 0.18 (VS-IMSRG)	**$0.15^{+0.08}_{-0.03}$**
^{22}O	2^+_1	0.40	0.46	0.69(28)
	2^+_2	0.064	0.043	-

^{20}O was measured. In Section 3.1 we will briefly recall the results of this measurement, and then we will move on to investigate a number of other light neutron-rich C, N and O isotopes populated in the same experiment (see Chapter 3). The study of bound states in these systems to derive observables, which can be compared to modern theoretical predictions, is the main topic of Part II.

1.5.2 Near-threshold states

Resonances lying in close proximity to particle-emission thresholds are called near-threshold states. These unbound states are at the basis of our understanding of the creation of elements in nucleosynthesis processes taking place in stellar environments. The most famous example of this kind is found in ^{12}C (see Figure 1.7): the prediction and then the discovery of the so-called Hoyle-state, from the name of the British astronomer who predicted its existence in 1954 [54], just 287 keV above the α-decay threshold, has been a real breakthrough. The presence of this resonant state at the "right" energy of 7.65 MeV boosts the production of ^{12}C through the capture of an α-particle by the very shortly-living ^{8}Be ($\sim 10^{-16}$ s), in a triple-alpha process that otherwise would be rather weak. On this mechanism relies the explanation of the abundances of ^{12}C and ^{16}O in the Universe [55].

In general, the importance of these states for nucleosynthesis relies on the existence of γ-decay branches, toward the ground state, which dictate the production rate of the

nucleus of interest, following the capture into the near-threshold state. In some nuclei on the neutron-deficient side of the valley of stability, the γ transition strength from near-threshold states has been measured by employing fusion reactions that strongly populate the states of interest. For nuclei located on the neutron-rich side, instead, such measurements are extremely difficult, because the processes used here to populate near-threshold states have rather low cross sections.

From the nuclear structure point of view, near-threshold states are predicted to exhibit a strong collectivization. This property is considered as a direct probe of the impact of the continuum on the structure of light systems and the key microscopic mechanism at the basis of a number of different features observed in light nuclei, like the emergence of nuclear clustering [16] (see Section 1.3).

The SMEC (see Section 1.2.2) considers the nucleus as an open quantum system and it explicitly points out that near each particle-decay threshold, namely p and n thresholds, should exist a "narrow" and collective state of the same particle character [56], as indeed observed in several light systems (see Figure 1.7). This finding, being in full agreement with the Ikeda rule (see Section 1.3), gave confidence in the SMEC approach, as the one which can explain the near-threshold collective phenomena. The presence of such a state is a signature of a deep change in the near-threshold shell-model wave function and the direct manifestation of continuum-coupling correlations. This generic collectivization phenomenon is also predicted by the SMEC model to affect the γ-ray emission from near-threshold states, which could be enhanced in the case of strongly collective near-threshold states [56, 57].

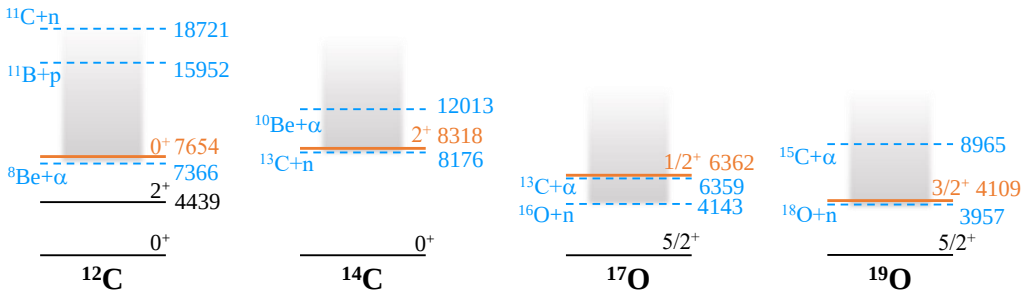

Figure 1.7: Example of light nuclear systems displaying near-threshold states (orange solid line). Black solid lines correspond to selected low lying states, blue dashed lines to particle thresholds in ^{12}C, ^{14}C, ^{17}O and ^{19}O, respectively from left to right. Energies are given in keV [53].

If the effect of near-threshold collectivisation predicted by the SMEC is experimentally confirmed, a strong impact is expected on our understanding of nucleosynthesis involving nuclei lying on the neutron-rich side of the valley of stability. In fact, there is no pertinent theoretical argument to support that this collectivisation mechanism should not occur in the vicinity of other types of thresholds. Indeed, experimental evidence of near-threshold states in the vicinity of more complex thresholds, such as, for example, those associated with α, triton, deuteron, ^{3}He or more complex clusters, has been already provided (see Figure 1.7).

It is important to note, however, that at present it is impossible to calculate the γ-ray branch from near-threshold states coupled to cluster-emission thresholds, within the SMEC. In addition, the predictions from the SMEC could not be verified thus far in neutron-rich systems, because experimental information on the γ decay from near-threshold states is very limited to some specific cases (*e.g.*, ^{12}C [58]): the branching for the γ decay, in fact, is of the order of 10^{-3}-10^{-5} and makes its measurement a real challenge. Knowledge can, however, be advanced nowadays by using modern experimental capabilities and by selecting the appropriate nuclear systems. This point will be addressed more in details in Part III, where a near-threshold resonance in ^{11}B, will be searched using gamma-particle coincidence measurements.

1.5.3 Unbound states

As already mentioned in Section 1.1, theoretical models suitable to describe bound states properties can no longer be reliable when unbound states are considered, and vice versa. The presence of the continuum, in fact, strongly influences the properties of unbound states [59]. Recently developed theoretical models, such as GSM (see Section 1.2.1), which include the coupling to the continuum in order to describe both bound and unbound states, would therefore profit from experimental validations aiming at a detailed investigation of resonant states in the continuum, including their decay properties, from which information on the resonant state wave function can be inferred. This type of validation can be performed, for example, considering particular unbound excitations, such as the so-called "stretched states".

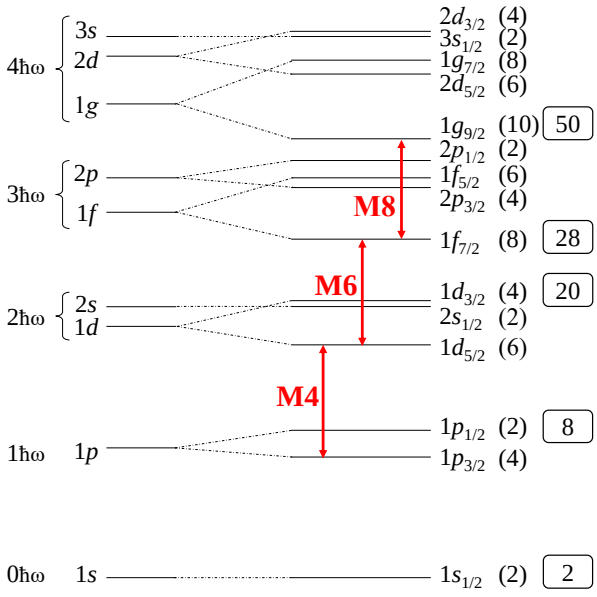

Figure 1.8: Excitation scheme of M4, M6 and M8 transitions in $1p$-shell ($1p_{3/2} \rightarrow 1d_{5/2}$), $2s1d$-shell ($1d_{5/2} \rightarrow 1f_{7/2}$), and $1f2p$-shell ($1f_{7/2} \rightarrow 1g_{9/2}$) nuclei, respectively.

Among the nuclear excitations, stretched states are one of the simplest known. They are single-particle excitations characterised by a single particle-hole component. Both the excited particle and the residual hole have the largest angular momenta, j_p and j_h respectively, within their shells, that furthermore couple to the largest total angular momentum $J_{max} = j_p + j_h$ [60]. In the SM picture, these configurations arise from high-multipolarity magnetic transitions $(j_p j_h^{-1})^J$: $(1d_{5/2}1p_{3/2}^{-1})^{4^-}$ in $1p$ shell (M4), $(1f_{7/2}1d_{5/2}^{-1})^{6^-}$ in $2s1d$ shell (M6), $(1g_{9/2}1f_{7/2}^{-1})^{8^-}$ in $1f2p$ shell (M8), and so on, as exemplified in Figure 1.8.

Transitions to stretched states are relatively simple, as no other one-particle-one-hole configuration could couple to the same total angular momentum. States of this kind, having the same parity and quantum numbers, should occur at least $2\hbar\omega$ higher in excitation energy. The configuration mixing should then be minimal due to the uniqueness of the maximally stretched particle-hole excitations. However, the nuclear wave functions of these states do not necessarily reflect their purity: instead of the stretched configuration alone, admixtures of more complicated multi-particle-multi-hole configurations inside the same shell are expected. This mixing causes the fragmentation of the M4 strength among a number of different final states [61, 62]. Therefore, direct measurements of the characteristics of stretched states, such as decay schemes, should offer relevant material to verify up-to-date theoretical methods, such as Gamow Shell Model calculations. Understanding the features of these states can also help to extend the knowledge on nuclear dynamics, including transition amplitudes, transition densities, and isospin properties [60, 63]. The study of M4 stretched states decay pattern in selected light nuclei will be the topic of Part IV.

Chapter 2

Experimental techniques

In this Chapter we will address the experimental techniques that will be used in the present work: gamma-ray and charged-particle spectroscopy and lifetime measurement techniques.

2.1 Gamma-ray and charged-particle spectroscopy

Gamma-ray spectroscopy is a widely-employed technique to identify and quantitatively investigate radionuclides through the study of their gamma-ray energy spectra, measured in gamma spectrometers. Gamma rays are an excellent probe for nuclear structure studies: they can be used to reconstruct nuclei level schemes, to measure excited states spin and parity (J^π) and lifetimes (τ), from which the details of the nuclear wave functions can be inferred. These observables are established measuring transition energies (E_γ), transition rates and branching ratios, angular distributions and correlations. Establishing coincidence or anti-coincidence relationships is one of the most important techniques employed in gamma spectroscopy, that on the one hand allows to reconstruct gamma cascades and level schemes and on the other hand permit to suppress the background or reject partial energy deposition events, such as Compton scattering events.

From the instrumentation point of view, in the last decade, the increasingly demanding necessity to cope with new challenging measurements, in particular at the upcoming radioactive ion beam (RIB) facilities, a common effort has been made to develop new cutting-edge detector arrays. On the one hand, high-resolution γ-ray spectrometers, like the Advanced GAmma Tracking Array (AGATA) in Europe (see Section 4.1) or the Gamma-Ray Energy Tracking In-beam Nuclear Array (GRETINA) in the United States [64], are now available and they are constantly upgraded. On the other hand, these state-of-the-art spectrometers need to be complemented with other ancillary detectors, such as light charged-particle arrays (MUGAST [65], EUCLIDES [66], TIARA [67]), heavy-ion spectrometers (VAMOS++ [68, 69], PRISMA [70]), and neutron detection systems (Neutron Wall [71], NEDA [72]).

Gamma spectroscopy is the main technique that will be employed in the present work to investigate light neutron-rich nuclei, as anticipated in the previous chapter. Different detection systems for the measurement of γ rays will be presented in each Part, with details on their experimental configuration (number of detectors, geometry,

detection materials), performance (energy resolution, efficiency) and purpose. Both state-of-the-art (*e.g.*, AGATA in Section 4.1 and PARIS in Section 4.2) and more traditional (*e.g.*, GALILEO in Section 7.2.1) gamma spectrometers will be discussed, with their electronic chains and analysis software. These arrays are made of a variety of different detectors: segmented germanium detectors without anti-Compton shields, phosphor-sandwich inorganic scintillation-based detectors, traditional High-Purity Germanium (HPGe) crystals with anti-Compton shields and large-volume $LaBr_3$(Ce) crystals.

Both γ-γ and γ-particle coincidence measurements will be exploited. The gamma-ray spectroscopic studies presented in this work are in fact complemented by charged-particle detection techniques, which give access to additional information not available with pure gamma spectroscopy. For example, the direct decay from an excited state to the ground state of its daughter nucleus via the emission of a particle cannot be measured using gamma-spectroscopy studies, as no gamma rays are emitted.

In the case of the present Thesis we will exploit the measurement of heavy-ion reaction products, inelastically scattered or evaporated light charged particles in coincidence with gamma rays to tag reaction channels, reconstruct the excitation energy spectrum of the nuclei of interest, and to perform precise Doppler-shift corrections of the gamma-ray energy spectra. Different charged-particle detection systems (VAMOS++ in Section 4.3, KRATTA in Section 11.1, GALTRACE in Chapter 7) will be also presented in the work.

Gamma and charged-particle spectroscopy are common well-established techniques, therefore we will not discuss them in details here. An extensive coverage of the techniques and instruments that are important in the detection and spectroscopy of ionizing radiation can be found in Refs. [73, 74].

2.2 Lifetime measurement techniques

Part of the Thesis (see Part II) will be devoted to measure the lifetimes of selected excited states in some nuclei of interest. We will introduce here the reasons behind the importance of measuring excited states lifetimes and the techniques available. We will concentrate in particular on the Doppler-Shift-Attenuation Method (DSAM), of which we will present a novel implementation in Chapter 5 to extend the technique to nuclear-state lifetimes of the order of tens-to-hundreds femtoseconds in low-energy heavy-ion binary reactions.

The knowledge of the lifetime τ of a nuclear state provides essential information on the structure of the state itself and valuable observables to test theoretical nuclear models. The state lifetime is directly connected to the transition probability $T(^{E}_{M}\lambda)$ to a given final state, which contains information on the wave function composition of the initial and final states. The partial decay time τ_γ, relative to a particular γ transition, can be expressed in terms of the transition probability $T(^{E}_{M}\lambda)$ as in Equation (2.1), where E and M stand for the electric and magnetic character of the radiation, respectively, and λ is the transition multipolarity.

$$\tau_\gamma = \frac{1}{T(^{E}_{M}\lambda)} \tag{2.1}$$

The total lifetime τ of the state is then expressed as:

$$\tau = \tau_\gamma \frac{I_\gamma(^E_M\lambda)}{I_{TOT}} \tag{2.2}$$

where $I_\gamma(^E_M\lambda)$ is the intensity of the transition and I_{TOT} is the sum of the intensities of all the γ transitions that depopulate the state.

Transition probabilities are then directly proportional to the reduced transition probabilities $B(^E_M\lambda)$, through the conversion relations reported in Table 2.1. Reduced transition probabilities are defined as follows [75]:

$$B(^E_M\lambda; I_i \rightarrow I_f) = \frac{1}{2I_i+1} |\langle\psi_f| \,|\mathcal{M}(^E_M\lambda)|\, |\psi_i\rangle\,|^2 \tag{2.3}$$

where $\mathcal{M}$ is the electric (E) or magnetic (M) transition operator and I_i and I_f are the spin of the initial and final states connected by the γ transition. The reduced transition probability is directly proportional to the matrix element involving the initial and final states wave functions ψ_i and ψ_f. The wave functions carry the information on the nuclear structure and this dependence makes the reduced transition probability (and therefore the lifetime) one of the best probes to investigate the nuclear interaction.

Table 2.1: Conversion relations between the transition probabilities $T(^E_M\lambda)$ and the reduced transition probabilities $B(^E_M\lambda)$. $B(^E_M\lambda)$ are expressed in units of e^2 $fm^{2\lambda}$ and the transition energies E_γ in MeV [74].

λ	$T(E\lambda)$ [s^{-1}]	$T(M\lambda)$ [s^{-1}]
1	$1.59\times10^{15}\,E_\gamma^3\times B(E1)$	$1.76\times10^{13}\,E_\gamma^3\times B(M1)$
2	$1.22\times10^{9}\,E_\gamma^5\times B(E2)$	$1.5\times10^{7}\,E_\gamma^5\times B(M2)$
3	$5.67\times10^{2}\,E_\gamma^7\times B(E3)$	$6.28\times\,E_\gamma^7\times B(M3)$
4	$1.69\times10^{-4}\,E_\gamma^9\times B(E4)$	$1.87\times10^{-6}\,E_\gamma^9\times B(M4)$

The excited states lifetimes can be measured via direct or indirect techniques, the former involving for example timing measurements or analysis of the emitted gamma radiation. In the indirect methods, the lifetime is inferred from a measurement of the width Γ of the excited state of interest ($\tau = \hbar/\Gamma$), a technique that is applied to the case of unbound resonance states.

Depending on the range in which the lifetime falls, a variety of techniques are available to measure the lifetime. Here is a summary of some relevant direct techniques with the associated range of application.

Direct measurement [$\tau > 10^{-3}$ s] the lifetime is directly measured observing the exponential decay of the activity A as a function of time ($A = A_0 e^{-kt}$), as the mean lifetime can be expressed in terms of the decay constant k through the relation $\tau = 1/k$ [76].

Fast timing [10^{-3} s > τ > 10^{-11} s] the lifetime of a nuclear state is determined from the time difference between the coincident radiation populating the state and the one de-exciting it [76].

Plunger [10^{-10} s > τ > 10^{-12} s] the lifetime is measured exploiting a movable plunger, placed behind a thin target at a distance d, to stop the recoil nuclei formed in an excited state with a velocity v_r. The energy of gamma rays emitted when the nucleus is still in flight will be Doppler shifted, while for those emitted when the nucleus has been stopped in the pluger no shift can be observed. The fraction F of the not-shifted gamma-ray intensity is directly related to the lifetime through $F = e^{-d/(v_r\tau)}$ [74].

DSAM [10^{-11} s > τ > 10^{-14} s] this technique relies on the Doppler-shift attenuation process that the energy of a γ ray undergoes, when it is emitted by a decelerating nucleus inside of a stopping material [77]. The lifetime is extracted analysing the line shape of the γ-ray peaks associated to the de-excitation of the state of interest. See Section 2.2.1 for more details.

A review of the experimental techniques, both direct and indirect, for the measurement of mean lifetimes τ of excited nuclear states can be found in Ref. [78].

2.2.1 DSAM

In the most commonly used version of the Doppler-Shift-Attenuation Method (DSAM), an excited state is populated in a nuclear reaction and it decays via gamma emission while the nucleus is recoiling in matter, namely in the target or in the target backing. Without the presence of a stopping material, the energy of the γ-rays emitted in-flight would be seen as fully Doppler-shifted, following Equation (2.4)

$$E_\gamma = E_\gamma^0 \frac{\sqrt{1-\beta^2}}{1-\beta cos(\theta_{rel})} \tag{2.4}$$

where $\beta = v_r/c$ is the relativistic factor, with v_r the emitting-ion velocity and c the speed of light in vacuum, E_γ^0 the energy of the γ ray depopulating the level of interest observed at rest, and θ_{rel} the relative angle between the momentum vectors of the recoiling ion and the emitted gamma ray.

When the emitting nucleus slows down and eventually stops inside the material, the Doppler shift becomes attenuated. In fact, the velocity of the recoiling ion continuously decreases inside the material and the γ-ray energy varies smoothly from the shifted to the unshifted energy, with an average energy shift expressed as in Equation (2.5).

$$\Delta E_\gamma(\theta_{rel}) = F(\tau) E_\gamma \beta cos(\theta_{rel}) \tag{2.5}$$

Here $F(\tau)$ is an attenuation coefficient depending on the nuclear state mean lifetime τ and on the stopping power. The resulting gamma-ray line shape depends on the lifetime, as shown in Figure 2.1, where the gamma rays are assumed to be measured in the forward direction with respect the ions recoil and a fixed stopping power is considered. No shift is expected to be observed in the gamma-ray energy spectrum for lifetimes longer than the stopping time of the nuclei in the material. A full Doppler shift is expected instead for very short lifetimes, as the energy loss in the material is negligible on those time scales.

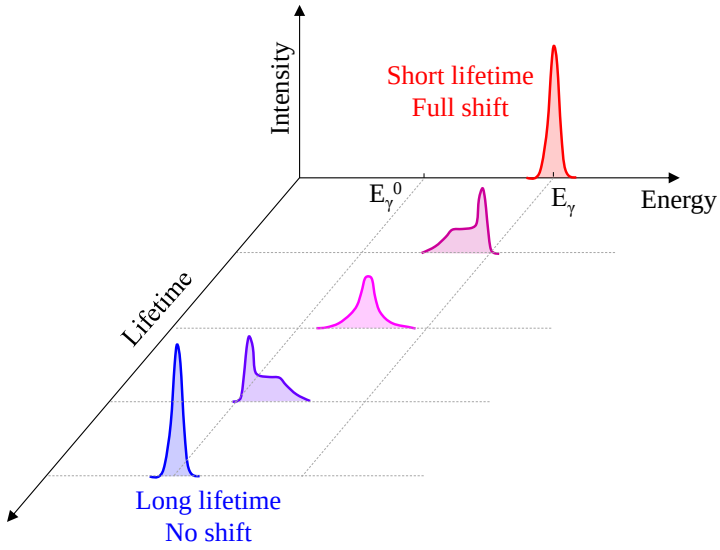

Figure 2.1: Schematic representation of the lifetime effect on the energy spectrum of gamma rays emitted from a recoiling nucleus in a material with a fixed stopping power. A full Doppler shift is expected for short lifetimes (negligible energy loss at the moment of the decay), while no shift can be observed for long lifetimes (nuclei stopped in the material).

The lifetime can be extracted analysing the line shape of the gamma-ray peak, simulating an energy spectrum taking into account the stopping power of the ions in the material, the velocity distribution of the nuclei at the decay time, the feeding of the state of interest, and the detectors response. The lifetime measurement becomes an optimization problem in which the simulated energy spectrum is iteratively compared to the experimental data, until a χ^2 minimum is found for a specific lifetime value.

The standard DSAM technique, however, cannot be directly applied in cases in which the velocity distribution of the decaying nuclei is not well defined by the reaction kinematics. This is the case, for example, of highly-dissipative reaction mechanisms, which lead to complex velocity distributions of the reaction products. A novel Monte Carlo implementation of the DSAM, that extends the technique to measure short lifetimes (~10-100 fs) of states populated in deep-inelastic binary reactions, will be presented in Section 5.2. Such a method has been developed in the framework of this Thesis.

Part II

Study of N and C isotopes with AGATA+PARIS+VAMOS

Chapter 3

Physics case

In Part I, a general introduction to state-of-the-art theoretical calculations has been presented. The common goal of all these methods is to probe nuclear interactions and describe nuclear properties in a broad variety of nuclei, including exotic systems outside the valley of stability. This goal can be addressed from the Shell Model (SM) point of view, or with a bottom-up approach, like in the case of *ab initio* methods. In this context, light nuclei in the mass region between $10 < A < 20$ represent an accessible source of valuable information for testing this type of approaches, especially the *ab initio* ones, that cannot be presently extended to much heavier systems mainly due to computational capabilities.

Testing the quality of different *ab initio* approaches was indeed the main idea behind an experiment realised at the Grand Accélérateur National d'Ions Lourds (GANIL) in Caen, France, in July 2017 [52], through the measurement of the lifetime of the second 2^+ state in ^{16}C and ^{20}O (see Chapter 4 for the experiment details). In the experiment, these nuclei were populated with low-energy transfer and deep-inelastic processes induced by a ^{18}O beam at 126 MeV of total kinetic energy on a thick ^{181}Ta target. As a by-product of the reaction, several other neutron-rich isotopes of B, C, N, O and F elements were produced, among which ^{14}C and ^{18}N are of particular interest and will be discussed in this work.

For many nuclei in this region, little is known of the excited states and electromagnetic transitions, and some information comes from very old experiments. Therefore, a precise and extensive investigation of such systems can help to extend and improve the available spectroscopic information and confirm previous results. High-precision γ spectroscopy was performed by measuring the γ rays emitted from the excited states of these nuclei with the Advanced GAmma Tracking Array (AGATA) [79–81].

The present Part of the Thesis is organised as follows: in this chapter, we will firstly recall in Section 3.1 the results obtained for the ^{16}C and ^{20}O cases, as a remarkable example that demonstrates the role of light neutron-rich nuclei in assessing nuclear structure calculations, including first-principle approaches. Then, in Section 3.2 and Section 3.3, we will introduce the ^{14}C and ^{18}N physics cases, respectively. In Chapter 4, we will describe the experiment and the set-up, while in Chapter 5 we will address firstly the data analysis in Section 5.1. Secondly, in Section 5.2 we will concentrate on the development of a new version of the Doppler Shift Attenuation Method (DSAM) to measure nuclear excited

states lifetimes in tens-to-hundreds femtoseconds range, exploiting known lifetimes in ^{17}O and ^{19}O to validate the method. Then, in Section 5.3 we will discuss the application of the new technique to ^{17}N and ^{14}C. Lastly, in Section 5.4 we will present the gamma spectroscopy of bound states in ^{18}N.

The Thesis' Author was personally involved in the analysis of the dataset, within a collaboration between the Milano and Kraków research groups. The investigation of the additional nuclei produced in the reaction was completed during the first two years of the PhD program. In parallel, the author contributed to the development, detailed documentation and application of the new lifetime-measurement technique.

3.1 The case of ^{16}C and ^{20}O

The lifetime measurement of 2_2^+ states in ^{16}C and ^{20}O (see Figure 3.1 for the level schemes) was achieved by analysing the Doppler-shifted γ-ray lines emitted by the excited nuclei, exploiting a novel Monte Carlo implementation of the standard DSAM [82] (see Section 5.2). In ^{20}O, a lifetime $\tau(2_2^+) = 150^{+80}_{-30}$ fs was measured, and considering the $2_2^+ \rightarrow 2_1^+$ branching ratio of 79(5) %, one gets a partial lifetime of 190^{+102}_{-40} fs. In ^{16}C, an upper limit $\tau(2_2^+) < 180$ fs was estimated. These values are reported in the last column of Table 1.1 in blue bold.

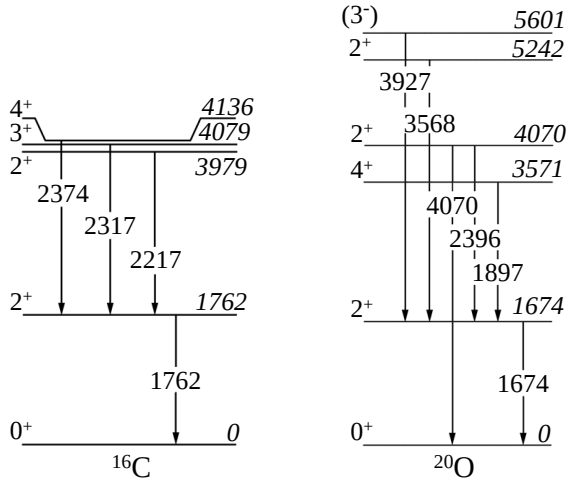

Figure 3.1: Partial ^{16}C (left) and ^{20}O (right) level schemes.

Figure 3.2 displays the comparison between theoretical predictions of MBPT, VS-IMSRG for oxygen and NCSM for carbon and the experimental values for the partial lifetimes of the $2_2^+ \rightarrow 2_1^+$ transitions in the two nuclei. The MBPT (τ = 275 fs - dashed blue line) and VS-IMSRG partial lifetimes (τ = 249 fs - solid blue line) agree well with the measured value only when NNN interactions are considered. When they are neglected, the partial lifetime is nearly 60 % longer (dashed green line). A similar behaviour is observed in ^{16}C, where the NCSM value calculated with NN+NNN interaction (τ =

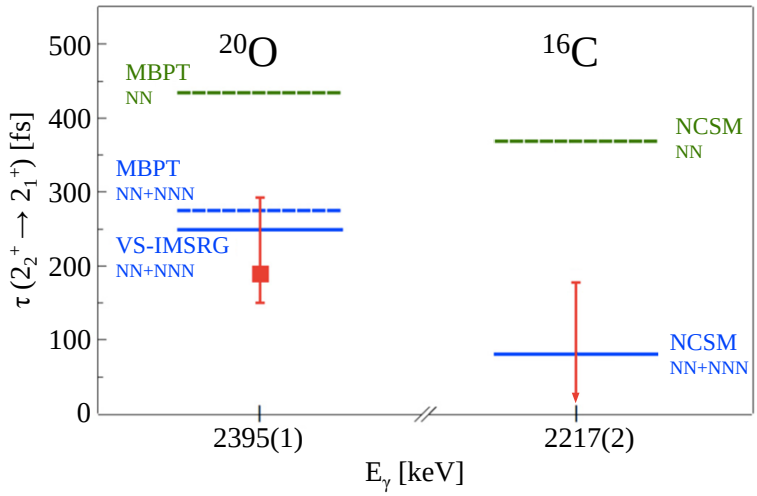

Figure 3.2: Partial lifetimes for $2_2^+ \rightarrow 2_1^+$ decays. Left: ^{20}O, experiment (red symbol) compared to MBPT (dashed lines, with and without NNN interactions), and VS-IMSRG (solid line) results. Right: ^{16}C, experimental limit (red arrow) compared to NCSM predictions with (solid blue line) and without(dashed green) NNN interactions. The energies reported are the ones of the γ rays associated to the transitions: in the case of ^{20}O, the value was measured in the same experiment, while for ^{16}C it is the most precise value present in literature [83]. Figure adapted from Ref. [52].

80 fs - solid blue line) is in agreement with the experimental observations, while the one calculated with two-body terms is not compatible.

All in all, NNN interactions are needed to accurately describe electromagnetic observables in these nuclei. In addition, the present example supports the crucial role of light neutron-rich nuclei in benchmarking nuclear structure calculations.

3.2 The case of ^{14}C

Three carbon isotopes are naturally found on Earth: ^{12}C (98.9 %), ^{13}C (1.1 %) [84] and traces of ^{14}C ($< 10^{-10}$ %). The latter is radioactive (with a half-life of 5730 y) and it is widely employed in radiometric dating applications. ^{14}C, with Z = 6 protons and N = 8 neutrons, is the only magic isotope of the C chain, therefore it is particularly attractive from the theory point of view. The unexpectedly long beta-decay half-life of ^{14}C has posed a major theoretical challenge for many years, as standard realistic nucleon-nucleon (NN) interactions alone appeared inadequate to replicate the effect. At last, in 2011, the experimental half-life was successfully reproduced with *ab initio* NCSM calculations, using a Hamiltonian from the chiral EFT including three-nucleon (NNN) forces [85].

Figure 3.3(a) shows the experimental excitation energies of the 2_1^+ states of even-even isotopes in the C isotopic chain, from mass number A = 10 to A = 20, while Figure 3.3(b) reports the corresponding reduced transition probabilities (B(E2)) of the $2_1^+ \rightarrow 0_1^+$ electromagnetic decays. These data provide evidence of the nuclear structure evolution in the isotopic chain: an abrupt increase of the state energy, accompanied by a drop in the

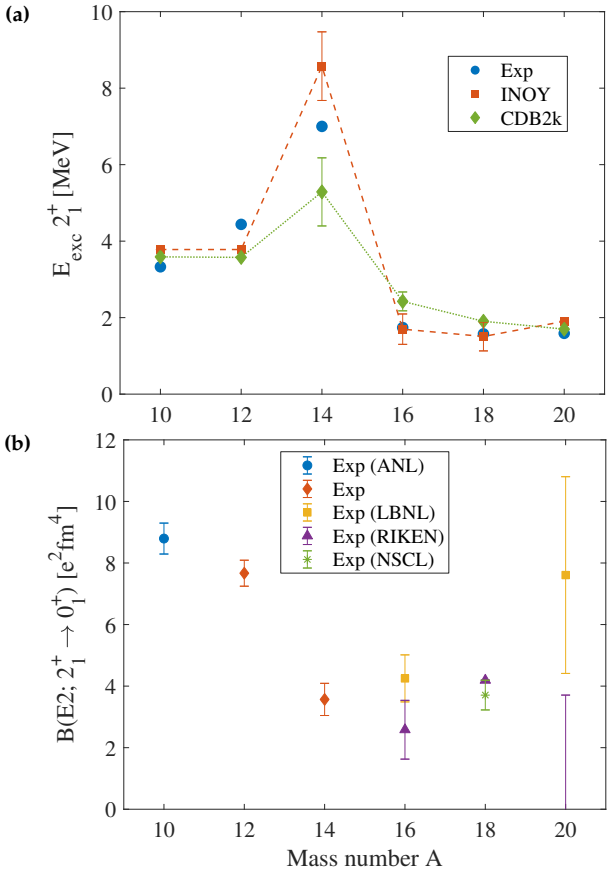

Figure 3.3: (a) Comparison between experimental (blue dots) excitation energies of the 2_1^+ states in the carbon isotopic chain and predictions from NCSM calculations with two different interactions [44] (red squares and green diamonds). (b) Experimental B(E2) values for the $2_1^+ \rightarrow 0_1^+$ transitions, in the same isotopic chain [53], from different experiments.

B(E2) value, is the signature of a possible shell closure. In the case of ^{14}C, the 2_1^+ state is actually located at much higher energy than in the neighbouring ^{12}C and ^{16}C. However, the only experimental B(E2) value available so far, which comes from an electron scattering measurement realised in 1972 and published in a conference proceedings [86], does not correspond to a minimum. Recent theoretical calculations for 2^+ states in the carbon isotopic chain, performed within large-scale No-Core Shell Model (NCSM) [44], can in principle reproduce this kind of systematics. However, these calculations are strongly dependent on the phase space considered and the approximations introduced in the interaction treatment. A different behaviour of the ^{14}C case cannot be excluded on the basis of these model.

Additional measurements are therefore highly needed to clarify this peculiar behaviour, and provide solid experimental comparison for *ab initio* theory predictions [44]. In this work we will present the measurement of the 2_1^+ state lifetime (and consequently

of the B(E2) value) in ^{14}C, employing the novel implementation of the DSAM discussed in Section 5.2 [82].

3.3 The case of ^{18}N

The so-called *p-sd* nuclei, *i.e.*, systems with nucleons in *p* and *sd* shells (see Figure 1.4), are of particular interest for two main reasons: first, their isotopic chain is known up to the neutron drip line and even beyond [87–93], while this is not the case of heavier elements; second, their structure has an influence on nuclear astrophysics processes as well [46–50]. Moderately neutron-rich nuclei belonging to this group, studied with γ spectroscopy, can validate nuclear structure predictions, in order to improve the accuracy in describing a number of properties, such as level ordering or decay branchings. In this context, we will focus on the poorly known ^{18}N, which is among the nuclei essential for nucleosynthesis in supernovae, according to predictions including light as well as heavy nuclei in the extended flow paths at the basis of the production of seed nuclei and *r*-process elements [46–49] (see Figure 3.4).

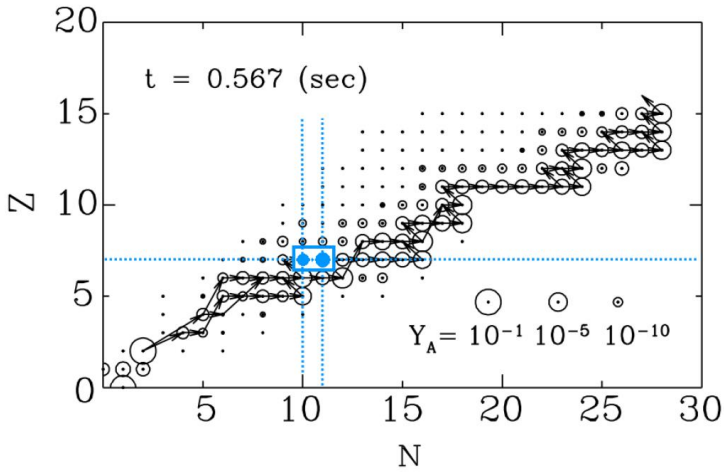

Figure 3.4: Abundances of light nuclei at a specific time scale (the typical time of *r* process [46]) of a type II super-novae explosion. The extended flow path for the production of heavier systems is shown. The ^{17}N(n,γ)^{18}N reaction is highlighted in blue. Figure reprinted from Ref. [94].

^{18}N has one proton hole in the *p* shell and three neutrons outside the N = Z = 8 core, *i.e.*, in the *sd* shell. It represents a good testing ground to investigate multi-shell *p-sd* interactions, which are used in large-scale shell-model calculations to reproduce the structural properties of neutron-rich light nuclei and their drip lines at the same time. For example, the YSOX interaction of Ref. [7], has been successful in reproducing simultaneously ground- and excited-states energies and drip lines of most of *p-sd* shell nuclei, employing cross-shell $\langle psd|V|psd\rangle$ and $\langle pp|V|sdsd\rangle$ matrix elements based on the VMU monopole-based universal interaction, and phenomenological inter-shell matrix elements. In particular, this interaction correctly predicted the ordering of low-lying

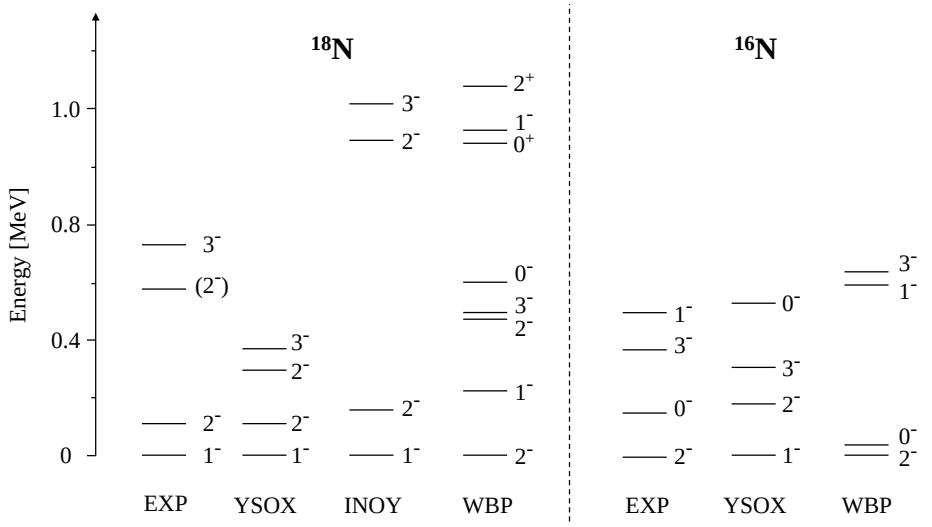

Figure 3.5: Comparison between the experimental level scheme of ^{18}N and ^{16}N and theoretical ones, obtained with shell model (YSOX [7] and WBP [94]) and *ab initio* (INOY [98]) calculations.

states in N = 11 isotones, including ^{18}N, where other interactions, such as WBP and WBT [95], failed [96, 97] (see Figure 3.5 for a comparison between theoretical models). However, SM calculations with the YSOX interaction did not manage to figure out the long-term problem of simultaneously describe the level ordering in both ^{16}N and ^{18}N [7].

^{18}N has been investigated in previous experiments, employing charge-exchange [99], beta-decay [100], fusion evaporation [101] and neutron transfer [102] reactions (see Figure 3.6 for details). These experiments identified a total of eight bound levels above the 1^-_1 ground state and below the neutron-separation energy (S_n = 2.828(24) MeV [103]). Three excited states were firmly located below 1 MeV, at 115, 587 and 742 keV, with spin 2^-_1, (2^-_2) and 3^-_1, respectively. The gamma decay between them was also observed. At higher energies, three additional levels were placed at 1.17(2), 2.21(1) and 2.42(1) MeV, with large energy uncertainties, while two levels located at 1735 and 2614 keV observed in beta-decay studies [100], were tentatively proposed as positive-parity (1^+) states. The level at 1.17(2) MeV, observed in the ^{17}N(d,p)^{18}N reaction by Hoffman *et al.* in Ref. [102], was interpreted as a single (1^-_2) state, or a doublet of unresolved 0^-_1 and 1^-_2 states.

Within the SM framework, a limited number of states is expected in ^{18}N below the neutron emission threshold S_n. In particular, calculations carried out with different interactions [7] predict 10 negative-parity states: two 1^- (including the g.s.), three 2^-, three 3^-, one 0^- and one 4^- states. These bound states can be interpreted as arising from the coupling of one proton in the $p_{1/2}$ orbital to the lowest members of the multiplet of states originating from:

(i) three neutrons in the $d_{5/2}$ orbital;

(ii) two neutrons (coupled to spin 0) in the $d_{5/2}$ orbital and one neutron in the $s_{1/2}$

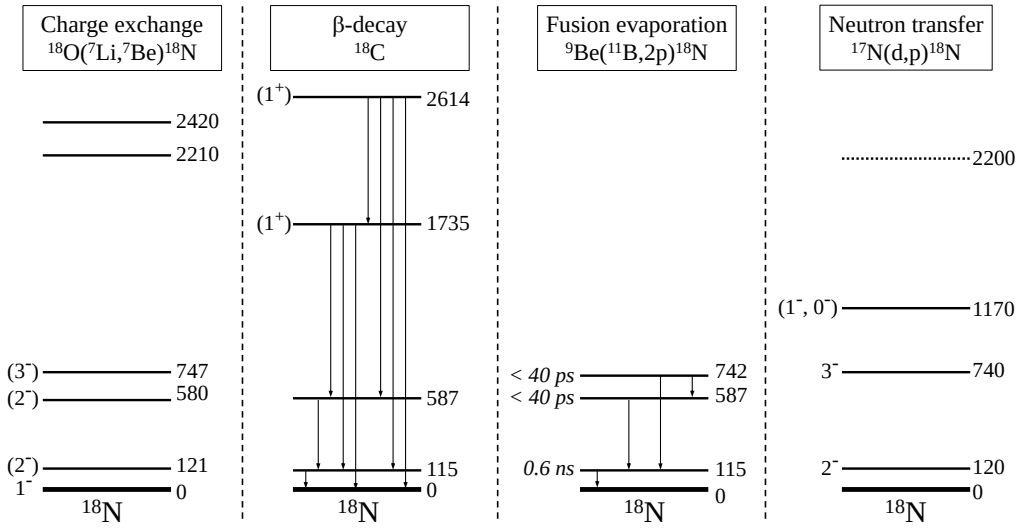

Figure 3.6: Summary of the spectroscopic information available in literature about ^{18}N [99–102].

orbital.

For example, in the described framework, the first four states in ^{18}N (including the g.s.) are the result of the coupling between a proton in the $p_{1/2}$ orbital with the $3/2^+$ g.s. and the $5/2^+$ first-excited state in ^{17}C, producing the $[1^-_1$ (g.s.), $2^-_2]$ and $[2^-_1, 3^-_1]$ doublets, respectively. The remaining negative-parity states, expected below S_n, should arise from the coupling of the $p_{1/2}$ proton with higher-lying states in ^{17}C, which are unbound ($S_n(^{17}\text{C}) = 734$ keV) and not entirely known experimentally. Positive-parity states in ^{18}N are instead calculated at higher excitation energies, above the neutron-separation energy.

More recently, advanced *ab initio* calculations of the excitation energy spectrum of ^{18}N have been published in Ref. [98], in the context of a systematic investigation of neutron-rich nitrogen nuclei. These calculations were performed within the NCSM framework (see Section 1.4.1) using three different NN potentials: inside non-local outside Yukawa (INOY) [104, 105], next-to-next-to-next-leading order (N3LO) [106, 107] from chiral effective field theory, and charge-dependent Bonn 2000 (CDB2K) [108]. The INOY potential is based on a two-body interaction, but includes three-body and non-local contributions at short range. The N3LO interaction is derived from chiral effective field theory, considering the NN part only, while CDB2K is a charge-depended non-local interaction. In these calculations, the ordering of the ground state and the first excited state is properly reproduced only with the INOY interaction, while the other two interactions give a 2^- as a ground state. Even with the INOY interaction, the state energies still significantly deviate from the experimental ones, in particular for higher-lying states (see Figure 3.5). In all the cases, no information is available above 2 MeV.

In this Part of the Thesis, we will present an extended γ spectroscopy of ^{18}N bound states and in particular we will propose the location of all the negative-parity states

below the neutron-separation energy. This study will help to extend the knowledge on the properties of proton-neutron interaction, including specific proton-neutron matrix elements, which play a key role in the level ordering of both ^{16}N and ^{18}N nuclei. In addition, the location of a specific state, the first-excited 1^- state in ^{18}N, is critical to derive the neutron-capture reaction rate on ^{17}N, relevant in nucleosynthesis processes in stellar environments [47, 48].

Chapter 4

Experiment and detection system

In this Chapter, we will describe the experiment denoted as *e676* and the detection system employed for the investigation of the physics case of interest to this Part of the Thesis, introduced in Chapter 3. The experiment took place in GANIL from 11th to 23rd July 2017 [52, 82]. A beam of ^{18}O at 126 MeV (corresponding to 7.0 MeV/u) reacted with a 4 µm thick ^{181}Ta target (6.64 mg/cm^2), tilted at an angle of 45° with respect to the beam direction. The beam induced direct-transfer and deep-inelastic reactions, producing several light neutron-rich nuclei, from Z=5 (boron) to Z=9 (fluorine), as shown in Figure 4.1. The

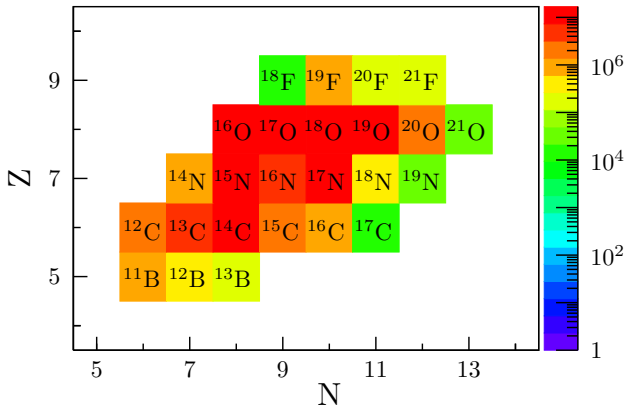

Figure 4.1: Isotopes populated and identified after the ^{18}O+^{181}Ta reaction. Two charge states have been considered. Figure adapted from Ref. [82] [a].

[a] Licensed under the CC BY 4.0 License [2].

target-crossing time of the projectile-like reaction products was ~ 130 fs, given a velocity $v \sim 10\,\%$ of the speed of light.

Originally, a thick ^{238}U target should have been employed with a beam of ^{18}O. For the ^{18}O+^{238}U multi-nucleon transfer reaction at $E_{c.m.} = 125$ MeV, calculations were carried out with a model based on the Langevin-type equation of motions and cross sections were obtained for the population of projectile-like fragments [109], as shown in Figure 4.2(a). This kind of model well describes multi-nucleon transfer and deep-inelastic processes in

low-energy collisions of ^{18}O, showing that they are more favourable than fragmentation reactions in producing light neutron-rich nuclei. In the *e676* experiment, a ^{181}Ta target was eventually used, owing to issues encountered during the production of a ^{238}U thick target. Nevertheless, this kind of calculations are still valid to evaluate the cross section order of magnitude. In Figure 4.2(b) a second example of cross section calculation is

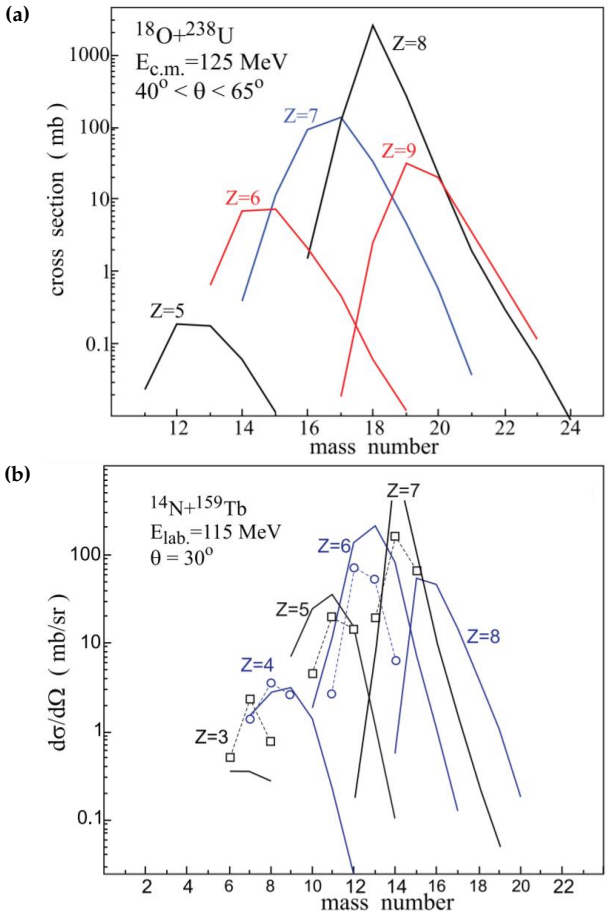

Figure 4.2: Isotopic distributions of projectile-like fragments in the ^{18}O+^{238}U reaction at $E_{c.m.}$ 0 125 MeV and 40° < θ <65° (a) and in the ^{14}N+^{159}Tb at E_{lab} = 115 MeV and θ_{lab} = 30° (b). Theoretical predictions are given with solid lines, while experimental data in panel (b) (taken from Ref. [110] for Z = 3–7) are shown with circles and squares symbols connected by dashed lines. Figure reprinted with permission from Ref. [109] under licence number RNP/21/SEP/044304. Copyright 2014 by the American Physical Society.

reported for the ^{14}N+^{159}Tb at E_{lab} = 125 MeV for an angle θ_{lab} = 30°. In the case of the ^{18}O+^{181}Ta reaction, we therefore expected a similar behaviour as predicted for the U target, but with smaller cross sections.

The experimental set-up, schematically illustrated in Figure 4.3, comprised two arrays for the detection of γ rays, namely 31 high-purity germanium detectors (HPGe) of

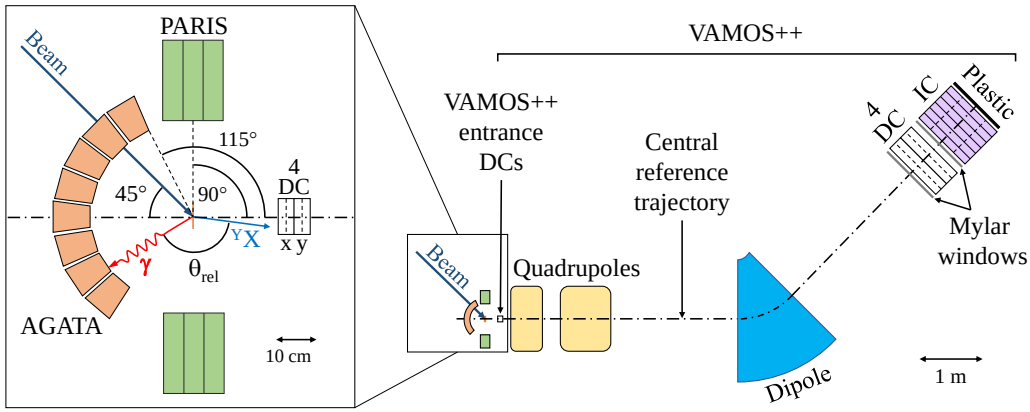

Figure 4.3: Illustration of the experimental set-up, including the detectors around the scattering chamber and the VAMOS++ heavy-ion recoil spectrometer. The main optical elements of the spectrometer (*i.e.*, the quadrupoles and the dipole magnet) are reported, together with the entrance and focal-plane detectors (Mylar windows, drift chambers, ionization chamber and plastic detector). In the zoom on the left, the AGATA+PARIS γ-detector arrays surrounding the target and the VAMOS++ entrance detectors (four drift chambers, for x and y position measurement) are shown. Figure adapted from Ref. [82] [a].

[a] Licensed under the CC BY 4.0 License [2].

AGATA [79–81] and two 9-fold phoswich clusters of the scintillation-based Photon Array for studies with Radioactive Ion and Stable beams (PARIS) [111], with two additional large-volume (3.5"×8") $LaBr_3$:Ce scintillators [112, 113]. The detection of the reaction products was performed with an upgraded version of the VAriable MOde high acceptance Spectrometer (VAMOS++) [68, 69, 114], placed at the reaction grazing angle θ_g = 45°, with an acceptance $(\theta_{acc}, \phi_{acc}) \sim$ (±6.9°,11.5°). AGATA was aligned with the centre of VAMOS++ and covered the angular range between nearly ±115° and ±175° with respect to VAMOS++ central reference trajectory, while PARIS and the two $LaBr_3$:Ce were at 90° (see zoom of Figure 4.3). Both AGATA and PARIS were at 23.5 cm from the centre of the scattering chamber where the target was placed, in the nominal AGATA position. A photo of the detectors surrounding the scattering chamber is reported in Figure 4.4.

Table 4.1 summarises the experimental set-up and acquisition specifications. In the following, we will give an overview of the three arrays, with some additional details on the specific configuration of the experiment.

4.1 The AGATA array

AGATA is a European research project, whose goal is to design and build an innovative germanium-based modular 4π γ-ray spectrometer. The array is employed in studies with both intense stable and radioactive ion beams to investigate the properties of atomic nuclei [79–81, 115, 116]. See Figure 4.5 for two photographs of the AGATA array at the GANIL laboratory.

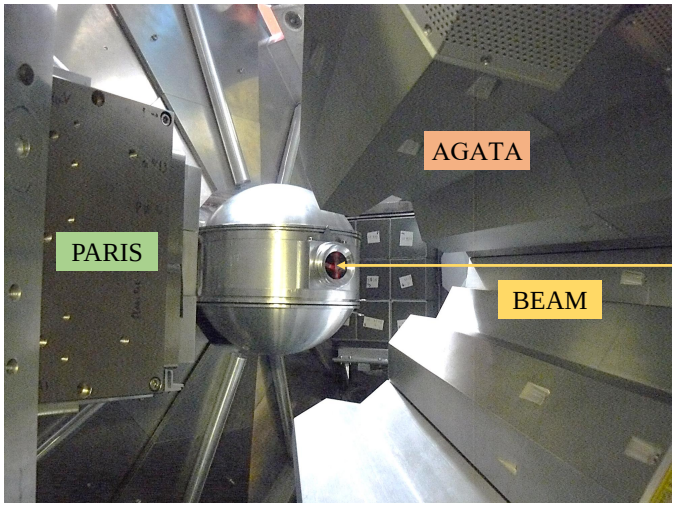

Figure 4.4: Photo of the detectors surrounding the scattering chamber. The two PARIS clusters (without lead shielding) are visible on the left and behind the scattering chamber, while the AGATA detectors are visible in the foreground on the right. The beam direction is also indicated, as the beam pipe was not mounted at that moment.

The array is composed of highly-segmented HPGe crystals: this feature, together with the use of advanced digital electronics, pulse-shape analysis (PSA) techniques and sophisticated algorithms, makes possible the gamma-ray tracking, *i.e.*, the reconstruction of the full energy and the first interaction point of the gamma rays that hit the spectrometer. This reconstruction is based on a precise energy and 3D position identification of each of the interaction points in the crystals, leading to unprecedented performance in terms of Compton rejection and efficiency.

In its final configuration, the AGATA spectrometer will consist in 180 hexagonal crystals, inserted on a mechanical structure with 12 pentagonal holes, which can serve as free positions for the couple of ancillary detectors and for the beam pipes. This geometry fulfil the requirement of a full coverage, minimising the detecting material and maximising the performance in terms of energy resolution, full-energy-peak efficiency and peak-to-total ratio [79].

AGATA is a "travelling" array, which has been located at the GANIL laboratory since 2014. It will be moved to INFN Laboratori Nazionali di Legnaro (LNL, Italy) in autumn 2021, after being previously operational at LNL in the period 2010-2011 and in GSI (Darmstadt, Germany) in 2012-2014.

4.1.1 Detectors and electronics

The AGATA detectors are tapered encapsulated electrically-segmented coaxial n-type HPGe crystals (see Figure 4.6). They external contact is divided into 36 non-identical segments: 6 longitudinal rings of 8, 13, 15, 18, 18 and 18 mm, starting from the front face, are each subdivided into 6 transversal sectors. The crystals have a diameter of $8.0^{+0.7}_{-0.1}$ cm

Table 4.1: *e676* experiment specifications summary.

Quantity	Value
Beam current	~ 7 enA
Trigger (coincidence)	(AGATA ∧ VAMOS) ∨ (PARIS ∧ VAMOS)
Coincidence count rate	~ 2 kHz
AGATA threshold	~ 30 keV
PARIS NaI(Tl) threshold	~ 400 keV
PARIS $LaBr_3$(Ce)/$CeBr_3$ threshold	~ 150 keV
VAMOS++ $B\rho$	0.75
VAMOS++ DC/IC gas pressure	10 mbar

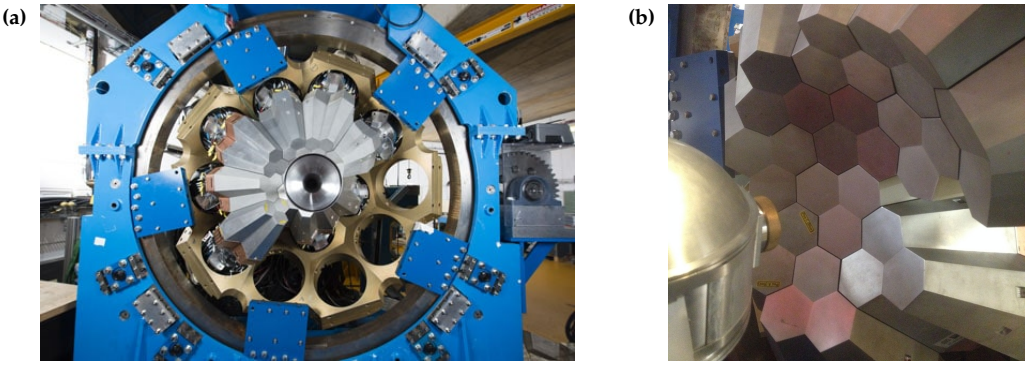

Figure 4.5: The AGATA spectrometer at GANIL. Panel (a) reprinted from Ref. [117] ©P.Stroppa/CEA. Photo of panel (b) courtesy of E. Clément.

at the rear and a length of (9.0 ± 0.1) cm. They are arranged into triplets (clusters) [119], contained in a common cryostat and can be of one out of three possible geometries, which slightly differ for the hexagon sides dimensions (A-red, B-green, C-blue). In the experiment presented here, 10 triple clusters (TC) and 1 double cluster (DC) were present, for a total of 32 crystals, and 31 actually working.

Each crystal is contained into a hermetically-sealed 0.8-mm-thick aluminium canister. A core contact, isolated with ceramic materials, is used to apply the high voltage and to collect the full-energy signal, leading to a total of 37 signals (36 segments + 1 core) read for each crystal. Dewars filled with liquid nitrogen maintain the detectors at a temperature of 90 K.

Regarding the AGATA readout electronics, each crystal is equipped with a digitiser, which serves as an interface between the detectors and the AGATA signal-processing system, and two pre-processing carrier cards in the Advanced Telecommunications Computing Architecture (ATCA) format or in the new GGP (Generic Gigabit Processor) one, which recently substituted the ATCA modules. The elements of the Front-End Electronics (FEE) are connected through optical fibres to achieve appropriate data-transmission rates and to maintain good electrical isolation. The pre-processing filter reduces the data

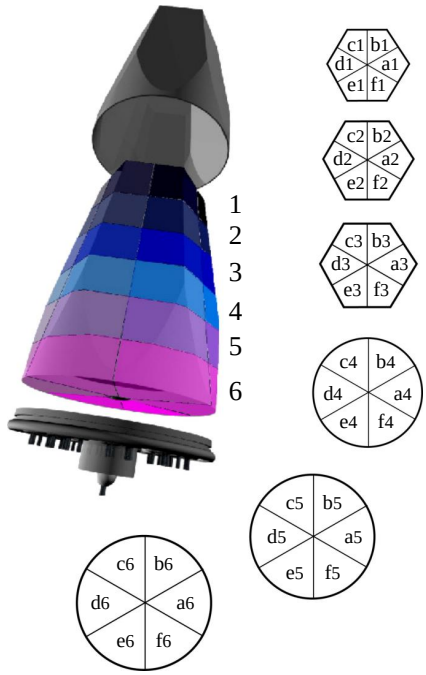

Figure 4.6: 36-fold segmented AGATA HPGe capsule. The external contact is subdivided into six rings, each again divided into six sectors. Figure adapted from Ref. [79][a]

[a] Licensed under the CC BY 3.0 License [118]

volume from the digitisers by a factor of ~ 100, by collecting and processing the data from the digitiser data stream only for those segments which registered an interaction of a γ-ray. The pre-processing stage, then, sends the filtered data to the PSA filter and in the end the data synchronisation and the triggering is performed by the Global Trigger and Synchronisation (GTS) system.

4.1.2 Pulse Shape Analysis

To fulfil the required spatial resolution of ~ 5 mm needed for the reconstruction of the γ-ray paths through the tracking algorithms, the segments granularity is not sufficient. In addition, the time ordering of the hits in the detectors is impossible to reconstruct with standard timing techniques, since all the interactions would be seen in coincidence. In fact, given a distance of 1 mm-1 cm between two subsequent γ-interactions, the estimated time between them would be of the order of 0.1-1.2 ns, significantly lower than the typical germanium time resolution $\tau_{res} \sim 10$ ns. The needed spatial resolution can be reached by using the so-called Pulse Shape Analysis (PSA) technique, which permits to identify the position where a γ-ray interacted inside the volume of each segment in the detector. It is based on the fact that the charge collection process, which follows the energy deposition in the detection material, induces signals in the electrodes, whose amplitude and shape

depend on the interaction point. This phenomenon is caused by the different charge-collection time and it reflects on the signal shape.

The PSA is carried out by comparing the experimentally measured signals and the position-dependent pulses of a reference basis. These reference signals can be simulated through the AGATA Detector Library (ADL) [120], or collected via scanning techniques of the crystals employing highly-collimated radioactive sources [121] or even *in-situ* techniques [122], in order to produce realistic bases, independent from simulation assumptions and free of a potential bias introduced by simulation boundary conditions.

4.1.3 Tracking

The sequence of interactions corresponding to each photon have to be recognized after the PSA, which provided the location and the energy of the individual hits. This identification is carried out using tracking algorithms, which allow the path of the interacting γ-ray in the detecting material, as well as its full energy and entering direction, to be reconstructed.

The tracking algorithms take into account the different mechanisms through which the radiation can interact with the detection material and the energy range in which they are dominant, namely the photoelectric effect ($\sim$ 100 keV), the Compton scattering ($\sim$ 100 keV-10 MeV), and the pair production ($>$ 10 MeV).

There are two primary methods to carry out the tracking [123]: the forward-tracking technique and the back-tracking one. The former method, requires the grouping of the interaction points into clusters in space. This clusterisation of the interaction points is justified by the forward-peaking character of the Compton scattering cross section, as well as the decreasing mean free path of photons with decreasing energy. The latter technique, on the other hand, reconstructs the photon path from the last interaction point, which coincides with the photoelectric interaction. This is possible since the final photoelectric interaction lies in a limited energy range between $\sim$ 100 keV and 250 keV, independently of the energy of the incoming γ ray [124].

4.1.4 Data processing and data replay

During an experiment, AGATA PSA and tracking are performed semi-online by the NARVAL Data AcQuisition (DAQ) system. Offline, these processes can be repeated employing a NARVAL emulator, and the procedure is called offline replay. NARVAL stands for "Nouvelle Acquisition temps-Reel Version 1.2 Avec Linux" and it is developed in a object-oriented language with Ada 95 [125]. In NARVAL, each process is carried out by a so-called actor, of which there are three types:

Producer collects data from hardware devices;

Filter or intermediary performs operations on the data, receiving input/sending output from/to one or more other actors;

Consumer can only receive inputs, works as a storage or a histogramer.

The data processing flow, schematically illustrated in Figure 4.7, is split into two levels: the local and the global level. In the local level, the crystals producer actors read out

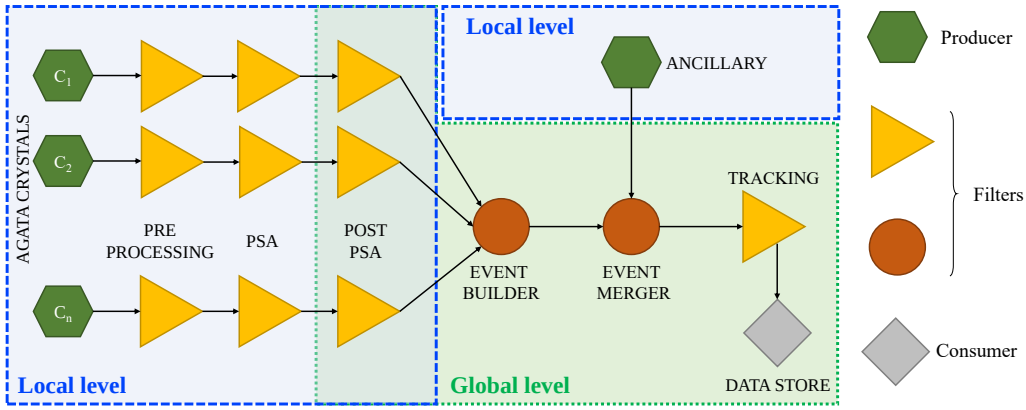

Figure 4.7: AGATA data-processing scheme. The PostPSA filter formally belongs to the local level, but it is incorporated as the first step of the global offline replay. See text for details.

the acquired data, collecting the traces (raw data). These data are then sent to the PreProcessing filter, which prepares the data for the PSA, performing preliminary energy calibrations, cross-talk corrections and time alignment. The local level then proceeds with the PSA stage and the PostPSA actor, which implements additional operations on the data, such as the neutron damage correction and the calibration of the core signal. This filter is used only during the offline replay, and even if it formally belongs to the local level, it is incorporated into the global replay process, as its first step. The ancillaries data are also collected by a producer in the local level, before being merged with the AGATA data in the global level. In the global level, the EventBuilder actor collects the data coming from each crystal and combines them to create the real events, via the timestamps. After that, the EventMerger intermediary merges the AGATA and ancillaries events, again using the timestamps. In the end, the tracking is performed and a final consumer receives and stores the tracked data.

In the present experiment, we chose to perform the offline replay, both at local and global level, in order to improve calibrations, recover some statistics, obtain better time alignments and to check neutron damage and cross-talk corrections. Since the local replay procedure is rather time-consuming, while the global replay is faster, the two levels have been carried out separately: the global replay had to be repeated many times on a small part of the statistics, before obtaining the final configuration files to be applied to all the experimental runs.

4.2 The PARIS Array

PARIS (Photon Array for studies with Radioactive Ion and Stable beams) is a European initiative with the aim of building an innovative γ-detection array, capable of energy-spin spectrometry measurements, calorimetry studies for high-energy photons and medium-resolution γ detection [111, 126]. These features require a sub-nanosecond time resolution to discriminate γ rays from neutrons, high granularity and high counting rate

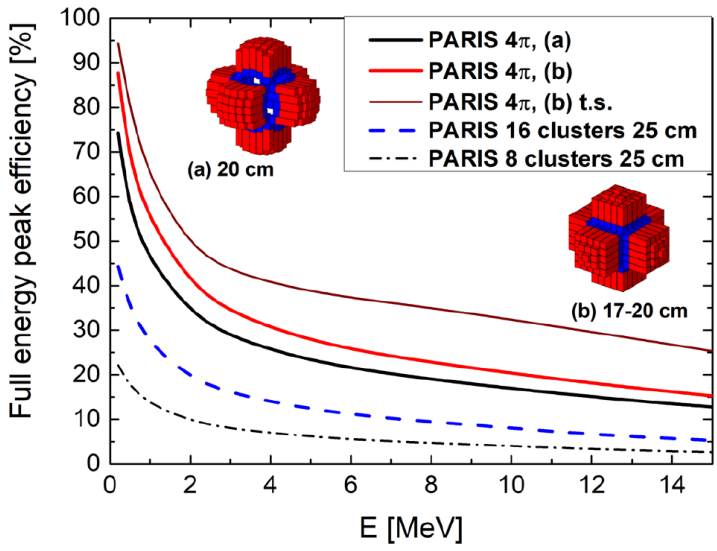

Figure 4.8: Absolute full energy peak efficiency for different geometries or sizes of the PARIS array. Two possible 4π geometries of PARIS, which can be created using 150 phoswiches, are also shown. The black dotted and blue dashed lines indicate the efficiency calculated considering 8 and 16 clusters, respectively, at a distance of 25 cm from the target. The efficiency of the two 4π geometries displayed is shown with the red and black lines. The brown line indicates the efficiency for the PARIS geometry shown on the right (geometry (b)), in the so-called "total sum" (t.s.) mode. In this latter mode, the energy deposited in the phoswiches by a single gamma ray summed up. Figure reprinted from [126] [a].

[a] Licensed under the CC BY 4.0 License [2]

(50 kHz) capabilities. PARIS is a large composite array of phoswich detectors, which can measure γ rays over a broad energy range, from few hundred keV to 40 MeV. Its geometry was designed to allow a suitable interoperability with other arrays, including AGATA. In its final configuration, the PARIS calorimeter will cover almost the whole 4π solid angle with 216 phoswich detectors. Figure 4.8 reports as an example two different PARIS 4π 150-phoswich configurations, with the corresponding absolute photopeak efficiencies.

4.2.1 Phoswich detectors

A phoswich, literally "phosphor sandwich", is a scintillation-based detection system composed of two or more scintillators, with distinct signal-shape features, optically coupled to each other and to a common photomultiplier tube (PMT). Pulse shape analysis permits the separation of each scintillator signal, identifying the events associated to the single crystal and those in which both fired [127].

The PARIS phoswich consists of two different optically-coupled scintillators: one $LaBr_3$(Ce) (or alternatively a $CeBr_3$) cube (2"×2"×2") in front of a NaI(Tl) parallelepiped (2"×2"×6"). Each phoswich is encapsulated in a hermetically sealed aluminium can and read out by 2"-diameter cylindrical Hamamatsu R7723-100 PMT, which collects the light

generated in both the crystals. A glass window separates the NaI(Tl) crystal from the PMT. The connection of a cylindrical PMT to a square-faced scintillator brings to a loss in the light collection, which is of the order of 20 %. However, the consequences on the detector performance are limited: the energy resolution worsens only of a factor ~ 0.4 % at 1 MeV [128].

The signals of $LaBr_3$(Ce) and NaI(Tl) can be simply discriminated on the basis of their decay time: the former has a decay time of the order of ~ 16 ns [129], while the latter has a decay time ~ 0.25 µs [130]. The more recent $CeBr_3$ scintillation material was proved to be comparable to $LaBr_3$(Ce) detectors in terms of time and energy resolution [131], and also in this case the decay time is considerably shorter (~ 20 ns [132]) than the NaI(Tl) one. A substantial difference between $CeBr_3$ and $LaBr_3$(Ce) is that $CeBr_3$ is free from internal radioactivity (due to the ^{138}La isotope), which cannot be used for calibration purposes, but that can be advantageous when low background levels are needed. The $CeBr_3$-NaI(Tl) combination has been successfully tested and now it is commonly employed in the PARIS phoswich [133].

The two phoswich shells have different functions: the $LaBr_3$(Ce)/$CeBr_3$ inner shell provides a fast time reference and the γ-rays multiplicity, while the NaI(Tl) outer shell detects high-energy γ-rays and can be used to reject Compton-scattering events. The information from both shells can be summed up through add-back techniques, enabling the possibility to reconstruct the multiplicity and the total deposited energy of incoming photons. Figure 4.9 shows a PARIS cluster, the typical square compact combination of nine phoswich detectors used in the experiments.

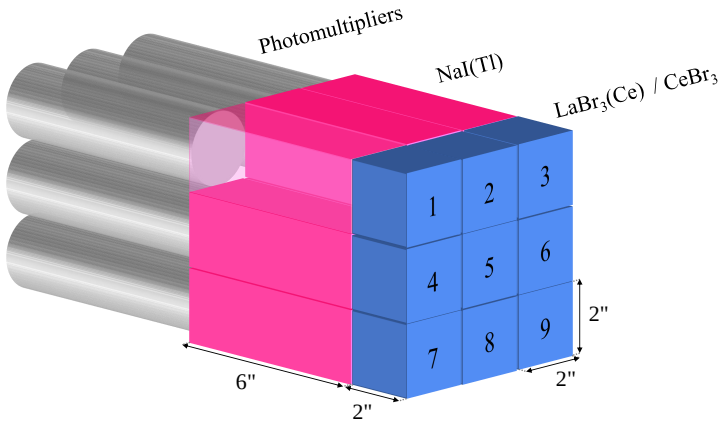

Figure 4.9: Nine-phoswich PARIS cluster illustration.

4.2.2 Configuration in the *e676* experiment

In the GANIL experiment two PARIS clusters were mounted, one $LaBr_3$(Ce)-NaI(Tl) and one $CeBr_3$-NaI(Tl). Each of the two clusters was shielded first of all with a 4 mm layer of lead in the front and an additional magnetic shielding made of 2 mm mu-metal plates (covering the PMTs and part of the crystals) and 10 mm of mild steel on the sides, due to

the intense magnetic fields induced by the VAMOS++ spectrometer. Additional mu-metal petals were inserted between the VAMOS++ quadrupole and the PARIS clusters [134] to ensure a better magnetic shielding. As already mentioned, to the two PARIS clusters two standard large-volume $LaBr_3$(Ce) were added, both shielded in the front face with 4 mm of lead and one of them also placed inside the magnetic shielding.

The electronic signals were collected by the PARIS Pro NIM module [135], which was treated as integral part of the VAMOS++ electronics. The count rate was limited to nearly 7 kHz. The thresholds were set to ~150 keV for the $LaBr_3$(Ce)/$CeBr_3$ and ~400 keV for the NaI(Tl). See Table 4.1 for experimental specifications summary.

4.3 The VAMOS recoil spectrometer

VAMOS is a large-acceptance spectrometer which employs a trajectory-reconstruction technique to select the reaction products from heavy-ion reactions [68, 114]. VAMOS has two operation modes:

Mass dispersive mode event-by-event identification of reaction products mass M, atomic number Z and charge state Q, by means of a reconstruction of ion trajectories in magnetic fields.

Velocity filter at zero degrees it separates the reaction products from the beam background and transports them to the focal plane.

VAMOS optical elements follow the QQFD pattern: it is composed of two quadrupoles, a Wien filter and a dipole magnet. A focal plane detection system is places after the dipole, with the aim of measuring the reaction products position and direction, the time of flight (ToF) and their energy. In the beginning, the VAMOS focal plane detectors were built with a section area of 400 mm×110 mm. More recently, the spectrometer underwent an upgrade of the focal plane detectors, which were substituted with larger acceptance ones. This solution permits a better transmission of the particles through the spectrometer, which in this configuration is called VAMOS++ [69]

4.3.1 The improved VAMOS++ spectrometer

After the upgrade, the VAMOS++ focal plane detectors have an active area of 1000 mm × 150 mm. Figure 4.10 presents a schematic view of the focal plane detection system in the standard configuration of Ref. [69], which is composed of one Multi-Wire Parallel Plate Avalanche Counter (MWPPAC), two Drift Chambers (DC), one segmented Ionization Chamber (IC) and a wall of 40 Silicon (Si) detectors. An additional MWPPAC is placed at the entrance of VAMOS++, close to the target, for ToF measurements. The two DCs identify the horizontal (x) and vertical (y) coordinates and therefore the scattering angles, needed to reconstruct the path of the particles. The IC provides information on the energy loss (ΔE), while the residual energy (E_{res}) is measured in the Si detector at the end of the focal plane.

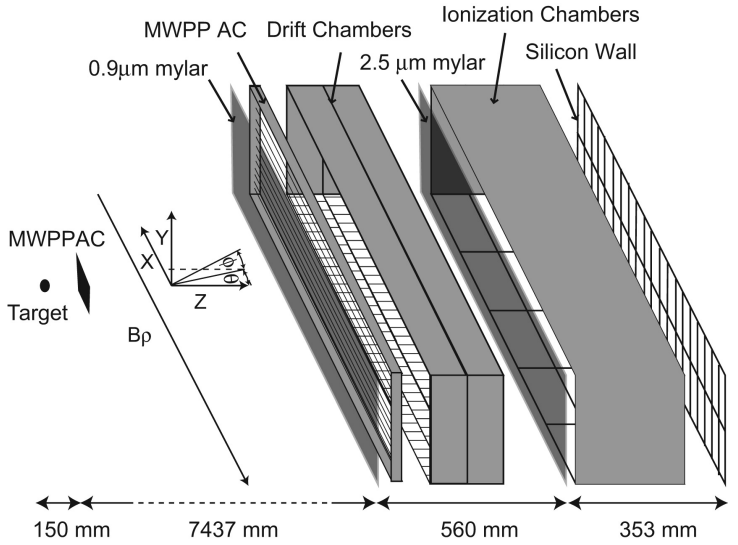

Figure 4.10: Schematic view of the VAMOS++ entrance and focal plane detectors in the standard configuration. Reprinted from Ref. [69] with permission from Elsevier.

The MWPPAC detectors were not present in the initial VAMOS configuration, in which the ToF was obtained with the use of a Secondary Electrons Detector (SED), placed between the two DCs.

4.3.2 Arrangement for the *e676* experiment

In the *e676* GANIL experiment described in this Thesis, VAMOS++ was used in mass-dispersive mode and rotated at 45° with respect to the beam direction, and aligned with the centre of the AGATA array. Some substantial differences in the entrance and focal plane detection system were introduced with respect to the standard configuration described in the previous section, as can be seen in Figure 4.3.

The specific experimental arrangement was composed of four DCs (instead of two), for the reconstruction of the magnetic rigidity $B\rho$ and the particles coordinates measurement, a segmented ionization chamber, divided into six columns and four rows, and one long plastic scintillator at the end of the focal plane, which substituted the Si wall. The plastic detector gave the trigger signal and was employed in ToF measurements, due to its very good timing performance, crucial for ions velocity reconstruction. No MWPPAC was present in the focal plane. The MWPPAC entrance detector was replaced by 4 DCs, 2 for the x coordinate and 2 for the y coordinate measurement, at 20 cm from the target. These DCs were employed in the identification of the ions entrance angles θ and ϕ, since the MWPPAC suffered from a low efficiency in the case of light ions. Regarding the optical elements, the Wien filter was not used in this case.

In conclusion, we report here some VAMOS++ operating parameters in the specific case of the *e676* GANIL experiment: $B\rho$ = 0.75 T m, gas pressure in focal DC and IC chambers 10 mbar. See Table 4.1 for the experimental specification summary.

Chapter 5

Data analysis

This Chapter is devoted to the data analysis of the *e676* experiment. We will first give in Section 5.1 a brief overview of the preliminary data treatment, involving AGATA offline full replay, energy/time calibrations and VAMOS++ ion selection and velocity measurement. This part have been already partially discussed in Refs. [82, 136–138], and we want to stress out the relevance of this step for the following data analysis.

In Section 5.2 we will discuss a novel Monte Carlo implementation of the DSAM (Doppler-Shift Attenuation Method). The new technique was developed to measure lifetimes of excited states in the tens-to-hundreds femtoseconds range in products of low-energy heavy-ion binary reactions, with complex velocity distributions. The new technique has been validated exploiting known lifetimes in ^{17}O, ^{19}O and ^{17}N. A detailed documentation of the software developed for the application of the new DSAM technique can be found in Appendix A.

In Section 5.3 we will show the application of the new DSAM technique in a number of relevant cases, namely ^{14}C and ^{17}N. Finally, in Section 5.4 we will present the gamma spectroscopy of ^{18}N bound states. See Appendix B, for a complete review of the gamma transitions observed in the nuclei populated in the experiment.

5.1 AGATA and VAMOS++ data processing

The goal of the data preparation was to reach the best gamma-ray energy resolution and peak-to-total ratio, in order to be sensitive to the phenomena that can modify the gamma-ray line shape, in particular the distortions introduced by the effect of the nuclear state lifetime. To reach the goal, careful time alignment of the AGATA crystals and very precise γ-ray energy calibrations had to be performed, through a full offline replay of the data. The energy and direction of the interacting γ rays in AGATA were reconstructed by the combined use of the PSA and of the Orsay Forward Tracking (OFT) algorithm [123], which allow to reach a position resolution of the order of 4 mm FWHM. In addition, precise mass measurement of the ions in the VAMOS++ spectrometer, together with their trajectory and velocity reconstruction was fundamental, as they influenced the Doppler correction of the AGATA data.

5.1.1 AGATA data processing

As already anticipated in Section 4.1.4, the analysis required the full replay of the data, both at local and global level. At the local level, we verified first of all the good recovery of the cross-talk effect. The cross-talk phenomenon, caused by parasitic electronic capacitive couplings, occurs in general in segmented germanium detectors when a γ ray interacts more than once in segments of the same crystal, resulting in energy losses and degraded resolution [139]. The cross talk can be corrected in the AGATA PreProcessing filter [140]. During the global replay, in the PostPSA filter we applied a software correction to the neutron-damage effect, which is caused by irradiation of fast neutrons that induce lattice defects inside the germanium crystals, degrading the energy resolution. This step can be performed after the PSA, since the latter is insensitive to the neutron damage. The interaction points extracted in the PSA filter can be used to model the trapping of the charge carriers in the lattice defects, as it depends on the path in the material, and to recover a good resolution.

In the PostPSA filter, time alignment and energy calibrations of the core signals are applied. The results of these two procedures are shown in Figures 5.1 and 5.2, respectively. The time alignment was introduced to enhance the peak-to-background ratio, by putting stringent gates on the prompt coincidence between VAMOS++ and AGATA. With the gate shown in Figure 5.1(b) we obtained an improvement of the peak-to-background ratio of a factor > 2, with a loss in the counts in the photopeak < 4 %.

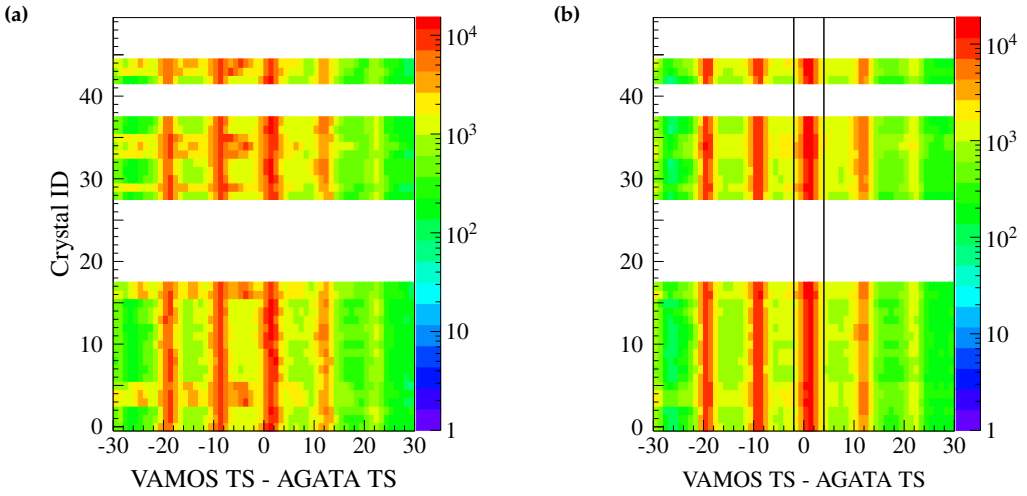

Figure 5.1: 2D time histograms before (a) and after (b) the time alignment procedure. On the x axis, the difference between the VAMOS++ and the AGATA timestamps (TS) is reported for each AGATA crystal (y axis). The gaps are due to the missing detectors in the AGATA flanges. The black lines in panel (b) refer to the prompt coincidence gate used in the analysis. The secondary peaks are non-prompt events associated to the radiofrequency of the pulsed beam. Figure adapted from Ref. [137] [a].

[a] Licensed under the CC BY 4.0 License [2].

After the time alignment, the energy calibrations of the AGATA core signals were performed exploiting two calibration sources : ^{152}Eu, for γ-ray lines below 1.5 MeV and AmBe:Fe, for lines above 5 MeV. Between 2 and 3 MeV, the radiation from ^{208}Pb (natural radioactivity) and ^{24}Mg (β decay of ^{24}Na populated via neutron capture of ^{23}Na in the PARIS NaI crystals), was additionally considered in the calibration. In this step, the so-called *ForceSegmentsToCore* option of the AGATA software package [141] was enabled: it replaces the summed energy measured in the crystal segments with the one measured in the core, for each γ event. This option allows the recovery of some missing energy, resulting in a reduction of the left-side tail of the energy peaks. For one crystal (ID no. 42), the core signal was degraded, therefore the segments were individually calibrated and their energy summed up, without imposing it to be equal to the energy measured in the core. At the end of the calibration process, discrepancies between tabulated and calibrated energies below 0.2 keV were obtained for most of the detectors, with only 4 detectors having discrepancies of ~ 0.5 keV. Figures 5.2(a) and 5.2(b) show, as an example, the portion of the AGATA energy spectrum around the ^{24}Mg 2754.007(11) keV line, with a rough (nearline) calibration applied during the experiment and after the proper offline calibration, respectively. The comparison of the total spectra is shown in Figure 5.2(c): an overall improvement in the FWHM of a factor 1.4 is achieved.

These are the main features of the AGATA data pre-sorting. For further details, a step-by-step documentation of the AGATA offline replay is available in Appendix A of Ref. [136].

5.1.2 The VAMOS++ data treatment

Regarding the VAMOS++ data treatment, the ions velocity v_V , mass number M and charge state Q were obtained with the standard VAMOS++ analysis procedure [68, 69, 142]. The ion velocity v_V was obtained from the relation $v_V = D/T$, where D and T are the ion path length and the time of flight (ToF), respectively, from the target to the focal plane plastic detector. The ToF was calculated using the focal plane plastic detector time signal and the beam pulse (RF) of the cyclotron (with a pulse time of 102 ns), as a reference. For a complete identification of the reaction products, the following expressions (Equations (5.1) and (5.2)) between the magnetic rigidity $B\rho$ (see 4.1), the measured VAMOS++ quantities (energy and ToF) and reaction residue characteristics (mass number M, velocity v_V and atomic charge state Q) were employed, as described in Ref. [68]:

$$M/Q = \frac{B\rho}{3.105\gamma\beta} \tag{5.1}$$

$$M = \frac{E_{tot}}{931.5016(\gamma - 1)} \tag{5.2}$$

where β and γ are the relativistic parameters $\beta = v_V/c$ and $\gamma = (1 - \beta^2)^{-1/2}$, being c the speed of light, and E_{tot} is the total energy (in MeV), obtained as the sum of the partial ΔE energy measured by the ICs and the residual energy E_{res} from the focal plane plastic detector. The charge state Q is then extracted combining Equations (5.1) and (5.2), via

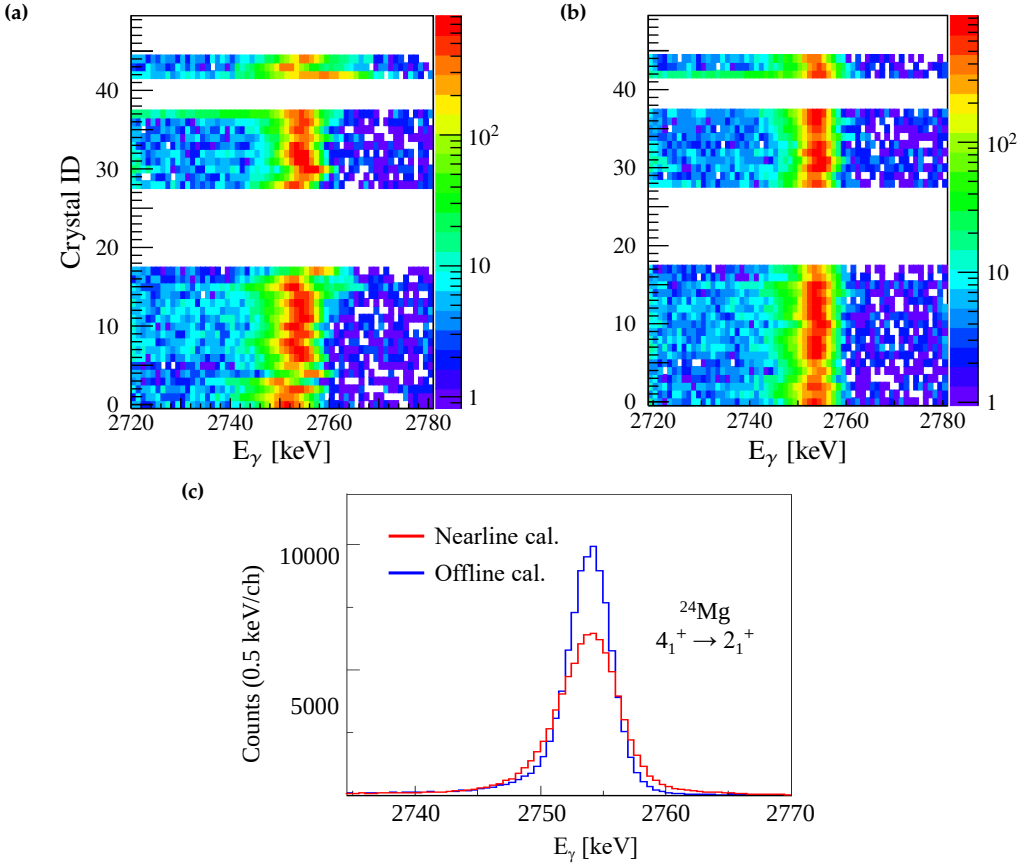

Figure 5.2: Examples of two-dimensional histograms showing the AGATA crystal identification number (Crystal ID, y axis) vs. gamma-ray energy (E_γ) spectra from calibration sources, in the region around the 2754-keV line from ^{24}Mg, before (a) and after (b) the offline energy calibration procedure. Panel (c) shows the corresponding energy spectra, summed over all AGATA crystals, from which an improvement of a factor of 1.4 is deduced in the FWHM. Figure adapted from Refs. [82, 137] [a].

[a] Licensed under the CC BY 4.0 License [2].

Equation (5.3):

$$Q = \frac{M}{M/Q} \tag{5.3}$$

The atomic number Z was determined from the correlation between the energy loss ΔE and the residual energy E_{res}, deposited in the ICs and plastic scintillator, respectively, as shown in Figure 5.3(a). The specific reaction product was then selected via graphical cuts in the Q vs. M/Q two-dimensional histogram. As an example, Figure 5.3 reports this kind of plot for the carbon (Z=6), nitrogen (Z=7), and oxygen (Z=8) isotopes.

Two corrections were introduced to the standard VAMOS++ identification method [82]: a correction of the ions ToF from the target to the focal plane detectors and a finite-

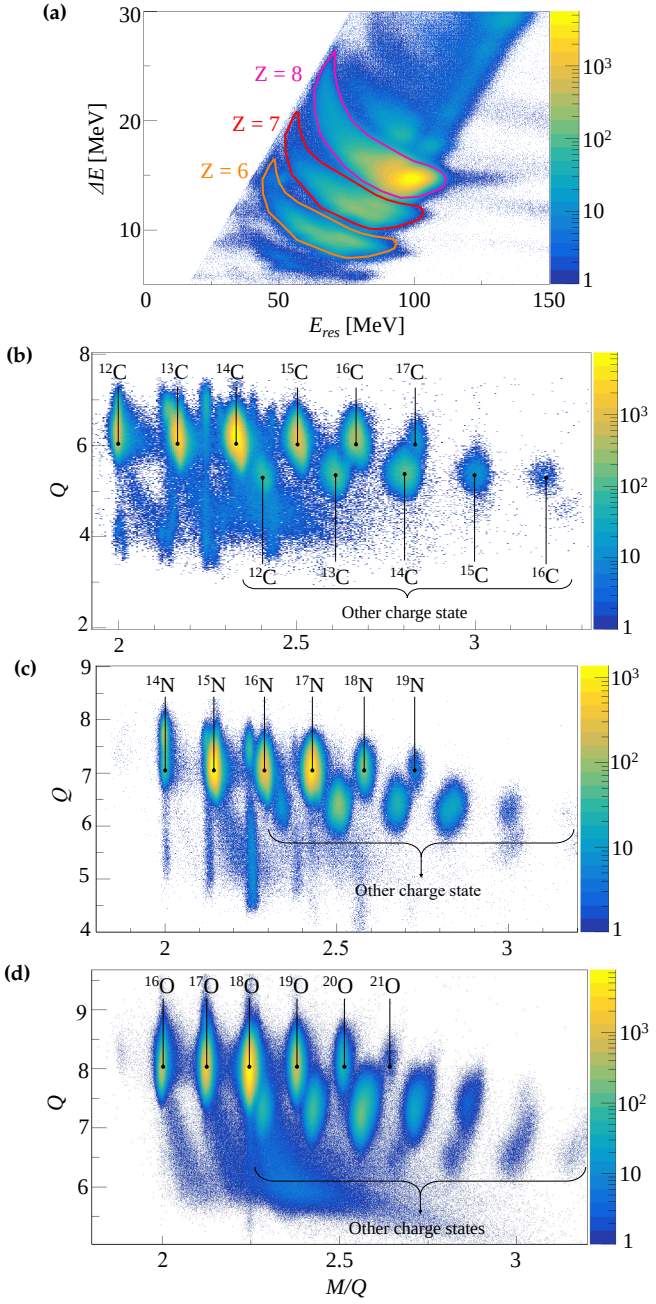

Figure 5.3: (a) Energy loss (ΔE) vs. residual ion energy (E_{res}) 2D histogram, obtained from the VAMOS++ data analysis. The regions corresponding to Z = 6, Z = 7 and Z = 8 are encircled. Plot of the ion charge Q vs. M/Q for carbon isotopes (Z=6) (b), for nitrogen isotopes (Z=7) (c), and for oxygen (Z=8) (d). Two charge states (or three in the case of O isotopes) are visible. Figure adapted from Refs. [82, 143] [a].

[a] Licensed under the CC BY 4.0 License [2].

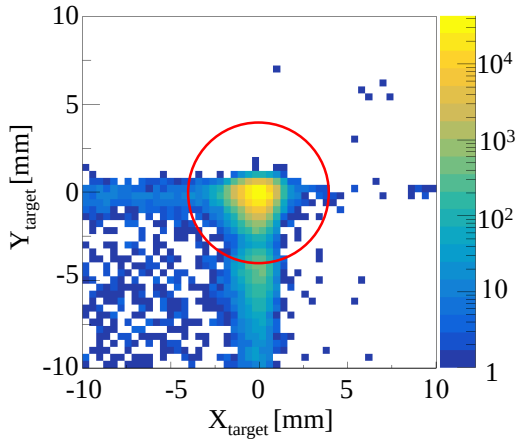

Figure 5.4: Beam-spot reconstruction obtained by using information on the x and y positions from the entrance DC detectors of VAMOS++. The red circle (with a 4 mm radius) delimits the acceptance area for the event reconstruction.

size beam spot instead of a point-like one. The first correction was necessary as a drift of the reconstructed ions mass was visible as a function of the experimental time. The drift was corrected exploiting the PARIS time response to the beam radiofrequency (RF), which was showing a similar behaviour. This correction improved the ions mass distribution FWHM by a factor 1.2. The second correction introduced a significant improvement of the AGATA gamma-ray Doppler-shift correction, with respect to the case in which a point-like beam spot was considered. The ions tracks were reconstructed using the two pairs of DCs at the entrance of the recoil spectrometer and considering the events with trajectories originating within 4 mm from the target centre, as shown in Figure 5.4. Furthermore, the use of the entrance DCs to measure the x and y positions (and therefore the θ,ϕ angles) of the reaction products, instead of the DCs in the focal plane, introduced an additional improvement of a factor 1.4 in the FWHM of the Doppler-corrected AGATA gamma-ray lines in the region around 2 MeV.

Lastly, it is important to mention an additional tuning, necessary to refine the Doppler-shift correction of the AGATA gamma-ray energy spectra. The ion velocity profile reconstruction in VAMOS++ is performed after the entrance drift chambers. Therefore, the energy loss in these detectors has to be recovered, before finalising the velocity used to perform the Doppler-shift correction according to Equation (2.4). Here, the relative angle θ_{rel} is determined as the angle between the direction of the reaction product measured in the entrance drift chambers and the emitted γ-ray direction, identified by the line that connects the target center and the first interaction point in AGATA. In Equation (2.4), the β relativistic factor is calculated event by event, using the emitting ions velocity immediately after the target, $v = v_V + \Delta v_V$, where v_V is the velocity measured in VAMOS++, while

$$\Delta v_V = T/(v_V^2 f(\theta, \phi)) \tag{5.4}$$

is a velocity correction based on the energy loss in the entrance drift chambers. In

Equation (5.4), T is a parameter and $f(\theta, \phi)$ is a function whose value is proportional to the path length in the entrance DCs of the reaction products. The T parameter is set with a two-step procedure: firstly, it is calculated with the LISE code [144], assuming the stopping power for oxygen (Z=8) ions (for which the spectrometer transmission was optimised), secondly, it is fine tuned considering the Doppler-shift corrected γ-ray energies for known transitions de-exciting long-lived states, *i.e.*, decaying after the target ($\tau > 1$ ps). Comparing their preliminary Doppler-shift corrected energy to their nominal energies, reported in literature, the final T parameter is established. The fine tuning procedure has to be repeated for each atomic number Z, and the corresponding variation in the velocity is of the order of ~ 0.5 %.

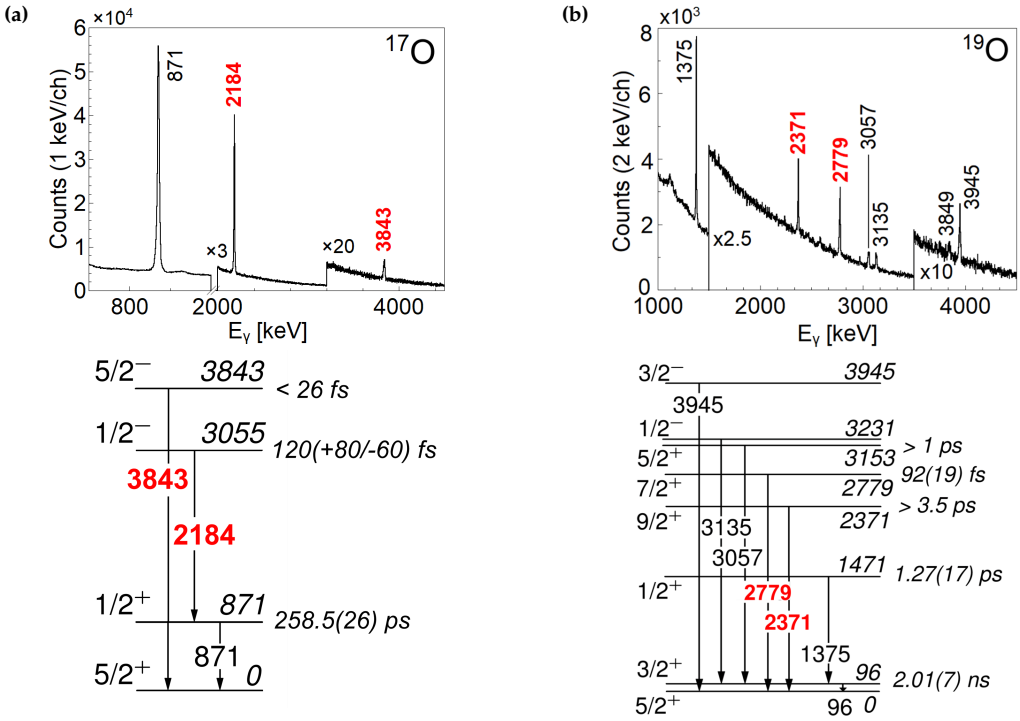

Figure 5.5: (a) ^{17}O and (b) ^{19}O γ-ray energy spectrum measured in AGATA (top), Doppler-shift corrected considering the ion velocity after the target, with corresponding level schemes (bottom). Energies, state lifetimes and spin/parity information are taken from literature [53]. Transitions marked in red are considered in the lifetime analysis discussed in the text. Figure adapted from Refs. [82] [a].

[a] Licensed under the CC BY 4.0 License [2].

Following the procedures described here, ion-gated AGATA γ-ray energy spectra were constructed and Doppler-shift corrected using the recoiling ions velocity after the target. As examples, Figures 5.5(a) and 5.5(b) show portions of Doppler-shift corrected γ-ray energy spectra of ^{17}O and ^{19}O and corresponding level schemes, respectively. Transitions of 2184- and 3843-keV energy in ^{17}O, and of 2371- and 2779-keV energy in ^{19}O

will be considered in the next Section to validate and test the new lifetime measurement technique.

5.2 New DSAM implementation

In this Section[1], we present a novel implementation of the DSAM to access nuclear state lifetimes in the tens-to-hundreds femtoseconds range for products of low-energy binary heavy-ion collisions. In such reactions, like the deep-inelastic process of the present experiment, the complex structure of the products velocity distribution, caused by large energy dissipation [109, 145–149], makes these processes unsuitable for DSAM [78]. Figure 5.6 schematically illustrates the interaction process taking place in the target and defines some relevant quantities that will be necessary for the following discussion.

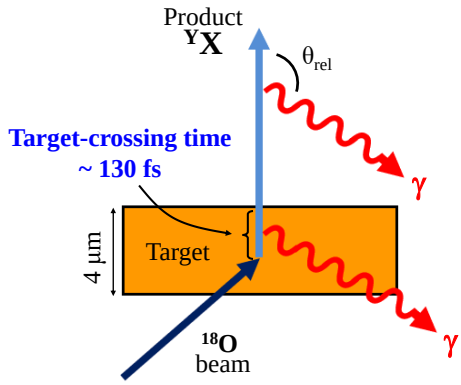

Figure 5.6: Illustration of the interaction process of an ^{18}O 126-MeV beam in a 4-µm thick ^{181}Ta target, resulting in a ^{Y}X reaction product which de-excites by γ-ray emission. θ_{rel} is the angle between the reaction product velocity vector, after the target (as measured in VAMOS++), and the emitted γ-ray direction. Figure adapted from Ref. [82] [a]

[a] Licensed under the CC BY 4.0 License [2]

The method is based on a recursive procedure which reconstructs the total kinetic energy loss (TKEL) distribution of the reaction products, matching the measured velocity distribution after the target. This TKEL distribution is used to simulate the reaction dynamics and the γ-ray emission. The simulated data are then treated using the same analysis procedure adopted for the γ-ray tracking and Doppler correction of in-beam data. By varying both the energy E_γ and the mean lifetime τ of the state of interest, the best fit values and their respective uncertainties are found, via a χ^2 minimization. In the case of the present experiment we are sensitive to lifetimes of the order of the target-crossing time (T_{cross} ~ 130 fs): the ranges of application of the method will be discussed later in Section 5.2.4.

The procedure consists of three major steps:

[1] Text and figures of this Section are adapted from Ref. [82], licensed under a Creative Commons Attribution 4.0 International License [2].

1. a preliminary Monte Carlo calculation to reconstruct the TKEL distribution, for the population of a given nuclear state of the projectile-like product;
2. the simulation of the AGATA Doppler-shift corrected γ-ray spectrum, which is based on the projectile-like velocity calculated from the reconstructed TKEL;
3. the two-dimensional χ^2 minimisation procedure, in τ-E_γ coordinates, based on the comparison between simulated and experimental γ-transition line shapes.

5.2.1 Reconstruction of the TKEL and initial velocity distribution

The key point of the entire procedure, that distinguishes this new method from standard DSAM, is the determination of the velocity vector of the projectile-like product at the reaction instant, for a given excited state population. In the case of low-energy binary heavy-ion reactions, the velocity distribution of the reaction product includes contributions from both direct (quasi-elastic) and more dissipative processes, which lead to the appearance of broad structures at lower velocities, as demonstrated in Figure 5.7 for the case of ^{19}O. Panel (a) shows the matrix E_γ vs. measured ion velocity, for AGATA Doppler-

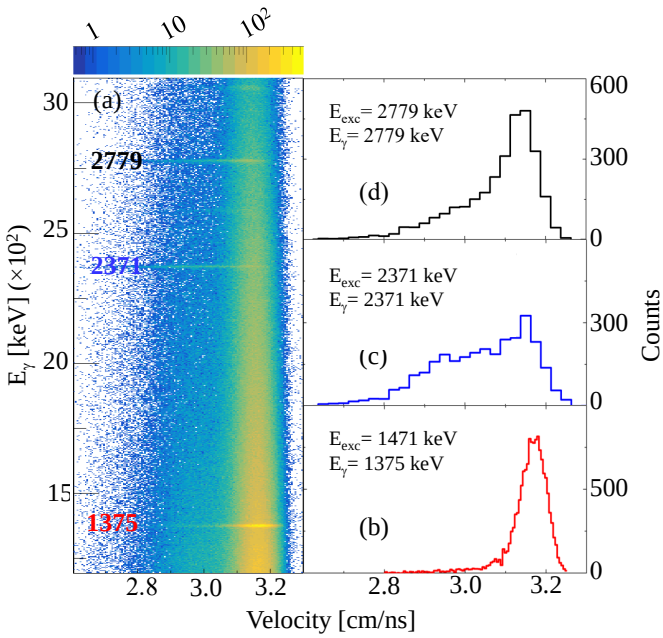

Figure 5.7: Two-dimensional plot of AGATA Doppler-shift corrected γ-ray energies vs. ions velocities, as measured in VAMOS++, in the case of ^{19}O (a). Velocity distributions obtained by gating on the 1375- (b), 2371- (c) and 2779-keV (d) γ rays depopulating the 1471-, 2371- and 2779-keV excited states in the same nucleus. Figure adapted from Ref. [82] [a]

[a] Licensed under the CC BY 4.0 License [2]

shift corrected γ rays. Transitions of energies 1375, 2371 and 2779 keV are clearly visible, depopulating excited states at 1471, 2371 and 2779 keV (see level scheme in Figure 5.5(b)).

Panels (b)-(d) show velocity distributions gated on each transition. Only in the case of the $1/2^+$ state at 1471 keV (see panel (b)), a Gaussian-like velocity distribution is observed, while decays from other states display significant contributions, at lower velocities, from dissipative processes.

Since dissipative contributions cannot be reliably calculated, a Monte Carlo procedure had to be developed to reconstruct the TKEL distribution, where TKEL is defined as the difference between the total kinetic energy before and after the collision. This calculation is performed prior to the simulation of the γ-ray emission and it is based on a recursive subtraction, from the measured velocity distribution, of the velocity components associated with consecutive bins of TKEL. The flow chart reported in Figure 5.8 schematically illustrates the procedure. In the first iteration, the velocity component associated with

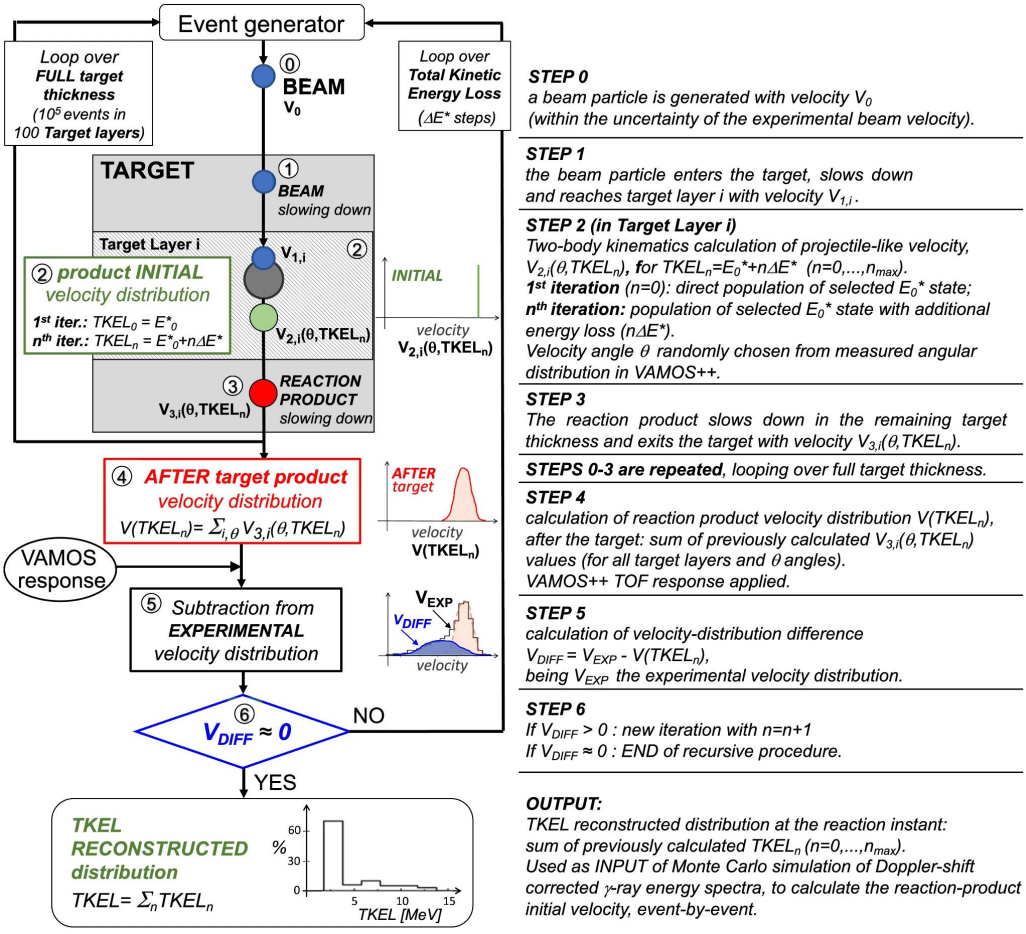

Figure 5.8: Flow chart (left) describing the TKEL iterative simulation process for a given projectile-like excited state E_0^*, with the description of the procedure steps (right). Figure reprinted from Ref. [82] [a].

[a] Licensed under the CC BY 4.0 License [2]

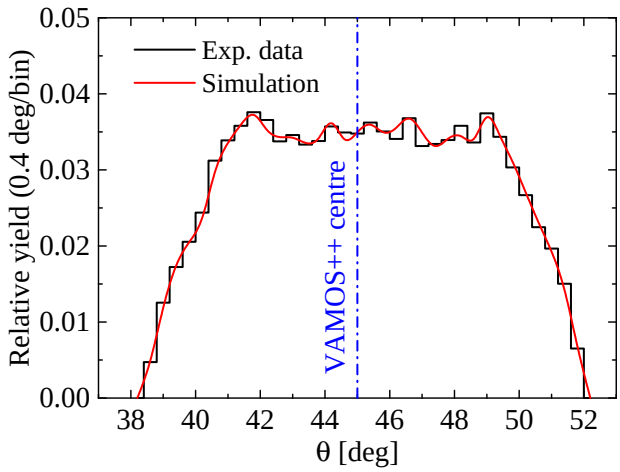

Figure 5.9: Comparison between the theta distribution of the ^{17}N ions, associated with the de-excitation of the 5515-keV level, as measured in VAMOS++ (black histogram) and the corresponding Monte Carlo calculations (red). See 5.3.1 for applications of the new DSAM method to the ^{17}N nucleus.

the direct population of the state of interest, at energy E_0^*, is calculated from the two-body reaction kinematics. The calculation is done looping over 100 target layers into which the target was divided: in each layer the beam-energy degradation is about 0.1 MeV, resulting in an energy loss of ~ 10 MeV in the full target. The reaction is assumed to occur randomly over the full target thickness, being the deep-inelastic reaction cross section (at energies ~ 60 % above the Coulomb barrier) almost constant for beam energy variations of the order of ~ 10 %, as in the present case. The slowing down of the beam and projectile-like reaction product and their energy and angular straggling in the target are also considered. For each event, a reaction product scattering angle is randomly selected from the measured angular distribution in VAMOS++ (see Figure 5.9). This automatically takes care of the acceptance of the magnetic spectrometer. The velocity distribution, after the target, is then folded with the VAMOS++ response which is dominated by the ToF uncertainty (with $\sigma = 1$ ns). The final simulated velocity distribution is then subtracted from the experimental one, after proper normalization.

In the next iteration, the second component of the projectile-like velocity distribution, associated with a TKEL increased by ΔE^*, is calculated following a procedure similar to the first iteration, and the corresponding final velocity distribution, after the target, is also corrected for the VAMOS++ ToF response and subtracted from the remaining measured velocity distribution. In the present analysis, a number n_{max} of 10 iterations was considered (with $\Delta E^* = 2$ MeV, consistently with the VAMOS++ energy resolution), in order to fully reproduce the experimental velocity distribution, although a few iterations were found sufficient in all treated cases.

As a result of this preliminary Monte Carlo calculation, the TKEL distribution associated with the population of a given E_0^* state of the projectile-like product is reconstructed (see bottom of Figure 5.8). Such a TKEL distribution will be used in the main simulation

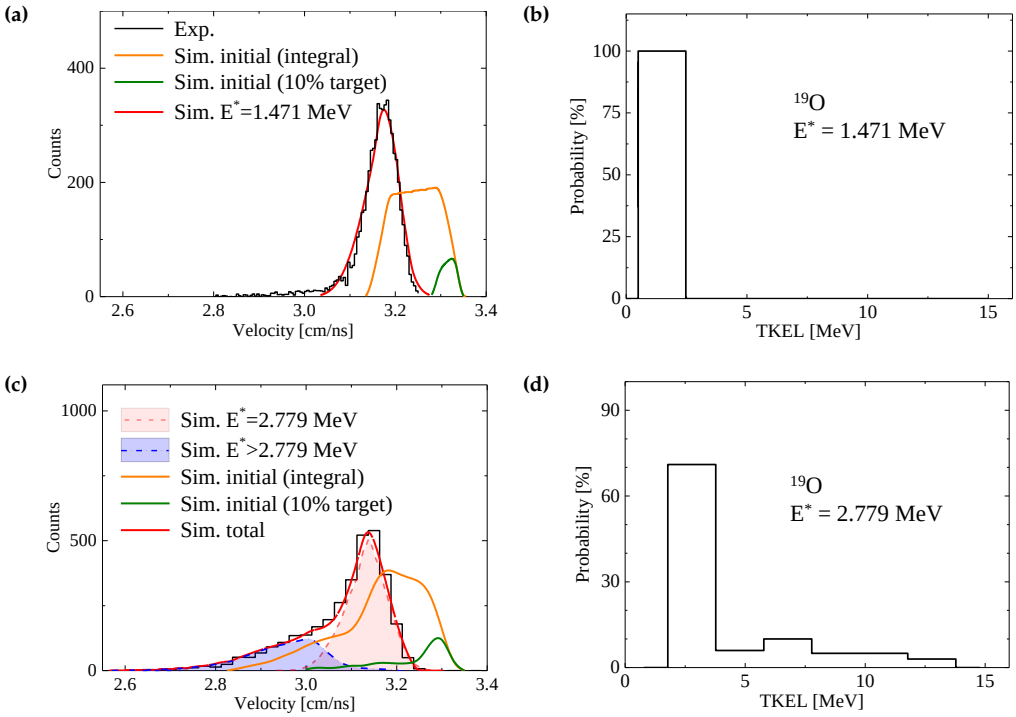

Figure 5.10: Panel (a): measured (black histogram) and simulated (red solid line) velocity distributions for the de-excitation of the 1471-keV state of ^{19}O. The unfolded total initial velocity distribution is shown by the orange line, while the green line displays the contribution from the first 10 target layers. Panel (c): same as in panel (a), for the de-excitation of the 2779-keV state of ^{19}O Red and blue distributions correspond to simulated direct (quasi-elastic) and dissipative components. Panels (b) and (d) give the reconstructed TKEL distributions (with 2 MeV/bin) for the corresponding state population reported in panels (a) and (c), respectively. Figure adapted from Ref. [82] [a].

[a] Licensed under the CC BY 4.0 License [2]

of the AGATA Doppler-shift corrected γ-ray spectrum to calculate, event-by-event, the projectile-like product velocity vector, at the reaction instant, from the reaction kinematics. Figure 5.10 displays, as examples, the velocity distributions for the ^{19}O product excited to the 1471-keV (a) and 2779-keV (c) states, and the corresponding simulated distributions. The measured (black histogram) and simulated (red line) velocity distributions have Gaussian-like shapes in the case of the 1471-keV state, which is characteristic for an exclusive direct population process. In contrast, the velocity distribution measured for the 2779-keV state has a complex structure, which is well described by a velocity profile with two separate contributions, associated with direct (red dashed) and dissipative (blue dashed) processes, respectively. In both panels, the orange solid line displays the unfolded total initial velocity distribution (*i.e.*, summed over the full target thickness), while the green line represents the contributions from the first 10 target layers. In each panel, the inset gives the reconstructed TKEL distribution for the corresponding state

population (in 2-MeV wide bins).

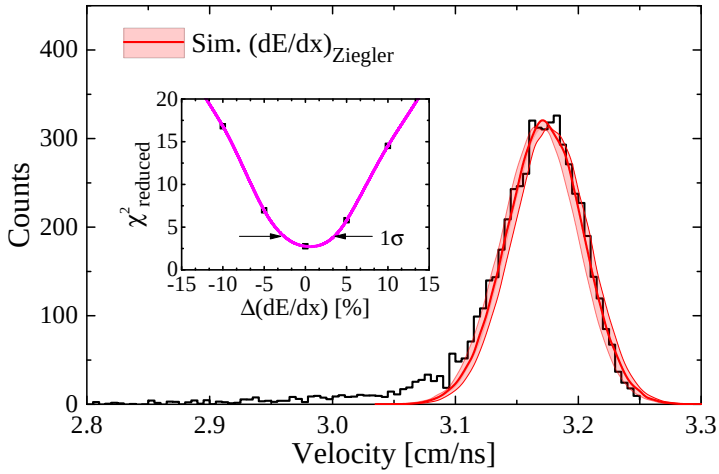

Figure 5.11: Measured velocity distribution for the de-excitation of the 1471-keV state in ^{19}O. The red-shaded band is obtained by varying by 5 % the stopping-power parametrization of Ziegler *et al*. [150]. Inset: reduced χ^2 curve for Monte Carlo simulations using different Δ(dE/dx) variation (in %) of the Ziegler stopping-power parametrization, pointing to a 1σ uncertainty < 5 %. Figure adapted from Ref. [82] [a].

[a] Licensed under the CC BY 4.0 License [2]

An important ingredient of the simulation is the stopping-power parametrisation, which was taken from Ziegler *et al*. [150, 151]. We evaluated the influence of this choice for our reaction by varying up to 20 % the prescribed value, in the case of a uniquely determined reaction kinematics (*i.e.*, the direct population of the 1471-keV state in ^{19}O). As shown in Figure 5.11, the simulated final velocity distribution (red band) reproduces the measured velocity profile within a 1σ uncertainty for a stopping-power variation < 5 %. We also compared the simulated velocity distributions extracted using the Ziegler *et al*. parametrization with different stopping-power laws, such as the one used by the code ATIMA [152], which is usually considered for higher energies. Differences in energy losses were of the order of 2-3 %, resulting in negligible effects in the subsequent analysis.

5.2.2 Simulation of gamma-ray spectra

Simulation calculations of an AGATA Doppler-shift corrected γ-ray line shape, for a transition depopulating a selected state, were performed in a two-step process.

In the first step, the γ events are prepared with a Monte Carlo procedure (with typical number of events of the order of 4×10^6), following a flow diagram similar to the one presented in Figure 5.8. For each event, after the beam particle reaches the target layer in which the reaction occurs, the velocity of the projectile-like product, at the reaction instant, is obtained from a two-body kinematics calculation assuming a TKEL value randomly chosen from the previously reconstructed TKEL distribution for the specific populated state. For each event, the velocity direction is again randomly selected within

the angular distribution measured in VAMOS++ (see figure Figure 5.9). A Doppler-shifted γ ray, emitted from the projectile-like product slowing down in the remaining target thickness, is simulated assuming a given γ-transition energy and a decay time randomly chosen on the basis of the excited state lifetime.

In the second step, the γ-ray events generated by the Monte Carlo procedure discussed above (each event containing information on γ energy, γ direction and the ion-velocity vector, after the target) are passed to the AGATA simulation package [153], which provides, as an output, the γ-ray energy deposited in the AGATA crystals. In the calculations, the AGATA-simulation code considers the actual configuration of the array in the measurement (*i.e.*, 31 crystals with the corresponding geometry).

The simulated γ-ray data are subsequently analysed with the AGATA OFT algorithm, following the same procedure applied to the experimental data. This allows to obtain the γ-ray energy and the relative angle between the γ-ray direction (reconstructed with the AGATA simulation package) and the ion velocity vector, at the decay point (resulting from the Monte Carlo simulation procedure performed in the first step, as discussed above). The γ-ray Doppler-shift correction is then performed. At this step, corrections are included to take into account the actual experimental energy resolution and the counting statistics of the AGATA detectors.

5.2.3 χ^2 analysis and minimisation surfaces

The evaluation of nuclear-state lifetimes in the time range of hundreds femtoseconds requires a detailed study of Doppler-broadened γ-ray line shapes, as a function of the relative angle θ_{rel} between the moving-source and the emitted γ-ray directions (see Figure 5.6). Figure 5.12 shows examples of simulated line shapes for the 2.779-MeV γ ray of ^{19}O, over the full continuous angular range $\theta_{rel} = 0°$-$180°$. In the simulations, three lifetime values are considered, *i.e.*, τ = 20, 100 and 2000 fs (panels (I), (II) and (III), respectively). In the short lifetime cases, a significant distortion of the overall line shape is observed, as shown in the projections reported in Figure 5.12(b). Such a line shape distortion is at the basis of the nuclear-state lifetime evaluation. We underline that a lifetime-analysis procedure based on a continuous-angle distribution, which is possible with γ-tracking arrays, acquires a significantly enhanced sensitivity, with respect to experiments done with conventional γ-ray arrays with detectors placed at discrete angles, relative to the beam axis. This improvement was already pointed out by Stahl *et al*. [154] and Michelagnoli *et al*. [155] for the restricted cases of reactions in which products have well-defined velocity vectors, such as Coulomb-excitation reactions. In our work, we broaden the applicability of such a continuous angle technique to reactions with complex structure of product velocity distribution, as in the case of low-energy binary, dissipative collisions. Crucial in this case is both the precise reconstruction of the emitted γ-ray direction by the tracking array, as well as the reaction-product-direction measurement by a magnetic spectrometer.

A closer view of the Doppler-broadened lineshapes is given by the projections of the simulated matrices on the γ-ray energy axis for $\theta_{rel} = (130 \pm 10)°$ and $(170 \pm 10)°$ (panels (V) and (VI), respectively), which correspond to the angular coverage of the AGATA

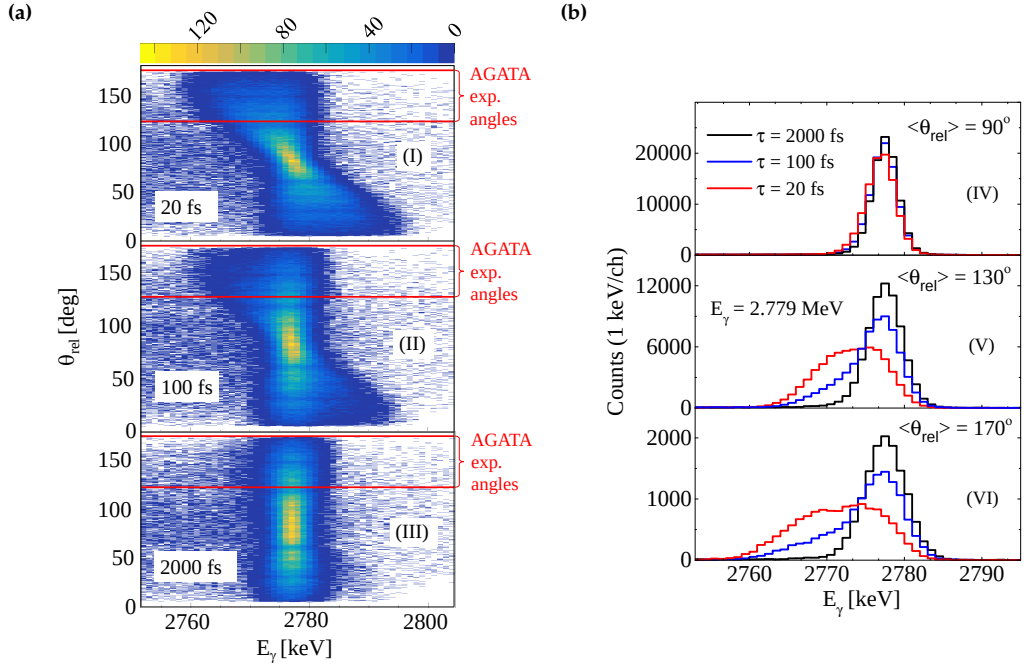

Figure 5.12: (a) Simulated two-dimensional (E_γ,θ_{rel}) Doppler-corrected line shapes, for the 2.779-MeV γ ray de-exciting the 2.779-MeV state of ^{19}O, assuming lifetime values of 20 (I), 100 (II) and 2000 fs (III). The horizontal lines give the AGATA angular coverage of the *e676* experiment. Panels (IV)-(VI): projections on the γ-ray energy axis for θ_{rel} = (90 ± 10)° (IV), (130 ± 10)° (V) and (170 ± 10)° (VI). Figure adapted from Ref. [82] [a].

[a] Licensed under the CC BY 4.0 License [2]

array in the GANIL experiment. It is seen that, for lifetime values much longer than the target-crossing time (*i.e.*, >> 130 fs), a symmetric line shape, with the same centroid energy, is observed at all angles (black histograms) after a Doppler-shift correction based on the ion final velocity (*i.e.*, after the target). A considerable line shape distortion is instead observed for shorter lifetimes, which can be used to obtain a precise estimate of τ for lifetimes of the order of the target-crossing time (blue lines). The lower limit for lifetime determination is found to be of the order of tens of femtoseconds, at which the γ line becomes broad and featureless, and significantly shifted in energy (red histograms). As discussed later, crucial for the analysis is also the precise γ-ray energy determination provided by the 90° detectors (panel (IV)), which are not affected by the Doppler shift. Altogether, this clearly indicates that the best conditions for precise lifetime determination will be reached by a tracking array with an extended angular coverage, as it is foreseen for AGATA in the coming future.

Coming now to the details of the lifetime analysis procedure, here developed, the technique relies on a two-dimensional χ^2 minimisation, in lifetime and transition energy coordinates (E_γ,τ). The χ^2 is calculated considering the measured and simulated Doppler-shift corrected spectra, over the available θ_{rel} angular range. In the presented

cases, γ-ray spectra associated with the three angular ranges $\theta_{rel} = (130 \pm 10)°$, $(150 \pm 10)°$ and $(170 \pm 10)°$ were constructed and simultaneously used in the minimisation procedure. The two-dimensional χ^2 surface is expected to show a minimum corresponding to the optimal state lifetime and transition energy. The total errors will be obtained by summing contributions from statistics and systematics, the latter arising from uncertainties in the stopping-power parametrisation, background subtractions and ion-velocity reconstruction. In the cases discussed below, these total errors are equivalent to the uncertainties extracted by considering the region with 80 % confidence level around the χ^2 minimum. We note that the lifetime obtained with the present procedure is the cumulative lifetime: it includes possible contributions from feeding transitions. In all cases here considered, such contribution is negligible, as indicated by the absence of γ rays populating the states of interest. These states are fed mostly directly in the transfer reaction or via neutron emission after the transfer process.

Figure 5.13(i) shows an example of lifetime analysis for a state in ^{17}O, for which a τ value of the order of 100 fs is reported in literature [53], well within the sensitivity range of the present technique. In this case, the 3055-keV, $1/2^-_1$ state in ^{17}O, which is depopulated by a 2184-keV γ ray, is considered (see level scheme in Figure 5.5(a)). Simulated and experimental γ-ray spectra are compared in three ranges of the relative angle θ_{rel}: 120°-140°, 140°-160° and 160°-180°, as shown in panels (a)-(c) of Figure 5.13(i). The corresponding two-dimensional χ^2 lifetime-energy surface is reported in panel (d). A well-defined minimum (marked with a white cross) is visible at $(E_\gamma,\tau) = (2184.3^{+0.3}_{-0.2}$ keV, 159^{+40}_{-30} fs), in agreement, within uncertainty, with the literature values of $\tau = 120^{+80}_{-60}$ fs and $E_\gamma = 2184.44(9)$ keV [53]. The errors are obtained by considering the region around the χ^2 minimum, indicated with a white contour in panel (d) (80 % confidence level, as discussed above). The red shaded bands in panels (a)-(c) are the results of the line shape simulations performed by varying E_γ and τ within the uncertainty region around the χ^2 minimum.

An additional example of a lifetime analysis in ^{19}O, exploited to validated the new DSAM technique, is presented in Ref. [82]. Moreover, in Ref. [52] is reported the lifetime measurement of the second 2^+ state in ^{20}O, located at 4070 keV excitation energy, which resulted in a lifetime $\tau = 150^{+80}_{-30}$ fs, as mentioned previously in Section 3.1 (see also later discussion).

5.2.4 Sensitivity limits

As discussed before, the time range accessible by the present lifetime analysis technique is dictated by the target-crossing time T_{cross} of the reaction products, that is ~ 130 fs for the GANIL experiment. The simulation showed that this range spans between ~ $0.2T_{cross}$ and ~ $4T_{cross}$. Consequently, for lifetime values a few times longer or shorter than T_{cross}, the here proposed two-dimensional χ^2 minimization procedure, in lifetime-transition energy coordinates (E_γ,τ), cannot provide a well-localized minimum. We expect, instead, a valley extending towards infinitely long lifetimes or towards zero.

To illustrate this aspect of the sensitivity limit, we consider in Figure 5.13(ii) the case of the long-lived 2371-keV state in ^{19}O, for which the lower limit $\tau > 3.5$ ps is reported

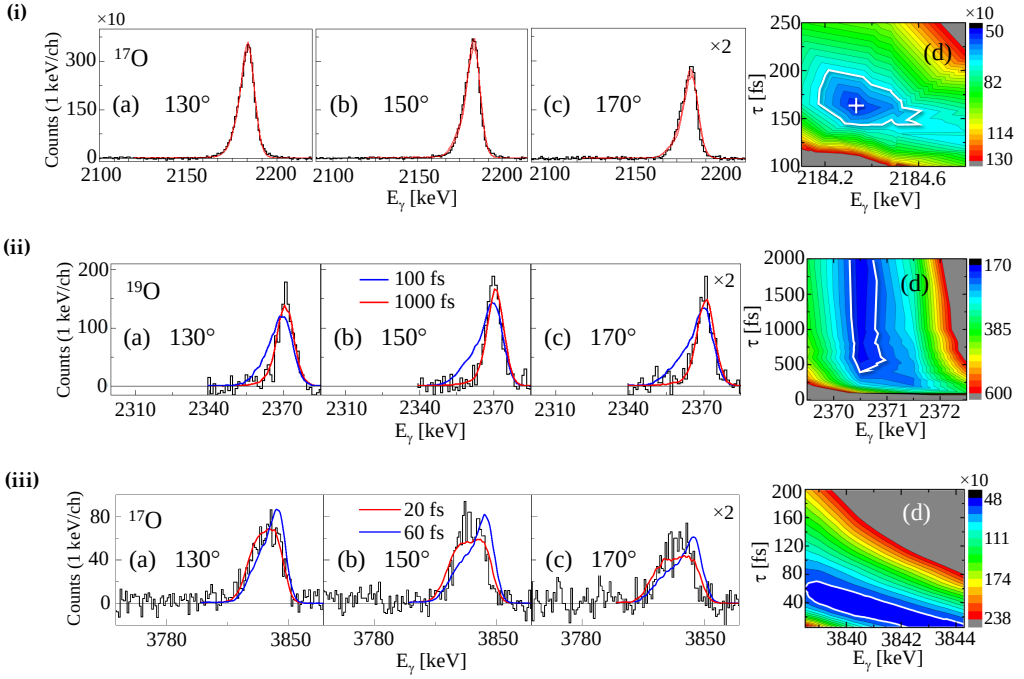

Figure 5.13: Doppler-shift corrected AGATA γ-ray energy spectra (black) and simulated ones, for the angular ranges of (130 ± 10)° (a), (150 ± 10)° (b) and (170 ± 10)° (c). Panels (d): corresponding two-dimensional χ^2 lifetime-energy surface, with the white cross and white contour line indicating the minimum and the uncertainty region. The cases of the 2184-keV line of ^{17}O (i), 2371-keV line of ^{19}O (ii), and the 3843-keV line of ^{19}O (iii) are shown. The red shaded bands in panels (a)-(c) of subfigure (i) are the results of the line shape simulations performed by varying E_γ and τ within the uncertainty region of the χ^2 map, *i.e.*, $(E_\gamma,\tau) = (2184.3^{+0.3}_{-0.2}\,\text{keV}, 159^{+40}_{-30}\,\text{fs})$. In subfigure (ii), the simulated curves corresponding to lifetime values of 100 fs and 1000 fs are displayed in panels (a)-(c) by blue and red lines, respectively. No well-defined minimum is present in the χ^2 map of panel (d). The results of the 2371-keV line analysis are: $\tau > 400$ fs at $E_\gamma = 2370.6^{+0.5}_{-0.3}$ keV. In subfigure (iii) the simulated curves corresponding to lifetime values of 20 fs and 60 fs are displayed in panels (a)-(c) by blue and red lines, respectively. Also in this case, no well-defined minimum is present in the χ^2 map of panel (d): a lifetime $\tau < 70$ fs is observed. Figure adapted from Ref. [82] [a].

[a] Licensed under the CC BY 4.0 License [2]

in literature [156]. Panels (a)-(c) display the Doppler-shift corrected 2371-keV γ ray (de-exciting the state), as measured in AGATA in the three angular ranges of 120°-140°, 140°-160° and 160°-180°, respectively. In all cases, a symmetric Gaussian line shape is observed, as expected for decays occurring outside the target, at times significantly larger than the target-crossing time. Simulated line shapes corresponding to $\tau = 100$ and 1000 fs are also shown in blue and red, respectively, for comparison. No minimum is obtained in the χ^2 map (see panel (d) of Figure 5.13(ii)), but a valley is observed, extending from $\tau > 400$ fs, at the γ-transition energy of $2370.6^{+0.5}_{-0.3}$ keV, which agrees well with the literature value. Figure 5.13(iii) shows the case of the short-lived 3842-keV

state in ^{17}O, for which the upper limit $\tau < 26$ fs is reported in literature [157]. The Doppler-shift corrected 3842-keV γ ray (de-exciting the state) is shown in panels (a)-(c) as measured in AGATA at the same angular ranges used for the previous case. At all the angles, a broad peak structure is observed around 3835 keV, which is consistent with a γ emission inside the target, from a very short-lived state. Simulated curves corresponding to $\tau = 20$ and 60 fs are also shown in red and blue, respectively, for comparison. Also in this case, no well-defined minimum is found in the χ^2 map (see Figure 5.13(iii)), but a valley is seen, extending from 70 fs down to 0 fs, with a strong dependence on the γ-ray transition energy. A lifetime $\tau = 20(20)$ fs is obtained if the γ-transition energy is taken to be 3842.3(4) keV, as reported in literature [53]. This shows the impact of a precise γ-ray energy determination, which could be best accomplished when the tracking array extends to 90°.

5.2.5 Relevance of AGATA performance

The quality of the results of the newly-developed lifetime analysis technique depends strongly on the Doppler-shift correction capabilities of the experimental set-up. In the case of γ-ray tracking arrays, such as AGATA, the interaction point is identified with unprecedented precision, with respect to conventional HPGe detectors (see Section 4.1). In a standard configuration of AGATA (at 23.5 cm from the target center), the angular resolution is around 1°, as a result of the combined use of Pulse Shape Analysis and tracking algorithms. With the use of a magnetic spectrometer, which also offers a resolution of 1° for the angle detection of the reaction products (as in the case of VAMOS++), the angle between the fragment velocity at the de-excitation point and the γ-ray direction can be determined with an accuracy of about 1.5°. Such a precision is crucial, together with an accurate measurement of the ion velocity, to perform a Doppler-shift correction which allows for a detailed study of the γ-ray line shape, like the one presented here.

Figure 5.14(b) gives, as an example, the line shape of the 2184-keV γ ray of ^{17}O obtained by determining the γ-ray interaction points using the full AGATA tracking procedure (blue histogram), or by considering the segment centres (red histogram), as it is done with conventional HPGe detectors (for the determination of the interaction points, see Figure 5.14(a)). In the latter case, the less precise Doppler-shift correction is found to limit significantly the line shape sensitivity to the lifetime and γ-ray energy determination. A shallower minimum is obtained in the lifetime-transition energy χ^2 surface with respect to the one reported in panel (d) of Figure 5.13(i), leading to much larger uncertainties in the final E_γ and τ values. In the specific case of the 2184-keV γ ray of ^{17}O, the uncertainty region is ~ 5 times more extended in E_γ and ~ 2.3 times wider in τ (see Figure 5.14(c)). Moreover, the χ^2 value at the minimum of the two-dimensional map is ~ 2.5 times larger than in the AGATA analysis performed with full tracking. A similar behaviour of the χ^2 map was observed (when the segment centres were considered) in the lifetime analyses of the $7/2^+$ and 2^+_2 states in ^{19}O and ^{20}O [52], respectively. Figure 5.14(c) displays the results of the line shape analysis in the case of Doppler-shift corrections based on full tracking (square symbols with error bars) and on interaction positions taken as segment centre (contour areas), in the (E_γ,τ) coordinates.

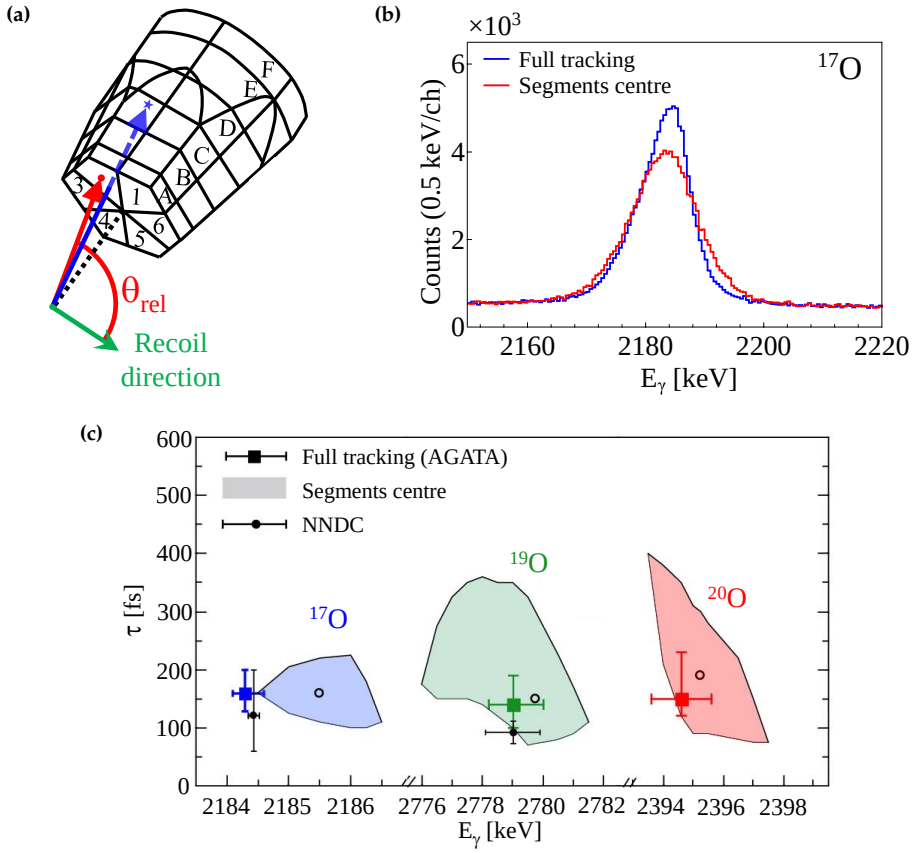

Figure 5.14: Panel (a): interaction of a γ-ray, emitted from a recoiling reaction fragment, in a segmented AGATA germanium detector. The real γ-interaction point is marked by a blue star, the segment center by a red point. Panel (b): AGATA Doppler-shift corrected 2184-keV, $1/2^-_1 \rightarrow 1/2^+_1$, γ transition of ^{17}O, obtained by applying a Doppler-shift correction based on the full tracking procedure (blue) or considering the segment center of the AGATA detector (red), as γ-ray interaction point. Panel (c): Lifetime values obtained with the present Monte Carlo technique for the 2184-keV, $1/2^-$ state of ^{17}O (blue), the 2779-keV, $7/2^+$ state of ^{17}O (green), and the 4070-keV, 2^+_2 state of ^{20}O (red), considering the γ-interaction points extracted with the AGATA full tracking procedure (square symbols) and the segment centres of the AGATA detectors (contour areas correspond to the uncertainty and the open circles indicate the best values, as directly taken from the corresponding χ^2 minimisation surfaces). For the two test cases of ^{17}O and ^{19}O, the NNDC adopted values [53] are given by circles symbols with error bars. Figure adapted from Ref. [82] [a].

[a] Licensed under the CC BY 4.0 License [2]

For the two test cases of ^{17}O and ^{19}O, the NNDC adopted values [53] (obtained with different reactions and lifetime techniques) are denoted by circles with error bars. The lifetime and energy determination is quite accurate if the tracking procedure is applied, while the analysis based on the segment-center interaction positions suffers from large

uncertainties in both lifetime and γ-energy coordinates. We note that these uncertainties would be much larger in the case of conventional HPGe arrays, where individual crystals are typically bigger than AGATA segments.

The new approach discussed in this work is expected to become an important tool for investigating exotic neutron-rich nuclei produced with intense isotope-separation on-line (ISOL) beams [158] in low-energy heavy-ion binary collisions: it will allow to obtain information on electromagnetic observables which can be used to test the quality of first-principles nuclear structure calculations, complementing common benchmarks based on nuclear-state energies.

In the following, we will present a number of applications of the newly developed technique to other nuclei produced in the experiment, with the deep-inelastic ^{18}O+^{181}Ta reaction. First of all, we will introduce an additional test to verify the reliability of the technique, exploiting a case in ^{17}N in which two gamma rays are emitted from the same state of interest. We will then apply the technique to other excited states in ^{17}N, ^{14}C, and ^{18}N.

5.3 Applications of the new DSAM technique

This Section is devoted to the applications of the newly developed lifetime-measurement technique. Firstly, we will address the analysis of short-lived states in ^{17}N [159]: the reliability of the technique will be additionally confirmed by measuring the lifetime of the 5515-keV $3/2^-$ state, which is depopulated by two different γ rays. The method will be also used to measure the lifetime of the 5170-keV $(9/2^+)$ state in the same nucleus. Comparisons with large-scale shell-model predictions will be given as well. Secondly, we will apply the lifetime-measurement technique to the 2_1^+ state in ^{14}C, whose physics case has been introduced in Section 3.2.

5.3.1 Lifetime analysis of short-lived states in ^{17}N

We consider here[2] the ^{17}N $3/2^-$ excited state located at 5515(3) keV, which de-excites via the 4141-keV γ ray to the $3/2_1^-$ state and the 5515-keV transition to the ground state, with comparable intensity (see Figures 5.15 and 5.16). These transitions can be used, independently from each other, to check the reliability of the new DSAM technique, by measuring the lifetime of the 5515-keV state, reported to be $\tau < 100$ fs [160].

As shown in Figure 5.17, we obtained two separate lifetime (τ) vs. γ-ray energy (E_γ) χ^2 minimisation surfaces. From these maps, we could extract both the γ-ray energy and an upper limit for the lifetime: $E_\gamma^{(1)} = 4141.0^{+0.7}_{-3.5}$ keV and $\tau^{(1)} < 60$ fs; $E_\gamma^{(2)} = 5515.0^{+1.7}_{-3.5}$ keV and $\tau^{(2)} < 60$ fs. The energies are well in agreement with the literature values, and the lifetimes agree with each other and with the literature, improving the upper limit by 40 %, and confirming the reliability of the technique.

In the same ^{17}N nucleus, a detailed investigation of the γ-ray energy spectrum highlighted a discrepancy between the literature energy and the measured one, in the case of

[2]Part of the text and figures of this Section are adapted from Ref. [159], licensed under a Creative Commons Attribution 4.0 International License [2], with kind permission of Società Italiana di Fisica.

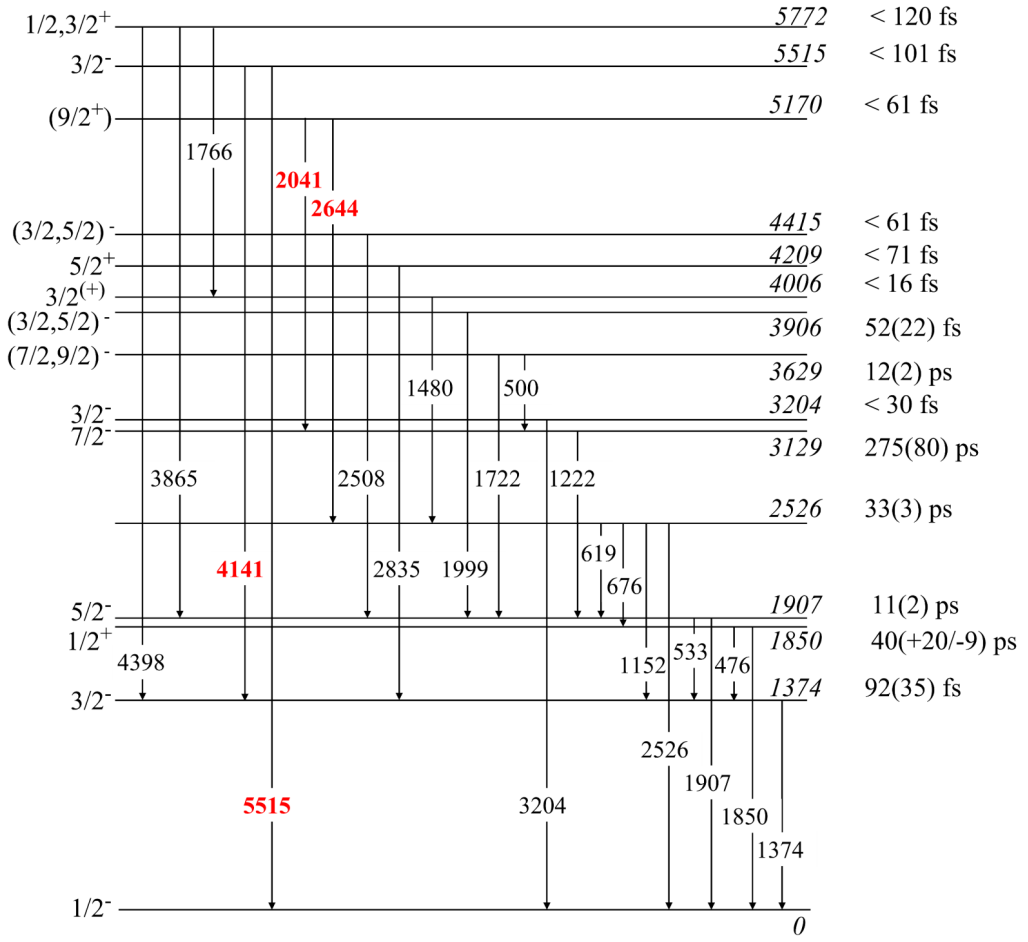

Figure 5.15: ^{17}N partial level scheme. Energies, lifetimes and spins are taken from the database [53]. Only the gamma rays observed in the experimental data of the present work are reported in the level scheme. Transitions marked in red are considered in the lifetime analysis. See Figure 5.16 for the corresponding γ-ray energy spectrum.

the $(9/2^+)_1 \rightarrow 7/2^-_1$ and $(9/2^+)_1 \rightarrow 5/2^+_1$ transitions, depopulating the 5170-keV state. The literature values are $E_\gamma^{(1)} = 2041(2)$ keV and $E_\gamma^{(2)} = 2644(2)$ keV [53], respectively, while we observed the associated peaks at higher energies, as shown in the inset of Figure 5.16, in the case of the 2041-keV line. The lifetime of the 5170-keV state is quoted to be shorter than 60 fs [160], therefore the discrepancy could be due to an imprecise energy measurement or to a wrong lifetime estimate. In particular, if the lifetime would be much longer, the peak should appear at higher energies in our data, since AGATA is placed at backward angles. By applying the new DSAM method, we extracted the lifetime of this state, considering the 2041-keV transition only, which had better statistics. Figure 5.18(a) shows the corresponding χ^2 map, where the white cross marks the absolute minimum, and the white contour delimits the uncertainty. The comparison between the experimental and

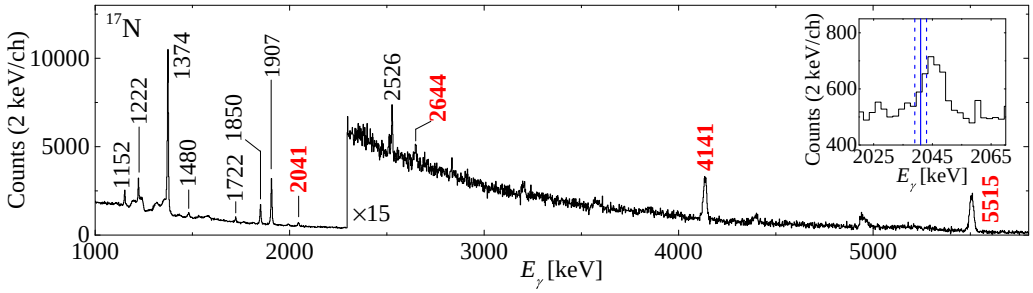

Figure 5.16: ^{17}N AGATA Doppler-shift corrected gamma-ray energy spectrum. Only the most intense transitions are shown, the level scheme reported in Figure 5.15 summarises all the transitions observed. The energies of interest for the discussion are shown in red (literature values [53]). The inset displays a zoom around the 2041-keV line, with the blue vertical line referring to the energy value quoted in literature [53], with its uncertainty (dashed blue lines). Figure adapted from Ref. [159][a] with permission of Società Italiana di Fisica.

[a] Licensed under the CC BY 4.0 License [2]

simulated data is shown in Figure 5.18(b). A lifetime $\tau = 35^{+110}_{-30}$ fs for a γ-ray energy of $2045.0^{+1.2}_{-1.7}$ keV was measured, in agreement with the lifetime literature value of Ref. [160], thus pointing to an imprecise earlier measurement for the γ-ray energy. Therefore, the re-measured energy of the $(9/2^+)_1$ state is $5174.0^{+1.3}_{-1.8}$ keV, while the $(9/2^+)_1 \rightarrow 5/2^+_1$ transition energy is $2647.8^{+1.4}_{-1.9}$ keV.

Discussion

The new implementation of the DSAM-analysis technique to low-energy binary reactions has allowed to determine the lifetime of the $3/2^-$ and $(9/2^+)$ states in ^{17}N at 5515 and 5174 keV, respectively. As a result, we provided a precise energy measurement for the $(9/2^+)$ state, previously reported at lower energy, and an improved upper limit to the lifetime of the $3/2^-_3$ state ($\tau < 60$ fs).

The results have been compared to modern large-scale shell-model calculation predictions. The lifetime value measured for the $3/2^-_3$ state is in line with the one obtained using the YSOX interaction (τ=0.5 fs) [7]. The same theoretical calculations locate the state at 7.081 MeV. On the contrary, the lifetime of the $(9/2^+)_1$ state, $\tau = 35^{+110}_{-30}$ fs, is found to be more than an order of magnitude shorter than the predicted value for the corresponding state, which is calculated at much higher energy, ~7.3 MeV. The difficulty of the shell-model approach in reproducing positive-parity states in nitrogen isotopes is well known, and it is related to the calculated size of the N=8 gap. This finding confirms the relevance of high-precision γ spectroscopy of light neutron-rich nuclei (see also discussion on ^{18}N in 5.4), such as N isotopes, provides key observables sensitive to the properties of the nuclear interaction, which are essential to improve and benchmark the most advanced theory approaches.

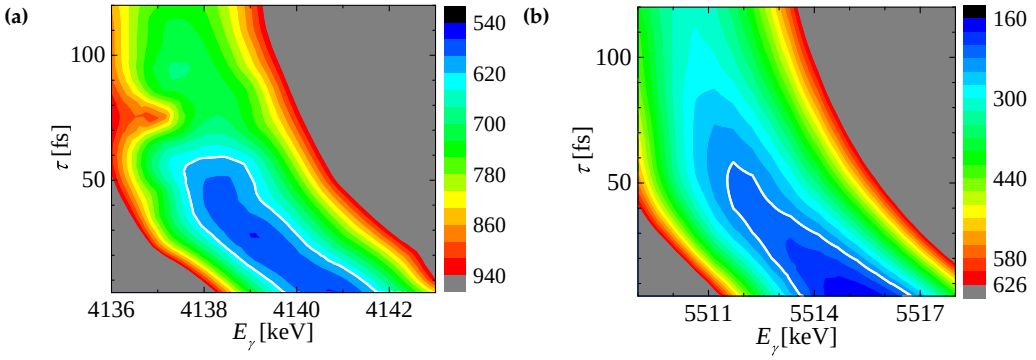

Figure 5.17: Two-dimensional χ^2-minimisation maps obtained after the comparison between measured and simulated data for the $3/2^-_3 \rightarrow 3/2^-_1$ and $3/2^-_3 \rightarrow$ g.s. transitions in ^{17}N, at 4141 keV (a) and 5515 keV (b), respectively. The white contours delimit the uncertainty. Figure adapted from Ref. [159][a] with permission of Società Italiana di Fisica.

[a] Licensed under the CC BY 4.0 License [2]

5.3.2 Investigation of ^{14}C

In this Section we will address the lifetime measurement of the 2^+_1 excited state in ^{14}C to clarify the apparently anomalous trend of the B(E2) reduced transition probabilities in the carbon isotopic chain (see Section 3.2 for details on the physics case).

The selection of the events associated to ^{14}C is analogous to the one described in connection to the nitrogen isotopes: the atomic number Z=6 is chosen in the ΔE vs. E_{tot} plot reported in Figure 5.3(a). A charge (Q) vs. mass/charge (M/Q) 2D-histogram is produced (see Figure 5.3(b)) for the carbon isotopes and a graphical cut is applied considering the regions associated to the specific isotope of interest, in this case ^{14}C (3.6×10^6 events).

The high-energy part of the AGATA Doppler-corrected gamma-ray energy spectrum of ^{14}C is shown in Figure 5.19, while Figure 5.20 displays the level scheme. In the γ-ray spectrum, only the energy region above 5 MeV is shown, displaying the most intense gamma rays, namely the 6092.4-, 6726.5- and 7010-keV transitions [53], depopulating the 1^-_1, 3^-_1, 2^+_1 states, respectively. In the experimental spectrum we observed also other less intense transitions (495.35, 613 and 1248 keV) at lower energies. These gamma rays are reported for completeness in the level scheme in Figure 5.20.

Here, we concentrate on the 7010-keV $2^+_1 \rightarrow 0^+_1$ g.s. transition. Exploiting the novel lifetime-measurement technique introduced before (see Section 5.2), we measured the lifetime of the 2^+_1 state, by analysing the line shape of this gamma transition. The analysis was performed after checking the technique reliability and AGATA response stability also at such high energies, simulating the ^{14}C 6726.5-keV transition (see level scheme in Figure 5.20) line shape with a 95 ps lifetime [53], as shown in Figure 5.21. Since the simulation gave a consistent result, we proceeded with the analysis and extracted the (E_γ,τ) χ^2 minimisation surface for the $2^+_1 \rightarrow 0^+_1$ g.s. transition, shown in Figure 5.22(a). Like in the case of the 1663-keV gamma-ray in ^{18}N, the limited statistics made impossible

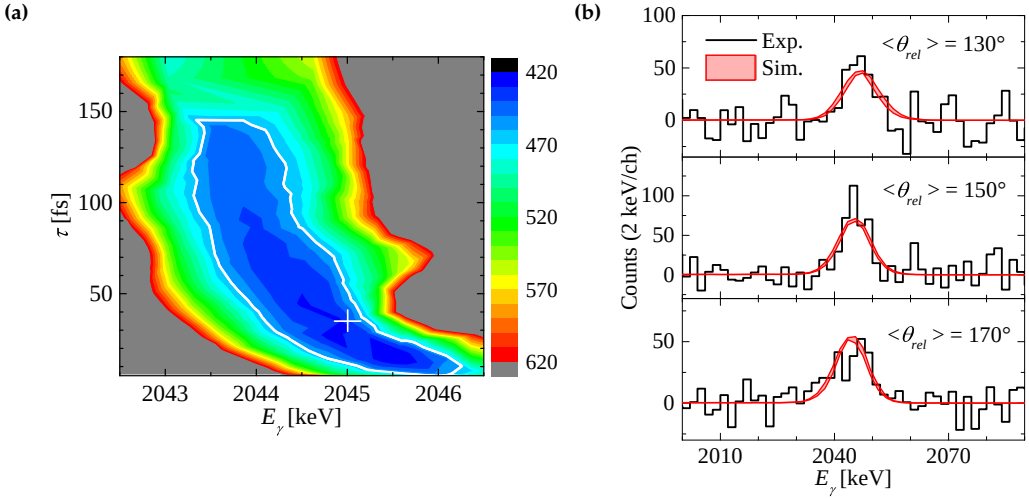

Figure 5.18: Panel (a): same as Figure 5.17 for the 2041-keV $(9/2^+)_1 \rightarrow 7/2_1^-$ transition. The white cross marks the χ^2 minimum. Panel (b): comparison between the experimental data (black histogram) and the simulated ones within the uncertainty (red shades) for the 2041-keV transition, for three ranges of angles (θ_{rel}) between the recoiling ion direction and the emitted γ ray direction (mean value for each range, $\Delta\theta = 20°$). Figure adapted from Ref. [159][a] with permission of Società Italiana di Fisica.

[a] Licensed under the CC BY 4.0 License [2]

the splitting of the experimental γ-ray spectrum in different sub-spectra, on the basis of the θ_{rel} angular range. In the χ^2 map, a valley extending towards lifetimes < 100 fs is visible, in a wide energy range (more than 10 keV). No absolute minimum, nor a delimited uncertainty region was achieved with the lifetime-energy analysis. This result cannot be used alone to extract the lifetime of the 2_1^+ state and the B(E2) value. However, if this map is combined with a very precise value of the γ-ray energy, a well defined lifetime value can still be extracted. For example, Figure 5.22(b) shows the comparison between the experimental background-subtracted AGATA gamma-ray spectrum (black histogram) in the region of the transition of interest, compared to three different simulated curves, obtained with a fixed energy value. The curves correspond to the spectra simulated considering a γ-ray energy of 7010 keV (the one reported in the database [53]) and three different lifetime values, namely 13 fs (green), 50 fs (red) and 100 fs (blue). For this specific energy (7010 keV), the simulated curve associated to $\tau = 13$ fs, which corresponds to the only lifetime value available in literature [86], clearly does not fit the experimental data. A more suitable lifetime would be in the range of 50 fs.

Discussion and results

The gamma-ray energy reported in the NNDC database (adopted from the review of Ref. [162]) and used to simulate the gamma-ray line shape of the $2_1^+ \rightarrow 0_1^+$ g.s. transition in Figure 5.22(b), has a quite large uncertainty of 4 keV, therefore it is not a reliable value to

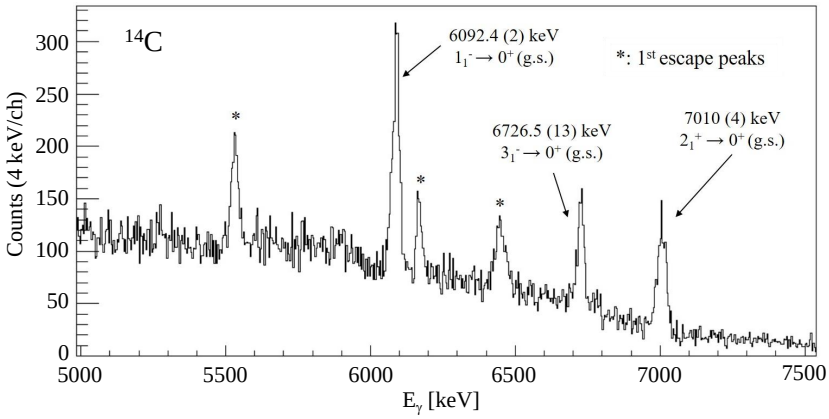

Figure 5.19: Partial AGATA Doppler-corrected γ-ray energy spectrum of ^{14}C. Energies taken from the database [53].

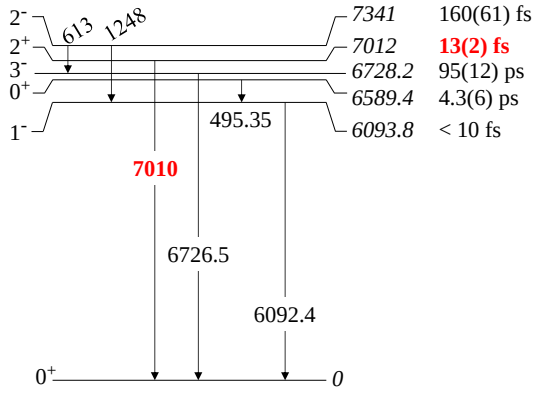

Figure 5.20: Partial ^{14}C level scheme. All the energies (in keV), lifetimes and spin/parity values are taken from the NNDC database [53]. In red is highlighted the transition of interest, with the reported lifetime value of 13(2) fs [86].

be used to extract the lifetime. In fact, once the energy uncertainty is taken into account, a lifetime of 65^{+32}_{-50} fs is obtained, with a large errorbar extending toward lower lifetimes: this measurement cannot exclude the lifetime value previously reported in literature to be 13(2) fs [86]. Alternatively, if we combine the χ^2 surface and the information on the lifetime reported in literature, we obtain a value for the gamma-ray energy of 7018(4) keV (see cross on the bottom-right side of Figure 5.22(a)). In addition to this, the energy measurement reported in the NNDC database does not refer to a direct measurement of the gamma-ray line, but it is deduced from the level excitation energy corrected for the nucleus recoil (E_R) induced by the gamma-ray emission (see Equation (5.5)).

$$E_R = \frac{E_\gamma^2}{2Mc^2} \tag{5.5}$$

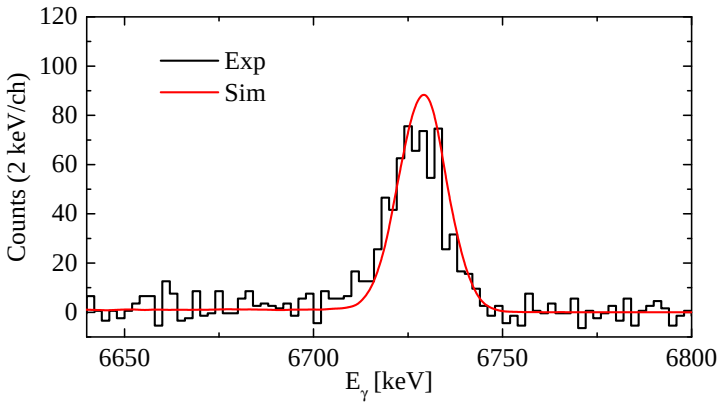

Figure 5.21: Comparison between experimental (black histogram) and simulated (red) data for the 6726-keV line in ^{14}C de-exciting the 3^-_1 long-lived state (see level scheme in Figure 5.20). The simulation has been performed considering a lifetime value for the excited state of 95 ps, as reported on the database [53].

In Equation (5.5) the induced recoil (E_R) is expressed as a function of the emitted gamma-ray energy E_γ and the mass M of the nucleus (c is the speed of light). This correction is of the order of ~ 2 keV for a 7-MeV gamma ray depopulating an excited state in ^{14}C.

The only direct γ-ray measurement available is the one reported in Ref. [163] to be 7011.7(52) keV. The direct measurement, performed in 1969 with Ge(Li) detectors exploiting a ^{7}Li+^{9}Be reaction, is affected by an even larger uncertainty than the value reported in the database. In more recent works, in which gamma rays of ^{14}C (see for example Ref. [164]) have been reported with high accuracy, no observation of the $2^+_1 \rightarrow 0^+_1$ g.s. transition has been reported.

Since no direct gamma-ray energy measurements are available in literature, we came back to the indirect observation of the excitation energy of the 2^+_1 state of interest. The value reported in the database is not the most accurate: Piskoř in 1990 measured an excitation energy for the 2^+_1 state of $E_{exc} = 7011.4(8)$ keV [161] in a ^{13}C(d,p)^{14}C reaction. However, we have to mention that the reliability of Piskoř's 2^+_1 excited state energy cannot be totally confirmed. Most of the ^{14}C excited-states energies reported in Piskoř's paper [161] are well in agreement with the ones quoted in other works by Ajzenberg-Selove [165] and in particular by Firestone [164], the latter having a very good accuracy, as shown in Table 5.1. However, the 3^-_1 excitation energy (6731.58(11) keV) appears to be overestimated with respect to the one reported in the paper of Throop (6728.1(14) keV) [163], adopted by the database [53]. Piskoř imputed this discrepancy to the lack of statistics in Throop's work. In addition, other Throop's values appeared to be underestimated with respect to a more recent work adopted in the Ajzenberg-Selove's review [165]. The gamma ray de-exciting the long-lived 3^-_1 state in our dataset appears at a significantly lower energy ($E_\gamma = 6726.8(8)$ keV) with respect to the gamma-ray energy corresponding to Piskoř's excitation energy value after recoil correction (6729.8 keV, see Equation (5.5)), but still in agreement with the energy reported in the database ($E_\gamma = 6726.5(13)$ keV).

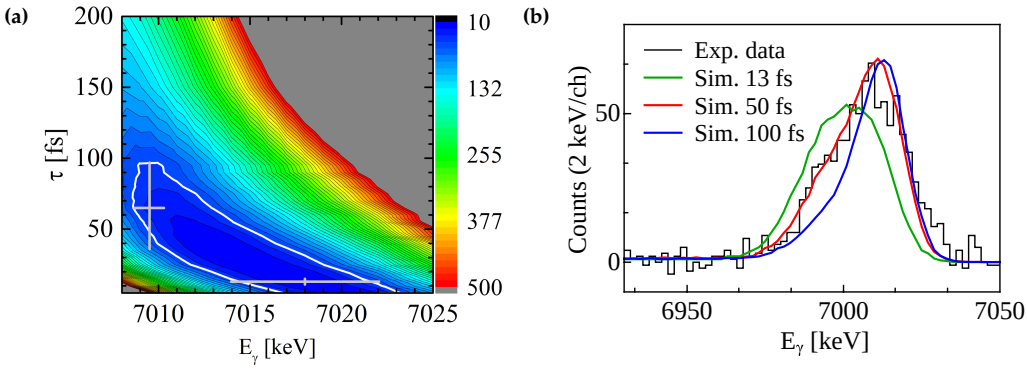

Figure 5.22: Panel (a): (E_γ,τ) χ^2 minimisation surface for the $2_1^+ \rightarrow 0_1^+$ g.s. transition in ^{14}C. The white contour delimits the uncertainty region. The two crosses identify the minima (with corresponding uncertainties in both lifetime and gamma-ray energy) obtained combining the χ^2 surface and the lifetime available in literature (τ = 13(2) fs [86], right cross) or the energy extracted from Piskoř's work (E_γ = 7009.5(8) keV [161], left cross). See discussion in the text for more details. Panel (b): AGATA Doppler-corrected background-subtracted γ-ray energy spectrum (black histogram) in the region of the transition of interest of panel (a), compared to three simulated line shapes. Simulated curves obtained considering a fixed γ-ray energy of 7010 keV and lifetimes of 13 (green), 50 (red) and 100 fs (blue).

In our experimental work, the energy calibration at such high energies (6-7 MeV) turned out to be reliable, as confirmed by the comparison of the energies of gamma rays depopulating long-lived states (no lifetime-induced Doppler shift) observed in other reaction products (*e.g.*, ^{16}O), with precisely-known literature values. In addition, in ^{13}C a very precise energy of the $5/2^+ \rightarrow$ g.s. (being the $5/2^+$ a long-lived state with τ = 12.4(20) ps) gamma-ray transition is quoted in the database to be 3853.170(22) keV [53]. Our experimental value of 3853.3(4) keV is well in agreement with the one of the database, confirming also the reliability of the Doppler-correction fine tuning performed for the carbon isotopes, following the procedure described in Section 5.1 at page 50. The corresponding excitation energy reported in the database for the ^{13}C $5/2^+$ state, E_{exc} = 3684.507(19) keV, is also compatible to the one quoted in the same Piskoř's work (3853.67(20) keV) in which ^{14}C data have been published.

Summarising, most of the excitation energies reported in Piskoř's experimental study are consistent, except the ^{14}C 3_1^- state one. In our data, we cannot simultaneously reproduce both Piskoř's energies of the gamma rays depopulating long-lived states in ^{13}C and ^{14}C, $5/2^+$ and 3_1^- states respectively, while we are always consistent with the values reported in the NNDC database [53].

Regarding the ^{14}C 2_1^+ state of interest for the present work, Piskoř's excitation energy is in agreement with the one from a previous work [165], which in turn is affected by a large uncertainty. Therefore, we cannot state with complete certainty that Piskoř's value is reliable. However, since we did not find sufficiently strong evidence against its reliability and since this is the most recent and precisely known value available, we will consider it in our analysis to extract the lifetime of the ^{14}C 2_1^+ state.

Table 5.1: Comparison between the excitation energies in keV of the excited states in ^{14}C (see level scheme in Figure 5.20), as reported by Piskoř [161], Ajzenberg-Selove [165] and Firestone [164]. Most of the values are well in agreement between the three sources, except the energy of 3^-_1 state (see text for further details).

^{14}C excited state J^π	Piskoř	Ajsenberg-Selove	Firestone
1^-_1	6094.05(11)	6093.8(2)	6093.88(8)
0^+_2	6589.58(39)	6589.4(2)	6589.60(9)
3^-_1	6731.58(11)	6728.2(13)	/
0^-_1	6902.24(18)	6902.6(2)	6902.72(10)
2^+_1	7011.4(8)	7012.0(42)	/
2^-_1	7342.65(32)	7341.4(31)	/

The excitation energy corresponds to $E_\gamma = 7009.5(8)$ keV, after the recoil correction (from Equation (5.5)). If we consider such a value and we combine it with our χ^2 map we obtain a lifetime $\tau = 65^{+32}_{-29}$ fs, associated to the χ^2 minimum at that specific energy. First of all, the gamma-ray energy value deduced from Piskoř's work is not in agreement with the one we deduced from the combination of the χ^2 surface and the lifetime value previously reported in literature ($E_\gamma = 7018(4)$ keV). In addition, the lifetime is not compatible with the previous one reported in literature [86] (see cross on the left side of the χ^2 map of Figure 5.22(a)) and results in a much lower B(E2) reduced transition probability.

With the lifetime of Ref. [86], B(E2; $2^+_1 \rightarrow 0^+_1$) = 3.7(6) e^{2}fm^4(corresponding to 1.9(6) W.u.), while with the lifetime measured in the present work B(E2; $2^+_1 \rightarrow 0^+_1$) = $0.7^{+0.4}_{-0.3}$ e^{2}fm^4 ($0.37^{+0.20}_{-0.17}$ W.u.), nearly five times smaller than the previous estimate. Figure 5.23 displays the updated plot of the B(E2; $2^+_1 \rightarrow 0^+_1$) reduced transition probabilities (previously reported in Figure 3.3(b)), with the ^{14}C point extracted in the present work (blue star symbol). The new point corresponds to a minimum, as it is typically expected in magic nuclei in isotopic chains.

In conclusion, we managed to extract an updated value for the reduced transition probability B(E2; $2^+_1 \rightarrow 0^+_1$) = $0.7^{+0.4}_{-0.3}$ e^{2}fm^4 in ^{14}C, combining the present lifetime-energy analysis performed with the newly developed technique described in Section 5.2, and an already available measurement of the 2^+_1 state excitation energy, quoted in literature with sufficient accuracy. This result is crucial to understand the nature of ^{14}C, in comparison with theory predictions. At the moment, the available large-scale NCSM calculations [44] strongly depend on the phase space and the interaction treatment, therefore this additional experimental measurement could be considered in the next future to benchmark this kind of theoretical model and the interactions used.

Furthermore, the present analysis strongly points toward the necessity of extending the angular coverage of state-of-the-art gamma-ray tracking arrays to 90°, where the gamma-ray energies are not affected by Doppler shifts. This improvement would permit to obtain high-precision gamma-ray energies within the same experiment, making studies like the one reported here more reliable. Investigations involving the light neutron-rich side of the valley of stability or hard-to-reach exotic nuclei in general, where spectroscopic

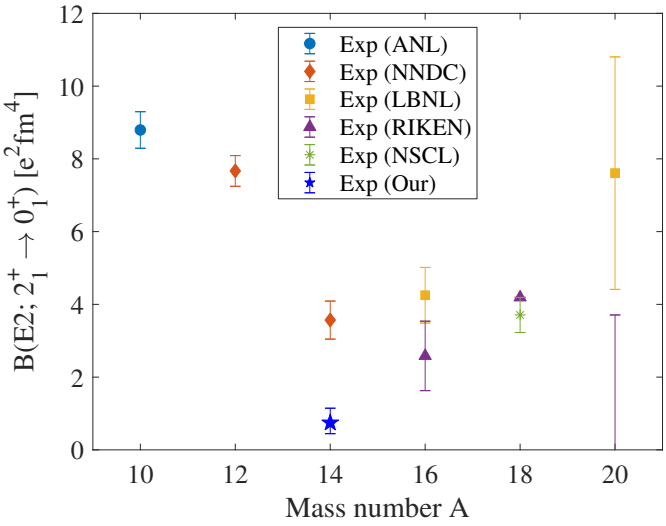

Figure 5.23: Same as Figure 3.3(b), updated with the B(E2; $2_1^+ \rightarrow 0_1^+$) experimental value in the ^{14}C nucleus, measured in this work.

information is still limited, would greatly profit from this kind of extension.

5.4 Gamma spectroscopy in ^{18}N

In this section[3] we will discuss the high-resolution γ-ray spectroscopy of ^{18}N, whose physics case has been introduced in Section 3.3. Six states are newly identified, which, together with the three known excitations, exhaust all negative-parity excited states expected below the neutron-emission threshold. In addition, the new lifetime-measurement technique described in Section 5.2 will be exploited to measure the lifetime of a newly discovered state, at 2404.6(13) keV. A comparison with large-scale shell-model calculations performed in the *p-sd* space, with the YSOX interaction will be also presented.

In Figure 5.3(c), we already showed the identification plot of the nitrogen ions, corresponding to a total of 4.8×10^6 events, out of which 2.6×10^5 belong to ^{18}N. Figure 5.24(a) shows the AGATA γ-ray spectrum obtained by gating on the ^{18}N ions regions, corresponding to two charge states, as shown in Figure 5.3(c). The spectrum has been Doppler-corrected on an event-by-event basis, considering the product velocity vector measured in VAMOS++, as discussed in Section 5.1 in connection to the data processing. Previously known 114.6-, 155-, 472.7- and 627-keV transitions are marked in black [53, 101, 102], while newly observed γ rays at 1091(1), 1147(1), 1205(1), 1566.0(10), 1663.0(8), 1721.0(11), 2073.4(8), 2301.0(8), and 2416(2) keV are indicated by red labels. Green stars mark lines from the target-like $^{180;181}$W binary-reaction partners, which are broadened and shifted due the Doppler-shift correction for the ^{18}N product, applied to this spectrum. Spectra constructed by gating on the 114.6-keV ($2_1^- \rightarrow 1_1^-$ (g.s.)) and 627-keV ($3_1^- \rightarrow 2_1^-$)

[3]Part of the text and figures are adapted from Refs. [143, 166], both licensed under a Creative Commons Attribution 4.0 International License [2]. Ref. [166] is reused with kind permission of Società Italiana di Fisica.

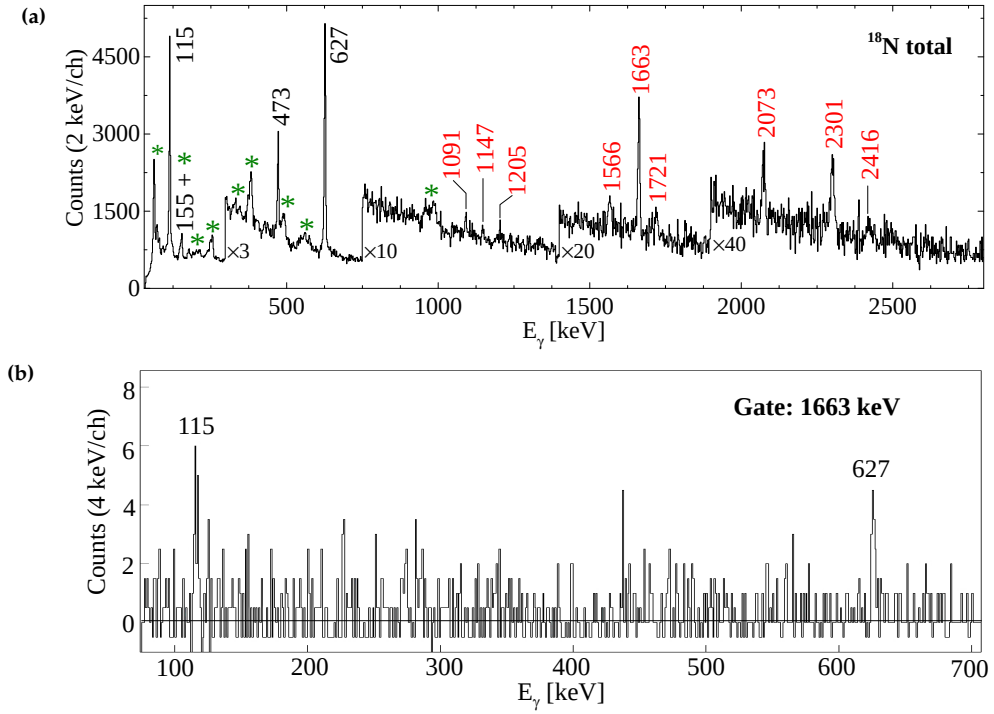

Figure 5.24: (a) AGATA Doppler-corrected γ-energy spectrum of ^{18}N. Energies of already known transitions are shown in black [53, 100, 101], those of newly observed gamma rays in red. Contaminant lines from ^{180,181}W binary-reaction partners are marked by green stars. (b): γ-ray spectrum in coincidence with the 1663-keV line, showing the coincidences with the 115- and 627-keV transitions.

transitions confirmed the coincidence relationships between the 114.6-, 472.7-, 155- and 627-keV rays, reported earlier [101]. They also showed the presence of the newly found 1663.0-keV line (see Figure 5.24(b)) [166, 167]. Such a transition was therefore placed in cascade with the 627.0-keV and 114.6-keV gamma rays, depopulating a state at 2404.6 keV, as shown in the level scheme of Figure 5.25(a). None of the other new lines could be seen in the coincidence spectra, either due to the limited statistics or their possible direct feeding to the 1^- ground state. Next, by inspecting energy differences between gamma rays, three new levels were identified. First, we considered the 1566- and 1721-keV transitions which differ by 155 keV, what equals the energy difference between the 3^-_1 and (2^-_2) states, at 741.6 and 587.3 keV. One may then assume that they de-excite a state at E_{exc} = 2308 keV, with relative branchings of 57(11) and 43(11) %, respectively. Similarly, the 2301- and the weak 2416-keV gamma rays could de-excite a level placed at 2416 keV, feeding the first-excited 2^-_1 state and the 1^-_1 ground state, with relative branchings of 78(11) and 22(11) %, respectively.

The group of three weak transitions observed at 1091, 1147 and 1205 keV required special attention, as they could be related to the existence of a 1^- state or a doublet of unresolved 0^-_1 and 1^-_2 states, reported by Hoffman *et al.* [102] at 1.17(2) MeV. It is very

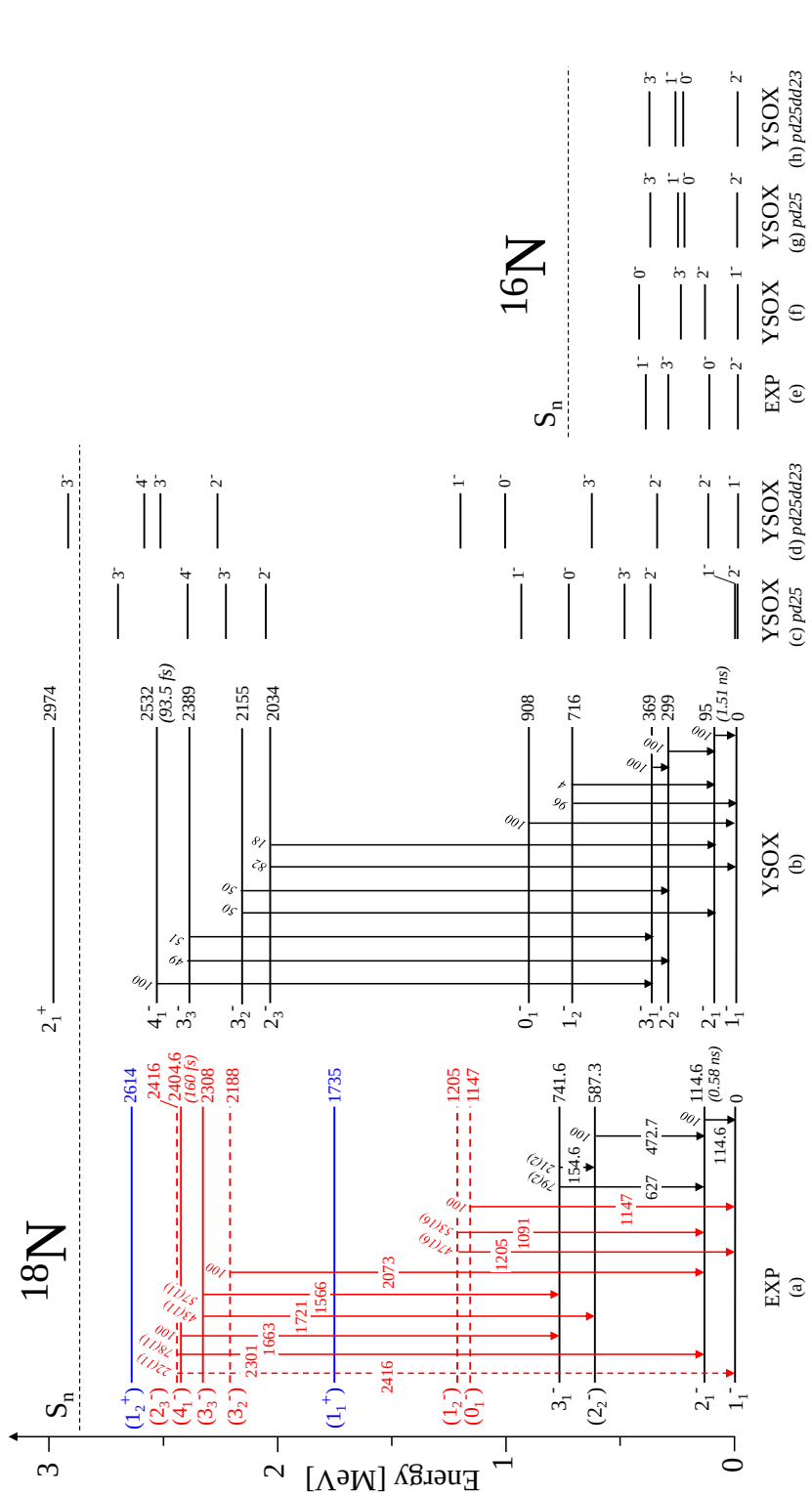

Figure 5.25: (a): experimental decay scheme of ^{18}N, as obtained in the present experiment. In black, previously-known levels and transitions [53, 101, 102]; in red, newly found ones (dashed lines for tentative). Positive-parity states observed in beta-decay studies [100] are marked in blue. (b): decay schemes of ^{18}N predicted by shell-model calculations using the YSOX interaction of Ref. [7]. (c)-(d): ^{18}N shell-model predictions with YSOX, with modified matrix elements involving proton-$p_{1/2}$ neutron-$s_{1/2}$ (c) and *sd* (d) orbitals. (e): experimental bound states of ^{16}N [53]. (f)-(h): shell-model predictions of ^{16}N obtained with the original [7] (f) and modified YSOX interactions (g)-(h), as in panels (c) and (d) (see text for details). Figure adapted from Ref. [143] with permission of Società Italiana di Fisica.

likely that the 1205- and 1091-keV gamma rays, having an energy difference of ∼ 115 keV, feed the 1^-_1 g.s. and the 2^-_1 state (at 115 keV) from a level at $E_{exc} = 1205$ keV, with relative branchings of 47(16) and 53(16) %, respectively. The other 1147-keV line could instead populate directly the 1^-_1 g.s. from a level at $E_{exc} = 1147$ keV. This placement is consistent with the existence of a doublet of unresolved states with 1.17-MeV average energy, as suggested by Hoffman *et al.* in Ref. [102]. Finally, the remaining newly observed 2073-keV line was proposed to feed the 2^-_2 state from a level at 2188 keV, in agreement with both the indication of a presence of a state at ∼ 2.2 MeV, as reported in charge-exchange and (d,p) studies [99, 102], and theory considerations discussed below. The resulting level scheme is presented in Figure 5.25(a).

In the level scheme, we report also the lifetime information for the 114.6-keV state ($\tau = 0.58(16)$ ns, from Wiedeking *et al.* [101]), and for the new state at 2404.6 keV. In the latter case, the lifetime value was extracted from the line shape analysis of the intense 1663-keV transition, employing the Monte Carlo procedure described in Section 5.2 [82, 166]. In contrast to the lifetime-analysis cases reported before, we could not split the energy spectrum in three angular ranges due to the limited statistics. The corresponding χ^2 lifetime-energy surface is reported in the inset of Figure 5.26: a global minimum is present in the map at $\tau = 160^{+740}_{-100}$ fs for $E_\gamma = 1663.0(8)$ keV. The comparison between the simulated data and the background-subtracted experimental spectrum is reported in the same figure, where the red band corresponds to the 1σ uncertainty region. We underline that the transition energy is well constrained, while the lifetime error bar extends quite largely towards longer lifetimes, even though the region is still confined. This effect can be imputed to the lack of statistics and to the fact that the analysis cannot be performed for different angular ranges, losing part of the sensitivity to the lifetime (see also discussion in Section 5.2.5). As a consequence, we cannot exclude a lifetime value of several hundreds of femtoseconds. Given the above transition energy, we could extract the energy of the newly discovered state, *i.e.*, $E_{exc} = 2404.6(13)$ keV. Note that this value is obtained considering the energy of the $3^-_1 \rightarrow 2^-_1$ transition to be 627(1) keV, as quoted by Wiedeking *et al.* in Ref. [101], in order to avoid any lifetime effect of our energy measurements, *i.e.*, Doppler-shifted energies. The $2^-_1 \rightarrow$ g.s. transition energy considered in the excitation energy evaluation is the one measured in the present work, *i.e.*, $E_\gamma = 114.6(1)$ keV, since the lifetime of the first excited state is quoted to be of $\tau = 582(165)$ ps from recoil-distance measurements [101], therefore our energy measurement is not affected. For completeness, the energy of the (2^-_2) excited state reported in Figure 5.25(a) ($E_{exc} = 587.3(2)$ keV) was obtained considering the $(2^-_2) \rightarrow 2^-_1$ transition energy quoted in Ref. [100] to be $E_\gamma = 472.7(2)$ keV: our value is in agreement with the one quoted in literature [53]. In the level scheme we report also the $3^-_1 \rightarrow (2^-_2)$ transition, previously observed by Wiedeking *et al.* in Ref. [101] at 155 keV, and present also in the current experiment at the energy of 154.6(3) keV. This transition is hardly visible in the total energy spectrum due to the presence of a Doppler-smeared partner gamma-ray contaminant, but in the $\theta_{rel} = 120°$–$140°$ angular range, the contaminant line moves to lower energies and the ^{18}N peak becomes clearly visible.

Similar considerations are at the basis of the excitation energy evaluation of the other newly found excited states, with the difference that for them no lifetime information is

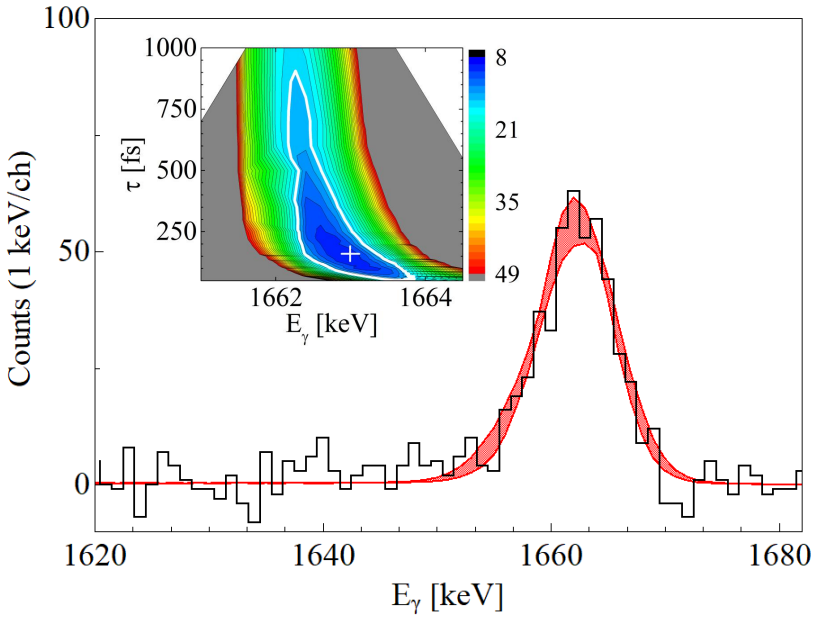

Figure 5.26: Gamma-ray energy spectrum of ^{18}N in the region of the 1663-keV γ ray, as measured with AGATA over the entire angular range (black histogram). The red-shaded band is the result of the line shape simulation, performed by varying E_γ and τ within the uncertainty region of the corresponding two-dimensional χ^2 lifetime-energy surface shown in the inset. The white cross and white contour line indicate the minimum and the uncertainty region, corresponding to 80 % confidence level. The minimum is located at E_γ = 1663.0(8) keV and $\tau = 160^{+740}_{-100}$ fs.

available and we cannot exclude few-keV shifts in their energies due to short-lifetime effects.

Theoretical interpretation

In previous works, the structure of the bound states in ^{18}N was calculated by using a shell-model approach with various interactions: the WBP and WBT interactions [95], and the YSOX interaction [7], mentioned above. Recent *ab initio* calculations are also available, but limited to ~1 MeV of excitation energy (see Section 3.3) In this work, we interpret our experimental findings with the help of the YSOX shell-model calculations. In Figure 5.25(b), the ^{18}N level and decay scheme calculated with the YSOX interaction are displayed. As discussed in earlier works, the ordering of the first four states (1^-_1, 2^-_1, 2^-_2, 3^-_1) is well reproduced (contrary to the case of WBP and WBT), as well as the decay pattern. However, the second- and third-excited states are predicted at lower energies, approximately at half the excitation energies observed in the experiment. A few hundred keV above the third excited state, 1^- and 0^- excitations are predicted, lying ~200 keV apart from each other. They correspond to the experimental doublet located at 1147 and 1205 keV. On the basis of the comparison between calculated and observed decay patterns (*i.e.*, two branches from the level at 1205 keV to the 2^-_1 and 1^-_1 g.s., and

a decay from the level at 1147 keV exclusively to the 1_1^- g.s.), we tentatively assign spin-parity 0^- to the 1147- and 1^- to the 1205-keV states. Above 2 MeV, calculations predict four negative-parity states. They can be related to the five states located experimentally. The level at 2405 keV is the most strongly populated. Based on the fact that deep-inelastic reactions populate preferentially yrast states, we assign to it spin-parity 4^-. In this case, the experimental lifetime value could be determined (see Figure 5.26), yielding the value $\tau = 160^{+740}_{-100}$ fs, which is in line with the calculated value of 93.5 fs. Further, the decay pattern of the experimental 2308- and 2416-keV levels are consistent with the calculated decay schemes of the 3_3^- and 2_3^- states at 2389 and 2034 keV. Therefore, we assign to them spin-parity 3^- and 2^-, respectively. Consequently, the level at 2188 keV will have spin-parity assignment of 3^-, as it is associated with the calculated 3_2^- state at 2155 keV.

As shown in Figure 5.25(a) and (b), the shell-model predictions with the YSOX interaction, although providing a rather satisfactory description of the excitation spectrum and decay scheme of ^{18}N, do not reproduce the ordering, in particular, of the 0_1^- and 1_2^- states around 1.17 MeV. These states arise from the coupling between a proton hole in the $p_{1/2}$ and a neutron in the $s_{1/2}$ orbitals. The ordering of higher-lying states, above 2 MeV, is more difficult to interpret, since the location of such states may be affected by being in the vicinity of the neutron threshold.

An attempt was made to improve the agreement between data and shell-model predictions, by adjusting selected cross-shell *p-sd* two-body matrix elements by about 20-30 % (more attractive interactions were used). At first, to reverse the order of the 0_1^- and 1_2^- levels in ^{18}N and become consistent with the experimental data, the matrix elements for the $\pi p_{1/2}$-$\nu s_{1/2}$ orbits were adjusted. Next, the spacing among calculated levels was improved by varying the matrix element involving the $\pi p_{1/2}$-$\nu d_{5/2}$ orbitals. Such calculations are labelled as *pd25* in Figure 5.25. Further, within the *sd*-shell part, the two-body matrix element $\langle \nu d_{5/2}(J)|V|\nu d_{5/2}(J)\rangle$ for $J^\pi = 2^+$ was also varied. Results are labelled as *pd25dd23* in Figure 5.25. This last change leads to an increase of the spacing among the average energies of the (1_1^- g.s., 2_2^-), (2_1^-, 3_1^-) and (0_1^-, 1_2^-) pairs (see Figure 5.25(d)). As mentioned in Section 3.3, in the weak-coupling scheme, these pairs correspond to a proton in the $\pi p_{1/2}$ orbit coupled to the $3/2_1^+$, $5/2_1^+$ and $1/2_1^+$ states of ^{17}C, with dominant configurations $\nu d_{5/2}^3$, $\nu d_{5/2}^3$ and $\nu d_{5/2}^2(0^+)s_{1/2}$, respectively. An improvement in the transition probabilities is obtained. In particular, for the decay from the 3_1^- state, two branches leading to 2_1^- and 2_2^- with similar intensities are calculated, in better agreement with the experiment.

The changes of matrix elements introduced above lead also to the correct reproduction of the spin and parity of the ground state and first-excited state in ^{16}N, as shown in Figure 5.25(e)-(h). The 2^- level in ^{16}N, which is dominantly of $\pi p_{1/2}\nu d_{5/2}$ nature, is lowered by the more attractive $\pi p_{1/2}$-$\nu d_{5/2}$ interaction, and becomes the ground state in agreement with the experiment. The 0^- excitation becomes the first-excited state, after the adjustment of the $\pi p_{1/2}$-$\nu s_{1/2}$ cross-shell matrix elements, which reverses the order of the 0_1^- and 1_1^- states. Altogether, the improved description of the ^{18}N and ^{16}N data appears to be mainly related to the adjustment of the $\pi p_{1/2}$-$\nu d_{5/2}$ monopole term, which makes it more attractive than in the original YSOX interaction [7]. We note that the modifications introduced above in the calculations preserve the basic properties of the N

isotopes. In particular, the neutron drip line remains at ^{23}N for both the modified YSOX interactions.

Final remarks

The high-resolution γ-spectroscopy investigation of ^{18}N, with the AGATA array, has allowed to newly identify a total of six excited states. Such states, together with the three already known excitations, exhaust all negative-parity excited states expected in ^{18}N below the neutron-emission threshold. Large-scale shell-model calculations performed in the *p-sd* space, with the YSOX interaction, reasonably reproduce the experimental data, apart from the ordering of the 0^-_1 and 1^-_2 states, which originate from the coupling between a $p_{1/2}$ proton and a $s_{1/2}$ neutron. It is found that selective variations of two-body *p-sd* cross-shell and *sd* inter-shell matrix elements restore the level ordering in ^{18}N, simultaneously reproducing the ground and first-excited state in ^{16}N, for the first time. These results help constraining cross-shell proton-neutron effective interactions in the *p-sd* space, so far little explored in comparison with similar investigations in the *sd-pf* shell [168].

It is also important to underline that the location of the 1^-_2 excitation in ^{18}N is expected to have strong impact on neutron-capture cross-section calculations in r-process modelling including light neutron-rich nuclei [94].

Part III

Searching for a narrow near-threshold resonance in ^{11}B

Chapter 6

Physics case: γ decay from near-threshold resonances

In this Part of the Thesis, we will concentrate on the study of electromagnetic (EM) decays of unbound near-threshold states in light neutron-rich systems, in connection to the appearance of collective phenomena (see Section 1.5.2). Measuring the γ decay from the near-threshold state would represent a breakthrough, as this phenomenon is almost unexplored due to its very low branching (10^{-3}-10^{-5}), although the EM radiation is the most sensitive probe to the details of the excited states structure. This will serve also as a test to Shell Model Embedded in the Continuum (SMEC) theoretical calculations (see Section 1.5.2). In addition, this research line has brought to the technological development of an upgraded version of the TRacking Array for light Charged particle Ejectiles (TRACE) [169, 170], composed of position-sensitive Si pixel-type telescope detectors. The relationship between the near-threshold states and collective phenomena in many-body systems from a phenomenological and theoretical point of view has been already introduced in Part I in Section 1.3. In the following, we will introduce the case of ^{11}B, which has been studied in an experiment realised in February-March 2021 at Laboratori Nazionali di Legnaro (LNL), near Padova in Italy, with the newly-developed version of TRACE, coupled to the GALILEO γ-ray detection set-up [171], from which the GALTRACE name. We underline that the the upgraded version of TRACE was specifically requested for the present research line. Before proceeding with the description of the experiment and data analysis in Chapters 8 and 9, respectively, we will give in Chapter 7 an overview of the GALTRACE developing, testing and commissioning, that has been done in the last three years.

During the PhD program, the present Thesis' Author has been directly involved in the technical development and testing of the new GALTRACE array. She contributed to the realisation of the experiment on ^{11}B, of which she was the spokesperson. She also contributed to the preliminary data analysis of this latter experiment.

6.1 The case of ^{11}B

^{11}B is an interesting system in the context of the investigation of near-threshold states in light neutron-rich nuclei. The existence of a resonance just above the proton-emission threshold is an open question: it could explain the very rare β^- delayed proton emission process (β^-p$^+$), taking place in the ^{11}Be$\rightarrow$ β^-+^{11}B$\rightarrow$ p +^{10}Be decay, that would proceed through the population of such a resonant state.

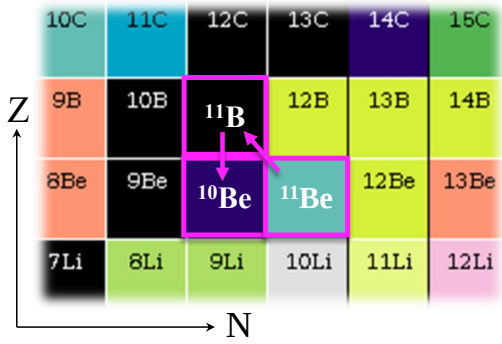

Figure 6.1: Portion of the nuclear chart, showing the path of the β^--delayed proton emission from ^{11}Be.

The $\beta^- p^+$ mechanism, where the β^- decay feeds excited states that subsequently emit a proton, is generally forbidden by the unfavourable energy balance. This is related to the fact that the β^- decay and the proton emission move a nucleus in almost opposite directions on the nuclear chart. As displayed in Figure 6.1, the β^- mechanism points towards more stable nuclei, while the proton emission points to systems away from the valley of stability. There are only a few neutron-rich nuclei for which β^--delayed proton emission is energetically allowed. However, due to the very narrow energy window available for protons, theoretical calculations predict very small branching ratios [172], of the order of 10^{-8}, even for the most promising case, namely ^{11}Be.

In ^{11}Be, given a β^--decay Q value of 11.5092 MeV and a proton energy separation in ^{11}B of 11.2285 MeV, the energy available for β^--delayed protons is only 280.7 keV, as shown in Figure 6.2. Since it is very difficult to measure protons of such low energy, an experiment [173], performed in 2012 at the Isotope mass Separator On-Line facility (ISOLDE) at CERN, aimed at looking for this decay by detecting the final nucleus ^{10}Be rather than the emitted protons. As a result, evidence for the decay was found with a surprisingly large intensity $8.3(9) \times 10^{-6}$, two orders of magnitude above the theoretical prediction of 3.0×10^{-8} [172]. Very recently, the data reported in Ref. [173] were critically reviewed by the same authors after a second test performed in 2015 with a similar experimental set-up[174]. They proposed a new upper limit 2.2×10^{-6}, still very high with respect to theory predictions. According to the theoretical considerations presented after the first experiment of Ref. [173], this unexpectedly high decay rate can be understood if the decay proceeds through a new single-particle resonance in ^{11}B, which couples strongly to the proton channel and only weakly to other decay channels, and it is strongly fed in ^{11}Be beta decay.

Another experiment, performed at TRIUMF, in Canada, with the Isotope Separator and Accelerator (ISAC), directly measuring the β^--delayed protons emitted from ^{11}Be was recently reported in Ref. [175]. Here, the emitted-protons energy distribution was measured with the prototype Active Target Time Projection Chamber and the authors concluded that the decay has the branching ratio of $8.0(2) \times 10^{-6}$. They claimed also that the decay proceeds sequentially through a narrow resonance located at 11.425(20) keV in ^{11}B,

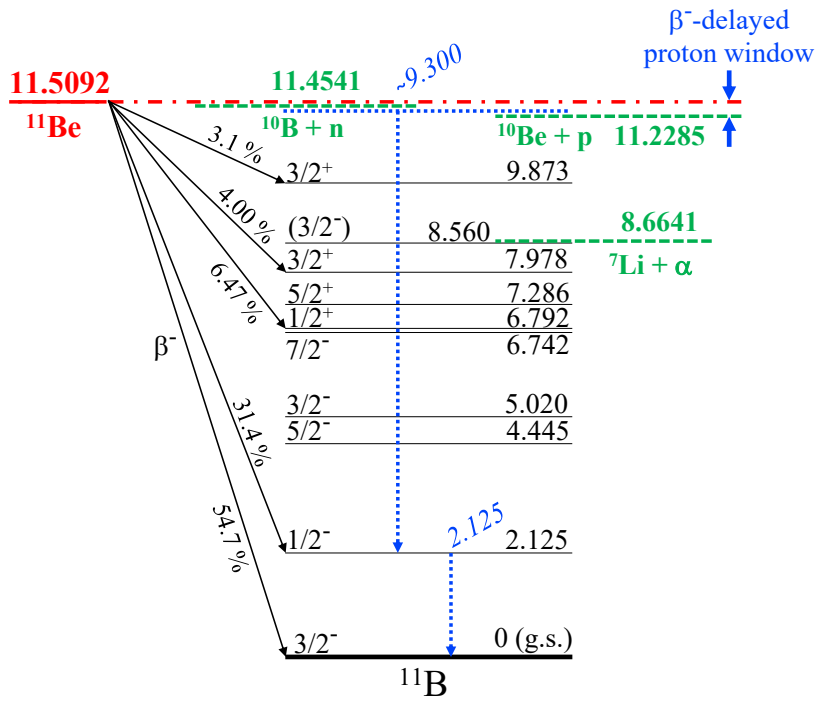

Figure 6.2: ^{11}B level scheme. Particle-emission thresholds are reported with dashed-green lines. On the left, the black arrows indicate the main β^--decay branches of ^{11}Be. On the right, the narrow 280-keV energy window available for the delayed proton emission is shown. The possible location of the near-threshold resonance and its γ cascade (~9.3 MeV gamma ray followed by the $1/2^-_1 \rightarrow g.s.$ 2.125-MeV transition) are represented with blue-dotted lines.

slightly above the proton-separation energy, with a width of 12(5) keV and spin/parity $J^\pi = (1/2^+, 3/2^+)$. The branching ratio for β^-p^+ decay of ^{11}Be observed in Ref. [175] exceeds by a factor of nearly 5 the final value adopted in Ref. [174] with the indirect measurement. This rose some doubts about the result obtained via the direct measurement of β^--delayed protons, especially in connection to the background treatment [176].

The question of the existence of a resonance state, with a sizeable single-proton character, just above the proton-separation energy in ^{11}B, is related to the universal phenomenon of near-threshold collectivity of the nuclear open quantum systems, introduced in Section 1.5.2. Within the SMEC approach, the strongest collectivization in ^{11}B is predicted for a $1/2^+$ state at $E_{exc} = 11.370$ MeV, around 142 keV above the proton-emission threshold [177], as displayed in Figure 6.3. The wave function of this $1/2^+$ eigenstate carries the features of the nearby proton-decay threshold, *i.e.*, such state can be viewed as a core-coupled proton state $\left[^{10}\mathrm{B} \otimes \mathrm{p}\right]$ with a negligible $\left[^{7}\mathrm{Li} \otimes \alpha\right]$ component. The properties of such a state are determined mainly by the coupling to the proton channel, which gives the maximal collectivization inside the window for beta-delayed proton emission from ^{11}Be. The coupling to the closed neutron channel (the state is located below the neutron-emission threshold) does not substantially change this picture: only a slight variation is

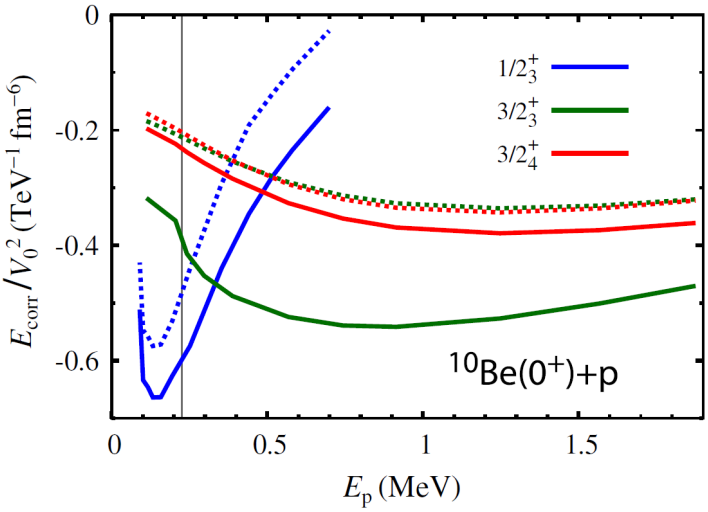

Figure 6.3: Real part of the continuum-coupling correlation energy as a function of the proton energy in the continuum (E_p), calculated within the SMEC approach, for three states ($1/2_3^+$, $3/2_3^+$, and $3/2_4^+$) close to the proton-emission threshold (corresponding to $E_p = 0$). Solid lines correspond to calculations that take into account both proton and neutron reaction channels. The dashed lines correspond to calculations in which the neutron reaction channel is ignored. The neutron-emission threshold is marked by the grey vertical line. The $1/2_3^+$ SMEC eigenstate (in blue) presents a minimum in the correlation energy 142 keV above the proton-emission threshold: a collective resonance is expected in this case. Figure reprinted with permission (license No. RNP/21/SEP/044548) from Ref. [177], Copyright 2020 by the American Physical Society.

introduced in the magnitude of the continuum-coupling correlation energy (solid lines in Figure 6.3), as a function of the proton energy above the proton-emission threshold. This result is in agreement with the proposition of Refs. [173, 178] that the $\beta^- p^+$ decay may be interpreted as a quasi-free decay of the ^{11}Be halo neutron into a single-proton state, coupled to the ^{10}Be core.

All in all, new experiments which would clarify the issue of the existence of a near-proton-threshold state in ^{11}B are highly needed. In view of this, the high collectivity of the $1/2^+$ narrow resonance predicted by SMEC just above the proton emission threshold, could be exploited to verify its existence in an alternative way. In fact, the resonance should have relatively high probability of gamma decaying towards bound states. Indeed, according to the SMEC calculations, the E1 gamma branch from the $1/2^+$ near-threshold state feeding the first excited $1/2^-$ state at 2125 keV (see Figure 6.2 for the decay scheme) has an intensity of 2.8×10^{-3} with respect to the main proton-decay mode [179], which could permit to measure experimentally its electromagnetic decay. For these reasons, an independent search for the ^{11}B near-threshold state, using its gamma decay as a probe, has been attempted in a one-week experiment realised at LNL in February/March 2021 with the GALILEO spectrometer and the GALTRACE charged-particle array, that will be described in Chapter 8. The crucial point of the experiment was to populate ^{11}B in its unbound states via the evaporation of a single proton in a fusion reaction of ^{6}Li+^{6}Li and

implement an efficient proton-gamma measurement, exploiting GALILEO+GALTRACE coincidences.

Chapter 7

Development of the GALTRACE particle-detection array

In the context of the research line devoted to study electromagnetic decays from near-threshold states in light neutron-rich systems (see Chapter 6), and to fulfil the necessity of new charged-particle detection ancillaries for advanced γ-ray spectrometers (see Section 2.1), the GALileo TRacking Array for light Charged particle Ejectiles (GALTRACE) has been recently developed [169, 170, 180]. It was designed to be coupled to the GALILEO array [171] and then it will be upgraded and adapted to the future AGATA campaigns. The array is meant to provide particle identification (and consequently reaction channel tag), energy and position information to perform event-by-event γ-ray Doppler correction and excitation-energy reconstruction of the nuclei of interest.

In this Chapter, we will describe in details the GALTRACE charged-particle detection array, with the commissioning experiment realised in July 2019. We will then report on the tests of the detectors that followed in preparation to the experiment that will be described in the next Chapter, to study the ^{11}B physics case. This technical activity has represented a substantial fraction of the three-year PhD program.

7.1 Detectors and electronics

The GALTRACE array is composed of pixel-type silicon detectors, mounted in ΔE-E telescopic configuration. The detectors were produced at the Bruno Kessler Center in Information and Communication Technology (FBK-ICT). The thin ΔE detector has a thickness of 200 µm, while the E layer is 1 or 1.5 mm thick. Both the ΔE and E detectors have an active area of 50×20 mm^2, divided into 60 pixels of 4×4 mm^2 area each on the junction side, forming a matrix of 12×5 pixels. The dimension of the pixels guarantees an angular resolution of few degrees when the detector is placed at a distance $\gtrsim$5 cm from the target position. Although the detector of the E layer has the same segmentation of the ΔE counterpart, the pixels are grouped in four 3×5 regions, read by 4 preamplifiers, in order to reduce the total number of channels. A common electrode covers the entire ohmic side of the detector. The depletion voltage was estimated to be 15 V, yielding a bulk capacitance of 3 pF with a measured leakage current of 3 nA for the thin silicon [169]. Figure 7.1 shows the GALTRACE detectors in the ΔE and E configurations, mounted on their printed circuit board (PCB), with the readout segmentation specified. The detector PCB incorporates the load resistances and the power supply filtering. It was specifically

designed to be used in both configurations: when exploiting the connectors on one side all 60 anodic channels are available separately (ΔE), when using the connectors on the other side the pixels are interconnected in four groups (E).

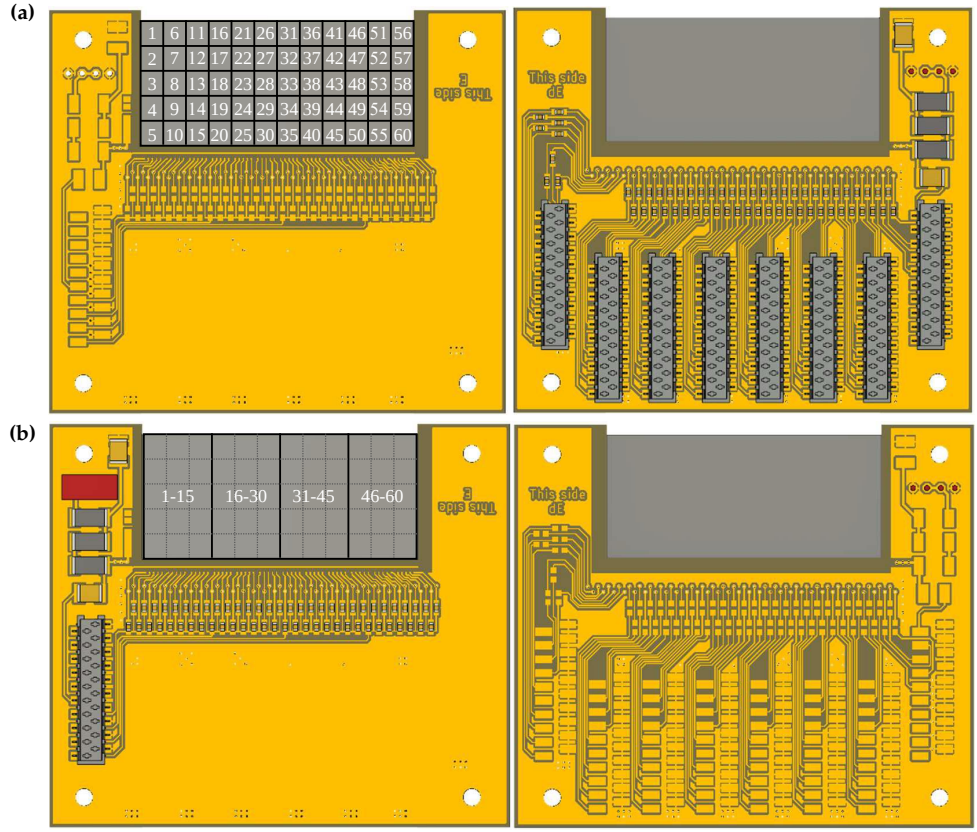

Figure 7.1: GALTRACE Si pixel-type detector in (a) ΔE and (b) E configurations, mounted on the PCB (printed circuit board).

The detector readout is performed with dedicated ASIC (Application Specific Integrated Circuit) charge-sensitive preamplifiers (CSP), designed by the electronics group of INFN-Milano [181]. Each chip is constituted of eight channels for anodic signals and one channel for cathodic ones (see Ref. [181] for other technical details). The preamplifier ASICs are mounted on dedicated PCBs (see Figure 7.2) with wire bonding. A copper cap ensures mechanical protection and electrical shielding to the ASICs. Both the detector and the preamplifier PCBs mount the same MicroMATCH 20-pin connector type, to ensure compactness, mechanical stiffness and connection resistance.

The output preamplifier signals are in single-ended mode and they are converted into differential ones through single-ended-to-differential (SeDiff) modules, before being sent to the digitisers of the GALILEO infrastructure. The SeDiff modules, designed at INFN-LNL, are built around the AD8139 integrated operational amplifier and are compliant with the preamplifier standards in terms of dynamic range, bandwidth and noise. They

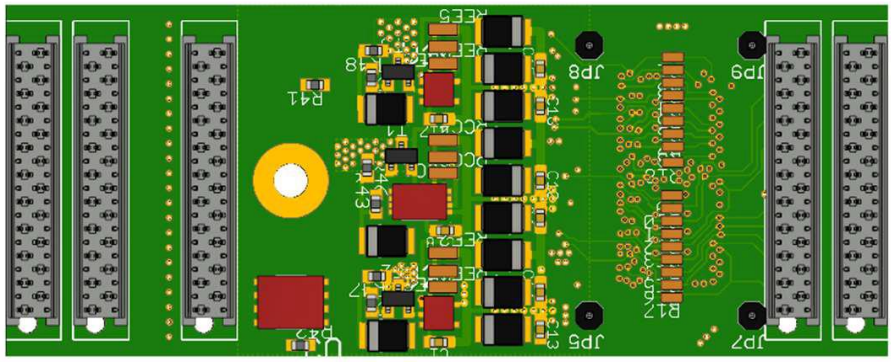

Figure 7.2: GALTRACE preamplifier PCB. The ASIC is mounted on the opposite side. The two connectors on the right take as input the signals from the detectors, while the two on the left are the output. The connector in the middle is devoted to the power supply of the preamplifier and the I^2C interface.

allow long cabling via an MDR-26 connector to the digitiser racks, where the waveforms are sampled with 14-bit precision at 100 MHz.

The read-out of one complete ΔE-E telescope requires 64 preamplifier anodic channels and 2 cathodic ones, the latter powered separately and used as trigger. Therefore, 8 ASICs for a total of 4 preamplifier boards are needed, which are all placed in vacuum close to the detectors. The quality of the preamplifiers and the short connections permit the implementation of PSA to discriminate the detected particles [169, 170].

7.2 Commissioning experiment

The GALTRACE array commissioning was one of the main goals of a test experiment realised at LNL in July 2019 [182]. The physics case chosen to validate the GALTRACE performance involved the investigation of the electromagnetic decay from the near-threshold resonance in ^{19}O, located at 4109 keV, *i.e.*, 153 keV above the neutron-emission threshold (see Figure 1.7).

The experiment lasted 3 days, from 9th to 12th July 2019, for a total of ~45 hours of in-beam data acquisition. The ^{19}O state of interest was populated through a ^{7}Li(^{13}C,p)^{19}O fusion-evaporation reaction. The beam of ^{13}C, accelerated with the PIAVE-ALPI accelerator [183, 184] to a total kinetic energy of 23 MeV and a current of ~5 enA, impinged on a ^{7}LiF target, 150 μg/cm^2 thick, deposited on a 30 μg/cm^2 ^{12}C backing. The experimental setup comprised the gamma-ray spectrometer GALILEO [171], composed of 14 Compton-suppressed HPGe detectors placed at 23.5 cm from the target and in three rings at backward angles with respect to the beam direction (152°, 129° and 119°). Three ΔE-E telescopes of GALTRACE were placed inside the reaction chamber covering the angular ranges 95°-115° (T0), 65°-85° (T1) and 55°-75° (T2), respectively. Only the two telescopes

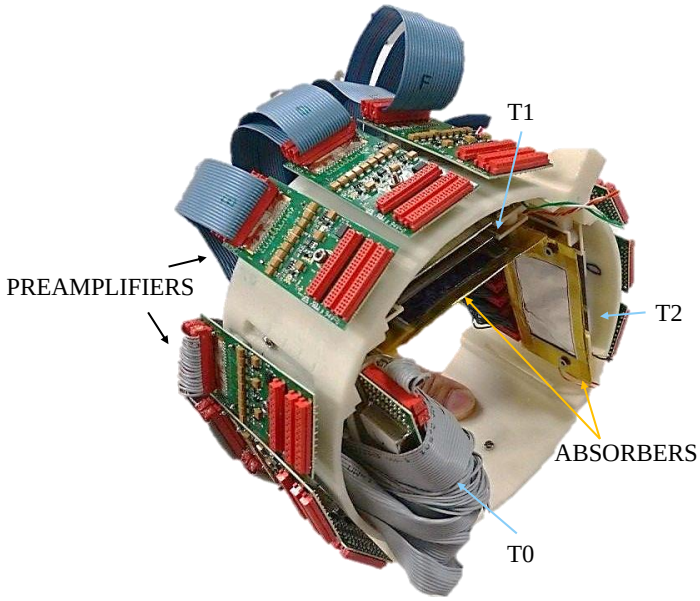

Figure 7.3: GALTRACE Si pixel-type detectors configuration of the July 2019 experiment. The three telescopes (T0, T1 and T2) are indicated, with the associated preamplifier boards. The Al absorbers of T1 and T2 are also visible.

in the forward direction (telescopes T1 and T2) were fully operational. T1 and T2 E layers had a thickness of 1.5 mm, while the telescope at backward angles (T0) had an E layer of 1 mm. In front of T1 and T2 telescopes an Al absorber of 33 µm and 44 µm, respectively, was put to stop alpha particles and scattered Li and heavier ions, in order to protect the detectors from damaging and reduce the counting rate. In addition, the absorbers helped in reducing the background from unwanted reaction channels. Figure 7.3 shows the GALTRACE experimental configuration: the three telescopes are mounted on a specifically designed 3D-printed plastic ring surrounded by the preamplifier boards. The absorbers are also visible. This ring with the detectors and preamplifiers was inserted in the scattering chamber.

Before proceeding with the description of the experiment analysis, we will give a brief overview of the GALILEO detection system.

7.2.1 GALILEO

GALILEO is the resident array for advanced in-beam γ-ray spectroscopy studies, constructed and installed at INFN-LNL in Italy [171]. The GALILEO project consists of a 4π high-resolution array using GASP [185] HPGe tapered detectors and HPGe capsules of the EUROBALL [186] Cluster, mounted in triple cryostats. All the detectors are surrounded by BGO Anti-Compton (AC) shields, which in turn are covered by a Pb layer, which avoids direct γ-ray interactions. The GALILEO project is organised into two phases, the first took place from 2015 to 2020 and the second started in 2021.

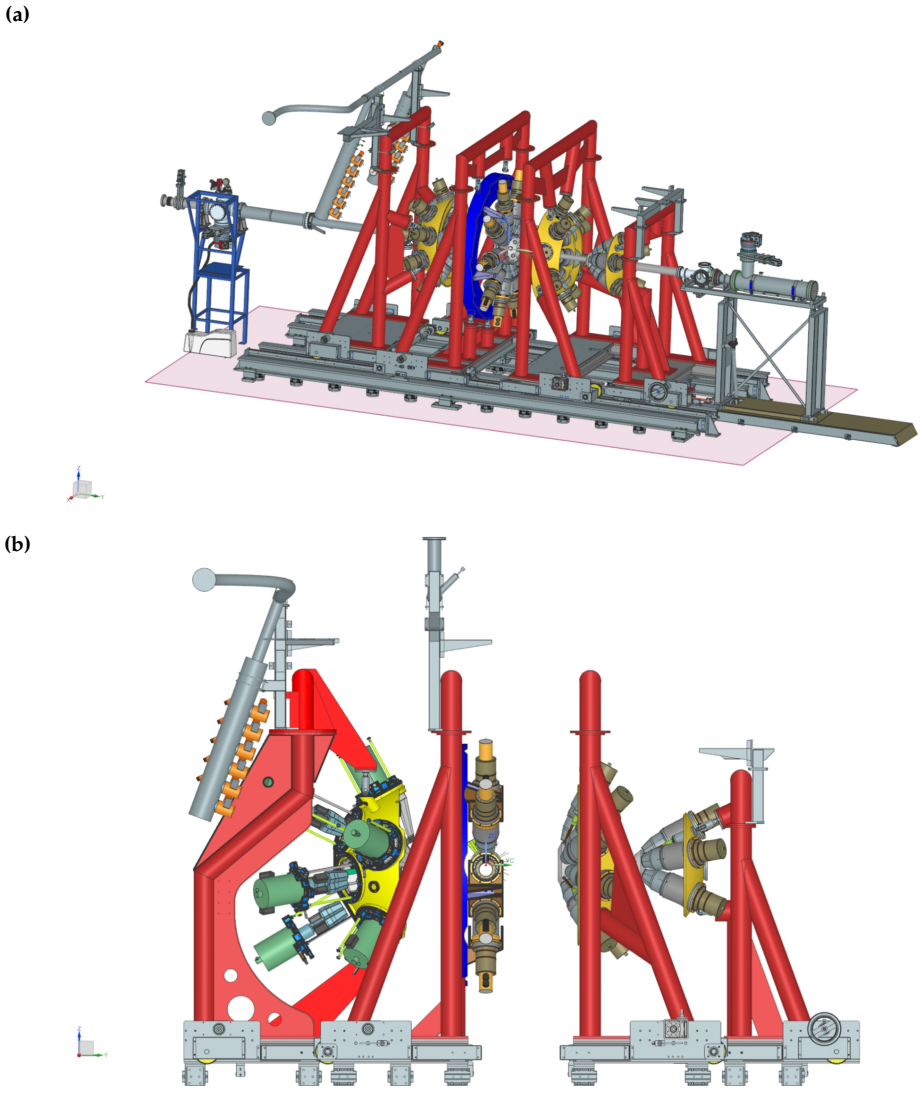

Figure 7.4: GALILEO Phase I (a) and Phase II (b) configurations. Reprinted from Ref. [171] with permission from Elsevier.

The detectors in the array are mounted on the mechanical structure shown in Figure 7.4: two shells, upstream and downstream, and an additional ring in the middle. The upstream shell is a whole hemisphere accommodating, in the Phase I, up to 15 single HPGe detectors, and 10 GALILEO Triple Clusters (GTC) during Phase II, while the downstream shell is divided in two sub-units, allocating 10 and 5 tapered detectors, respectively. The middle ring have space for 10 HPGe detectors, which can be substituted by large-volume $LaBr_3(Ce)$ for the measurement of high-energy gamma rays. Two pumping units, one upstream and one downstream guarantee the operational vacuum of 10^{-6} mbar in the scattering chamber.

In its Phase I configuration, the array was composed of 25 Compton-suppressed HPGe GASP-type crystals placed at 225 mm from the interaction point, as shown in Figure 7.4(a). The GASP detectors are coaxial HPGe crystal ~82 mm long and ~72 mm wide, tapered in the front with a cone of 10°. Each AC shield is made of 8 separate BGO crystals, read by as many PMTs. In this phase, the detectors were distributed onto four rings at 152° (5 detectors), 129° (5 detectors), 119° (5 detectors) and 90° (10 detectors), with respect to the beam line. In Figure 7.4(a), the full configuration is shown, with two additional movable portals in the forward direction (beam comes from the left), which were removed in Phase I to accommodate other large ancillaries. In this configuration, the overall photopeak effciency was about 2.1 % at 1332 keV and, at the same energy, the resolution was 2.3 keV.

In GALILEO Phase II, ten triple clusters with AC shields were produced reusing the already existing HPGe and BGO crystals of the EUROBALL array (see Figure 7.4(b)). Each tapered HPGe, with a diameter of 70 mm and a length of 78 mm, was individually encapsulated in a 0.7 mm thick Al canister. Three encapsulated HPGe crystals are placed in a common triple cryostat, surrounded by 9 BGOs, read by 12 PMTs.

The final GALILEO Phase II configuration comprises: 10 GTC at 245 mm from the target, 5 at 149° and 5 at 118.5°, coupled to 25 GASP-type detectors, 10 at 90°, 5 at 61°, 5 at 51°, and 5 at 28°. The overall gain in efficiency from Phase I to Phase II is of a factor two.

The GALILEO Phase I configuration is the one present at the time of the commissioning experiment in 2019. In the specific case of the experiment, only the upstream shell was present, for a total of 14 GASP-type HPGe crystals at backward angles.

This GALILEO Phase II setting, instead, was the one present in the ^{11}B experiment realised in February/March 2021. All the detectors of the upstream shell, of the central ring and of the bigger downstream shell subunit were mounted, for a total of 20 GASP HPGe and 10 GTC. The smaller downstream shell subunit was not present at that moment.

Electronics

The GALILEO Front-End Electronics (FEE) is based on a novel digital electronics, able to work under high-counting rate conditions. The signals coming from the detectors are read out through charge-sensitive preamplifiers, which feature a fast-reset technique for dead time and dynamic range optimization. The signals pass through the digitisers, designed for an upgraded version of the AGATA electronics [79], composed of six Digi-Opt12 boards [187] and two Control Cards [188], the latter providing clock and synchronization signal.

7.2.2 Data analysis

This Section is devoted to the analysis of the commissioning experiment, with particular emphasis on the GALTRACE performance. In the following, we will concentrate on the analysis of the ΔE layers only, as a careful inspection of the E layers data highlighted that the bias voltage applied was not sufficient to fully deplete the detectors. This issue was one of the main points in the GALTRACE tests that preceded the ^{11}B experiment and

that will be treated afterwards. The T0 telescope will be also excluded from the analysis since its ΔE detector was not working properly throughout the test.

Energy calibration

The first step in the analysis included the calibration of the ΔE detectors using a double alpha source (^{241}Am + ^{244}Cm) for the telescope T1 and a triple alpha one (^{241}Am + ^{244}Cm + ^{239}Pu) for the telescope T2. The energies of the most intense α particles emitted are: ^{241}Am → 5.486 MeV, ^{244}Cm → 5.805 MeV and ^{239}Pu → 5.155 MeV. The non-calibrated alpha spectra of T1 and T2 individual pixels are displayed in Figure 7.5 and Figure 7.6, respectively. All the pixels were working except telescope T1 pixel no. 20 and telescope T2 pixels no. 43, 44 and 46.

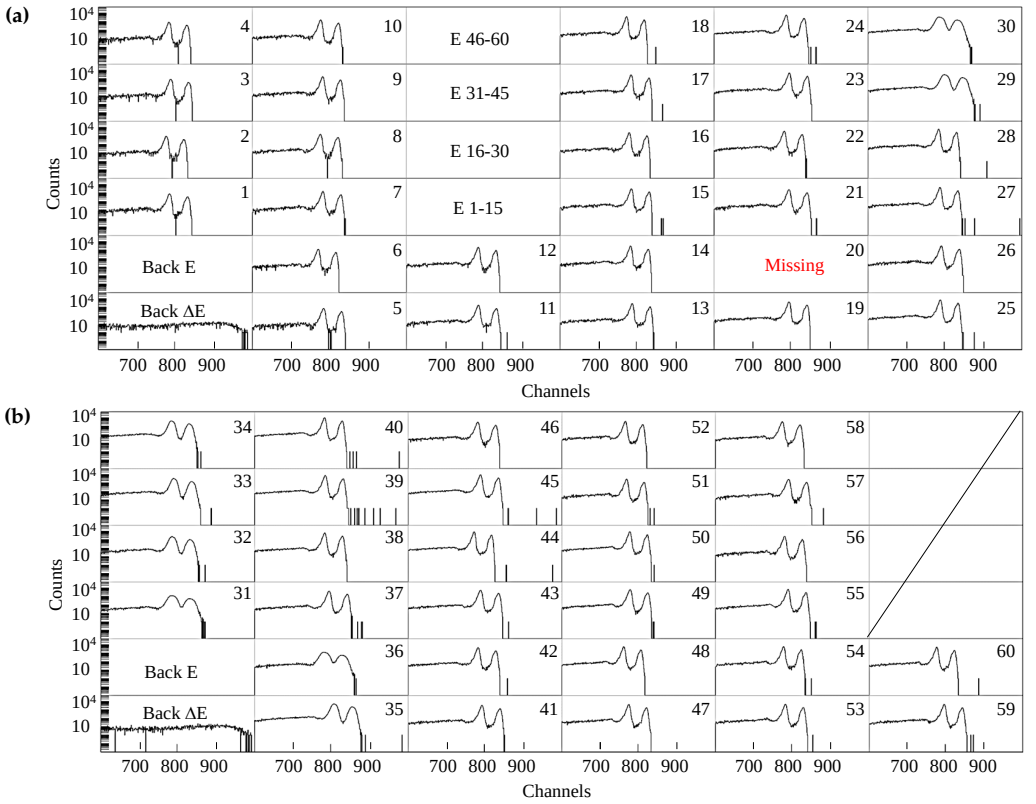

Figure 7.5: Non-calibrated alpha energy spectra of the T1 telescope ΔE layer in logarithmic scale. (a) Pixels from 1 to 30 and (b) from 31 to 60. The "back" refers to the signal associated to the common electrode on the ohmic side of the silicon. The ΔE back peaks are not visible since they are off the x-axis scale. The E channels reported in panel (a) are empty, since the E detector was switched off, as the alpha particles stopped in the ΔE layer. Pixel no. 20 was not working. The last four plots of panel (b) are ruled out as they are associated to empty channels in the digitisers, not connected to any pixel.

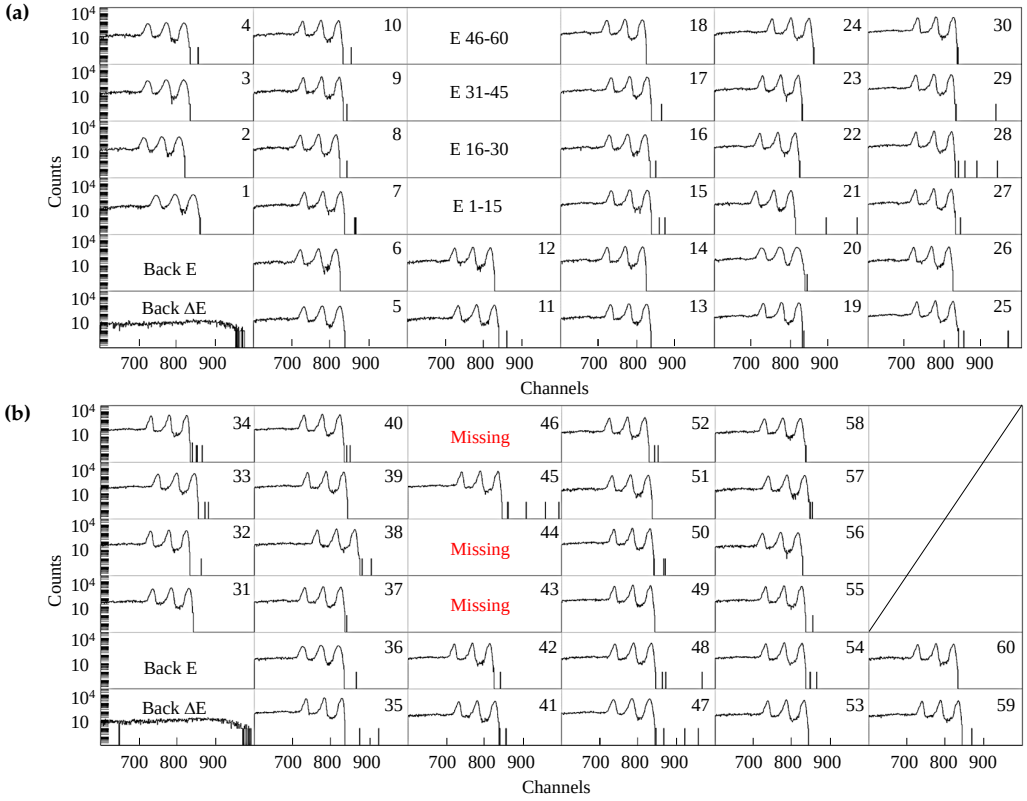

Figure 7.6: Same as Figure 7.5 for the T2 telescope.

After a Gaussian fitting of the peaks with the TkT software [189], a linear regression was performed for each pixel. The result of the calibration is reported in Figure 7.7, which shows the total calibrated alpha energy spectrum, summing all the two telescope pixels. The FWHM of the three main peaks are: 54 keV at 5.155 MeV, 59 keV at 5486 MeV and 64 keV at 5805 keV, for an average of 60 keV. Almost all the pixels were well aligned in energy after the calibration and had similar FWHM, except the pixels in telescope T1 from no. 29 to 36, which had a considerably worse resolution, with a FWHM ~90 keV, as can be seen in Figure 7.5.

Pulse Shape Analysis

The subsequent step of the analysis concerned the discrimination of the charged particles interacting in the detector coming from the different reaction channels (*i.e.*, p, d, t and alpha), using digital PSA techniques. PSA is based on the concept that the shape of the electronic signals depends on the type of charged particles interacting in the detector material.

During the experiment, the PSA was performed directly on the binary data acquired by the digitisers, extracting two discriminating parameters: the rise time (τ_{rise}) and the maximum derivative of the signal (I_{max}). For the rise time, the time difference between the

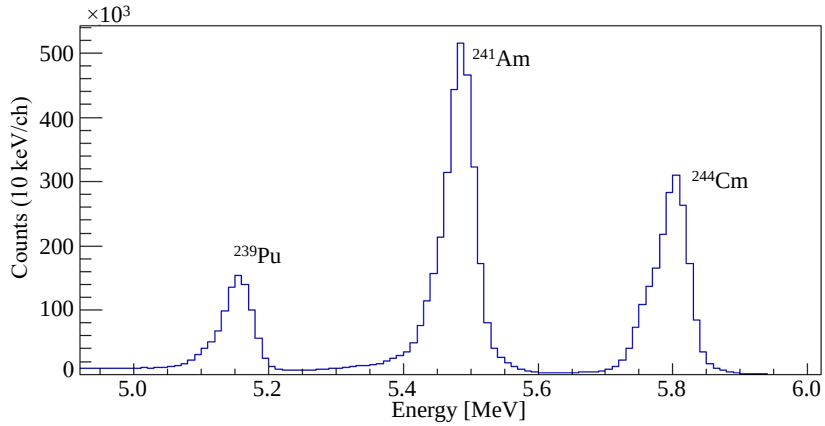

Figure 7.7: Total calibrated alpha energy spectrum, obtained summing all the telescopes pixels. The average energy resolution is of ~60 keV.

t_{70} and t_{30} instants, in which the pulse is at the 70 % and 30 % of its amplitude respectively, is computed. In order to extract the two time values, firstly the maximum amplitude V_{max} is calculated by averaging the three highest values of the signal amplitude. Secondly, t_{70} and t_{30} are calculated as the time when the signal height is at $0.3V_{max}$ and $0.7V_{max}$, after having fitted the sampled signal with an interpolating function. The maximum derivative of the pulse is calculated as the mean value among the five highest values of the signal derivative. These values are obtained though the interpolation of the pulse shape using the ROOT class TSpline3 [190] algorithm, which ensures the continuity of the first and second derivative. Figure 7.8 shows as an example the τ_{rise} vs. energy and I_{max} vs. energy two-dimensional particle-discrimination plots for the pixel no. 25 of telescope T2. From now on, we will use the I_{max} parameter to distinguish between the particles, putting gates on the I_{max} vs. particle energy matrix, like in Figure 7.8(b).

Gamma-ray analysis

The GALILEO gamma-ray spectra were firstly calibrated using ^{60}Co, ^{152}Eu and ^{133}Ba γ sources. After the calibration, we proceeded with checking the GALTRACE sensitivity to the reaction channels by looking at the gamma-ray energy spectra in coincidence with the evaporated particles.

The main evaporation residues, expected to be populated according to PACE4 simulation code [191], are the following: the proton emission channel comprises ^{19}O (1p, ~55 mb) for the reaction on ^{7}Li, ^{29}Si (1p 2n, ~200 mb) and ^{30}Si (1p 1n, ~130 mb) for the reaction on ^{19}F, and ^{23}Na (1p 1n, ~190 mb) for the reaction on the ^{12}C backing material; for the alpha emission channel: ^{15}N (1α 1n, ~750 mb, ^{13}C+^{7}Li), ^{27}Al (1α 1n, ~200 mb, ^{13}C+^{19}F) and ^{21}Ne (1α, ~250 mb, ^{13}C+^{12}C) are expected. A comparison between gamma-ray spectra gated on proton and alpha particles (see Figure 7.9) demonstrated an enhanced sensitivity to the different reaction channels, confirming the GALTRACE selectivity capabilities.

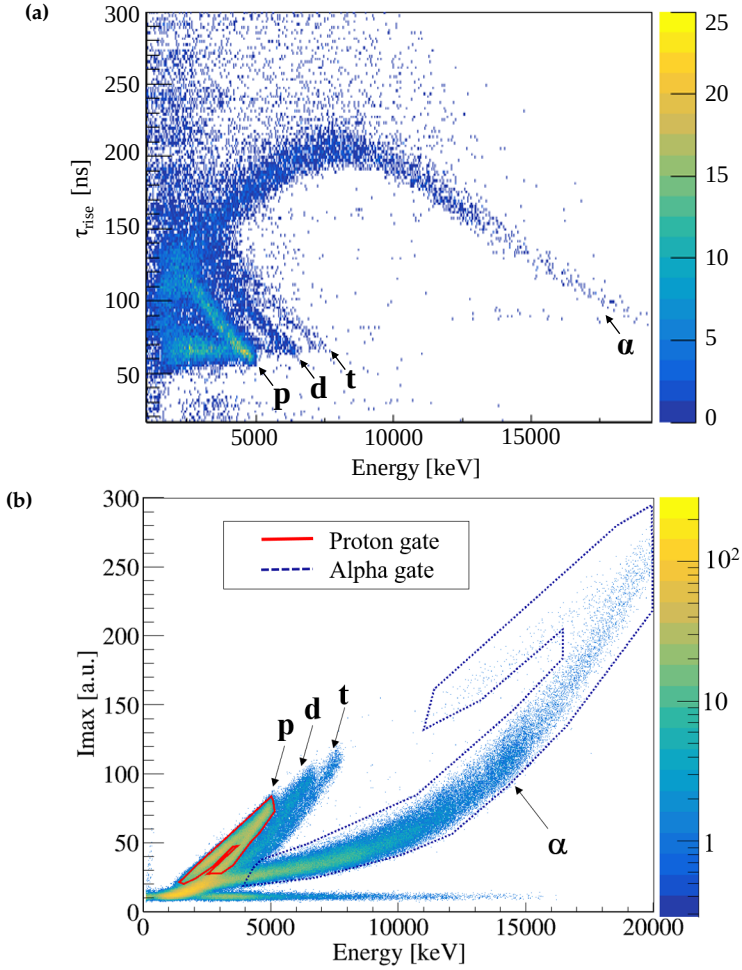

Figure 7.8: τ_{rise} vs. energy (a) and I_{max} vs. energy (b) matrices for the pixel no. 25 of telescope T2 ΔE. Partial statistics. In panel (b) an example of the gates put on protons and alpha particles are indicated in red and dashed-blue, respectively. Panel (b) reprinted from Ref. [182]

The last step of the analysis involved the investigation of the gamma-ray Doppler correction (DC). Here we will concentrate only on the reaction channels involving a single evaporated charged particle (p or α): in this case the reaction kinematics can be analytically reconstructed. In particular, we will refer to the ^{12}C(^{13}C,α)^{21}Ne reaction, since it was the only channel with a single emitted charged particle with a sizeable cross section. The other reaction channel in which a single proton is evaporated, namely ^{7}Li(^{13}C,p)^{19}O, was not sufficiently intense to be investigated in the short test experiment.

The DC can be implemented in two different ways: an average Doppler correction or a kinematically reconstructed one. In the former case, the mean v/c and angle of the evaporation residues are simulated with the PACE4 code, as schematically illustrated in the left panel of Figure 7.10(a). In the latter case, the energy and position information of

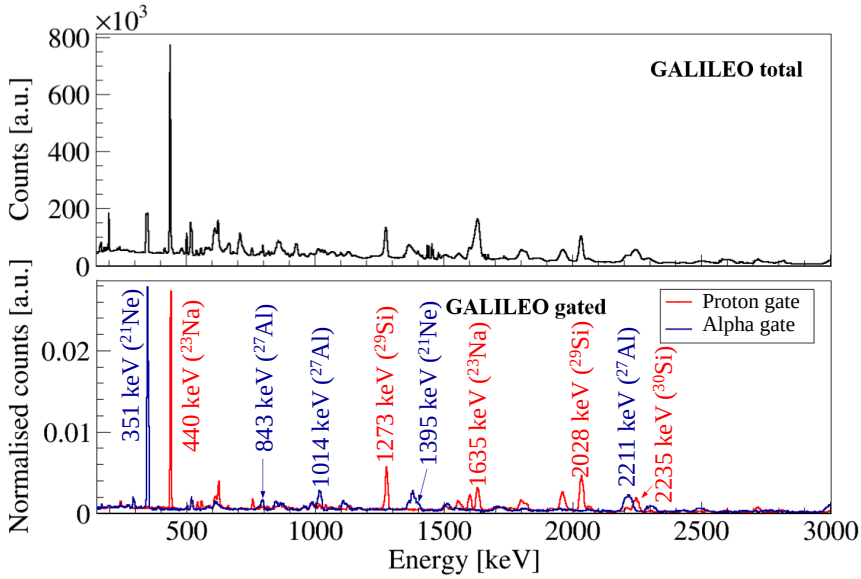

Figure 7.9: GALILEO Doppler-corrected gamma-ray energy spectrum (upper panel) with no gate condition on particles. Proton- (red) and alpha-gated (blue) spectra (lower panel). The labelled peaks come from reaction channels in which protons (red) or alpha (blue) particles are emitted. No major contaminations between the two gates were identified. Figure reprinted from Ref. [182].

the evaporated particles interacting in the GALTRACE detectors are used to reconstruct the direction and energy of the reaction residues (see right panel of Figure 7.10(b)) and then to precisely correct the energy of the emitted gamma rays. The kinematics reconstruction was performed with the Nuclear Physics Tool (NPTool) [192], a ROOT/Geant4 [190] based data analysis and Monte Carlo simulation package for low-energy nuclear physics experiments.

The kinematically reconstructed DC resulted in a significant improvement in the FWHM of the γ-ray transitions, as shown in Figure 7.10(b). For example, the ^{21}Ne gamma ray at 1120 keV passed from a FWHM of 32.0(16) keV to a value of 8.7(2) keV.

In conclusion, the analysis of the commissioning experiment demonstrated the overall good performance of the GALILEO+GALTRACE setup. Although the statistics for the study of the ^{19}O case was too limited to extract any physical information, the production of ^{21}Ne, associated to a single α particle emission, allowed us to check all the important parameters for further studies involving a similar detection system.

7.2.3 Additional remarks

The commissioning experiment made possible to highlight weaknesses and limitations of the mechanical set-up of GALTRACE. In particular, the preparation of the experiment posed some difficulties in the mounting and cabling of the GALTRACE detectors, that appeared to be particularly fragile. The 3D-printed support ring (visible in Figure 7.3) and the frames on which each telescope was mounted made the set-up preparation very

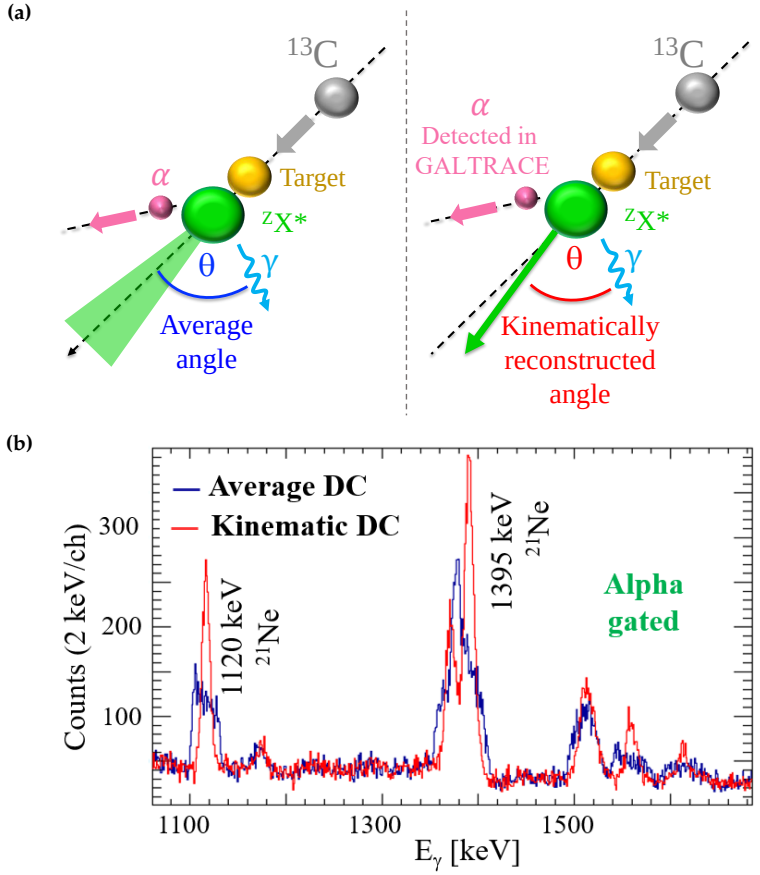

Figure 7.10: (a) Schematic drawing of a fusion-evaporation reaction with a ^{13}C beam on a target nucleus, leading to the population of a ^{Z}X* residue, after the evaporation of an α particle from the compound nucleus. The reaction residue de-excites via γ emission. In panel (a) (left), the mean angle θ used in the γ-ray Doppler-shift correction is indicated. In panel (a) (right), θ the kinematically reconstructed. (b) Portion of an alpha-gated GALILEO gamma-ray spectrum. The blue histogram is produced with an average Doppler correction, while the Doppler correction of the red spectrum has been kinematically reconstructed from the measured energy and angle of the alpha particles detected in GALTRACE. A significant improvement in the FWHM of the γ-ray transitions is visible in the case of the kinematically-reconstructed Doppler correction. Panel (b) reprinted from Ref. [182].

time consuming, with a high risk of damaging the detectors in the process. The fact that the ring could not be separated into two semicircles posed the main issue. The telescope frames were rather flimsy and did not protect the detectors and their wire bonding, besides the fact that they were not particularly suitable to permit the mounting of the absorbers. The insertion of GALTRACE in the scattering chamber was also critical due to the necessity of having short output connections, in order to avoid the cables to be hit by the beam. The entire process of mounting GALTRACE required several hours and,

once closed, the scattering chamber could not be easily re-opened for the calibrations. In view of other experimental campaigns with an increased number of telescopes, the GALTRACE mechanical support had to be re-designed, to guarantee an easier, safer and faster mounting process.

Finally, the bias voltage of the thick detectors had to be further investigated since they appeared to be not fully depleted. The detectors tests that followed the commissioning experiment and the new design of the mechanical supports are presented in Appendix C.

Summarising, an early version of the GALTRACE array has been tested during a commissioning experiment that, on the one hand, demonstrated its selectivity capabilities and its good performance and, on the other hand, arose some technical and mechanical issues. These problems were solved with a new mechanical infrastructure and through a careful testing process of each detector's features. After the refinements, the full GALTRACE configuration was ready to be employed in the experiment meant to investigate the ^{11}B physics case, that will be described in the next chapter.

Chapter 8

^{11}B experiment and detection system

In this Chapter, we will illustrate the experiment meant to investigate ^{11}B, in order to search for a narrow near-threshold resonance around 11.4 MeV, with gamma-particle coincidences. The physics case has been already introduced in Section 6.1.

A week-long experiment has been realised at Laboratori Nazionali di Legnaro (LNL) between the end of February and the beginning of March 2021. ^{11}B was populated in a fusion/evaporation reaction induced by a ^{6}Li beam at 7 MeV of total kinetic energy, impinging on a ^{6}Li^{19}F target, 500 µm/cm^2 thick. The nucleus of interest was produced via the emission of a single proton by the excited ^{12}C compound nucleus (CN). The emitted protons and the other charged particles associated to the population of other reaction residues were measured in the GALTRACE array placed in the forward direction. The gamma rays emitted by the reaction products were measured in the GALILEO spectrometer. We summarise here the goals and strategy of the measurement, then in Section 8.1 we will give some details on the reaction mechanism and the experimental conditions, while in Section 8.2 we will briefly sum up the characteristics of the experimental set-up.

The aim of the experiment described in the present work, was to probe the existence of a near-proton-threshold narrow resonance by searching for a gamma-decay emission from the $1/2^+$ near-threshold state predicted by Shell Model Embedded in the Continuum (SMEC) calculations at 11.370 MeV, and experimentally suggested to be located at 11.425(20) MeV (see Section 6.1 for details). According to the SMEC model, the gamma decay of the $1/2^+$ resonance would preferentially go to the first excited $1/2^-$ state located at 2.125 MeV, with a $\sim$9.3 MeV E1 transition. Owing to the enhanced collectivization effect caused by the coupling to the continuum, the gamma-ray branching should be of the order of $\sim$0.3 % with respect to the total decay intensity given mostly by protons. Consequently, if such a resonance exists, a coincidence should be detected between the 2.124-MeV gamma ray de-exciting the first-excited $1/2^-$ state of ^{11}B and $\sim$5-MeV protons, emitted from the ^{12}C compound nucleus and directly populating the narrow resonance. Vice versa, by gating on the $1/2^-_1 \rightarrow 3/2^-_1$ g.s. 2.124-MeV transition in ^{11}B, a peak should appear, around 11.4 MeV, in the excitation spectrum of ^{11}B, reconstructed from the measured evaporated protons. Direct observation of the 9.3-MeV E1 transition connecting the $1/2^+$ near-threshold state and the $1/2^-$ first-excited state should also be possible, although this is the most difficult observation, due to the limited efficiency for high-energy γ rays.

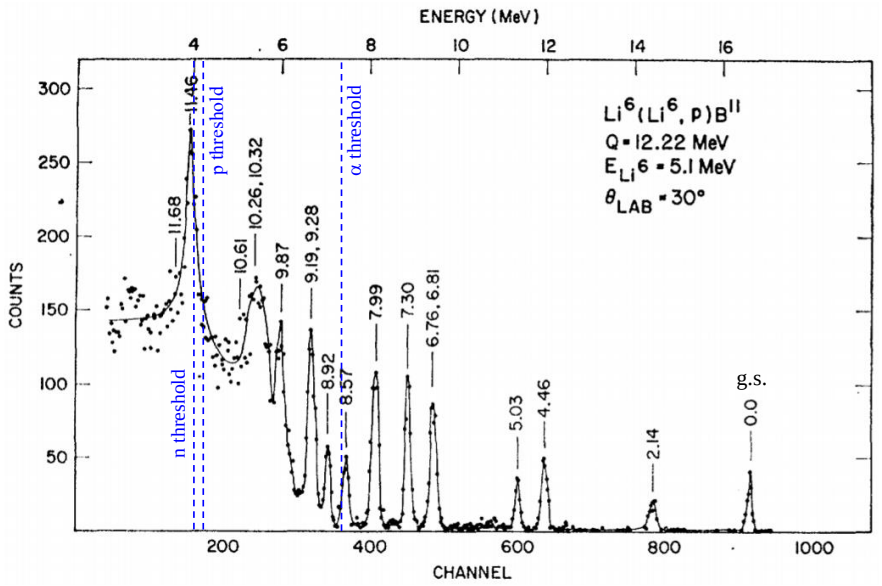

Figure 8.1: Proton spectrum from the ^{6}Li(^{6}Li,p)^{11}B reaction, recorded at $\theta = 30°$, employing a 5.1 MeV ^{6}Li beam and a 65.3 µg/cm^2 ^{6}LiF target, with a backing of 1.7 mg/cm^2 Al. Unbound states correspond to energies higher than 8.665 MeV. Alpha-, proton- and neutron-emission thresholds are indicated by dashed blue lines. Figure reprinted with permission from Ref. [193], under License number RNP/21/AUG/043944. Copyright 1966 by the American Physical Society.

8.1 Reaction mechanism and kinematics

Fusion reactions are one of the most favourable reaction mechanisms for the population of unbound resonances in nuclei like ^{11}B and they have been applied in the '60s-'70s to locate the majority of these states, with precise evaluation of individual level cross sections [53]. Figure 8.1 shows the proton spectrum measured by K.G. Kibler [193] at $\theta = 30°$ for ^{6}Li(^{6}Li,p)^{11}B reaction at $\theta = 30°$, with a 5.1 MeV ^{6}Li beam and a 65.3 µg/cm^2 thick ^{6}LiF target, with a 1.7 mg/cm^2 Al backing. In Kibler's work an E (solid state) and ΔE (proportional counter) detection system was employed. All sharp peaks correspond to states in ^{11}B: those with excitation energies above 8.665 MeV, the α-emission threshold, are unbound states. As shown in Figure 8.1, the 11-12 MeV region of interest, where the hypothetical narrow resonance should be located, is dominated by the presence of a pronounced resonance (with a width of ~ 135 keV), which is reported to decay by alpha emission [53], and by a large background from three- and five-particles decay channels. From the proton spectra measured over the entire angular range, Kibler deduced cross sections for the population of individual states in ^{11}B. The emission of protons leading to these states was found rather isotropic and with cross sections in the 100 to 500 µb/sr range, quite independent of the specific state.

For the experiment, we decided to employ the same reaction of Ref. [193], with a LiF target. The lithium fluoride target material was evaporated on a copper backing layer with a thickness of 150 µm/cm^2, the target being mounted with the Cu layer on the

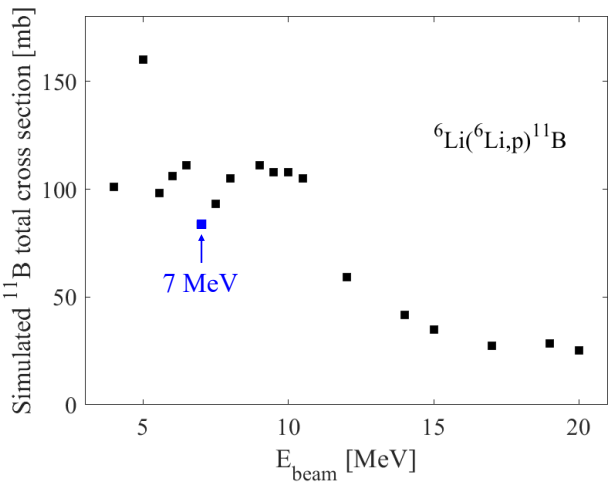

Figure 8.2: Simulated cross section for the population of ^{11}B in a ^{6}Li(^{6}Li,p)^{11}B fusion/evaporation reaction, as a function of the beam energy. Simulations performed with the PACE4 simulation code [191].

side of the incoming beam. The ^{6}Li beam, accelerated by the Tandem-XTU accelerator [194], was delivered at the experimental point with a total kinetic energy of 9 MeV and a current of few pnA. This was the lowest possible energy available with the Tandem-XTU operating at its minimum voltage of 3 MV. The beam energy was then lowered to 7 MeV with a Ni degrader, 2.14 mg/cm^2 thick.

Between 5 and 10 MeV, the total cross section for the population of ^{11}B was expected to be rather constant (~ 100 mb), as shown in Figure 8.2, but going down to 7 MeV of beam energy was necessary to remain below the Coulomb barrier for reactions on both ^{19}F and Cu, in order to strongly suppress fusion from such target components. The fusion on the Ni degrader was also suppressed. We point out here that no evident fusion or Coulomb-excitation reactions on Ni or Cu were subsequently observed during the experiment. In table Table 8.1 we reported the simulated total cross section for the population of the residues produced in the ^{6}Li + ^{6}Li fusion/evaporation reaction, assuming a beam energy of 7 MeV. For each residue, the particles evaporated from the compound nucleus are also given. The cross sections has been calculated with the PACE4 simulation code [191], which however did not return any sizeable cross section for the production of ^{10}B. This nucleus have been instead observed with sizeable intensity in the past, in experiments involving the same reaction mechanism (see for example Ref. [195]). ^{10}B is associated to the emission of one proton and one neutron (or a deuteron) from the compound nucleus, and it could be one of the major contaminants observed when a coincidence with protons is requested. For completeness, in Table 8.2 we report the simulated cross sections for the ^{6}Li+^{19}F reaction exit channels, which are anyway expected to be observed in the experimental data.

The protons, evaporated from the ^{12}C compound nucleus (populated at an excitation energy of 31.7 MeV), directly feed both bound and unbound excited states in the ^{11}B

Table 8.1: Simulated total cross section (σ) for the population of the reaction residues in the ^{6}Li + ^{6}Li fusion/evaporation reaction with a beam energy of 7 MeV.

Residue	σ [mb]	Residue	σ [mb]
^{12}C (CN)	0.396	^{8}Be (1α)	95.6
^{11}C (1n)	229	^{7}Be (1α+1n)	38.4
^{11}B (1p)	83.6	^{7}Li (1α+1p)	139

Table 8.2: Same as Table 8.1 for the ^{6}Li + ^{19}F reaction with a beam energy of 7 MeV.

Residue	σ [mb]	Residue	σ [mb]
^{24}Mg (1n)	26.3	^{23}Ne (2p)	4.44
^{24}Na (1p)	12.6	^{21}Ne (1α)	15.9
^{23}Mg (2n)	4.37	^{20}Ne (1α+1n)	117
^{23}Na (1p +1n)	108	^{17}O (2α)	17.6

evaporation residue. Ideally, the energy of the protons at a given angle are well defined, and correspond to the difference between the excitation energy of the compound nucleus, the proton binding energy and the energy of the final state in the residue. As we will discuss more in details in the next chapter, in the specific case of the present experiment, the protons measured at a specific angle would not be mono energetic. Protons emitted after the reaction taking place at the beginning or at the end of the target would have an energy difference of the order of 600 keV, due to the beam energy loss inside the target material. Figure 8.3 shows the kinetic energy versus angle, in the laboratory frame, for evaporated protons directly populating the ground state (g.s), the first- and second-excited bound states at 2.125 and 4.445 MeV (blue lines) and a hypothetical unbound state chosen to be located at 11.5 MeV, *i.e.*, inside the energy window in which the near-threshold state of interest is expected. We note that all resonance states reported in the 11-12 MeV region are rather broad (*i.e.*, with widths larger than 100 keV), therefore they should not give rise to sharp kinematics lines. From Figure 8.3, it is seen that at forward angles ($< 90°$) the energy of protons feeding the states of interest is lower than ~ 16 MeV (except for the g.s.), which means that protons should be fully detected in a 1.7-mm thick Si detector, like a typical GALTRACE telescope. In particular, the ~ 5 MeV protons, associated with the hypothetical 11.5 MeV state, will be fully stopped in a 200 μm Si ΔE layer of GALTRACE (see next Section for details on the set-up).

8.2 Experimental set-up features

The experimental set-up comprised the GALTRACE array for the detection of light charged particles and the GALILEO spectrometer for the measurement of gamma rays. The properties of both GALTRACE and GALILEO arrays have been already discussed in the previous Chapter (see Sections 7.1 and 7.2.1). Here we will give the details regarding the specific configuration of the ^{11}B experiment. Figure 8.4 reports some photographs of

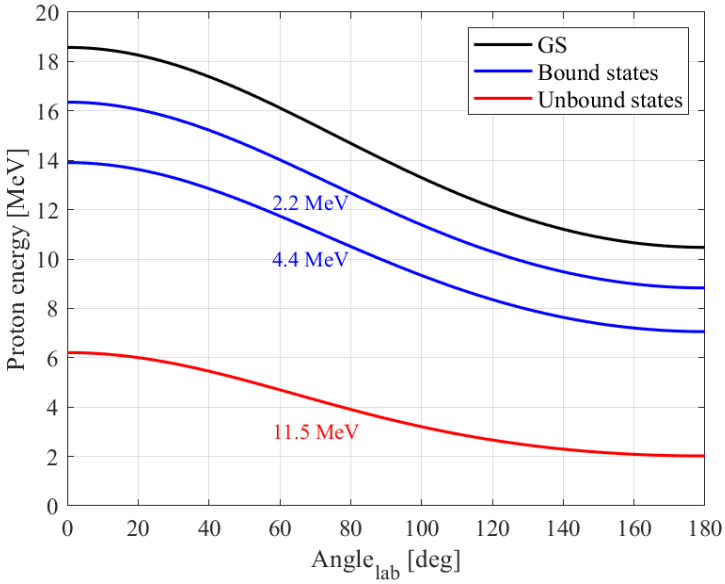

Figure 8.3: Proton energy vs. angle in the laboratory frame for the ^{6}Li(^{6}Li,p)^{11}B reaction, employing a 7 MeV ^{6}Li beam. The kinematic curves are given for protons directly populating the ground state (g.s.), the excited bound states at 2.125 and 4.445 MeV (blue lines) and the possible near threshold state of interest, at 11.5 MeV.

the array, namely the downstream hemisphere of GALILEO in panel (a), the GALTRACE array inside the scattering chamber in the experimental configuration, panel (b), and in the configuration used to calibrate the detectors.

The full GALTRACE configuration should have comprised four telescopes, but one of them was damaged during the installation, therefore only three fully functioning telescopes were present during the experiment. The detectors were biased with the voltages reported in Table 8.3 and they were placed a distance of ~7 cm from the target, covering the angular range between ~45° and 60° with respect to the beam direction.

Table 8.3: GALTRACE detectors bias voltage applied in the experiment to obtain the detectors' full depletion.

Detector ID	**Voltage [V]**	
	ΔE	E
C1	35	300
C3	35	325
C4	40	325

The actual angular coverage of a single GALTRACE telescope is shown in a θ vs. ϕ plot in Figure 8.5, with details on the position of each ΔE pixel (Figure 8.5(a)) or groups

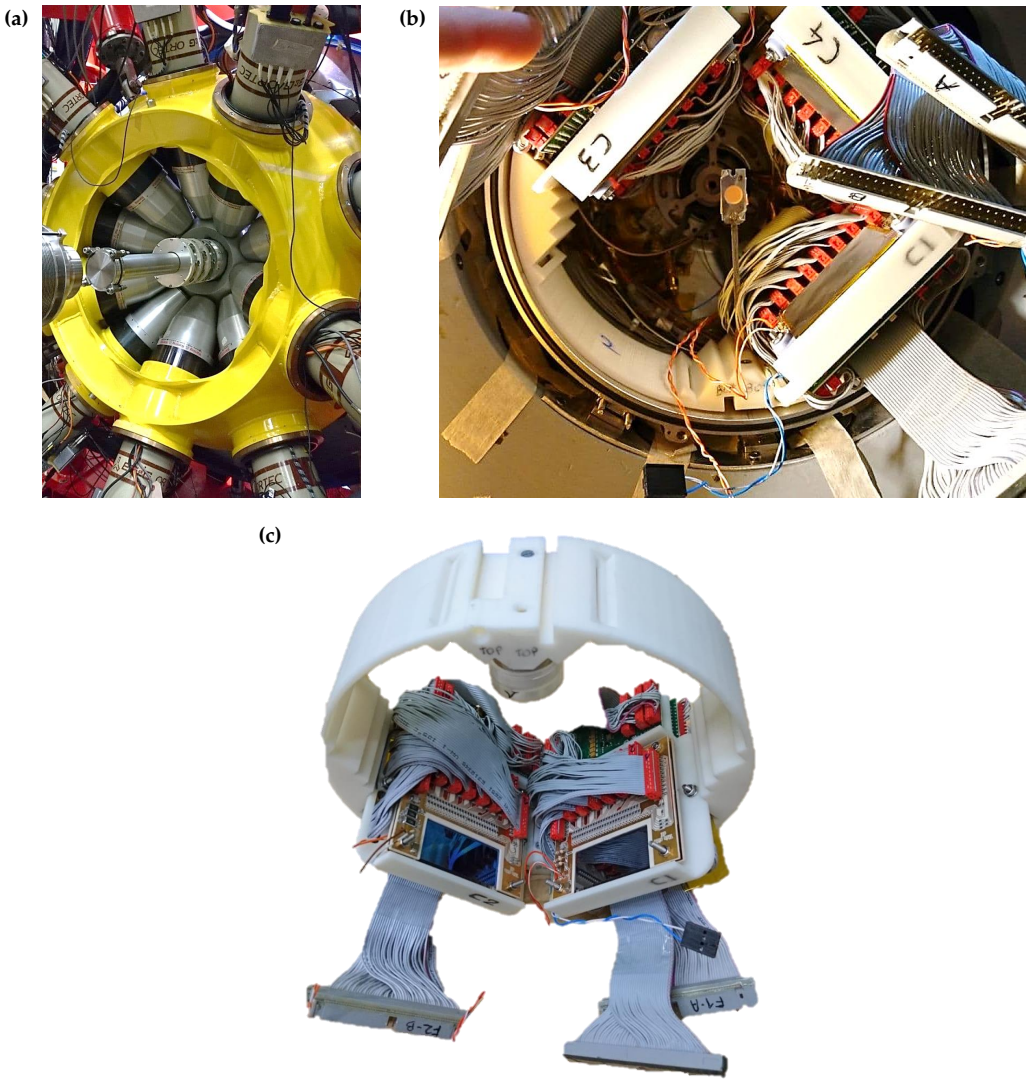

Figure 8.4: Panel (a): view of the GALILEO downstream GASP-type detectors. In the centre of the photograph, the flange through which the GALTRACE signals are transported outside the vacuum chamber is visible (before the cables were connected). Panel (b): inside of the scattering chamber, with the final experimental configuration of GALTRACE with three complete telescopes. In the centre, the target mounted on its aluminium holder can be seen, the beam coming from behind the target. Panel (c): GALTRACE configuration used during the calibration process, without Al absorbers. The cylinder attached to the internal part of the ring, on top of the detectors, is the radioactive alpha source used for the calibrations.

of pixels in the thick E detector (Figure 8.5(b)). Theta (θ) and phi (Φ) are defined as the polar angle with respect to the beam direction and the azimuthal angle with respect the the vertical axis, respectively (see Figure 8.5(c)). The GALTRACE geometrical coverage

in this configuration with three telescopes is around 4 % of the total solid angle.

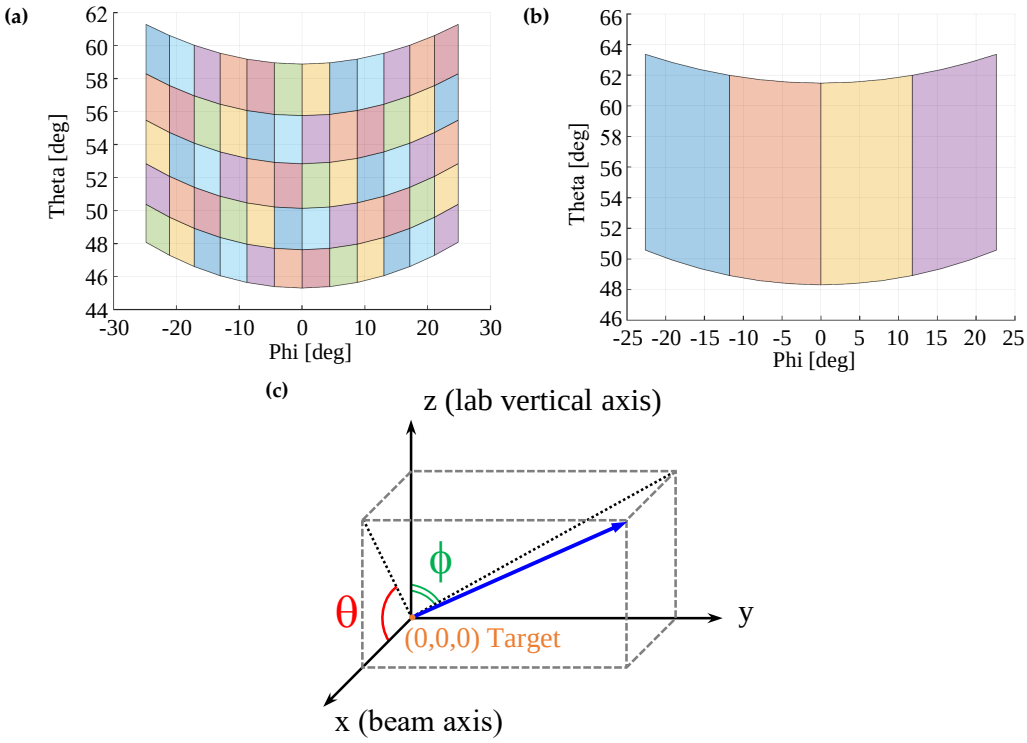

Figure 8.5: Angular coverage of the GALTRACE ΔE (a) and E (b) detectors. Panel (c): schematic representation of the reference frame considered in the experiment. The target position coincides with the origin of the reference frame and θ and Φ are the polar and azimuthal angles, with respect to the beam direction (x) and the laboratory vertical axis (z), respectively. For simplicity, in panels (a) and (b) the azimuthal angle has been considered to be 0 at the centre of the detectors. See Figure 8.4(b) for the final experimental configuration of GALTRACE. In this reference frame the planar detectors appear deformed, since they are mapped in spherical coordinates.

In front of each telescope an Al absorber, 11 µm thick, was placed to stop all the elastically scattered ^{6}Li nuclei of the beam. The absorbers were also introduced to reduce the background induced by alpha particles evaporated in the reaction. The absorbers were removed during the calibrations (see Figure 8.4(c)), that were performed using a double-alpha (^{241}Am-^{244}C) and a triple-alpha (^{241}Am-^{244}C-^{239}Pu) radioactive sources.

The GALILEO array, employed in its Phase II configuration (see Section 7.2.1), comprised 20 GASP HPGe and 10 GTC at 245 mm from the target. The GTC were placed at backward angles: two rings at 149° and 118.5°. The GASP-type detectors, shown in Figure 8.4(a) were organised in three rings at 90°, 61° and 51°. The Phase-II downstream 5-detector ring at 28° was not present. In this configuration, the GALILEO photopeak efficiency is ∼2.1 % at 2.1 MeV and 0.3 % at 9.3 MeV (see Figure 8.6), the two gamma-ray energies of interest for the investigation of the ^{11}B near-threshold resonance physics case.

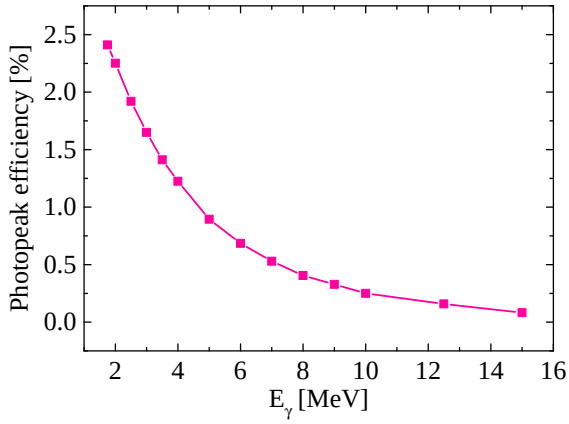

Figure 8.6: Simulated GALILEO photopeak efficiency, as a function of the γ-ray energy. The simulation takes into account the add-back in the GTCs.

Table 8.4: Typical counting rates used in the experiment. The rates of GASP, GTC and GALTRACE are intended for single detector.

System	Rate [kHz]
Total	50-60
GASP	0.8-1
GTC	2
GALTRACE	4-6

In Table 8.4 are reported the typical values of the counting rates observed during the experiment in each subsystem. The counting rates are intended for single detectors, not the entire array. The experiment was conducted in triggerless mode.

Chapter 9

Data analysis of ^{11}B experiment

In this Chapter, we will illustrate the data analysis of the experiment carried out at LNL, and meant to populate ^{11}B via a ^{6}Li+^{6}Li fusion/evaporation reaction, in order to search for a near-threshold resonance, just above the proton-emission threshold, exploiting gamma-particle coincidence measurements (see Chapter 8). The data analysis of the experiment was accomplished in the context of a Master Thesis [196], therefore in this work we will mainly recall the crucial points of the analysis, in order to give a complete picture for the existence of the near-threshold state of interest.

In particular, in Section 9.1, we will introduce the GALILEO and GALTRACE data preprocessing, which included preliminar and in-beam calibrations, particle identification and additional corrections. In Section 9.2, we will illustrate the gamma-particle coincidence analysis technique, used to investigate the existence of the ^{11}B near-threshold state, and we will provide some results.

9.1 Data pre-processing

In this Section, we will deal with the GALILEO and GALTRACE data pre-processing. We will show the preliminary GALTRACE energy-calibration procedure, the particle identification on the basis of ΔE-E and PSA techniques and an in-beam recalibration (see Section 9.1.1). For what concerns the GALILEO array, very precise gamma-ray energy calibrations were performed, and additional corrections, such as pile-up rejection and Galileo Triple Cluster position refinement, had to be introduced in the sorting (see Section 9.1.2).

9.1.1 GALTRACE data processing

The ΔE and E layers of the three GALTRACE telescopes (T0, T2 and T3) were firstly calibrated employing ^{241}Am+^{244}Cm double-alpha (for T0) and ^{241}Am+^{244}Cm+^{239}Pu triple-alpha (for T2 and T3) sources. An automated version of the procedure described in Section 7.2.2 was employed to perform the linear calibration of all the pixels. The results of the calibration for telescope T2 are shown in Figure 9.1.

After the calibration, we proceeded by identifying the charged particles detected, by means of two different techniques, namely ΔE-E discrimination and Pulse Shape Analysis (PSA). The ΔE-E discrimination can be used only for those particles that have sufficient

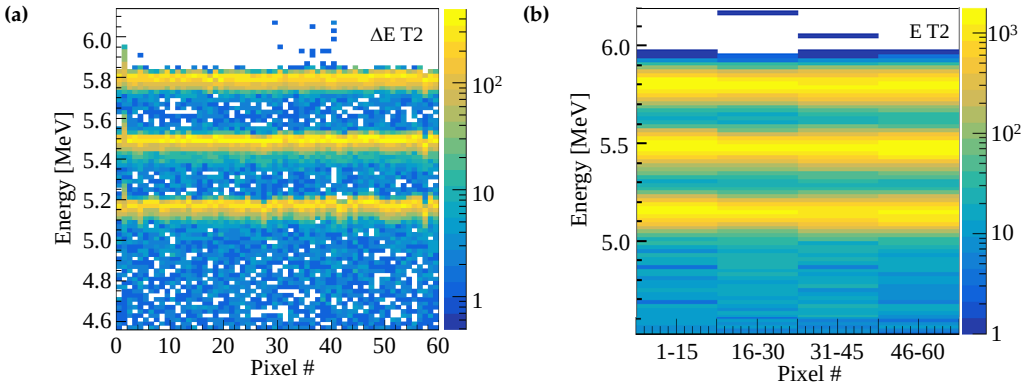

Figure 9.1: Calibrated energy vs. pixel number matrix for the ΔE (a) and E (b) layers of telescope T2.

energy to cross the ΔE layer and stop inside the thick E one, while with PSA also the low-energy reaction products that stop inside the thin ΔE detector can be identified.

The ΔE-E method is based on the fact that particles with dissimilar atomic number Z have different stopping power, and release different fractions of their kinetic energy in the thin and thick layers of the telescope. In a ΔE-E energy matrix, events associated to different charged particles arrange on distinct curves, whose shape depends on mass, charge and kinetic energy. Figure 9.2(a) displays, as an example, the ΔE-E energy matrix, obtained for the telescope T2. The two visible curves correspond to protons and deuterons, while the high density region, observed at low E energy, corresponds to particles that stopped inside the ΔE thin detector.

The GALTRACE PSA technique has been already introduced in Section 7.2.2, in connection to the data analysis of the GALTRACE commissioning experiment. The same technique was employed also in this case. Figure 9.2(b) shows an example of PSA I_{max} vs. energy deposited in the ΔE 2D identification plot, obtained considering the pixel #16 of telescope T0. Gates associated to proton events were set in these kind of ΔE-E and PSA plots to select the events of interest for the population of ^{11}B (red contours in Figure 9.2).

With the selected proton events, a two-dimensional matrix with proton energy (E_p) as a function of θ was produced (see Figure 9.3), where θ is the angle with respect to the beam direction at which the protons have been measured (defined considering the centre of the ΔE pixel in which they were detected), as shown in Figure 8.5. In this matrix, the predicted kinematic lines (see Figure 8.3), associated to the population of ^{11}B in its ground and excited states, were observed.

The kinematic lines appeared, first of all, rather broad (FWHM ~ 1 MeV): this effect is mainly due to the energy loss of the beam inside the thick target (of the order of ~ 700 keV), which results in the production of protons within a large energy spread for the population of the same state in ^{11}B. Secondly, the kinematic lines appeared shifted towards lower energies by nearly 500 keV with respect to simulated curves, calculated with the NPTool software [192]. This discrepancy can be either due to a non ideal calibration at high energy (~ 15 MeV), as the energy calibration was performed considering alpha particles

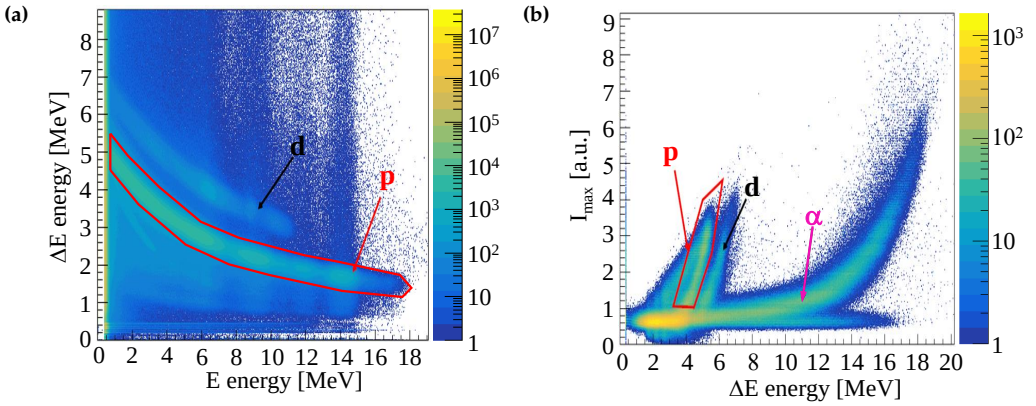

Figure 9.2: Two-dimensional GALTRACE particle-identification plots: T2 telescope ΔE-E energy matrix (a) and I_{max} vs. energy deposited in the ΔE of pixel #16 of telescope T0 (b). The red contour represents an example of gate set on the protons for the subsequent proton-gamma coincidence analysis.

with energies in the ∼5 MeV range, or to inaccuracies in the treatment of energy losses.

An in-beam linear recalibration was performed considering the peaks associated to the population of the ground and first-excited ^{11}B states, in the E_p vs. θ projection on the energy axis. The recalibrated matrix is illustrated in Figure 9.3, with the corresponding simulated kinematic lines considered for the recalibration.

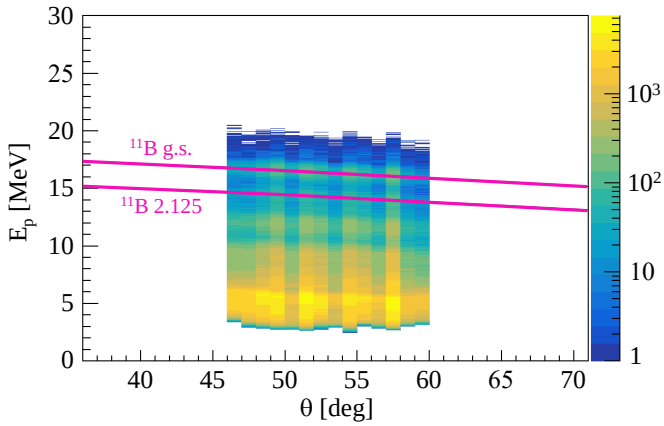

Figure 9.3: Proton energy (E_p) versus laboratory angle (θ), after in-beam recalibration. The two curves overlapped to the matrix correspond to the simulated kinematic lines associated to the population of ^{11}B in its ground (top) and first-excited 2.125-MeV (bottom) states.

9.1.2 GALILEO preliminary data treatment

The first step in the GALILEO data treatment involved a preliminary calibration with radioactive sources, followed by a precise investigation of the detectors' stability through-

out the experiment. For this stability check, seven in-beam gamma transitions, ranging from ~ 200 keV to ~ 6 MeV, which are not subject to Doppler shift (*i.e.*, the emitting nuclei are stopped at the time of emission) were considered. The centroids of the peaks of interest were extracted for each detector and experimental run, with a script that exploited the Search() function of the TSpectrum ROOT class [190]. This process needed to be automated as number of peaks to be measured was about 10^4, given 46 GALILEO working crystals and 47 runs.

Plotting the energy of the measured peaks as a function of the run number, some anomalous patterns were identified: jumps of several tens of keV in energy were observed, depending on the run number. Figure 9.4(a) shows, as an example, the measured centroid for the 6129-keV line in ^{16}O, as a function of the experimental run number, in one of the GALILEO detectors. ^{16}O was most probably produced in a ^{12}C(^{6}Li,d)^{16}O reaction, being ^{12}C a contaminant presumably settled on the target during the vacuum pumping process. A jump of ~ 35 keV was measured in the centroid position in the case considered in Figure 9.4(a). A similar behaviour was observed for most of the GALILEO detectors, which could be caused by the Analog to Digital Converter (ADC) modules, that suffer from non linearity at high-rate regimes. Therefore, an in-beam run-by-run linear recalibration was applied for each crystal. The result of the recalibration procedure was very good, as no significant shifts (discrepancies < 0.5 keV) with respect to the nominal energy could be observed in all the energy ranges (see Figure 9.4(b)).

After the recalibration, the gamma-ray energy resolution for the total GALILEO array (all the detectors summed) was measured to be FWHM ~ 5.5 keV at ~ 1.6 MeV and FWHM ~ 8.5 keV at ~ 6.1 MeV.

Additional corrections

In addition to the run-by-run recalibration, other corrections had to be introduced to improve the peak-to-total ratio and the Doppler-shift correction.

First of all, for the events for which a coincidence was detected between the HPGe crystals and the corresponding BGO anti-Compton shields in a time window > 100 ns (coincidences in a time window < 100 ns are directly discarded without being written to disk), a threshold on the BGO energy was set. Events above the threshold were discarded, in order to improve the peak-to-total ratio, without losing events triggered on the BGO noise at low energy, which could not be associated to Compton scattering.

Secondly, in order to reject pile-up events, we kept only those events, for which a compatibility relationship was assessed between the signal amplitude measured with a fast analyser (1 µs) and a longer (15 µs) shaping time (trapezoidal main shaper). Events for which a different signal amplitude was obtained, on the basis of the shaping time considered, were discarded, as this was the fingerprint of the pile-up phenomenon.

Finally, an optimisation of the GTC detectors' position, which strongly influences the Doppler-shift correction, was carried out, as a shift in the Doppler-shift-corrected gamma-ray energy spectra was observed for these crystals, with respect to the GASP-type ones, which were correctly aligned to the nominal energy. Details on the optimisation procedure are reported in Ref. [196]. Figure 9.5 shows the GTC (red) and GASP (blue)

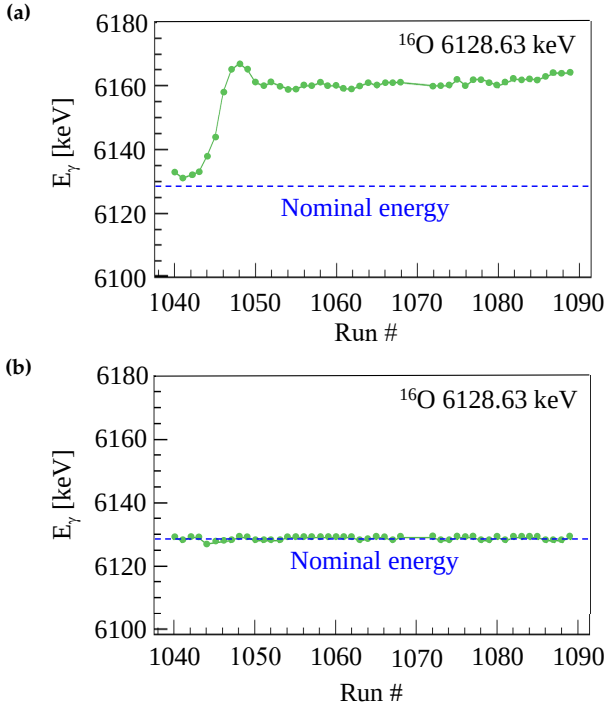

Figure 9.4: ^{16}O 6129-keV transition centroid measured in the GALILEO detector #16, as a function of the run number, before (a) and after (b) the run-by-run linear recalibration procedure. The nominal energy reported in literature (6128(4) keV [53]) is shown with a blue dashed line.

Doppler-corrected gamma-ray energy spectra before and after the GTC position optimisation, in the region of the 2124.5-keV ^{11}B transition, the nominal energy (2124.473(27) keV [53]) is reported with a green dashed vertical line.

9.2 Data analysis

At the end of the data preprocessing, the ^{11}B excitation energy has been reconstructed on the basis of the reaction kinematics, considering only the events associated to the emission of protons (see Figure 9.2), stopping in both the thin and thick GALTRACE telescope layers. Figure 9.6 shows the result of the reconstruction, without imposing any gamma coincidence: peaks associated to the population of ^{11}B were recognised. Given the energy resolution of $\sim$ 700 keV, only the population of the ^{11}B ground and first-excited 2.125-MeV states are well resolved, as highlighted in the inset, while the peaks associated to other excited states largely overlap, especially in the high-energy part of the spectrum ($>$ 10 MeV), where a high-density of states is expected. As mentioned in the previous section, the degradation of the energy resolution is caused by energy losses and energy straggling of the beam and the emitted particles inside the Ni degrader, the ^{6}LiF thick target, the Cu backing and the Al absorbers in front of the GALTRACE detectors. In addition, since we expect an almost constant probability for the reaction to take place

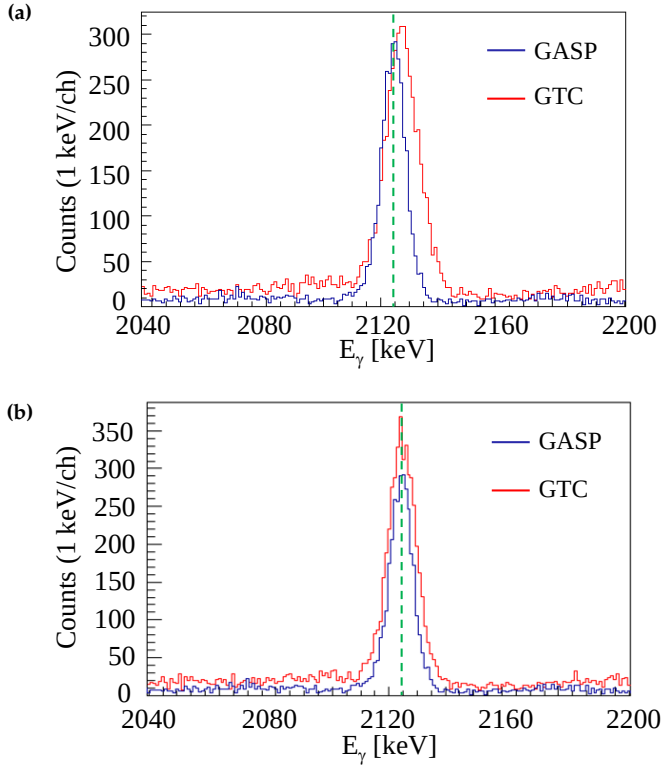

Figure 9.5: GASP (blue) and GTC (red) Doppler-shift-corrected γ-ray energy spectra, before (a) and after (b) the GTC position optimisation. The green dashed vertical line marks the energy reported in the database for the 2124-keV transition (2124.473(27) keV [53]) depopulating the first-excited state ^{11}B.

over the entire target thickness (0.5 mg/cm^2), protons produced when the reaction occurs at the beginning or at the end of the target have a difference in energy of the order of ~700 keV, this causing the main source of energy resolution degradation.

Once the population of the nucleus of interest has been assessed and the capability to reconstruct its excitation energy spectrum has been verified, we proceeded with the production of a two-dimensional gamma-ray energy (E_γ) vs. excitation energy (E_{exc}) matrix, imposing a coincidence with protons detected in GALTRACE. The matrix, with its projections on the gamma-ray and excitation-energy axes, is displayed in Figure 9.7. A vertical red dashed line separates the reconstructed events associated to protons stopped in the ΔE from events in which the protons passed through the thin detection layer and were stopped in the thick one.

In Figure 9.7(b), the gamma-ray energy has been Doppler-shift corrected on a event-by-event basis, considering the angle between the recoiling nucleus and the emitted gamma ray (θ_{rel}, see Equation (2.4)) as the one kinematically reconstructed (exploiting proton direction and energy), as already explained in Section 7.2.2, in connection to the commissioning experiment data analysis (see also Figure 7.10(a)). In the proton-

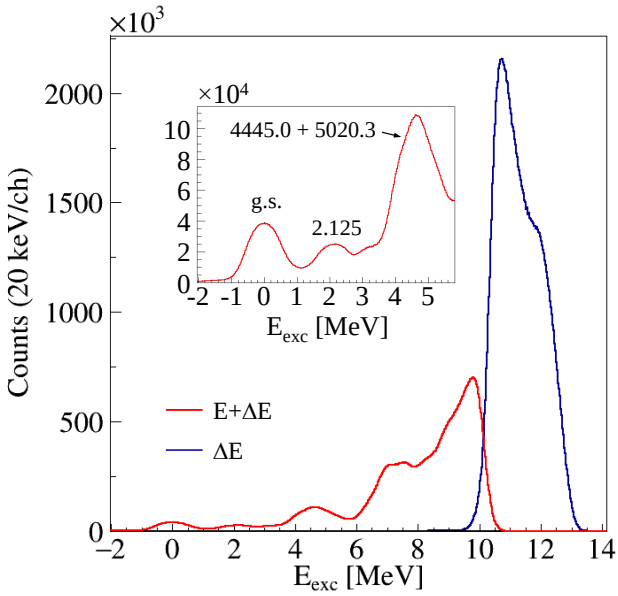

Figure 9.6: Excitation energy (E_{exc}) spectra of the ^{11}B nucleus reconstructed from the reaction kinematics, considering protons stopped in the ΔE (blue) or events in which the protons punched through the ΔE thin layer and were stopped in the thick E one (red). In the inset, the excitation energy spectrum with E_{exc} <6 MeV is displayed: the peaks associated to the population of the ^{11}B ground and first excited states are well separated. The overlapping peaks associated to the ^{11}B third- (4.445 MeV) and fourth-excited (5.020 MeV) states population are also visible in the inset.

coincident gamma-ray energy spectrum, gamma rays depopulating ^{11}B are clearly visible (see Figure 9.8 for the ^{11}B level scheme). Mainly two contaminants were identified in the spectrum: ^{10}B (blue circle symbol) and ^{23}Na (red stars). ^{10}B was produced in the ^{6}Li(^{6}Li,d)^{10}B transfer reaction, while ^{23}Na was associated to the deuteron emission channel, in the ^{6}Li+^{19}F fusion/evaporation reaction (see Tables 8.1 and 8.2). These two reaction residues can be observed in coincidence with protons following the deuteron breakup. Also the ^{7}Li 478-keV transition was observed, as ^{7}Li corresponded to the αp exit channel of the ^{6}Li+^{6}Li reaction (see Table 8.1).

Note that in the ^{11}B excitation energy spectrum reported in Figure 9.7(c), the peak associated to the population of its ground state disappears (see in comparison the singles excitation energy spectrum in Figure 9.6), as gamma coincidences are required.

9.2.1 ^{11}B near-threshold state

In order to search for the ^{11}B near-threshold state of interest, a detailed analysis of the proton-gamma coincidence events has been performed. We remind here some important information: the SMEC calculations predict the existence of a collective $1/2^+$ state at the excitation energy of 11.370 MeV in ^{11}B [177], close to the proton-emission threshold (S_p = 11.2285 MeV [53]). According to SMEC calculations, this resonance should decay towards the first-excited $1/2^-$ 2125-keV state with a gamma ray of ~9.3 MeV and a branching of

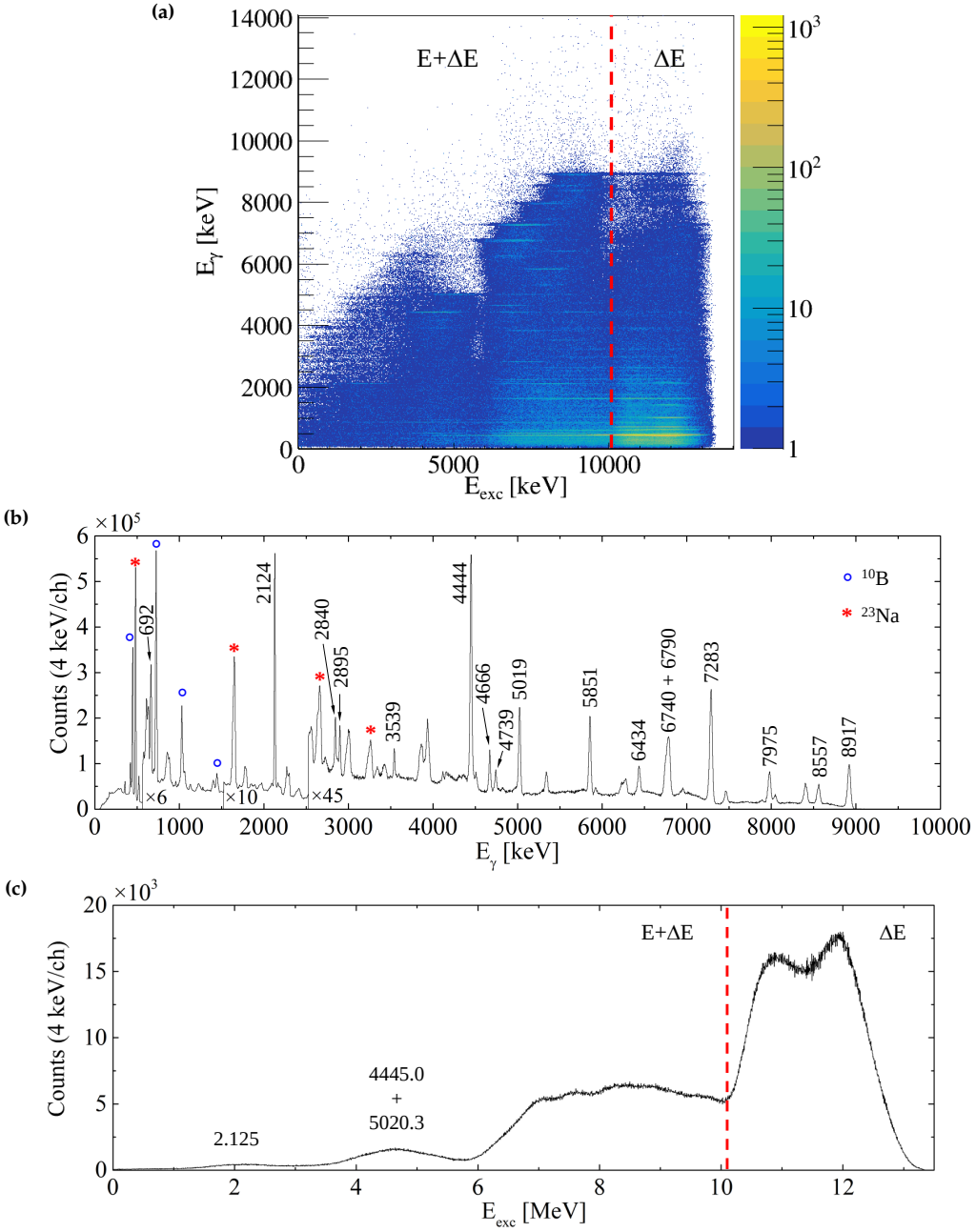

Figure 9.7: Panel (a): Doppler-shift corrected E_γ vs. E_{exc} matrix, obtained gating on the proton events detected in GALTRACE. The red dashed line discriminates between events reconstructed considering protons stopped in the ΔE layer, and those corresponding to protons passing through the ΔE and stopping in the thick E detector (E+ΔE). The projections of the matrix on the y and x axes are shown in panels (b) and (c), respectively. In panel (b), ^{11}B gamma rays (see level scheme in Figure 9.8) are indicated with energy labels, while those coming from contaminants, namely ^{10}B and ^{23}Na, are marked with blue (circle) and red (star) symbols, respectively.

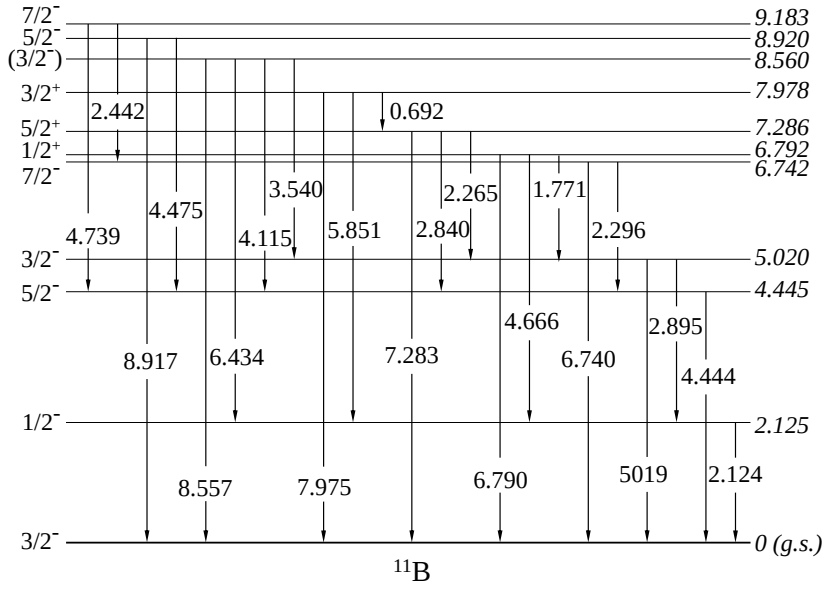

Figure 9.8: ^{11}B partial level scheme. The gamma-ray transitions observed in the experiment are indicated. Energies (in MeV) and spin/parity information are taken from the database [53].

the order of 2.8×10^{-3}, with respect to the emission of a proton. From the experimental point of view, the existence of a resonance at 11.425 MeV was suggested in the TRIUMF experiment of Ref. [175].

To search for traces of the gamma decay from such a hypothetical resonance, we introduced a 700-keV-wide gate in the E_p vs. θ matrix around the possible kinematic line [192], corresponding to the population of a 11.425-MeV state in ^{11}B, as illustrated in Figure 9.9(a). The region of interest for the corresponding Doppler-shift-corrected γ-ray energy spectrum is displayed in Figure 9.9(b). The possible γ decay from the resonance should be observed in the energy region between 9105 and 9385 keV, which correspond to excitation energies in ^{11}B of 11.228-11.509 MeV, *i.e.*, the 280-keV energy window available for the $\beta^- p^+$ decay of ^{11}Be (see Section 6.1). There is no clear evidence of the gamma transition in the region of interest (ROI), therefore we proceeded by extracting the probability with which we exclude the existence of a peak.

Firstly, the expected number of counts in the possible $\sim$9.3 MeV gamma transition was estimated assuming a cross section, for the population of the hypothetical resonance at 11.425 MeV, of $\sim$ 0.150 mb, *i.e.*, of the same order of magnitude of the cross section for the population of the 8.920-MeV nearby excited state in the same nucleus. We estimated the FWHM of a gamma transition at 9.3 MeV: we measured a FWHM of 41 keV for the peak at 8.9 MeV in the punch-through matrix (see Figure 9.7(a)), and we extrapolated an average FWHM in the region of the resonance of $\sim$ 50 keV, corresponding to a σ of 21 keV. The peak at 8917 keV (transition depopulating the 8.920-MeV state) was integrated, and the information on its area was combined with the GALILEO photopeak efficiency at 8.9 and 9.3 MeV, and the predicted gamma branching (3×10^{-3}). We estimated that the area

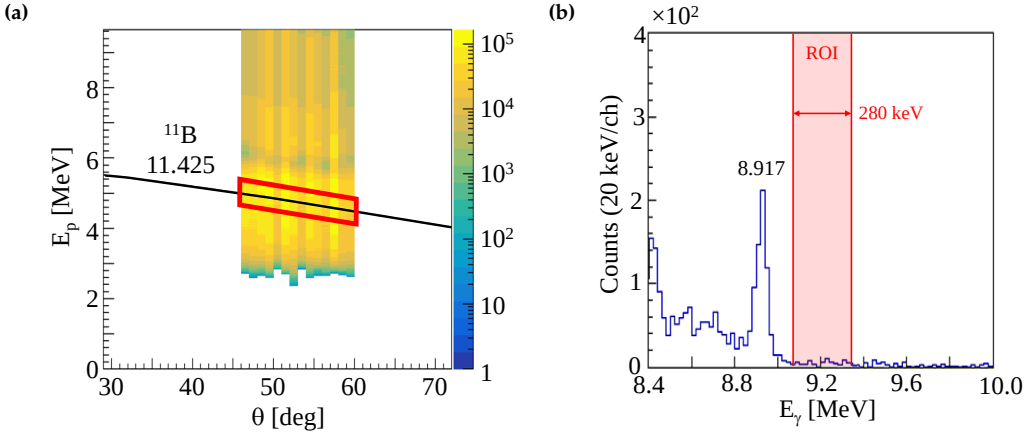

Figure 9.9: Panel (a): same as Figure 9.3, with a zoom on low-energy protons (high ^{11}B excitation energies); the kinematic line (black line) corresponding to the population of the ^{11}B 11.425-keV hypothetical resonance is shown. The red contour delimits the gate considered in the analysis: the selected events are associated to protons stopped in the ΔE layer. Panel (b): Doppler-shift-corrected gamma-ray energy spectrum, corresponding to the gate of panel (a). The red shaded band is the region of interest (ROI) for the search of a gamma transition depopulating the resonance under investigation. The 8917-keV, for which the protons should not stop in ΔE layer, is visible, as the gates set on the particle-identification plots (see Figure 9.2) partially select punch-though events.

of the 9.3 MeV transition should be 59(9), distributed in a Gaussian of $\sigma = 21$ keV, above the background.

To quantify a limit for the existence of a γ decay from the near-threshold resonance we followed the procedure described in Ref. [197], based on the comparison between the experimentally measured counts in the ROI and the expected value. Figure 9.10 illustrates the technique. The experimental γ-ray spectrum was produced with bins of 20 keV and was fitted to deduce the level of the background. Next, we defined a 60-keV-wide moving window: its width corresponds to three times the width of the expected Gaussian (3σ), namely $\sigma = 21$ keV, as explained before. Inside the moving window, the counts C of the spectrum above the fitted background level, are integrated, and the corresponding uncertainty σ_C is extracted. A 20-keV-bin discrete Gaussian of total area 59(9) (the expected counts in the resonance peak) and $\sigma = 21$ keV was simulated. The portion of the Gaussian area falling inside the 60-keV window, namely 51(8) counts, was considered. We then calculated the distance in number of standard deviations (x) between the measured counts (C) and the ones expected in the Gaussian (G) inside the window, following Equation (9.1). Here σ_G refers to the uncertainty on the Gaussian counts, not to the Gaussian width.

$$x = \sqrt{\frac{(C-G)^2}{\sigma_C^2 + \sigma_G^2}} \tag{9.1}$$

The window was subsequently moved in steps of 20 keV (*i.e.*, one bin), and the same

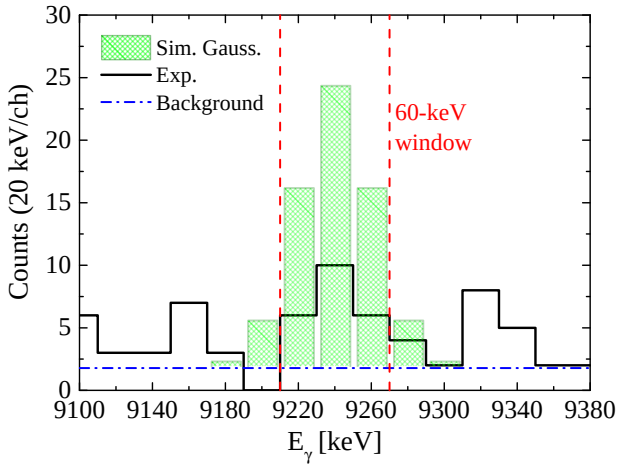

Figure 9.10: Schematic exemplification of the technique used to extract the limit on the existence of a gamma transition depopulating the 11.425-MeV ^{11}B hypothetical resonance. The black histogram corresponds to experimental data (in bins of 20 keV), in blue is reported the fitted background (dash-dot), and the shaded green column plot corresponds to the expected discrete Gaussian having a total area of 59(9) counts, and a width $\sigma = 21$ keV. The Gaussian has been simulated assuming a cross section for the population of the state of interest of the same order of magnitude of the nearby 8920-keV state, and a gamma branch of 3×10^{-3}. The Gaussian is directly drawn above the background level. The red dashed vertical lines delimit the 60-keV moving window. Note that not all the Gaussian area falls inside the moving window: only 51(8) counts fall within the window.

procedure was repeated, until the entire ROI was covered. Figure 9.11 shows the comparison between the measured and the expected counts inside the 60-keV moving window, for the entire ROI. The red line corresponds to the expected 51(8) counts of the simulated Gaussian inside the moving window.

From the extracted values of x, we could estimate the probability with which we exclude the existence of a peak in the ROI[1]. In the whole 280-keV region, we exclude the presence of a Gaussian γ-ray peak with a width $\sigma = 21$ keV and a total area of 59(9), with a confidence level $\gtrsim 99$ %. In conclusion, as a result of the GALILEO+GALTRACE experiment, we tend to exclude the existence of a narrow near-threshold resonance in ^{11}B, in the available energy window for a beta-delayed proton emission from ^{11}Be. This is under the assumption of a gamma branching of 3×10^{-3} (as predicted by the SMEC model) and a total cross section for the population of the hypothetical resonance of the same order of nearby states (*i.e.*, ~ 2 mb).

However, being our result dependent on the assumption of the population cross section and the state branching ratio for the gamma decay, the fact that we did not observe any trace of a gamma-ray transition could be either due to a much lower population cross section or a smaller gamma branch. As a consequence, the existence of the hypothetical near-threshold state itself is still an open question.

[1]From tabulated percentage probabilities [198].

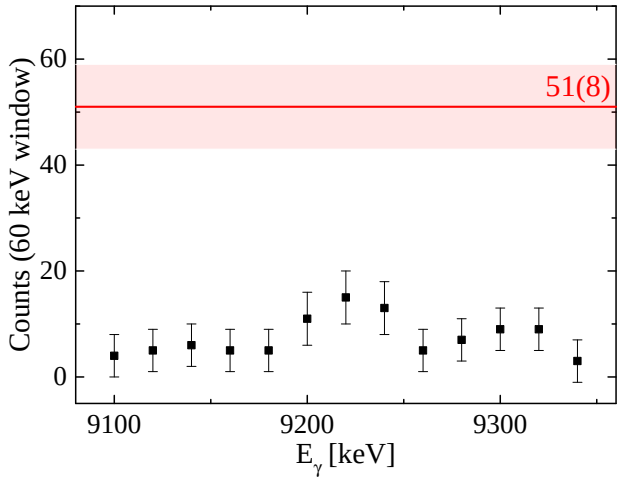

Figure 9.11: Experimentally measured counts (black squares), as a function of the gamma-ray energy. The points are extracted considering a 60-keV moving window and are compared to the expected counts (red line) in a Gaussian above the background of $\sigma = 21$ keV and total area 59(9) (51(8) counts inside the 60-keV window), associated to a possible ~ 9.3 MeV gamma transition. See text and Figure 9.10 for more details on the technique.

Part IV

Study of M4 stretched-configurations decay in ^{14}N and ^{16}O

Chapter 10

Physics case: M4 stretched-configurations decay

This Part of the Thesis is devoted to the investigation of the decay of M4 stretched excitations, whose general properties have been introduced in Section 1.5.3, in nuclei of ^{14}N and ^{16}O. The structure of this Part is the following: in the present Chapter we will firstly give an overview of the known M4 resonances in light nuclei in Section 10.1, and secondly, in Section 10.2, a first pilot experiment to investigate the ^{13}C case will be presented. In Sections 10.3.1 and 10.3.2 we will then address the specific physics case of M4 resonances in ^{14}N and ^{16}O. In Chapter 11 we will describe the experiment realised at the Cyclotron Center Bronowice (CCB) in Kraków, Poland, to study these systems, together with the experimental set-up employed. Finally, in Chapter 12 we will discuss in details the analysis and results of the experiment.

The experiment meant to investigate ^{14}N and ^{16}O was performed having the Author of this Thesis as spokeperson. The entire data analysis of the experiment was carried out during the second and third year of the PhD.

10.1 Stretched states in light nuclei

Stretched states (see Section 1.5.3 for details) are experimentally known to be well populated in electrons or hadrons (protons and pions) inelastic-scattering processes at large-momentum transfer [60]. With this type of reactions, the population of M4 stretched configurations have been largely studied in the past in several nuclei in the light mass region: ^{11}B [199, 200], ^{12,13,14}C [201–208], ^{14,15}N [206, 209–211] and ^{16,17,18}O [63, 212–216] (see Figure 10.1 and Table 10.1). Also M6 and M8 configurations were investigated in heavier systems, such as ^{28}Si [62, 217] and ^{60}Ni [218, 219], respectively.

The decay of stretched M4 states in light 1p-shell nuclei (note that ^{17}O and ^{18}O are not 1p-shell nuclei, they have one and two neutron in the $1d_{5/2}$ orbital, respectively) is expected to be dominated by the direct emission of light particles, especially protons and neutrons, but also d, t and α, followed by the emission of γ rays from the excited states in the daughter nuclei. However, despite the fact that the study of the decay of these states can give direct access to the wave function composition, experimental information on their decay is largely missing.

If we limit ourselves to 1p-shell nuclei for which M4 stretched states have been identified in the past (see Table 10.1), not all the nuclei present favourable features to experimentally investigate their M4 resonances decay. ^{11}B was previously studied with electron

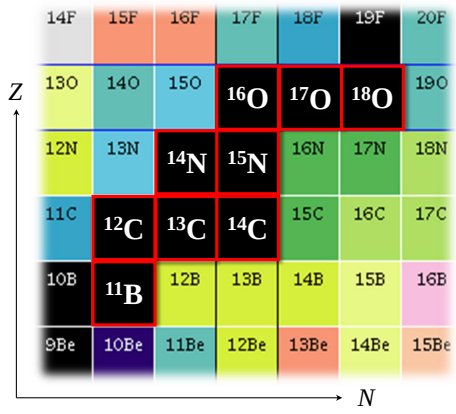

Figure 10.1: Portion of the nuclear chart in the light mass region: the nuclei for which M4 stretched states have been reported in literature are highlighted.

scattering [199] and although the excitation of the $11/2^+$ state should be mainly of M4 character, both magnetic and electric components were observed. Among the carbon isotopes, ^{12}C M4 resonance (see Figure 10.2(a), bottom spectrum) displays a mixing with other multipolarities [201, 207], while the investigation of ^{14}C (see Figure 10.2(a), top spectrum), although very promising (three well isolated and rather pure M4 resonances [201, 208]), would require a radioactive target. Only the stable ^{13}C has three well-isolated "pure" M4 resonances (see Figure 10.2(a), middle spectrum) and could be accessed experimentally [201–203]. Among the nitrogen isotopes, both ^{14}N [209, 210] and ^{15}N [211] show more complex but still accessible cases, with four M4 resonances each. A pure target of ^{15}N, in addition, would be rather complex to be produced, given the ^{15}N isotopic abundance of 0.364 %. ^{16}O displays three M4 states, which all lie in an energy window of 2 MeV [63, 212, 213], more difficult to access with in low-energy-resolution experiments.

In this context, a new research program was recently undertaken at the Cyclotron Center Bronowice (CCB) of the IFJ PAN (Kraków, Poland), with the aim of shedding light on the decay of stretched M4 resonances in light 1p-shell nuclei. This is done by extracting decay branching ratios from the resonance states to excited states in daughter nuclei, via γ-ray- and particle-coincidence measurements. The experimental work in this field is supported by a parallel development by members of the same research group of an advanced version of Gamow Shell Model theoretical calculations [220, 221] (see Section 1.2.1), that can be tested in this framework. Two experiments have been realised so far, one first pilot experiment to study ^{13}C and a second one to investigate ^{14}N (see Chapter 11).

10.2 The pilot experiment: ^{13}C investigation

A first pilot experiment has been performed at CCB in March-June 2019 and June 2020, with the aim of studying the decay of an M4 stretched state located at 21.47 MeV in ^{13}C, populated in a (p,p') reaction [222]. ^{13}C was a good candidate because three

Table 10.1: Summary of known M4 stretched excitations in light nuclei, all but ^{17}O and ^{18}O being $1p$-shell nuclei. The corresponding excitation energy in MeV and spin/parity are reported. The information on the reaction mechanism with which they were investigated is also reported: e → electron scattering, π → pion scattering, p → proton scattering.

Nucleus	Mechanism	Energy [MeV]	J^π
^{11}B	π	14.04	$11/2^+$
^{12}C	e,π	19.5	4^-
^{13}C	e,π,p	9.5	$9/2^+$
		16.08	$(7/2^+)$
		21.47	$(7/2^+, 9/2^+)$
^{14}C	e,π	11.7	4^-
		17.3	4^-
		24.3	4^-
^{14}N	e,π	15.1	$(3^-, 4^-)$
		16.9	(5^-)
		18.5	3^-
		20.1	$(3^-, 4^-)$
^{15}N	e,π	10.68	$9/2^+$
		12.52	$9/2^+$
		14.04	$(7/2^+, 9/2^+)$
		17.19	$(7/2^+, 9/2^+)$
^{16}O	e,π,p	17.79	4^-
		18.98	4^-
		19.80	4^-
^{17}O	e,π	15.78	$(13/2^-)$
		17.06	$11/2^-$
		20.14	$11/2^-$
		20.70	$(9/2^-)$
^{18}O	e,p	18.70	(4^-)
		20.36	(4^-)
		22.39	(4^-)

well-separated stretched M4 states at 9.50, 16.08 and 21.47 MeV, corresponding to the $(1d_{5/2}1p_{3/2}^{-1})^{4^-}$ excitation, have been already identified in the past, through inelastic electron- [201], pion- [203] and proton-scattering [202] reactions (see Figures 10.2 and 10.3).

In the (p,p') experiment of Ref. [202], the 21.47-MeV state was observed with a high intensity, well isolated from other resonances and with a width of 270 keV (see Figure 10.3(a)). A proton beam of 135 MeV was used, and the angular distribution of the

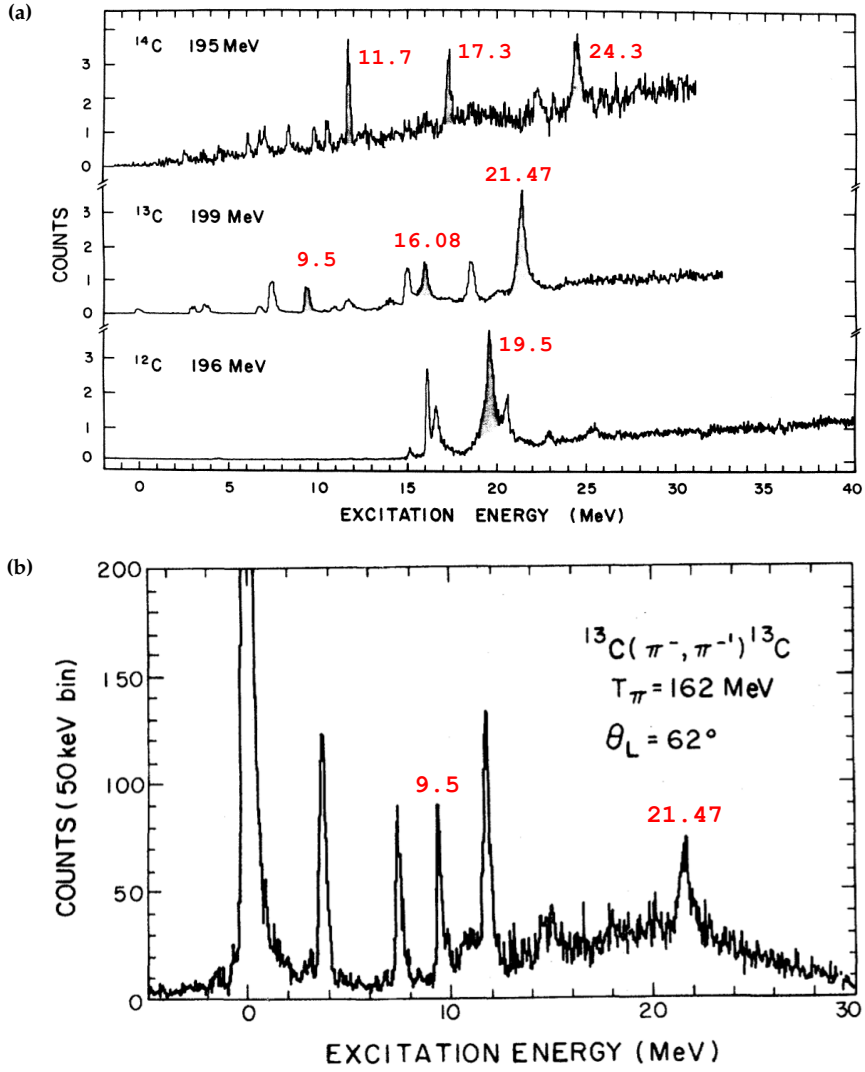

Figure 10.2: ^{13}C(e,e′) and ^{13}C(π^-,$\pi^{-\prime}$) reactions scattered electron (a) and pion (b) spectra, respectively. In panel (a), the spectra of electron scattered on ^{12}C and ^{14}C are also shown. The energies of the M4 resonances are shown with red labels. Figure of panel (a) reprinted with permission from Ref. [201], Copyright 1986 by the American Physical Society (license No. RNP/21/SEP/044422). Figure of panel (b) reprinted with permission from Ref. [203], Copyright 1982 by the American Physical Society (license No. RNP/21/SEP/044421).

inelastically scattered protons exciting the resonance presented a maximum at an angle of ~30° in the centre of mass reference frame (see Figure 10.3(b)).

Following the experimental evidence of Ref. [202], in the first part of the CCB pilot experiment (March-June 2019), the resonance of interest was populated in a (p,p′) reaction, employing a beam of the same energy (135 MeV) impinging on a pure ^{13}C thick target (197 mg/cm^2). To study the decay of the state, a proton-gamma coincidence technique

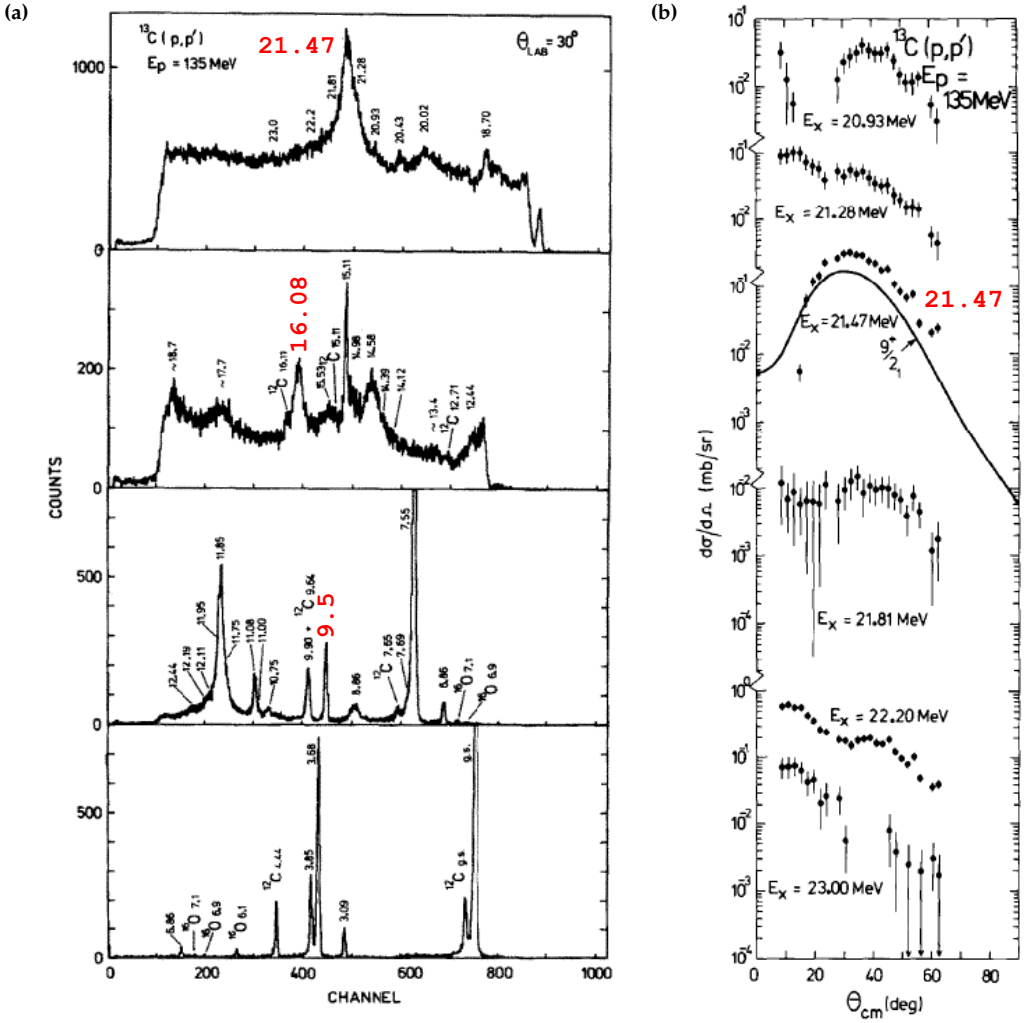

Figure 10.3: ^{13}C(p,p′) reaction at 135 MeV scattered proton spectra (a) and angular distributions (b). The ^{13}C excited states are indicated. The M4 stretched states peaks in (a) and angular distribution in (b) are shown with red labels. Figure reprinted from Ref. [202], Copyright 1988, with permission from Elsevier (license No. 5146511466801).

was exploited. Protons and γ rays were detected in a multi-array set-up, composed of six modules of the Kraków Triple Telescope Array (KRATTA) [223] at $\sim 36°$ with respect to the beam axis, two 9-fold clusters of the Photon Array for studies with Radioactive Ion and Stable beams (PARIS) [111] and four large-volume $LaBr_3$ crystals. In the second part of the experiment performed at CCB in June 2020, the additional possibility of investigating the decay of M4 resonances by proton-particle coincidences was tested. The same proton beam was employed but with a specially designed thin target (1 mg/cm^2) and an improved set-up, with 30 KRATTA modules and an additional thick position-sensitive Double-sided Silicon Strip Detector (DSSD), placed backwards at 138°.

The experiment turned out to be successful: first of all, a pronounced peak associated to the population of the M4 ^{13}C resonance was observed at 21.5 MeV in the reconstructed excitation-energy spectrum, as shown in Figure 10.4(a); secondly, a clear identification of the γ decay of excited states in daughter nuclei, in coincidence with the population of the M4 resonance, was obtained for the first time (see Figure 10.4(b)). In particular, proton-

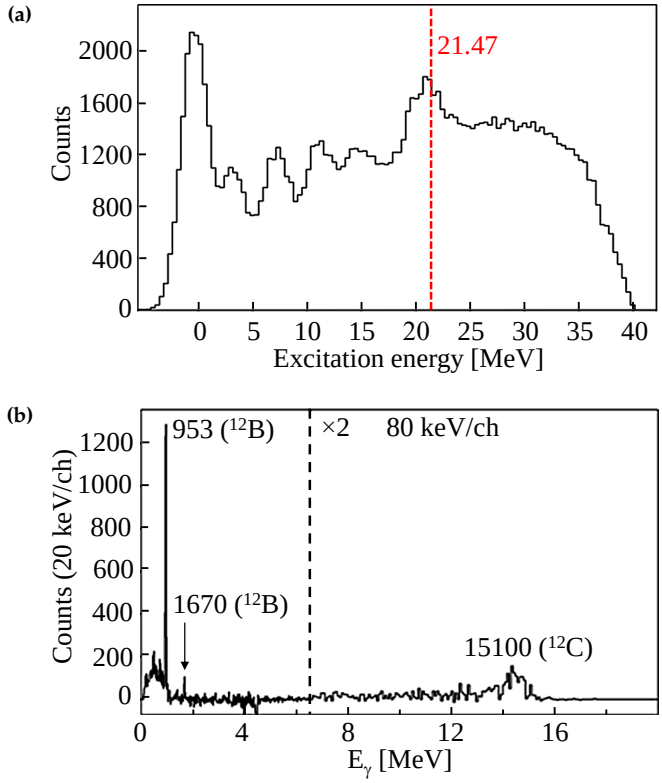

Figure 10.4: (a) ^{13}C excitation energy spectrum measured in singles (no coincidence with gamma rays), reconstructed from the energy of inelastically-scattered protons. (b) Gamma-ray energy spectrum gated on the 21.47-MeV ^{13}C stretched state. The gamma rays depopulating daughter nuclei are highlighted (energies in keV). Courtesy of N. Cieplicka-Orińczak.

and neutron-decay channels from the M4 resonance were observed. In the proton-decay channel, a strong branching (69(6) %) was measured to the 0.953-MeV first-excited state in ^{12}B, and a less intense one (7(2) %) to the 2.621- and/or 1.674-MeV higher-lying states of the same nucleus. In the neutron-decay channel, traces of a branching (24(5) %) towards the ^{12}C 15.11-MeV resonance were seen, while no sign of a population of the ^{12}C first-excited 4.44-MeV state was observed. The reconstructed decay scheme of the M4 resonance is reported in Figure 10.5. Moreover, the analysis of the second part of the experiment, made possible an estimation of the decay branch leading to the ground state of ^{12}B (< 23 %), which cannot be observed in proton-gamma coincidences, should also be possible using proton-particle coincidences.

The experimental data obtained served also as a test to a recently-developed version of

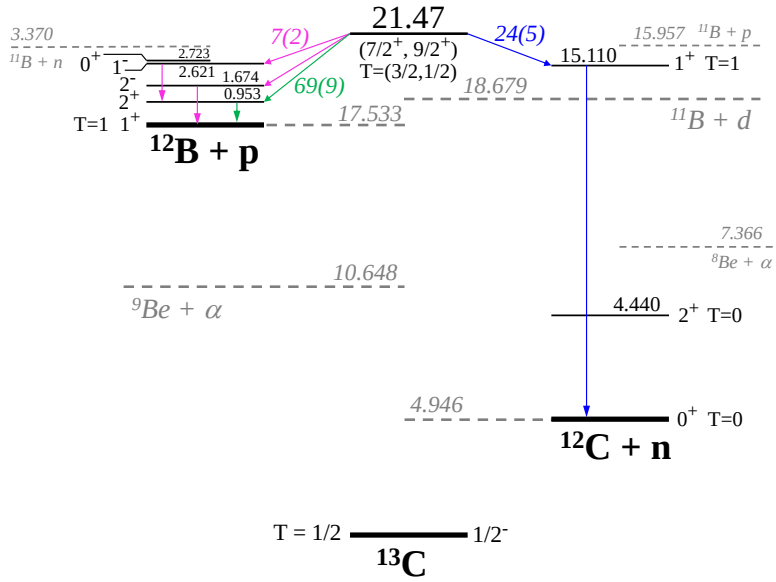

Figure 10.5: ^{13}C 21.47-MeV M4 state decay scheme. Dashed-grey lines indicate particle-emission thresholds. Energies expressed in MeV. Courtesy of N. Cieplicka-Orińczak.

the GSM, which was used to give an interpretation of the properties (spin/parity, isospin and wave function composition) of the M4 resonance. The calculations were performed with a model space specifically adapted to describe the 21.47-MeV M4 state of interest, which in literature is reported to be either $7/2^+$ or $9/2^+$. The calculations predicted that the resonance has $T = 3/2$ isospin and $7/2^+$ spin/parity. The $9/2^+$ $T = 3/2$ character has been excluded on the basis of calculated spectroscopic factors for the decay towards excited states in the daughter nuclei, which excluded some decay channels, that instead were observed experimentally and were predicted as possible in the case of the modelled $7/2^+$ state.

Summarising, the results of the pilot experiment clearly supported the power of the experimental set-up and assessed the validity of the technique, that can be directly extended to study other M4 resonances in the nearby nuclei in the same light mass region, as shown in Figure 10.1. This is the case of the second experiment performed within the M4 CCB research program, that will be the main topic of this Part of the Thesis.

10.3 Present case: ^{14}N and ^{16}O study

In the following, we will concentrate on two other more complex cases, namely ^{14}N and ^{16}O. In both these nuclei, M4 resonances arising from the $(1d_{5/2}1p_{3/2}^{-1})^{4^-}$ excitation were observed in the past [63, 209, 210, 212, 213]. ^{14}N should have been the only physics case of the second experiment realised at CCB, but a large ^{16}O contamination was observed. This contamination made the investigation of ^{14}N rather difficult, and only a qualitative analysis has been carried out for this nucleus. We concentrated therefore on the study

of ^{16}O stretched states decay, and this will be the main topic of this Part of the Thesis. However, since the ^{14}N case was the original aim of the experiment, we will discuss in detail also its physics case. This will be useful to understand the experiment data analysis, the qualitative results obtained and it will serve as a reference for future investigations.

10.3.1 M4 resonances in ^{14}N

M4 resonances in ^{14}N were observed following electron scattering [209] (see Figure 10.6(a)) and scattering of 162-MeV pions of both charges [210] (see Figure 10.6(b)). No investigation has been performed, thus far, using inelastic proton scattering, although high-energy protons are known to excite this type of stretched configurations, similarly to electrons and pions [207].

In ^{14}N, the ground-state spin is 1^+, and the $(1d_{5/2}1p_{3/2}^{-1})^{4^-}$ excitation strength can be distributed between 3^-, 4^-, and 5^- excited states. As shown in Figure 10.6(a), in the electron scattering experiment of Ref. [209], a strong M4 transition to a state at 16.91 MeV, tentatively 5^-, was observed, exhausting about 59 % of the M4 sum rule for $J = 5^-$. Significant M4 strength was also found at 20.1 and 15.0 MeV, probably corresponding to $J = 3^-$ or 4^- states. Evidence for a weak M4 transition at 18.5 MeV excitation was also reported and interpreted as a 5^- state.

A strong 5^- excitation was also observed in the π^+ scattering experiment of Ref. [210] at 16.9 MeV, together with the 20.1-MeV resonance, that was tentatively assigned with a 3^- spin and parity (see Figure 10.6(b)). These two states should have a predominant $T = 1$ isospin character, while all other resonances may have mostly $T = 0$ nature.

The experiment that we will present in the following is meant to study mainly the decay of the M4 resonance located at 20.1 MeV, which is rather well isolated from all other lower-lying excitations, but also on the one at 16.9 MeV, which should be quite intense, as it is visible in Figure 10.6. Figure 10.7 shows the expected decay pattern for the 20.1-MeV state. Because of the high neutron separation energy in ^{14}N (S_n = 10.553 MeV) and of the absence of bound states in ^{13}N (neutron-decay channel), no γ decay is expected after neutron emission: the only possibility would be the 4.439-MeV decay in ^{12}C, following the emission of one neutron and one proton with a total energy of 3.185 MeV. For the proton decay channel, one expects to observe the branches feeding the 3089-, 3685- and 3854-keV ^{13}C states, which decay to the ground state via the emission of 4 γ rays (*i.e.*, 3853, 3684, 3089 and 169 keV). In addition, the d- and α-decay branches are also expected. In the first case, only the decay of the 2^+ 4.439-MeV state to the ground state in ^{12}C should be observed, while 4 states with energies between 718 and 3587 keV can be populated in ^{10}B, after α emission, the main γ decays being 414, 718, 1022 and 2868 keV. All other decay channels will practically not be associated with γ-rays emission, either due to the limitation in the available energy, or due to the unbound nature of the final excitations.

10.3.2 M4 resonances in ^{16}O

In the ^{16}O nucleus, three M4 resonances have been reported in literature at the energies of 17.79, 18.98 and 19.80 MeV. They were populated in electron [212], pion [63] and proton

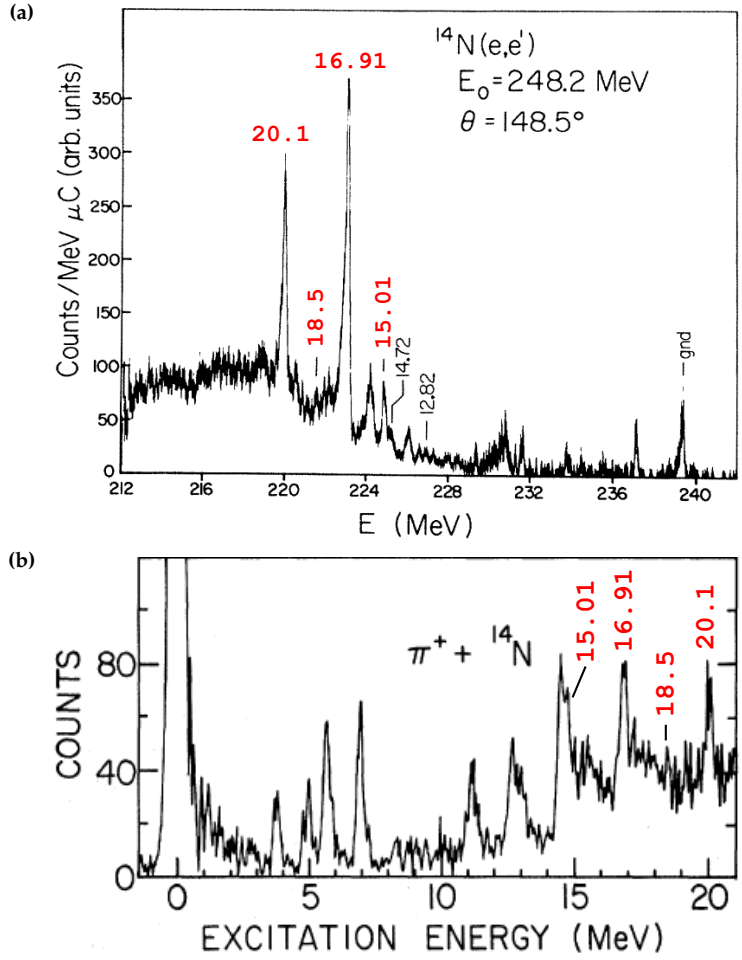

Figure 10.6: Spectra for electron (a) and pion (b) scattering on ^{14}N. The M4 resonances are indicated with red labels. Figure of panel (a) reprinted with permission from Ref. [209], Copyright 1984 by the American Physical Society (license No. RNP/21/SEP/044433). Figure of panel (b) reprinted with permission from Ref. [210], Copyright 1983 by the American Physical Society (license No. RNP/21/SEP/044438).

[213] inelastic-scattering reactions (see Figures 10.8 and 10.9). All these states are 4^-: the first and the third have isospin $T = 0$, while the second has isospin $T = 1$.

A very interesting feature about these configurations has been observed in the experiment with pions of Ref. [63]. The transitions to the $(4^-; T = 0)$ resonances at 17.79 and 19.80 MeV were found to be largely asymmetric comparing π^+ and π^- inelastic scattering. On the other hand, the π^+ and π^- cross sections for the $(4^-; T = 1)$ state at 18.99 MeV were equal. This phenomenon was interpreted as a three-state isospin mixing.

In the (p,p′) experiment of Ref. [213], the three 4^- resonances were strongly populated bombarding a 10 mg/cm^2 Mylar ($C_{10}H_8O_4$) target with a proton beam at 135 MeV. The inelastically scattered protons were measured at ~35° in the laboratory frame with respect

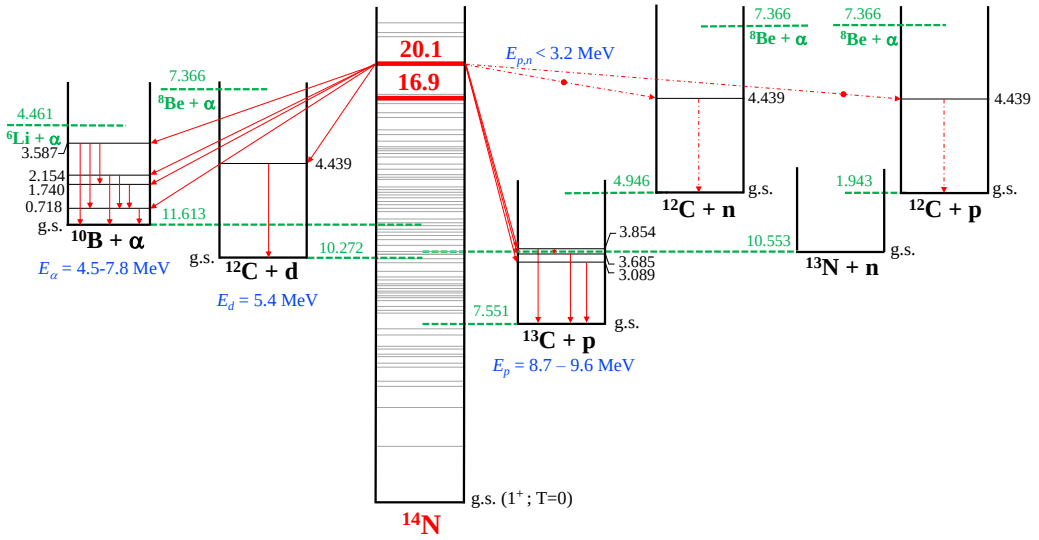

Figure 10.7: Expected decay pattern of the 20.1-MeV resonance in ^{14}N. Thresholds for particle emission are marked in green. The possible decays from the resonance to the excited states in daughter nuclei are indicated by red arrows, together with the subsequent γ decays. Energies of p, d and α associated to the direct population of the excited states are also given in blue. The 16.9-MeV resonance should have similar open decay channels, except the two-step p-n and n-p decays to ^{12}C, which are forbidden by the available phase space.

to the beam line, and the differential cross section for the population of these states was measured to have a maximum between 30° and 40°, as shown in Figure 10.9(b). Incidentally, these are almost the same experimental conditions of the experiment realised to study ^{14}N (see Chapter 11) and in which a large contamination of ^{16}O was found. This will be a crucial point to interpret the experimental data discussed in this Thesis.

Regarding the possible decay channels of the three M4 resonances in ^{16}O, the expected decay pattern is reported in Figure 10.10. All the three states can decay through α emission to the first-excited 2^+ state in ^{12}C at 4.439 MeV. For the proton-decay channel, the first resonance has sufficient energy to decay to the first or second excited states in ^{15}N, emitting low-energy (~400 keV) protons. For the other two resonances, branches to the first three excited states in ^{15}N (5.270, 5.300 and 6.324 MeV) are expected. In addition, the resonance at 19.80 MeV has enough space to decay also to the $5/2^+$ state at 7.155 MeV. The neutron-decay channel to excited states of ^{15}O is forbidden by the available phase space. However, a neutron decay to the ground state of ^{15}O cannot be excluded, but we would not be able to detect it, as no γ ray is emitted in this case. No d-decay channel to ^{14}N is expected, since the deuteron-emission threshold is located at 20.7363 MeV.

^{16}O is a rather exceptional case, as it is one of the very few systems for which the decay of the M4 resonances has been investigated in the past. Branching ratios for proton and α-particle decay of hole states in ^{16}O have been determined in the experiment by Breuer *et al.* presented in Ref. [224]. In the experiment, ^{17}O(d,t)^{16}O and ^{17}O(^{3}He,α)^{16}O reactions were employed to study such decays (see Figure 10.11). The case of ^{16}O would then

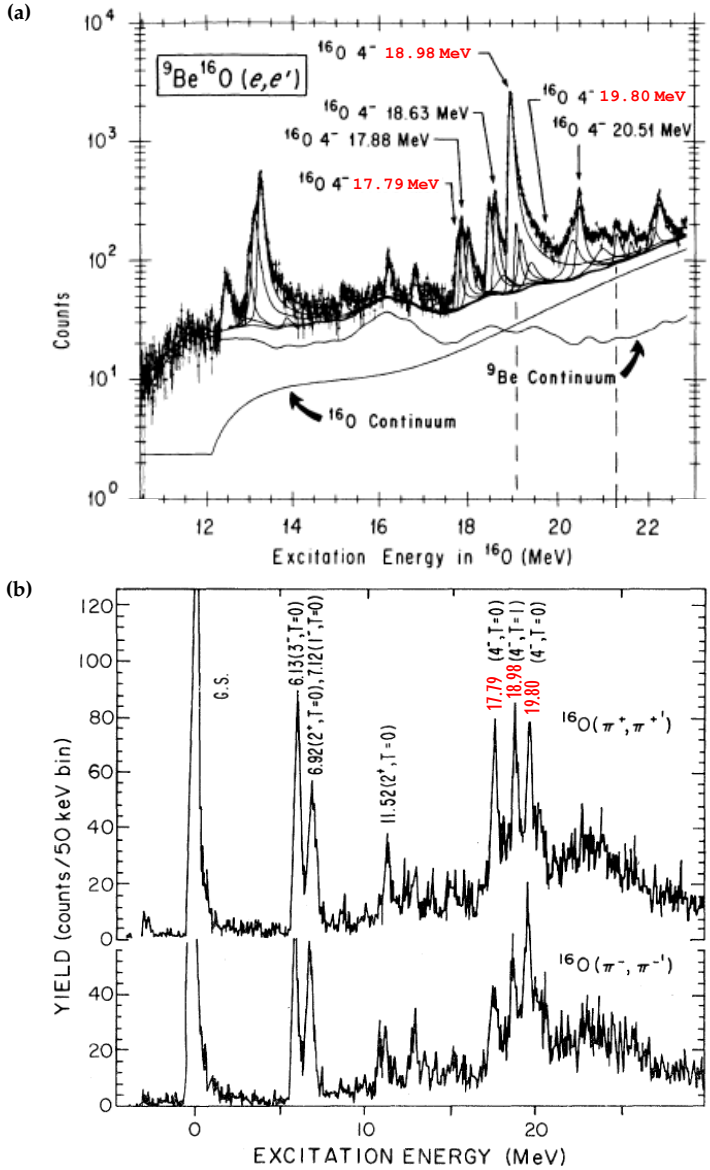

Figure 10.8: Spectra for electron (a), pion (b) and proton (a) scattering on ^{16}O. The M4 resonances are indicated with red labels. Figure of panel (a) reprinted with permission from Ref. [212], Copyright 1987 by the American Physical Society (license No. RNP/21/SEP/044440). Figure of panel (b) reprinted with permission from Ref. [63], Copyright 1980 by the American Physical Society (license No. RNP/21/SEP/044438). Figure of panel (a) reproduced from Ref. [213] with permission from CSIRO Publishing.

be particularly suitable to validate the experimental technique presented in this Thesis in Chapter 12, that exploits proton-gamma coincidence measurements to determine the decay branching ratios of the resonances of interest.

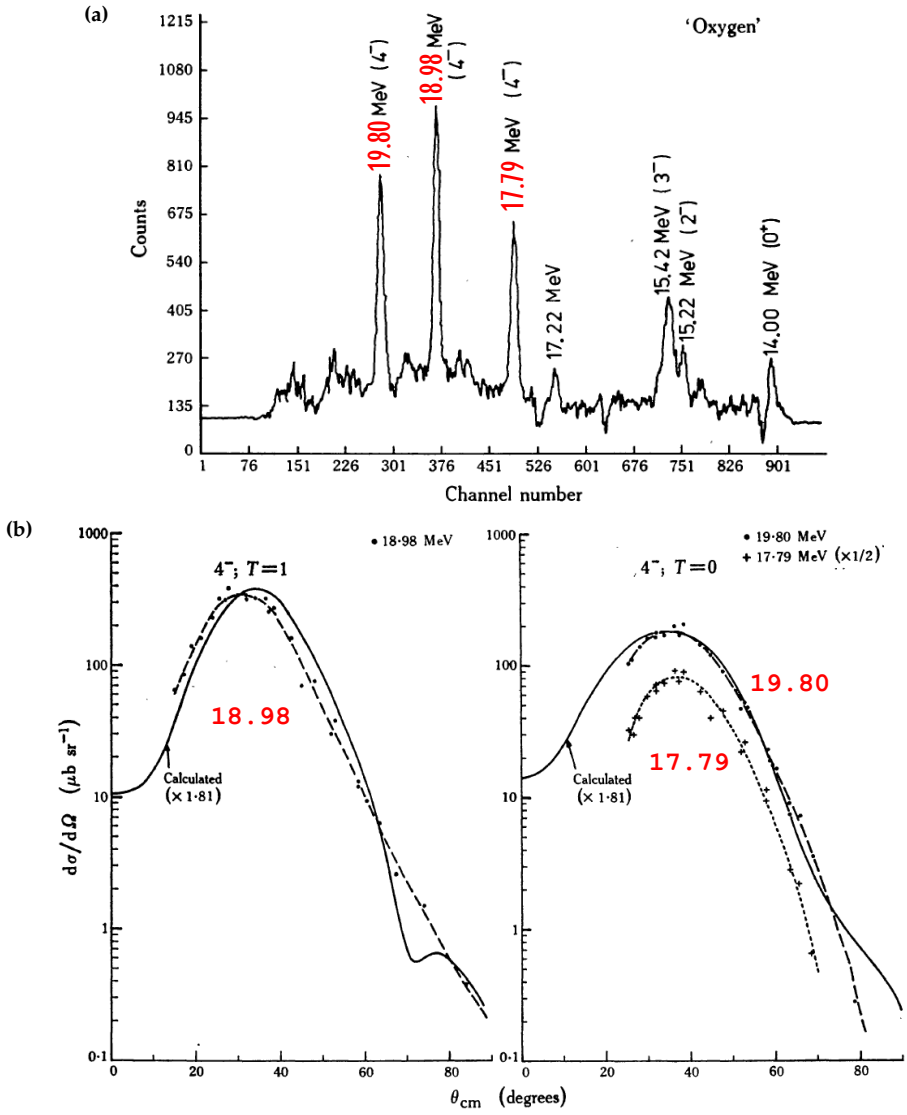

Figure 10.9: Panel (a): spectrum for proton scattering on ^{16}O. The M4 resonances are indicated with red labels. Panel (b): differential cross section for the M4 triplet in ^{16}O. The solid curves are the results of the microscopic distorted wave calculation, while the dashed ones highlight the trend of the experimental data. Figure reproduced from Ref. [213] with permission from CSIRO Publishing.

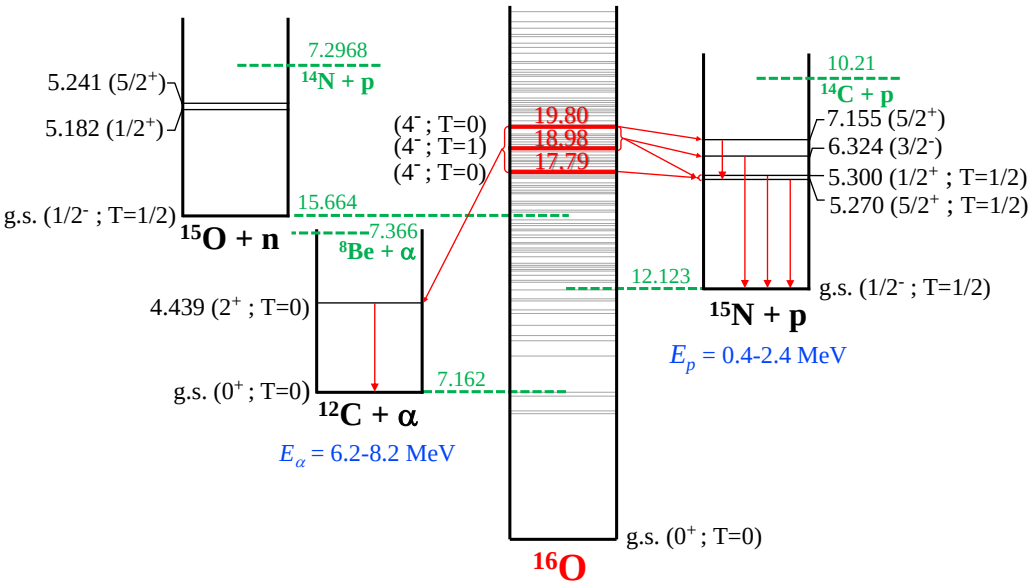

Figure 10.10: Same as Figure 10.7 for the three M4 resonances in ^{16}O.

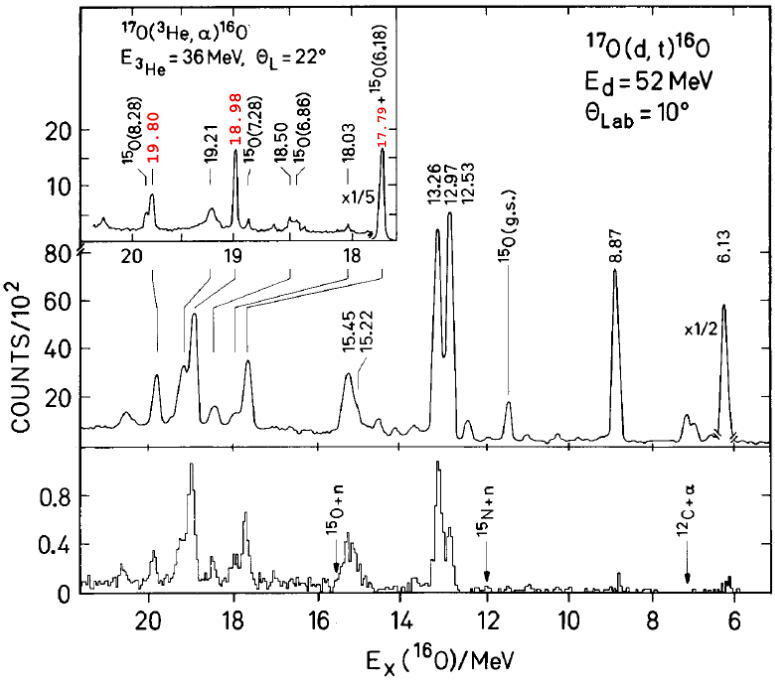

Figure 10.11: Spectrum of the ^{17}O(d,t)^{16}O reaction. Singles spectrum is reported in the middle, while in the bottom is shown the spectrum in coincidence with any outgoing charged particle. The inset on top left displays the spectrum of the ^{17}O(^{3}He,α)^{16}O reaction, where the triplet of M4 resonances of interest (red labels) is visible. Figure reprinted from Ref. [224], Copyright 1980, with permission from Elsevier (license No. 5147110161460).

Chapter 11

Experiment and set-up

In this Chapter we will describe the (p,p') experiment meant to investigate the ^{14}N M4 resonances, together with the experimental apparatus employed.

The experiment took place at the CCB facility of the IFJ PAN in Kraków where two cyclotrons are presently active to conduct scientific research and tumour proton radiotherapy [225]. The accelerator used in the experiment was the Proteus C-235 isochronous cyclotron installed at CCB in 2012, able to accelerate protons to an energy of 230 MeV. An energy degrader and selector allows the beam energy to be downgraded continuously to 70 MeV, with intensities up to 600 nA [226]. The beam time at CCB is shared between medical treatments and scientific research experiments, which are usually performed during the night, in the weekend or in periods in which no medical therapy is carried out. The experiment on ^{14}N was divided in two parts:

***e014*:** one week from 1st to 8th December 2019, both days and nights included, for a total of 72 h of data taking + 17 h of calibrations + 12 h of tests;

***e016*:** three long weekends, from Friday afternoon to Sunday evening in February-March 2020, for a total of 84 h of data taking + 26 h of calibrations + 4 h of tests.

The proton beam impinged on a lithium amide ($Li^{14}NH_2$) target 160 mg/cm^2 thick, produced at the IFIN-HH institute in Romania. This type of target was chosen as the H and Li (mainly ^{7}Li) components does not pollute the measurement. In fact, no gamma rays are expected from ^{7}Li decay products, namely ^{4}He, ^{6}He and ^{6}Li, as they have no bound states. ^{7}Li itself has only one bound state at 477.6 keV [53], which emits a γ ray of the same energy. However, during the analysis we discovered a large oxygen contamination, which can be caused by the hygroscopic properties of the compound, which can absorb humidity from the air. This issue will be largely discussed in the data analysis chapter.

The optimal proton beam energy, at which the M4 resonances in ^{14}N could be populated, was assessed at the beginning of the first data taking, which was preceded by a short excitation function measurement (see Figure 12.3). A beam energy of 135 MeV among 115, 135 and 155 MeV was chosen, with a current measured on the target between 3 and 5 pA.

Figure 11.1 illustrates a scheme of the experimental set-up, which is very similar to the one of the pilot experiment on ^{13}C, introduced in Section 10.2. The KRATTA array, placed

at forward angles in the 30°-42° range in θ, was coupled to four large-volume (3.5"×8.0") $LaBr_3$(Ce) detectors, two 9-phoswich PARIS clusters at 90°, and a DSSD placed backwards at 138°. Of the two PARIS clusters, one had $CeBr_3$-NaI(Tl) phoswich detectors, while the other had $LaBr_3$(Ce)-NaI(Tl) ones. Four plastic detectors were placed in front of each

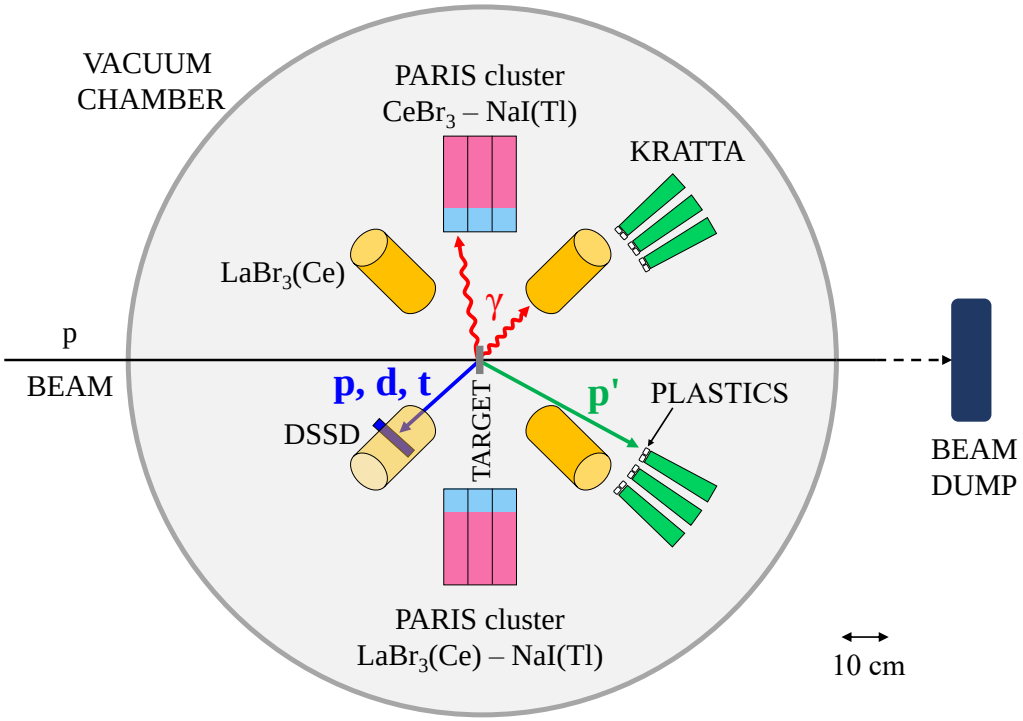

Figure 11.1: In- scale top view of the experimental set-up. The KRATTA telescopes, with in front the plastic scintillators, together with the two PARIS clusters, the four $LaBr_3$(Ce) detectors and the DSSD are shown. Only the pure crystals without hosting and PMTs are displayed. The set-up is sketched as projected on a horizontal plane passing through the target and, for simplicity, all the detectors are depicted as inside the large vacuum chamber. The $LaBr_3$(Ce) scintillators do not lie in this plane, they are placed above the target in dedicated top lid niches, forming an angle of 45° with respect to an axis orthogonal to the plane.

KRATTA module, to obtain trigger and position information.

In the first part of the experiment (*e014*), 24 KRATTA modules were present (for rows of six detectors), while in 2020 (*e016*) an additional row of six capsules was added, for a total of 30 telescopes. The KRATTA modules and the DSSD were inside the large vacuum chamber, which had a diameter of 1.5 m, while PARIS and the $LaBr_3$(Ce) scintillators were inserted in specifically designed niches in the vacuum chamber walls and lid, respectively, that allowed the detectors to be put close to the target without being placed in vacuum. In front of PARIS and the $LaBr_3$(Ce) the stainless-steel chamber wall had a thickness of 2 mm, that will be considered in the efficiencies simulations in the following analysis.

KRATTA was employed for the detection of the inelastically scattered protons of the

beam (p' in Figure 11.1). The scintillators, both the PARIS phoswich and the $LaBr_3(Ce)$ detectors, measured instead the gamma radiation emitted from the excited nuclei in the target, while the DSSD detected the emitted light particles from the decay of the nuclei in the target material (p,d,t). The DSSD will not be considered in the analysis of this specific experiment, as the target thickness prevented the charged particles emitted after the decay of the resonances of interest to escape the material. Therefore the analysis will be devoted to investigate scattered protons-gamma coincidences.

In Table 11.1 the distances of the detectors from the target are summarised and a photo of the inside of the vacuum chamber is reported in Figure 11.2. In the middle of

Table 11.1: Detection systems distances from the target.

System	Distance [mm]
DSSD	235
KRATTA	400
$LaBr_3(Ce)$	273
PARIS	270

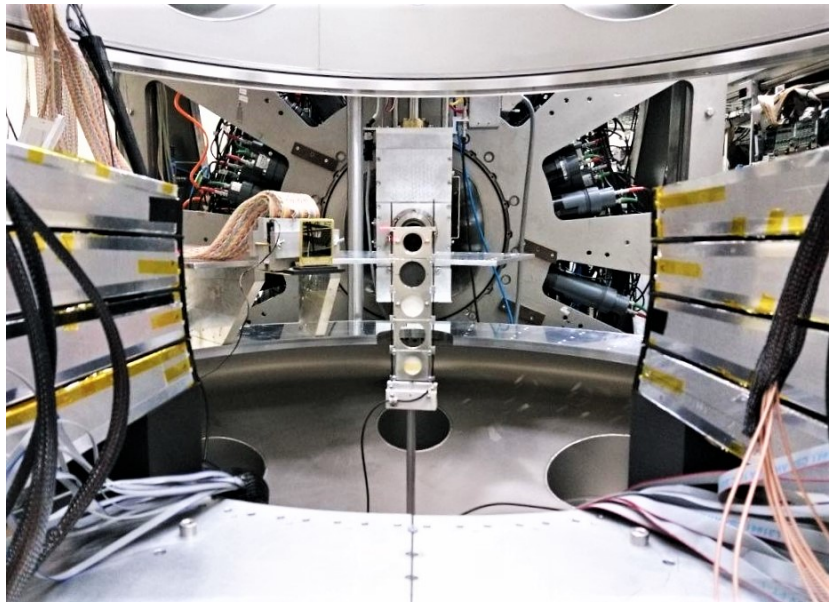

Figure 11.2: Experimental set-up photograph. The inside of the vacuum chamber is shown: in the middle there is the multi-target holder, on the left behind the target the DSSD is visible, while in the foreground on left and right sides there are the KRATTA modules, in the configuration of the *e014* experiment part (4 rows of 6 detectors). In the target holder there are the following materials, starting from the top: ^{13}C, ^{12}C, $Li^{14}NH_2$, empty and quartz (see text for details).

the photograph, a multi-target holder is visible: not only the lithium amide target was present (third position from the top), but also pure ^{13}C and ^{12}C targets (first and second

positions, respectively), and a quartz scintillator (last position). The ^{13}C and ^{12}C targets were used as a reference to test the set-up at the beginning of the measurement and after each interruption. The quartz scintillator was employed, together with a remote camera, during the beam preparation and focussing procedures: when hit by the beam, the quartz emitted light that was registered by the camera, and this information was used to focus and refine the beam position, until the light spot was well in the middle of the scintillation material. The target was then changed, manually moving the holder up or down from below the vacuum chamber.

In Figure 11.3 is shown the position with the corresponding ID numbers of the four $LaBr_3$(Ce) detectors, with respect to the beam direction (black arrow), as seen from the data acquisition software. For *e014* and *e016* w1 and w2 parts the $LaBr_3$(Ce) configuration remained the same (see Figure 11.3(a)), then it changed in *e016* w3 (Figure 11.3(b)), as the cables were exchanged, without physically move the detectors. This information will be exploited during the γ-ray Doppler-shift correction (see Section 12.1.2).

Figure 11.3: $LaBr_3$(Ce) detectors position and ID numbers in the experiment. Panel (a): configuration during *e014* and *e016* w1 and w2 parts. Panel (b): configuration during *e016* w3. The arrow defines the beam direction (see also Figure 11.1).

In the following, we will give some information about the KRATTA array, whose structure is important for the subsequent data analysis. The PARIS array has been already described in details in Section 4.2. Although the DSSD data will not be considered in the analysis, for completeness we will briefly recall the features of the detection system.

11.1 KRATTA

The Kraków Triple Telescope Array (KRATTA) is a detection system designed to measure energy, emission angle, and isotopic composition of light charged reaction products [223]. The array consists of 38 independent modules, which can be arranged according to the experimental need.

Each KRATTA module, schematically shown in Figure 11.4, consists of three identical, 500 µm-thick, large-area (28 mm×28 mm) Hamamatsu PIN silicon photodiodes, and two CsI(Tl) crystals 2.5 and 12.5 cm long, respectively, in a triple telescope configuration. The active area of a single telescope covers about 4.5 msr of the solid angle at the optimal distance of 40 cm from the target, the same considered in the experiment. The first photodiode (PD0) serves as a Si ΔE detector, while the second and the third photodiodes (PD1 and PD2) read the scintillation signal of the thin and thick CsI(Tl) respectively, and provide in addition a direct ionization signal.

As already anticipated, the specific configuration of the experiment comprised 24 (30) modules in 2019 (2020), arranged in two 3×4 (3×5) subgroups placed at each side of the beam line. Table 11.2 reports the angles associated to each KRATTA module, with

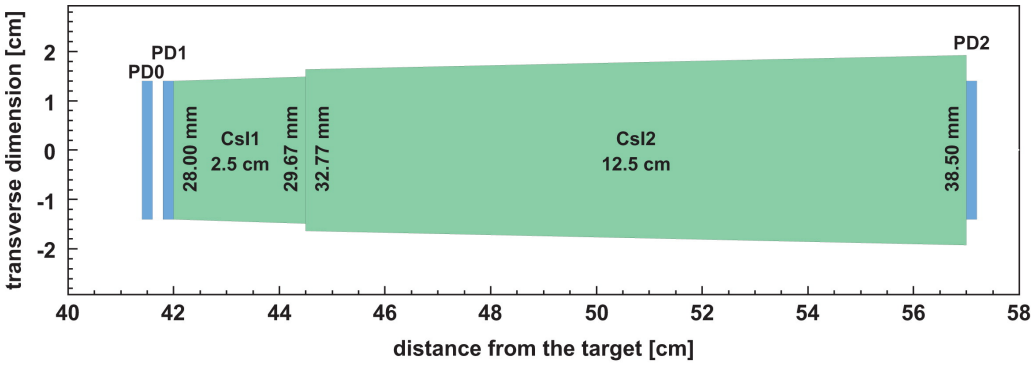

Figure 11.4: Layout of a single KRATTA module. Reprinted from Ref. [223] with permission from Elsevier. During the experiment, an overall energy resolution between 2 and 3 MeV was observed for the KRATTA array (see Section 12.1.1).

respect to the beam axis and measured in the centre of the crystals. The angles of the two subgroups are the same, as they are symmetric, therefore we report here the angles only once. The angle information is crucial for the calibration procedure and also for the γ-ray Doppler correction, that will be discussed in the next chapter.

Table 11.2: Angles in degrees of the KRATTA detectors, with respect to the beam axis, measured in the centre of the crystals. The angles refer to the subset of modules on the left side of Figure 11.2, and "Column 3" refers to the modules closest to the beam. For the other group of detectors, the angles are the same, but specular. In *e014* part, the first row of detectors was missing.

	Column 1	**Column 2**	**Column 3**
Row 1	43.332	37.639	32.041
Row 2	42.336	36.416	30.522
Row 3	42.0	36.0	30.0
Row 4	42.34	36.42	30.528
Row 5	43.339	37.649	32.052

Lastly, in Figure 11.5 we report the scheme of the electronic connections of the KRATTA modules. In the figure, the labels in the top left corner identify the modules ID number, that will be used from now on. The flash Analog to Digital Converter (ADC) channels at which each PD0, PD1 and PD2 were connected are specified below the circles reporting the KRATTA signal cables labelling. In the top right and bottom left corner of each module, the ID numbers of the plastic detectors placed in front of KRATTA are indicated in square brackets, together with the Constant Fraction Discriminator (CFD) module number and channels to which they were connected to get the time and trigger information. The alpha-numeric IDs close to the plastic number IDs refer to the plastics cable labels. The rectangle in the middle identify the power supply number. The detectors are separated in different colour groups, according the the flange through which their cabling passed outside the vacuum chamber.

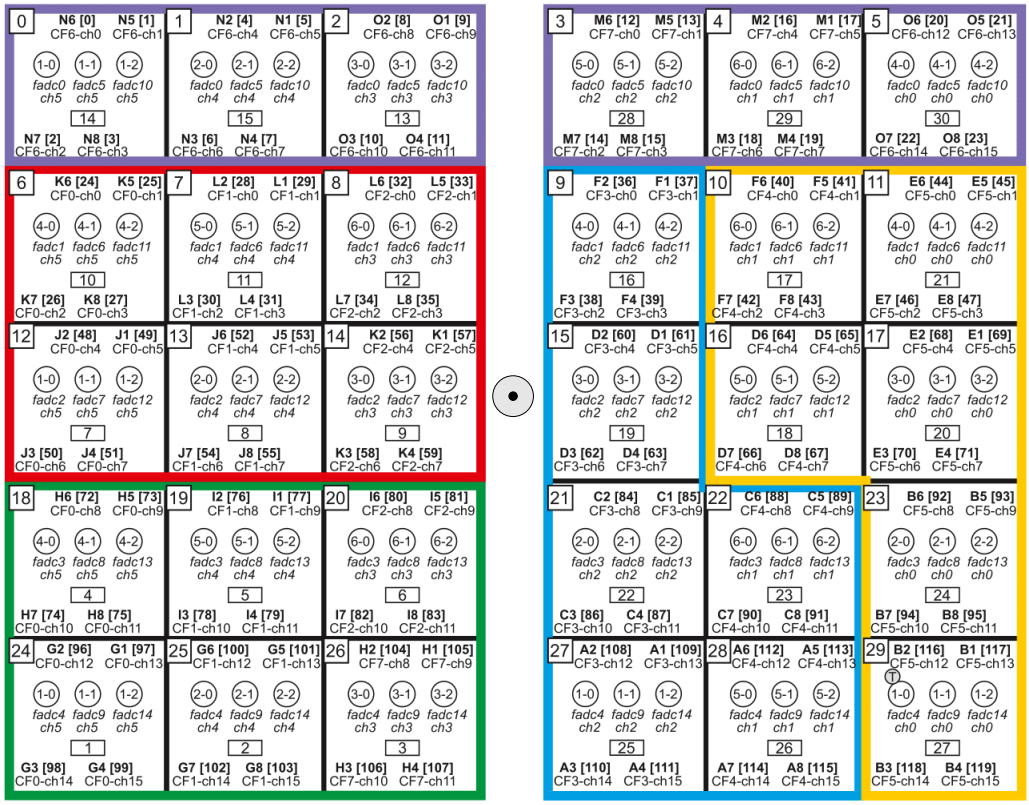

Figure 11.5: KRATTA connections scheme and identification numbers. The beam direction is toward the reader.

11.2 DSSD

The Double-sided Silicon Strip Detector (DSSD) of the present experiment (see a photograph in Figure 11.6) is manufactured by Micron Semiconductor Ltd with a W1 design

[227]. It has a 49.50 mm×49.50 mm active area and a thickness of 1500 µm. The silicon is divided into 16 strips on the junction side and 16 orthogonal strips on the ohmic side, to allow both horizontal and vertical position identification.

Figure 11.6: Photograph of the DSSD mounted in the scattering chamber.

A scheme of the acquisition chain is reported in Figure 11.7. The DSSD signals are firstly preamplified, then they pass through the MegAmp modules, before their amplitude and time information is digitised and finally sent to the a computer disc.

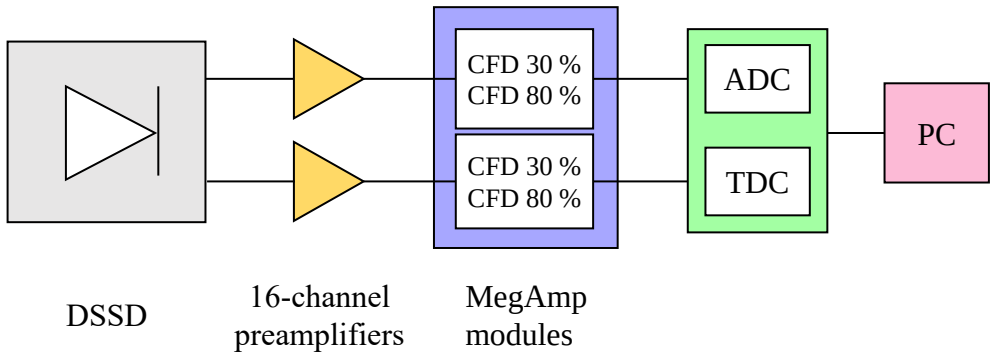

Figure 11.7: DSSD acquisition line.

The MegAmp is a highly-integrated multi-detector pulse shape amplifier. It has been developed in INFN Milano to deal with a variety of input signals. In fact, it is capable to accept standard signals from charge sensitive preamplifiers, or fast signals as in the case of scintillation detectors read by PMT [228]. When many channels are acquired, as in the case of DSSD detectors, the MegAmp sequentially readout system grants a reduction in the complexity and cost of the acquisition system.

Each MegAmp consists of a single NIM module with 16 amplifier channels. The energy section consists in a spectroscopy amplifier, while the timing section allows to have both timing and pulse-shape information. In particular, two Constant Fraction Discriminators (CFD) identify the 30 % and 80 % points of the signal leading edge. A Time to Amplitude Converter (TAC) circuit, which takes the start and stop signals from the CFD, measures the rise time of the input signal.

In the case of the DSSD employed in the present experiment, the rise time information, combined with the energy, allows to discriminate between light charged particles and therefore identify the reaction channel.

Chapter 12

Data analysis

In the present Chapter we will deal with the complete data analysis of the proton inelastic scattering experiment (both *e014* and *e016* parts), realised at CCB, to investigate ^{14}N and ^{16}O M4 resonances decay, from the data preprocessing, to the extraction and interpretation of the results. Firstly, we will address the data preprocessing, including detectors calibrations, time alignment procedures, definition of time gates, Doppler-shift correction of the γ-ray energy spectra and production of excitation energy vs. gamma-ray energy matrices for the two nuclei of interest, namely ^{14}N and ^{16}O. Secondly, we will identify the daughter nuclei produced after the decay of the nuclei excited in the scattering reaction. Finally, we will discuss the analysis of the excitation energy vs. gamma-ray energy matrices, in order to obtain the decay pattern of the M4 resonances of interest and the relative branching ratios.

Table 12.1: Experimental run numbers (start and stop) with corresponding proton beam energy (E_p) or calibration source. The trigger is defined in the last column. The possible triggers are PLA, KRA, PAR or SIL, meaning plastic (in front of KRATTA), KRATTA, PARIS or DSSD, respectively. The $\vee$ symbol indicates that the data are acquired without any coincidence condition. Coincidences are indicated with the $\wedge$ symbol.

Exp.	Start #	Stop #	E_p [MeV]	Trigger
e014	8083	8184	155	PLA $\vee$ KRA
	8185	8259	115	PLA $\vee$ KRA
	8373	8465	135	(PAR $\wedge$ PLA)
	8477	8480	135	(PAR $\wedge$ PLA) $\vee$ SIL
	8485	8502	135	(PAR $\wedge$ PLA) $\vee$ SIL
	8510	8610	135	(PAR $\wedge$ PLA) $\vee$ SIL
	8641	8754	135	(PAR $\wedge$ PLA) $\vee$ SIL
	8755	8831	135	(PAR $\wedge$ PLA) $\vee$ SIL
	8833	8934	135	(PAR $\wedge$ PLA) $\vee$ SIL
	8935	9109	135	(PAR $\wedge$ PLA) $\vee$ SIL
	9115	9142	110	PLA $\vee$ KRA
	9143	9172	130	PLA $\vee$ KRA

Continues on next page

Table 12.1 continued from previous page

Exp.	Start #	Stop #	E_p [MeV]	Trigger
	9173	9201	145	PLA ∨ KRA
	9225	9246	135	PLA ∨ KRA
	9247	9257	120	PLA ∨ KRA
	9285	9299	^{60}Co	PAR
e016	3608	3609	^{60}Co	PAR
w1	3727	3745	135	PLA
	3746	3863	135	(PAR ∧ SIL) ∨ (PLA ∧ SIL) ∨ (PAR ∧ PLA)
	3866	3902	155	PLA
	3903	3937	145	PLA
	3938	3995	125	PLA
	3996	4009	115	PLA
	4010	4457	135	(PAR ∧ SIL) ∨ (PLA ∧ SIL) ∨ (PAR ∧ PLA)
e016	4482	4496	135	PLA
w2	4498	4509	135	(PAR ∧ SIL) ∨ (PLA ∧ SIL)∨(PAR ∧ PLA)
	4517	4582	135	(PAR ∧ SIL) ∨ (PLA ∧ SIL) ∨ (PAR ∧ PLA)
	4584	4749	135	(PAR ∧ SIL) ∨ (PLA ∧ SIL) ∨ (PAR ∧ PLA)
	4750	4783	155	PLA
	4784	4801	115	PLA
	4802	4812	135	PLA
	4813	4871	135	(PAR ∧ SIL) ∨ (PLA ∧ SIL) ∨ (PAR ∧ PLA)
	4872	4877	135	PLA (test runs)
	4878	4933	135	(PAR ∧ SIL) ∨ (PLA ∧ SIL) ∨ (PAR ∧ PLA)
	4934	4945	135	PLA
e016	4946	4959	135	PLA
w3	4960	5218	135	(PAR ∧ PLA)
	5222	5262	155	KRA
	5263	5298	145	KRA
	5299	5328	125	KRA
	5329	5356	115	KRA

Before discussing the analysis, we report in Table 12.1 the information regarding the trigger used during the experiment, the relative numbers of the data subsets (runs) in which the experiments have been divided for acquisition purposes, and the proton beam energy (in MeV) considered. In particular, it is important to distinguish between the runs acquired without imposing any coincidence between the different arrays (referred as "singles" in the following), and the ones in which a coincidence condition has been introduced. In fact, the former are considered mainly for calibration purposes and should be treated in a different way. Runs with a radioactive source, for the gamma-ray detectors calibration and efficiency measurement, are also listed. The runs are subdivided between the *e014* and *e016* parts. The latter is additionally divided into three subsets (w1, w2 and

w3), as the data were acquired on three different long weekends in February and March 2020. For each weekend the calibrations had to be repeated, as time conditions, detectors gain and cabling could potentially change.

12.1 Detectors calibrations and data processing

In this Section we will describe the procedures used to calibrate the telescopes of the KRATTA arrays, the $LaBr_3$(Ce) scintillators and the phoswich of the PARIS clusters. We will also describe in details the preparatory steps necessary to sort the data.

12.1.1 KRATTA modules

The calibration of the KRATTA modules described in the following aims at producing calibrated reconstructed excitation energy spectra of the nuclei of interest, through a 4-step procedure:

1. definition of time gates on PD1 and PD2 signals;
2. definition of proton cuts on the PD1 vs. PD2 energy matrix;
3. pre-sorting of non-calibrated KRATTA proton energy spectra, with fitting of the elastic-scattering proton peaks;
4. extraction of calibration parameters and excitation energy reconstruction on the basis of the reaction kinematics.

In the first step, in order to select only the events associated to the reaction, gates on KRATTA PD1 and PD2 time signals had to be introduced. These time gates are different for each module, for each part of the experiment (*e014*, *e016* w1, w2 and w3), and they depend on the trigger (singles and coincidences, see Table 12.1). Figures 12.1(a) and 12.1(b) display for example the PD1 and PD2 time signals, respectively, as a function of the KRATTA module number, for two singles runs of the *e016* w2 experiment part. The corresponding projections of PD1 and PD2 time signals associated to the KRATTA module #26 are shown for example in Figures 12.1(c) and 12.1(d), respectively. As can be seen in panels (a) and (b) of Figure 12.1, some modules had missing time signals, while others presented bad signal patterns (noisy channels, multiple or anomalously large peaks). These detectors had to be excluded from the subsequent analysis. For the detectors with both PD1 and PD2 good time signals (see for example panels (c) and (d) of Figure 12.1) software gates were introduced to exclude events outside the most intense peak, associated to the scattered protons on the target material.

The second step of the data preparation involved the definition of graphical cuts in the PD1 vs. PD2 non-calibrated energy matrices, to restrict the KRATTA data to the events associated to protons. This can be done as the ΔE-E telescopic configuration of the KRATTA modules permits to distinguish between the different incident charged particles. A simple ΔE-E technique is applicable as the charged particles pass through the first CsI scintillator and stop inside the second one (see Figure 11.4 for the telescope structure). The energy loss fraction in the two detectors is different for particles with

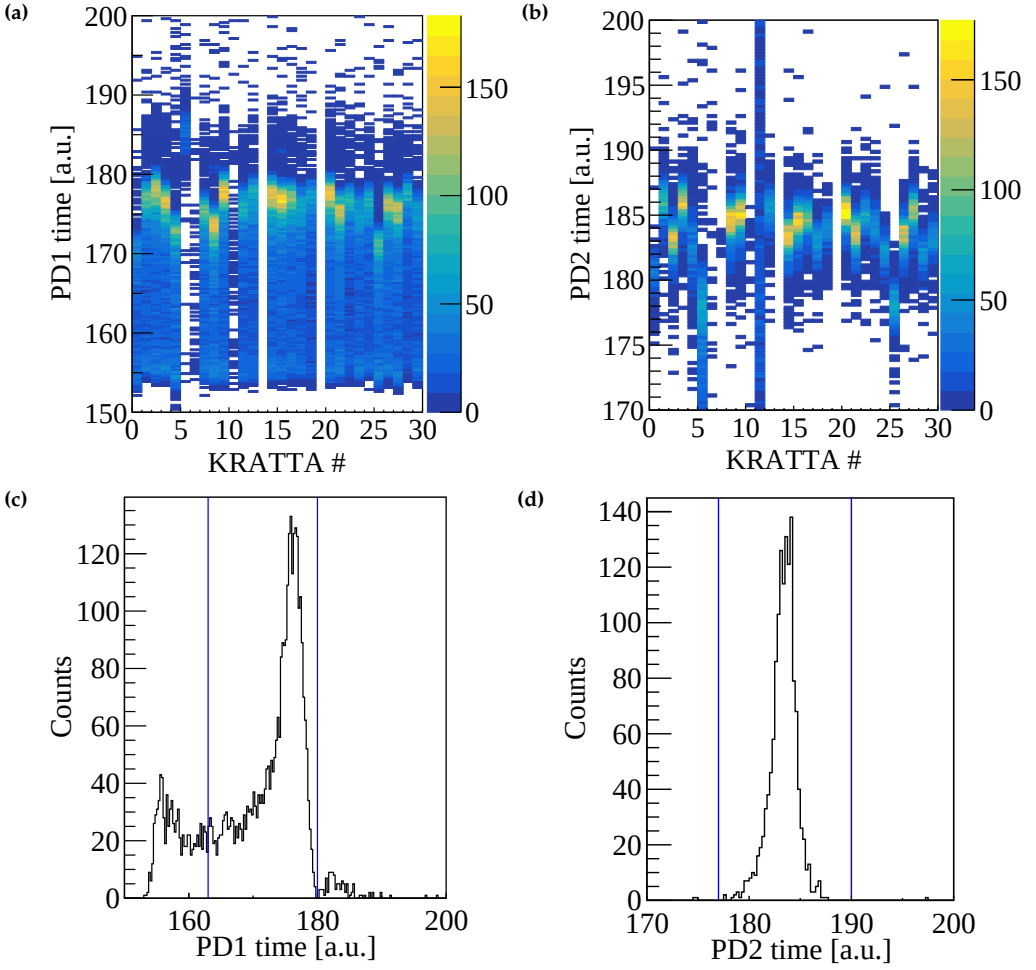

Figure 12.1: Panels (a) and (b): PD1 and PD2 singles time signals of the *e016* w2 experiment part, as a function of the KRATTA modules number, for runs no. 4944-4945. Panels (c) and (d): example of projections of panels (a) and (b), associated to the KRATTA #26 module. The time gates are displayed by blue vertical lines. The time gates are set for each module individually.

distinct atomic number Z, due to their different stopping powers. Figure 12.2 shows, as an example, the proton cut of the KRATTA module #22. The proton cuts are performed only once for each telescope, considering the singles runs at the highest beam energy (E_{beam} = 155 MeV): when a beam energy lower than 155 MeV is considered, the proton points still lie inside the cut, at lower channels (*i.e.*, at lower energies). Each module requires a different cut, and two separate sets of cuts are introduced for the *e014* and *e016* parts. In the *e016* part, the cuts are the same for the three w1, w2 and w3 subsets of data. Singles and coincidence data does not require separate proton cuts.

As a third step, after the definition of time gates and particle cuts, in order to perform the KRATTA calibrations, a preliminary sorting of the singles data had to be performed.

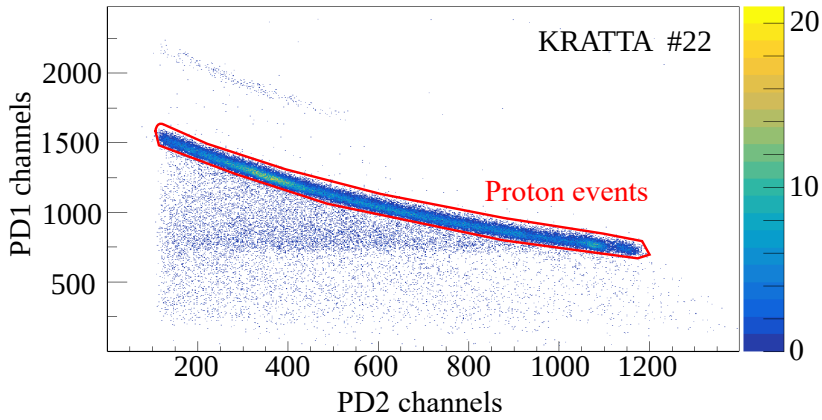

Figure 12.2: PD1 vs. PD2 non-calibrated energy matrix (in channels) for the KRATTA module number 22, obtained with a proton beam energy of 155 MeV. The red line defines the graphical cut selecting the set of points associated to proton events. Partial statistics.

The procedure is repeated for each set of runs with a different proton beam energy (*e.g.*, E_{beam} = 115, 135 and 155 MeV in *e016* w2). In this preliminary sorting, time- and particle-gated PD2 non-calibrated proton energy spectra were produced with the additional conditions of plastic multiplicity equal to 1 (we are interested in single scattered-proton events) and plastic vs. KRATTA correlation. The plastic-KRATTA correlation condition assures that each plastic that fired is associated to the correct KRATTA module in front of which it is placed. These specific conditions could not be applied to the last singles runs (runs 5222-5336) of the experiment sorting, as the plastic signals were not available due to a hardware malfunctioning. The calibrations of *e016* w3 KRATTA data were still possible even without these conditions: larger time gates had to be introduced as the precise plastics time reference was not available.

Figure 12.3 displays three examples of time- and particle-gated PD2 non-calibrated proton energy spectra obtained with three beam energies (*i.e.*, 115 (black), 135 (blue) and 155 MeV (red)) during *e014*, with the KRATTA telescope #22. In the 155-MeV spectrum, the peaks associated to the elastic scattering of protons on the target constituents are clearly visible. Starting from the left, the first peak is associated to the scattering on the hydrogen component, the second on the lithium one and the third onto ^{16}O. In the spectra obtained at lower beam energies, only the peaks associated to Li and ^{16}O can be seen, as the protons elastically scattered on H had energies lower than the detectors' threshold. As it will be discussed more in details later on, in connection to the identification of the daughter nuclei, a consistent oxygen contamination was observed. This contamination had to be taken into account in the calibration process, as the rightmost peak of the elastically scattered protons did not arise from the scattering on ^{14}N, which is present in smaller amounts in the target. In the spectra of Figure 12.3, in the same region of the elastically scattered protons on Li, there are also unresolved peaks associated to the population of ^{16}O excited bound states. In addition, in the 135-MeV spectrum reported in Figure 12.3 (blue line), the peak associated to the population of the M4 resonances

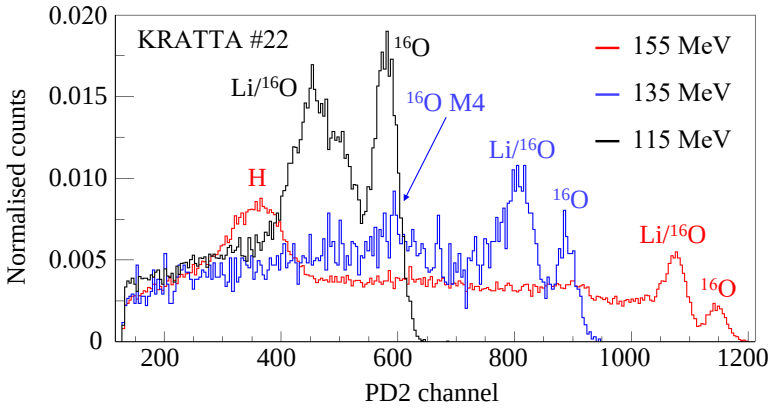

Figure 12.3: Normalised PD2 time- and particle-gated non-calibrated energy spectra (in channels) for the KRATTA module number 22, obtained with the plastic multiplicity equal to 1 and the plastic-KRATTA correlation additional conditions. Spectra corresponding to E_{beam} = 155 (red), 135 (blue) and 115 MeV (black) are shown. The most intense peaks are associated to the proton elastic scattering on the oxygen (rightmost), lithium (middle) and hydrogen (leftmost) components of the target. In correspondence to the elastic scattering on the Li component, there are also additional unresolved peaks associated to the excitation of ^{16}O to its excited bound states. The elastic scattering on ^{14}N is covered by the oxygen contamination. Around PD2 channel 600, an enhanced peak associated to the population of the M4 resonances in ^{16}O is visible in the 135-MeV spectrum: this proton beam energy (135 MeV), which best populates the resonances of interest, was chosen at the end of the preliminary excitation function.

of interest in ^{16}O can be observed around PD2 channel 600. The enhanced population of the states of interest was assessed during a preliminary excitation function, after which a proton beam energy of 135 MeV was chosen for the experiment. To obtain the energy calibration of the KRATTA modules, the rightmost peak associated to the elastic scattering of protons on ^{16}O in the presorted spectra was fitted with a Gaussian function to extract its centroid in channels. The fitting procedure was then repeated for each beam energy and detector.

In the last step, for every fixed beam energy, we calculated the energy of the protons elastically scattered on ^{16}O at the angles associated to the KRATTA telescopes (see Table 11.2), using the LISE code ($E_p^{LISE}(^{16}O)$) [144]. These energies were employed to extract the calibration coefficients for each module, via a quadratic regression, as shown for example in Figure 12.4 for the KRATTA #22 in the *e014* part. The coefficients of the quadratic interpolating curve ($y = A + Bx + Cx^2$) can be used to calibrate the KRATTA detectors, converting the measured channels into the energy of the protons measured in KRATTA:

$$E_p^{KRATTA} = A + B\,ch + C\,ch^2 \tag{12.1}$$

Since we are interested in the excitation energy of ^{14}N and ^{16}O, the proton energy spectrum has to be converted into the excitation energy, via Equation (12.2).

$$E_{beam} = E_p^{KRATTA} + E_{Y_X}^{kin} + E_{Y_X}^{*} \tag{12.2}$$

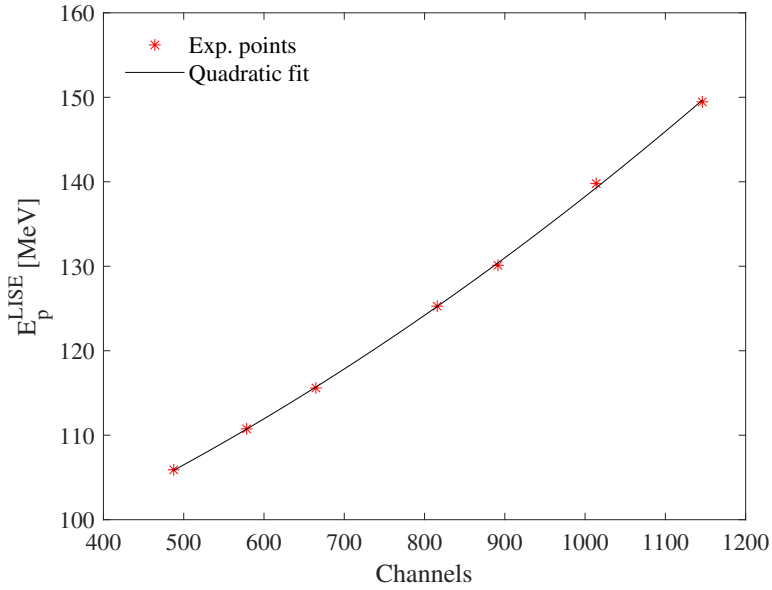

Figure 12.4: Example of quadratic regression for the calibration of KRATTA #22 in the *e014* experiment part.

Here $E^{kin}_{^{Y}X}$ is the kinetic energy of the nucleus of interest (^{Y}X refers either to ^{14}N or ^{16}O), while $E^{*}_{^{Y}X}$ is its excitation energy. $E^{kin}_{^{Y}X}$ can be expressed also as the difference between the beam energy and the kinetic energy of the scattered protons on the specific nucleus of interest (calculated with LISE):

$$E^{kin}_{^{Y}X} = E_{beam} - E_p^{LISE}(^{Y}X) \tag{12.3}$$

Substituting Equations (12.1) and (12.3) into Equation (12.2) and rearranging the terms, one can express the ^{14}N or ^{16}O excitation energy as:

$$E^{*}_{^{Y}X} = A^{*} + B^{*}\,ch + C^{*}\,ch^2 \tag{12.4}$$

where $A^{*} = E_p^{LISE}(^{Y}X) - A$, $B^{*} = -B$ and $C^{*} = -C$. Therefore, the excitation energy can be directly expressed in terms of the KRATTA channels and the conversion parameters to be applied during the sorting are deduced from the calibration coefficients previously calculated. In the present experiment, two sets of conversion parameters have been extracted for a fixed beam energy of 135 MeV (the energy considered during the coincidence runs, see Figure 12.3), one for the reconstruction of ^{14}N excitation energy and the other for ^{16}O: the calibration parameter remained fixed while the E_p^{LISE} is different for the two nuclei. The coincidence data were then sorted twice with these two sets of parameters. As an example, Figure 12.5 reports the calibrated excitation energy spectrum (in singles, runs 4802-4812 and 4934-4945) of ^{16}O, obtained with a beam energy of 135 MeV, summing all the detectors. An overall energy resolution between 2 and 3 MeV was achieved. The peak associated to the population of the three unresolved (due to the limited resolution) M4 stretched resonances of interest is visible around 19 MeV. A spectrum with the same

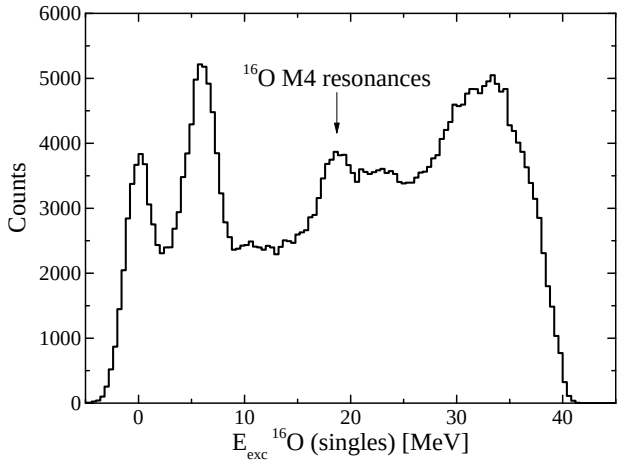

Figure 12.5: *e016* w2 singles ^{16}O calibrated excitation energy spectrum. In the energy region around 19 MeV is visible the peak associated to the population of the M4 resonances of interest for this work (17.79, 18.98, and 19.80 MeV). An identical spectrum, shifted toward lower excitation energies by 500 keV, is obtained in the case of the ^{14}N reconstruction.

shape, but shifted by 500 keV toward lower excitation energies, is obtained in the case of the ^{14}N reconstruction.

Drift correction in *e016* w3

The KRATTA telescopes remained stable throughout all the experiment, except during the *e016* w3 part. During this weekend the detectors' energy was observed to drift smoothly as a function of time. To correct the drift, we firstly extracted a preliminary calibration using the singles runs at the end of the weekend acquired with beam energies of 115, 125, 145 and 155 MeV. We then sorted the singles runs at the beginning of the weekend, acquired with a beam energy of 135 MeV, with the extracted coefficients. We then calculated the offset associated to the drift between the beginning and the end of the weekend, using as a reference point the peak associated to the population of the second excited state of ^{16}O at 6.130 MeV [53]. We then recalculated the conversion coefficients of Equation (12.2) introducing a linear drift over 20 intermediate steps. The coincidence runs (4960-5218) of the weekend were then divided into 21 subsets, 20 sets of 12 runs each and a last set of 19 runs (from 5200 to 5218). To the first 20 subsets we applied the recalculated conversion coefficients obtained introducing the linear rigid drift, while to the last subset we applied the first calibration obtained with the singles runs at the end of the experiment without any drift. After the sorting, we checked if this correction was sufficient to recover a good alignment of the spectra. The results of the test are shown in Figure 12.6. The measured energy of the 6.130 MeV peak is shown as a function of the runs subset number, for each KRATTA detector. The empty plots are bad detectors excluded on the basis of missing or anomalous PD1 or PD2 time signals, as mentioned before. The majority of the detectors (shown in blue) recovered a good alignment after

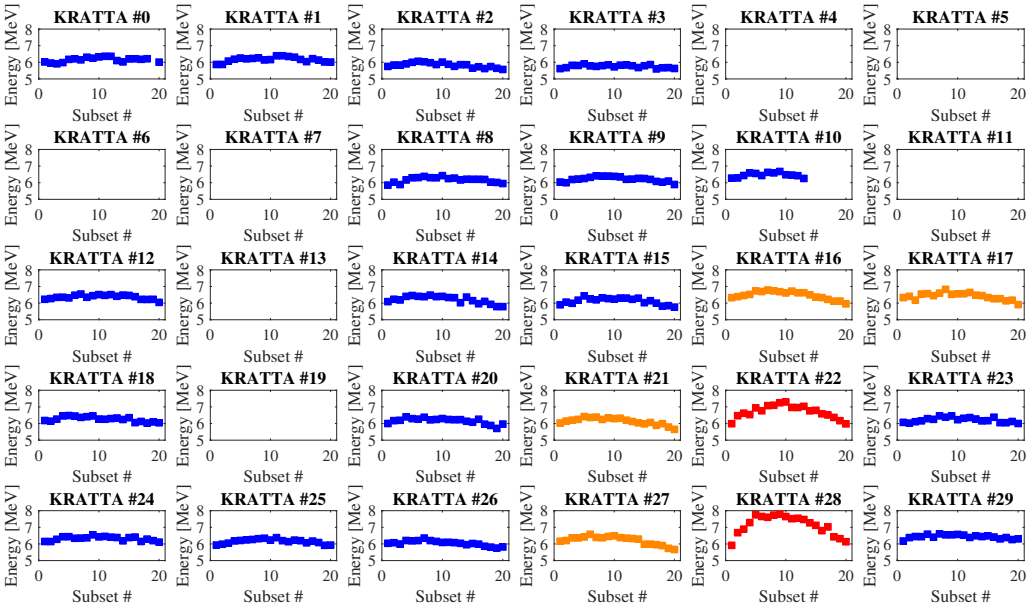

Figure 12.6: Measured energy of the second excited state of ^{16}O at 6.130 MeV as a function of the subset number, after the linear drift correction, for each KRATTA telescope. In blue are shown the detectors with dispersions $\lesssim$ 500 keV, in orange detectors with dispersions ~800 keV and in red the two detectors excluded from the analysis due to their dispersions > 1.3 MeV. These last two detectors could not be recovered, as they would have required a more complex treatment of the drifts.

the application of the correction, even if a small drift was still visible, with dispersions $\lesssim$ 500 keV. For some detectors (shown with orange dots), the dispersions were of the order of 800 keV, but still smaller than the nominal KRATTA energy resolution of ~ 2 MeV. KRATTA #22 and #28 (red plots), instead had dispersions > 1.3 MeV, comparable to the energy resolution of the detectors. Only these two detectors were therefore excluded from the analysis.

12.1.2 $LaBr_3$(Ce) scintillators

The four $LaBr_3$(Ce) scintillators present in the set-up for the detection of gamma rays were calibrated using three gamma transitions visible in the in-beam coincidence runs, namely the 511-keV line, the ^{27}Al 843.76-keV $1/2^+_1 \rightarrow$ g.s. transition, and the ^{12}C 4438.94-keV $2^+_1 \rightarrow$ g.s. transition. ^{27}Al was present in the surrounding materials (*e.g.*, in the target holder), while ^{12}C was a by-product of the reaction, populated after the decay of both ^{14}N and ^{16}O, via the emission of a deuteron and an alpha particle, respectively. Non-calibrated gamma-ray energy spectra were pre-sorted imposing no time gate (^{27}Al peaks are better seen in the background events), and the peaks of interest were fitted with a Gaussian function and a linear background. The calibration parameters were then extracted via a quadratic regression and the procedure was repeated for each experiment

part listed in Table 12.1.

Time alignment

Before proceeding with the sorting, time gates had to be introduced to exclude spurious events induced by the beam on the surrounding materials. To do so, $LaBr_3$ time vs. plastic ID matrices were sorted and analysed with an automatic script. For each LaBr-plastic pair, the script fitted the most intense peak (see Figure 12.7) with a Gaussian and returned its centroid. The information on the centroid was then introduced as an offset to align the intense time peaks around a common value (*i.e.*, zero) and set a unique tight time gate. Figure 12.7 reports as an example the time vs. plastic ID matrix for the

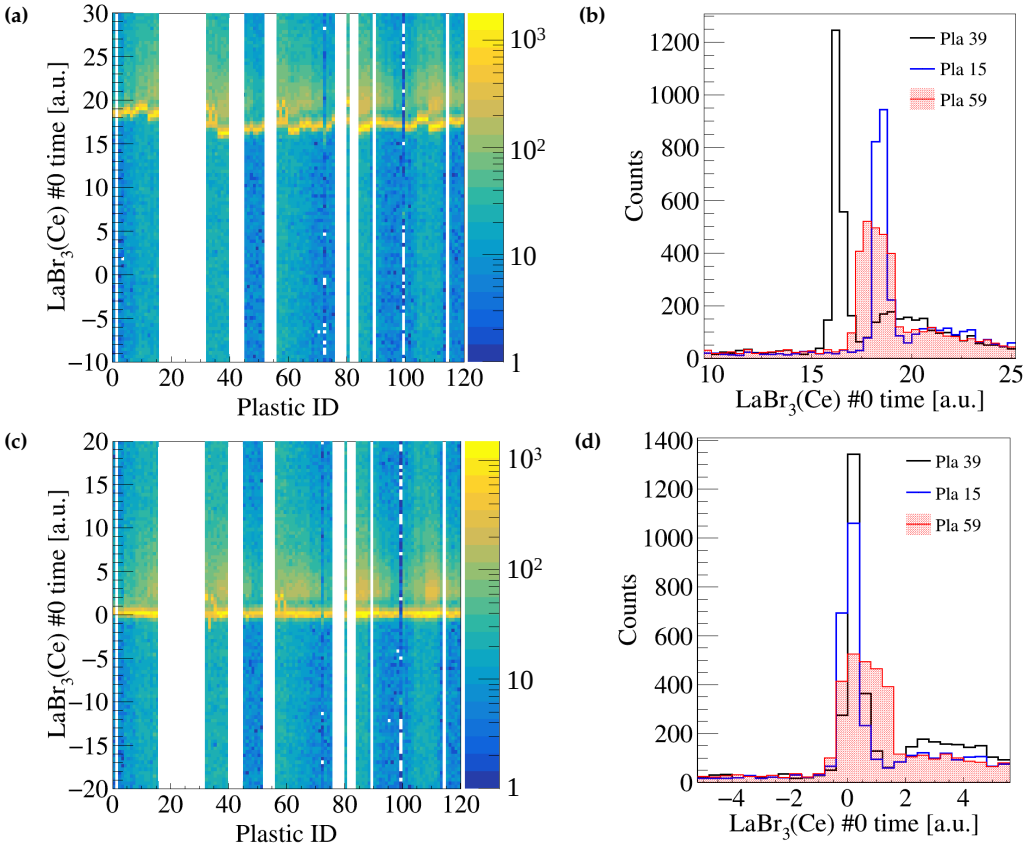

Figure 12.7: $LaBr_3$(Ce) #0 time vs. plastic ID 2D histogram for the *e016* w1 part, before (a) and after (c) the time alignment correction. The gaps are either due to not working plastics or excluded KRATTA telescopes for their anomalous time response. Projections on the time axis for three individual plastic IDs (#15, 39 and 59) are shown before (b) and after (d) the alignment. The plastic #59 displays a poorer time resolution with respect to the other two plastics. See text for details.

$LaBr_3$(Ce) scintillator with ID number 0 (the detectors ID goes from 0 to 3) before and after the time alignment correction, obtained summing all the coincidence runs of the *e016* w1 experiment part. The matrix was produced with the additional conditions of

plastic multiplicity equal to 1, plastic-KRATTA correspondence and by gating on protons in the KRATTA detectors, to reduce the background and obtain sharper peaks, easier to align. The empty bins are associated to missing plastics (not working for hardware malfunctions) or to groups of four plastics associated to the KRATTA modules excluded from the analysis (see Section 12.1.1). The procedure was repeated for every $LaBr_3$(Ce) detector and for the *e014* and *e016* experiment parts. For the *e016* part, the procedure had to be applied only once for all the three w1, w2 and w3 sub-parts.

After the $LaBr_3$-plastic time alignment, we still observed a few pairs with a different behaviour. In the majority of $LaBr_3$-plastic pairs we observed a very intense main peak (see Figures 12.7(b) and 12.7(d)) associated to the events of interest and a less intense secondary peak associated to spurious events. However, for some plastic IDs (ID # 33, 35, 57, 59) only one large peak was present. Their behaviour results most probably from the improper working of one CFD module (CFD2) which served for them all, as can be seen in the connection scheme reported in Figure 11.5. These plastics had to be excluded from the analysis, since there was no possibility to gate on the correct events.

Doppler-shift correction

After the energy calibration, the time alignment and gating procedures, a standard Doppler-shift correction could be applied to the the $LaBr_3$(Ce) gamma-ray energy spectra. The Doppler-corrected gamma-ray energy E_γ^0 was calculated reversing Equation (2.4). Firstly, the kinetic energy of the emitting nucleus is calculated on the basis of kinematics considerations, being known the beam energy, the excitation energy at which the nucleus is populated and the energy of the scattered protons (see Equation (12.2)). With this information, the relativistic β parameter is extracted. Then, the recoil direction of the nucleus is calculated considering inelastic-scattering reaction kinematics and the angles associated to the scattered protons, measured as the angles of the plastic detectors in front of KRATTA modules. The relative angle (θ_{rel}) between the momentum vectors of the recoiling nucleus and the emitted gamma ray is finally calculated assuming that the gamma ray interaction point coincides with the centre of the $LaBr_3$(Ce) front face. Two separate Doppler-shift corrections have been produced for the population of ^{14}N and ^{16}O.

Figure 12.8 shows the comparison between the Doppler-shift corrected (in red) and the non Doppler-corrected (in blue) gamma-ray energy spectra obtained summing the full experiment statistics (coincidence runs) of the four scintillators. The Doppler-shift correction shown in this case was calculated considering the excitation of ^{16}O. An improvement in the peak FWHM of the order of $\sim 20\,\%$ is observed in the case of the 4439-keV gamma transition de-exciting the 2_1^+ state in ^{12}C (populated by alpha emission from ^{16}O), which has a lifetime $\tau = 88$ fs [53]. A similar improvement is seen also for the 7115-keV in ^{16}O, which depopulates a state with $\tau = 12$ fs [53]. A significant worsening in the energy resolution is observed instead in the case of gamma transitions depopulating long-lived states (*e.g.*, the 6129-keV line in ^{16}O, $\tau = 26.5$ ps [53]), as the emitting nucleus was already stopped in the target at the emission moment. The $LaBr_3$(Ce) energy resolution is of the order of FWHM ~ 95 keV at 6.1 MeV: for the measurement, the ^{16}O

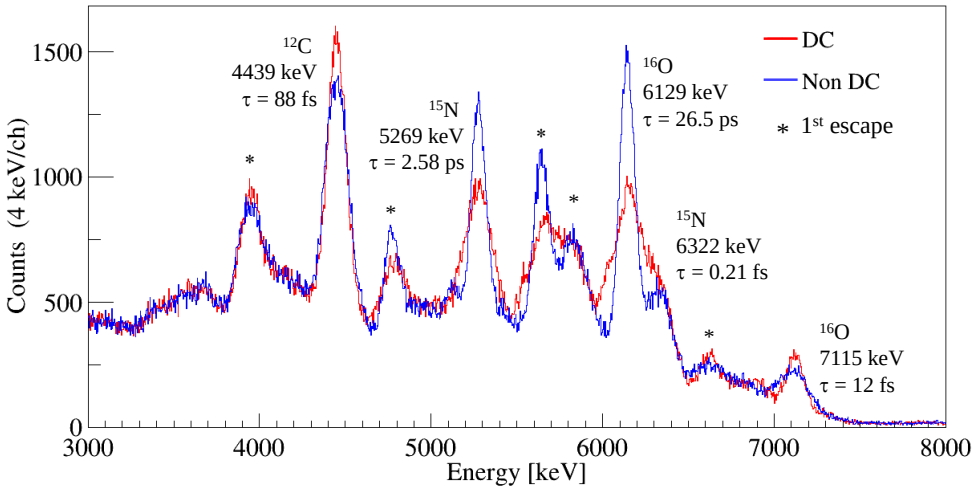

Figure 12.8: Non Doppler-shift corrected (blue) and Doppler-shift corrected assuming ^{16}O excitation (red) $LaBr_3(Ce)$ gamma-ray energy spectrum between 3 and 8 MeV. The peaks are labelled with the emitting nucleus, the tabulated energy in keV and the lifetime τ of the de-exciting state [53]. First-escape peaks are marked with star symbols. The Doppler-shift correction introduces an improvement in the energy resolution only for those gamma rays de-exciting short-lived ($\tau \sim$ 1-100 fs) states.

6129-keV transition in the non-Doppler-shift corrected spectrum of Figure 12.8 has been considered. In the following analysis we will consider both Doppler-shift-corrected and non-Doppler-shift-corrected gamma-ray energy spectra, depending on the gamma transition we are interested in. In addition, the comparison between the two spectra will be useful to identify transitions de-exciting either short- or long-lived states, which would appear unresolved otherwise.

Efficiency

In the following analysis, we will consider the experimental $LaBr_3(Ce)$ gamma-ray photopeak absolute efficiency as measured in the pilot experiment on ^{13}C, which had the same geometrical configuration of scintillators (see Section 10.2). In the pilot experiment the photopeak efficiency was measured exploiting a ^{60}Co radioactive source. The 1173-keV, 1333-keV peaks and the sum peak areas were measured and combined with the detectors' solid angle, the source activity at the acquisition time, the calibration time duration and the dead time to extract the photopeak efficiency at the corresponding energies. A simulation of the detectors response was then used to obtain the efficiency over the entire energy range of interest for the experiment ($\sim$ 100 keV-20 MeV).

12.1.3 PARIS phoswich

The calibration of the PARIS phoswich detectors requires a more complex procedure than standard scintillators. As mentioned in Section 4.2, the $LaBr_3(Ce)/CeBr_3$ and NaI

components are viewed by the same PMT and the associated gamma-ray events discriminated on the basis of their time response. In the experiment, V1730B digitizers [229] with a Pulse Shape Discrimination (DPP-PSD) firmware [230] were employed. The firmware allows to integrate the signal over two time ranges: we define *Q short* to be the integrated signal over a 200 ns time window, while *Q long* employs a 900-ns time window for the signal integration. Plotting the phoswich raw energy obtained with the short vs. long integration-time window one can discriminate between the two scintillation components. As an example, Figure 12.9(a) displays this kind of plot for the PARIS phoswich #10 (PARIS detectors IDs go from 0 to 17), summing over all the in-beam coincidence runs of the *e014* experiment part. Since $LaBr_3(Ce)/CeBr_3$ and NaI decay time are of the order of $\sim$10 ns and $\sim$250 ns, respectively, their raw energy will appear accumulating along separate straight lines with different slope. Between the two lines there will be the data associated to gamma rays detected in both the scintillators (*e.g.*, Compton-scattering events).

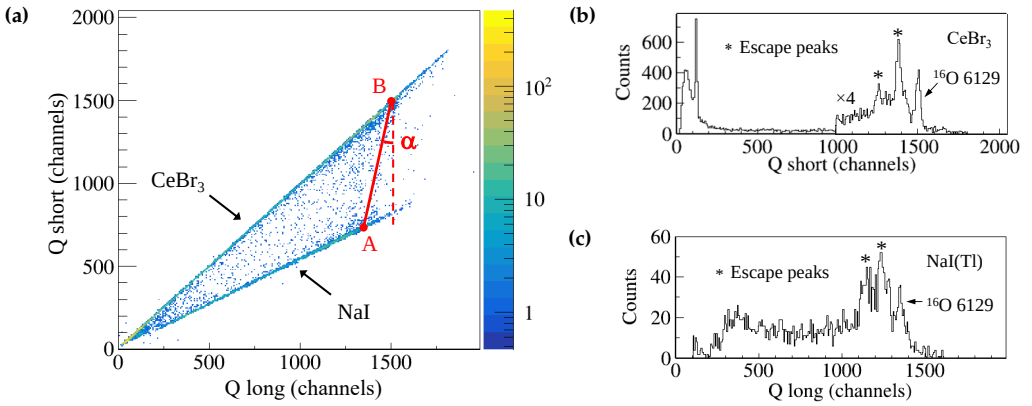

Figure 12.9: PARIS in-beam *Q short* vs. *Q long* plot for phoswich #10 (a): the $CeBr_3$ and NaI components are visible in the 2D plot. The $CeBr_3$ and NaI mono-dimensional spectra, obtained projecting on the y for the $CeBr_3$ component and on the x axis for the NaI one, after selecting the corresponding events with a graphical cut (excluding common events), are displayed in panels (b) and (c), respectively. In panel (a), in red is displayed the line that connects the ^{16}O 6129-keV gamma transition position in the two scintillators (rightmost peak in mono-dimensional spectra): the gamma events associated to both the detectors are distributed along this direction. The angle α between this segment and the red dashed vertical axis is calculated as $\alpha = \arctan\left[(x_B - x_A)/(y_B - y_A)\right]$, and it is used to apply the rotation needed to perform NaI energy calibration (see text for details). In the present case $\alpha = 10.2°$

For the calibration of the $LaBr_3(Ce)/CeBr_3$ and NaI energy signals, two different procedures are followed. $LaBr_3(Ce)/CeBr_3$ can be directly calibrated after setting a gate on its component in the *Q short* vs. *Q long* plot and projecting on the *Q short* axis (y axis), as displayed for example in Figure 12.9(b) in the case of PARIS phoswich #10. The NaI part, instead, is calibrated together with the data common to both the detectors. A simple projection on one of the axis of the NaI and common part is not straightforwardly possible, as the common events are distributed along a direction that is not perpendicular

to the axes, as highlighted by the red segment in Figure 12.9(a). As a consequence, the plot have to be rotated by an angle α defined as the angle between the segment along which the common events distribute and the vertical axis. After the rotation, the NaI and common part events can be projected on the *Q long* axis (x axis) and proceed with the regular calibration.

NaI rotation

The extraction of the α rotation angle was performed considering in-beam data. The procedure has been described in Ref. [231]. The best result would be obtained considering high-statistics radioactive source data, but the only ^{60}Co runs available in *e014* and *e016* w1 (see Table 12.1) did not have enough statistics for this procedure. In addition, the rotation angle appeared not to be constant throughout the experiment: in *e016* w3 (for which no calibration source runs have been acquired) α had to be recalculated.

The extraction of the rotation angle required first of all the introduction of two distinct graphical cuts on the $LaBr_3$(Ce)/$CeBr_3$ and NaI parts in the *Q short* vs. *Q long* plot, excluding the common events (see Figure 12.9(a)). The two regions were then projected on x and y axes, as shown for example in Figures 12.9(b) and 12.9(c). In the projections, three peaks are clearly visible in both the $LaBr_3$(Ce)/$CeBr_3$ and NaI spectra: the $3^-_1 \rightarrow 0^+_1$ g.s. 6129-keV transition (rightmost peak in mono-dimensional spectra of Figure 12.9) and its first and second escape peaks. The centroid of the peaks has been extracted with a Gaussian fitting and constituted the coordinates of three ($LaBr_3$(Ce)/$CeBr_3$, NaI) pairs of points in the *Q short* vs. *Q long* plot. In Figure 12.9, the A and B pair of points correspond to the position of the 6129-keV line lying on the NaI and $CeBr_3$ lines, respectively. The rotation angle α is defined as the angle that the $\overrightarrow{AB}$ vector forms with respect to the vertical axis.

The calculation of the rotation angle has been performed independently for the three pairs of points and then a mean value has been considered. As mentioned before, the angles were valid for *e014* and *e016* w1 and w2. In *e016* w3, the two PARIS clusters cabling was switched (PARIS 0-8 $\leftrightarrow$ PARIS 9-17), but a simple exchange of the two clusters angles was not sufficient. The same procedure described above had to be repeated for this subset of data to extract new α values. For three PARIS phoswich, the rotation angle could not be calculated: PARIS #0 (#9 in *e016* w3) presented both $LaBr_3$(Ce)and NaI detectors with a very bad resolution, PARIS #6 and #8 (#15 and #17 in *e016* w3, respectively) showed a NaI malfunction. These detectors have been removed from the subsequent analysis as they would have introduced noise. However, for the two modules with only the NaI not working properly, the $LaBr_3$(Ce)component was not discarded. No anomalous behaviour has been observed in the $CeBr_3$-NaI cluster. The photopeak efficiency of the PARIS array has been simulated excluding the aforementioned poor-quality crystals.

Each *Q short* vs. *Q long* plot has been rotated with a dedicated script by the associated α value and the rotated plot has been exploited to define new graphical cuts including both the NaI and common events. Projections on the x axis were then produced and used for the actual calibration process, described in the following. Figure 12.10 reports as an example the rotated *Q short* vs. *Q long* plot for the phoswich #10, with the corresponding

projection. The plot is obtained considering the *e016* w2 in-beam coincidence data.

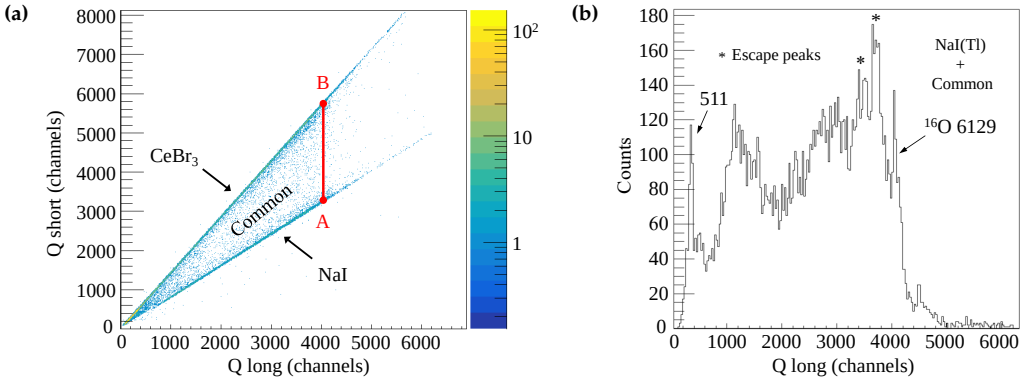

Figure 12.10: Panel (a): same as Figure 12.9(a), after the rotation procedure. Panel (b): projection on the *Qlong* axis (x axis) of the plot in panel (a), gated on the NaI and common part components.

Time alignment and calibration

Before proceeding with the calibration, a PARIS-plastic time alignment and gating procedure similar to the one described in Section 12.1.2, in the context of the $LaBr_3$(Ce) detectors data preparation, has been carried out also for each PARIS module. A time gate has been set to exclude background events. Once the cuts on the phoswich components and the time gates have been set, the calibration of $LaBr_3$(Ce)/$CeBr_3$ and NaI detectors proceeded as follows.

For the $LaBr_3$(Ce)/$CeBr_3$ component, three spectra with different gates on ^{16}O excitation energy (E_{exc}) or on time were produced to have clean peaks to be fitted for the calibration:

1. $E_{exc} < 10$ MeV;
2. $E_{exc} > 10$ MeV;
3. time gate excluding the main reaction peak (gate on background).

Then, two separate quadratic calibrations are applied, one for the low-energy region ($\leqslant 2313$ keV) and the second for the high-energy region ($\geqslant 2313$ keV). Table 12.2 summarises the gamma-ray lines considered in the extraction of the calibration parameters (see Section 12.2 for the identification of the reaction products).

For the NaI component we considered 511, 4439 and 6129 keV gamma-ray lines, measured in a spectrum with no gate on the ^{16}O excitation energy, due to the limited statistics, to perform a quadratic calibration. Four separate calibrations have been introduced for the *e014*, *e016* w1, w2 and w3 parts.

Add-back and Doppler-shift correction

At the end of the calibration procedure, before continuing with the the Doppler-shift correction, the so-called add-back method was applied. During Compton-scattering

Table 12.2: Gamma rays considered in the calibrations, with the information on the emitting nucleus and the conditions set to produce the spectra in which they have been measured. Additional comments are reported in the last column.

E_γ [keV]	Nucleus	Gate	Note
511	Pair production	$E_{exc} > 10$ MeV	At $E_{exc} < 10$ MeV the peak is polluted by the ^{7}Li $1/2^-_1 \rightarrow$ g.s. 478-keV line
843	^{27}Al	Background	^{27}Al in the surrounding materials
2313	^{14}N	$E_{exc} > 10$ MeV	$0^+_1 \rightarrow g.s.$ transition. 0^+_1 state populated by deuteron emission from ^{16}O
4439	^{12}C	$E_{exc} > 10$ MeV	$2^+_1 \rightarrow$ g.s. gamma transition. 2^+_1 state populated in both ^{14}N and ^{16}O decay
6129	^{16}O	$E_{exc} < 10$ MeV	Direct excitation of the ^{16}O 3^-_1 state

and pair-production events, more than one interaction can be registered in the crystals composing a single phoswich and inside different phoswich detectors of the same PARIS cluster. The total energy of the incoming photon can be reconstructed summing the calibrated energy detected in the different crystals when the event multiplicity is $\geqslant 2$. The add-back procedure is accomplished keeping the events detected in the two clusters apart. After the add-back process, both $LaBr_3$(Ce)/$CeBr_3$ and NaI are considered to produce the total PARIS calibrated gamma-ray energy spectrum.

Regarding the Doppler-shift correction, it has been applied as discussed in Section 12.1.2 for the $LaBr_3$(Ce) detectors, for multiplicity 1 events. For events with multiplicity $\geqslant 2$ (see Figure 12.11 for the events multiplicity distribution), which have been summed up to recover the total gamma-ray energy, the summed energy have to be Doppler-shift corrected. In this case, the relative angle between the recoiling nucleus and the emitted gamma ray is defined considering the centre of the detector associated to the largest energy deposition in PARIS to define the gamma-ray direction. This assumption is made considering the gamma-ray interaction mechanisms: the largest energy depositions should be associated to the first Compton-scattering event. Figure 12.12 shows as an example the total PARIS added-back gamma-ray energy spectrum in the 3-8 MeV region, with the full experiment statistics. As in the case of $LaBr_3$(Ce) detectors, an improvement of ~ 20 % is observed in the FWHM of the peak associated to the decay of the short-lived 2^+_1 state in ^{12}C after the Doppler-shift correction. An overall FWHM ~ 145 keV has been measured at 6.1 MeV, in the non-Doppler-shift-corrected spectrum of Figure 12.12.

12.2 Reaction products identification

At the end of data pre-sorting described in the previous section, full statistics excitation energy (E_{exc}) vs. gamma-ray energy (E_γ) matrices have been sorted, taking into account ^{16}O and ^{14}N excitation energy reconstruction. This two-dimensional proton-gamma matrices were instrumental in associating the excitations in the nuclei of interest with the

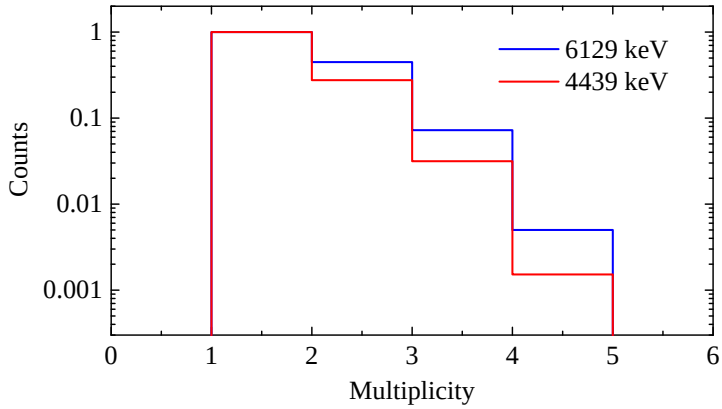

Figure 12.11: PARIS events multiplicity distribution for one of the two clusters (partial statistics). In red, it is shown the multiplicity distribution measured gating on the ^{12}C 4439-keV transition, while in blue the one corresponding to the ^{16}O 6129-keV gamma ray. Each distribution is normalised imposing the total counts in the bin associated to single-fold events to be equal to 1. In the ^{16}O 6129-keV case (blue), an increased number of events with multiplicity $\geqslant 2$ is observed, with respect to events with multiplicity equal to 1, as expected for higher transition energy.

corresponding gamma decay in both the parent and daughter nuclei. Note that the ^{16}O or ^{14}N matrices are not gated on the specific reaction product, but with this notation we intend that the excitation energy has been reconstructed for the the specific nucleus. The structure of the matrix is identical, they are only shifted in excitation energy by ~ 500 keV. Proton-gamma matrices have been produced considering both Doppler-shift corrected and non-Doppler-shift-corrected gamma-ray energy measured in the $LaBr_3$(Ce) detectors or in the PARIS array, separately. The matrices have been sorted considering calibrated data and with the following conditions:

- Plastic multiplicity equal to one;
- Cut on proton events in the KRATTA detectors;
- Time gates on KRATTA PD1 and PD2 time signals;
- $LaBr_3$(Ce)- or PARIS-plastic time gate;
- Plastic-KRATTA correspondence condition;
- Only for the PARIS phoswich, cuts on $LaBr_3$(Ce)/$CeBr_3$ and NaI-common part cuts + add-back.

As an example, Figure 12.13 shows the ^{16}O E_{exc} vs. non-Doppler-corrected $LaBr_3$(Ce) E_γ two-dimensional matrix, with the corresponding x and y projections.

The next step in the analysis of the experimental data consists in a preliminary identification of the nuclei produced in the reaction, through the associated gamma rays emitted. To do so, we produced two projections of the ^{16}O non-Doppler-corrected E_{exc} vs. E_γ matrix, gated on two different excitation energy regions: $E_{exc} < 10$ MeV and

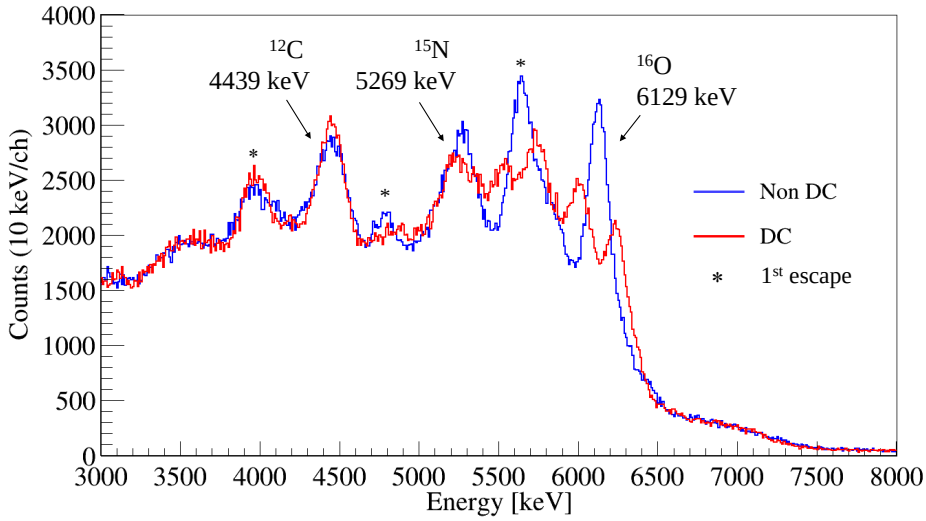

Figure 12.12: Same as Figure 12.8 for the PARIS array.

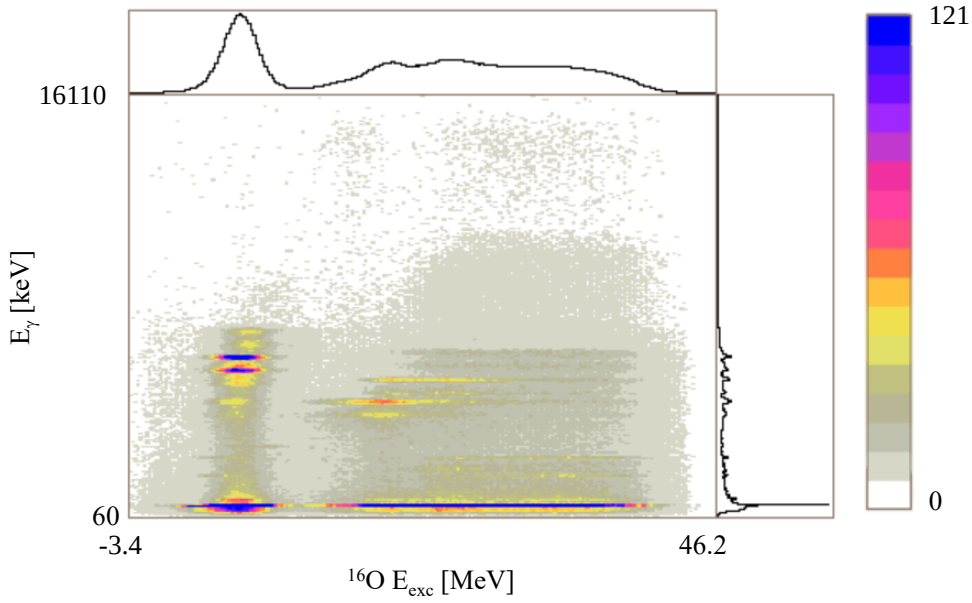

Figure 12.13: Full statistics $LaBr_3$(Ce) gamma-ray energy (E_γ, y axis) vs. ^{16}O excitation energy (E_{exc}, x axis) matrix, with x and y projections.

$E_{exc} > 13$ MeV. The low-excitation-energy- and high-excitation-energy-gated gamma-ray projections are reported in Figures 12.14 and 12.15, respectively. For this step we considered only the $LaBr_3$(Ce) detectors, as they feature a better resolution, compared to PARIS.

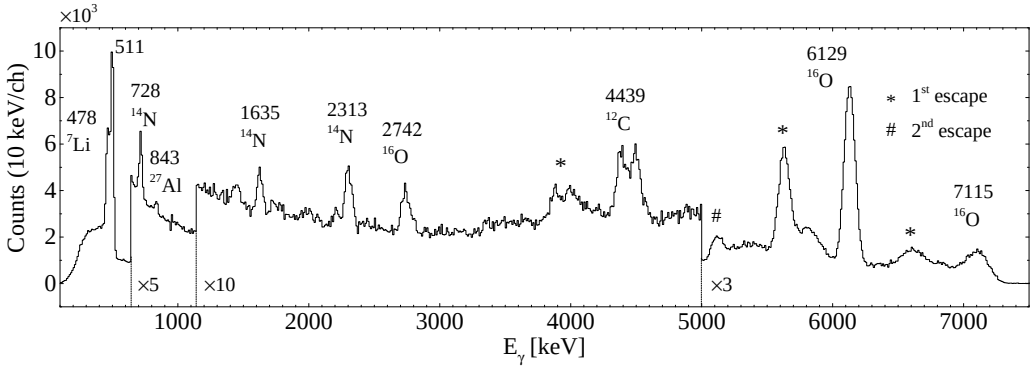

Figure 12.14: $LaBr_3$(Ce) gamma-ray energy spectrum obtained projecting the proton-gamma matrix of Figure 12.13, requiring ^{16}O $E_{exc} < 10$ MeV.

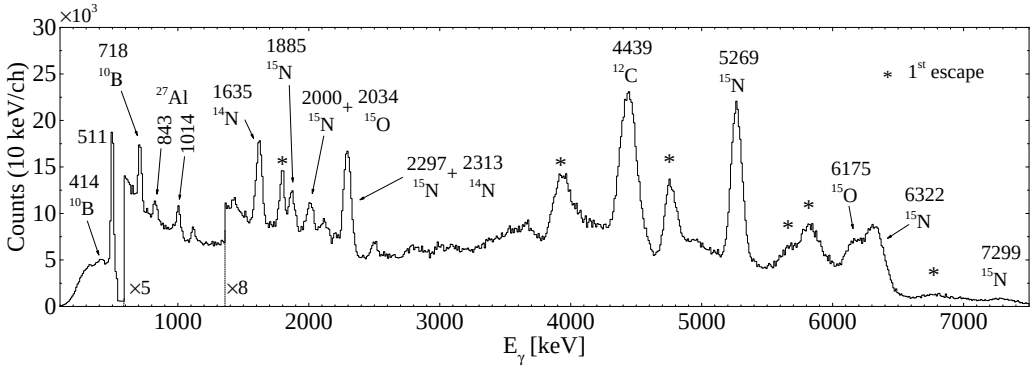

Figure 12.15: Same as Figure 12.14, ^{16}O requiring $E_{exc} > 13$ MeV.

In the low-excitation-energy-gated gamma-ray projection, we expected to observe gamma rays depopulating bound states of the nuclei present in the target, which have been directly excited in the scattering reaction. In fact, we observed ^{7}Li (478 keV), ^{14}N (728, 1635, and 2313 keV), and ^{16}O (2742, 6129, and 7115 keV) known gamma-ray transitions [53]. The intensity of ^{14}N and ^{16}O gamma rays could be used to estimate the extent of the ^{16}O target contamination. The intensity ratio between the $1^+_1 \rightarrow$ g.s. 2313-keV (^{14}N) and the $3^-_1 \rightarrow$ g.s. 6129-keV (^{16}O) transitions has been measured to be about 1/15, confirming the very relevant oxygen contamination. Traces of ^{27}Al gamma transitions are also present in the spectrum at 843 keV, caused by interactions with the surrounding materials, such as the target frame. The 4439-keV ^{12}C is also visible: the spectrum is non-Doppler-shift corrected, therefore the line appears doubled, while in the Doppler-shift-corrected spectrum the Gaussian shape is well recovered. The source of this peak

in coincidence with such low excitation energy is associated to contaminants, as ^{12}C can be present in the surrounding materials.

In the high-excitation-energy-gated gamma-ray projection we expected, instead, to observe gamma rays associated to the daughter nuclei populated after the decay via particle emission of the excited nuclei in the target. As already mentioned, no gamma rays arise form the ^{7}Li decay, as the possible decay products (^{4}He, ^{6}He, ^{6}Li) do not have any bound state. Regarding the decay of ^{16}O, we observed the intense population of ^{15}N (proton emission) and ^{12}C (alpha emission), and a less intense population of ^{15}O (neutron emission) and ^{14}N (deuteron emission). In particular, very intense ^{15}N $5/2^+_1 \rightarrow$ g.s. 5269-keV and ^{12}C $2^+_1 \rightarrow$ g.s. 4439-keV gamma transitions have been identified. In ^{15}N, the $5/2^+_1$ first an the $1/2^+_1$ second excited states, located at 5270 and 5299 keV, respectively, both decay to the ground state with gamma rays only 30 keV apart. With the $LaBr_3$(Ce) resolution (FWHM $\sim$ 95 keV at 6.1 MeV), these transitions would appear as unresolved. However, the gamma-ray peak width is compatible with a single gamma component, as its FWHM is consistent with the one of the intense ^{16}O 6.129-keV line. In addition, the first and second excited states lifetimes are 2.58(14) ps and 24(7) fs, respectively, and this makes possible to discriminate between the two gamma transitions exploiting the Doppler-shift correction. As already shown in Figure 12.8, the peak resolution degrades when the Doppler-shift correction is applied, therefore the gamma ray must be associated to the decay from a long-lived state, specifically the $5/2^+_1$ 5270-keV first excited state. This information is of particular importance for the reconstruction of the M4 resonances decay scheme in ^{16}O.

For what concerns the ^{14}N decay from unbound states, a clear population of ^{10}B (alpha emission) is observed (414 and 718 keV lines), while the channels associated to the emission of a proton and a deuteron, ^{13}C and ^{12}C respectively, cannot be reliably established, due to the oxygen contamination. No gamma ray is instead associated to the emission of a neutron, as ^{13}N has no bound states. Finally, traces of ^{27}Al are again visible at 843 and 1014 keV.

In this preliminary part of the analysis we did not associate any gamma ray to the decay of a specific resonance in ^{16}O or ^{14}N, this will be discussed in the next section.

12.3 M4 states decay scheme reconstruction

In this Section we will go further into the analysis of the proton-gamma two-dimensional matrix, establishing the relationship between the populated M4 resonances and their decay channels. As explained previously, the ^{14}N fraction was roughly 15 times less than the oxygen one and its decay product gamma rays were more difficult to identify. Therefore, we will start the analysis from ^{16}O, whose case is also of particular interest to validate the experimental technique.

12.3.1 ^{16}O M4 states decay

Unlike the pilot experiment in which the M4 resonance of interest in ^{13}C was well isolated from other resonances (see Section 10.2), the case of ^{16}O is more difficult, as a triplet of

M4 states is present around 18 MeV, in an energy window of just 2 MeV (17.79 MeV, 18.98 MeV, and 19.80 MeV). The energy resolution of the KRATTA telescopes (2-3 MeV), used to reconstruct the excitation energy, is not sufficient to discriminate between the three resonances, that appear as unresolved, as already observed in the singles spectrum of Figure 12.5.

Figure 12.16 shows the reconstructed excitation energy spectrum of ^{16}O obtained in coincidence with gamma rays measured in PARIS. A perfectly similar excitation energy spectrum was measured in coincidence with γ rays detected in the four $LaBr_3$(Ce). The

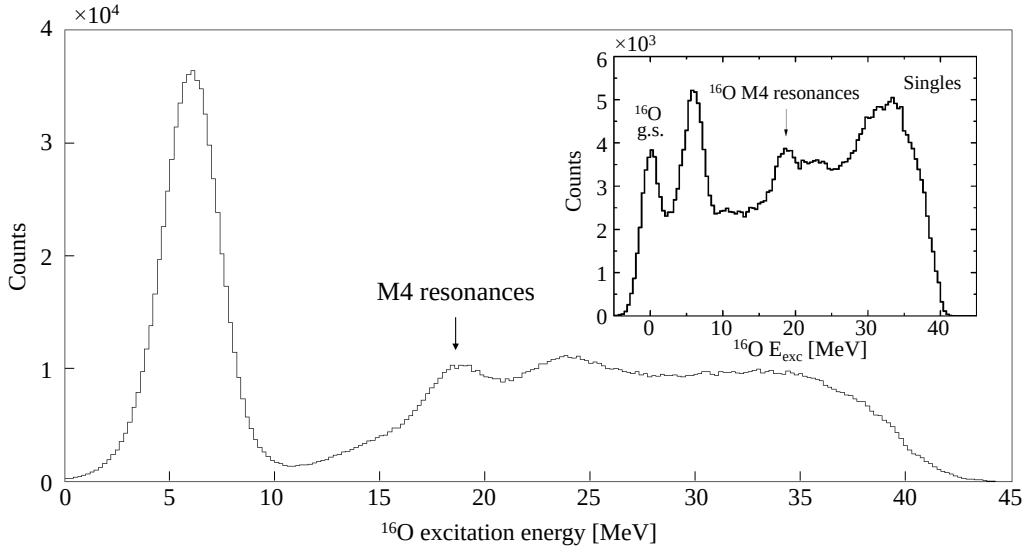

Figure 12.16: Full statistics ^{16}O excitation energy spectrum obtained in coincidence with gamma rays measured in PARIS. A similar spectrum is observed in coincidence with $LaBr_3$(Ce) gamma rays (see Figure 12.13). In the inset, it is shown the singles spectrum of Figure 12.5. The peak associated to the elastic scattering of protons on ^{16}O (*i.e.*, "^{16}O g.s." label in the inset) strongly present in the singles spectrum, disappears when proton-gamma coincidence is required, as in this case no gamma ray is emitted.

three resonances appear indeed as unresolved also in coincidence data and this makes impossible a standard analysis of the proton-gamma matrix. No reliable background-subtracted gates can be set on the excitation energy, to be projected on the gamma-ray energy axis. Vice versa, gates on the gamma-ray transitions, projected on the excitation energy axis, should be more reliable. Yet, the treatment of the background appeared to be rather complex, due to the presence of a high number of transitions and escape peaks that overlapped.

Consequently, we decided to use an alternative analysis approach. To illustrate the technique we will consider $LaBr_3$(Ce) data only, but a similar procedure have been repeated for the PARIS data. The two datasets were considered independently and then the results averaged, as a good grade of compatibility was found between the results obtained in the two cases.

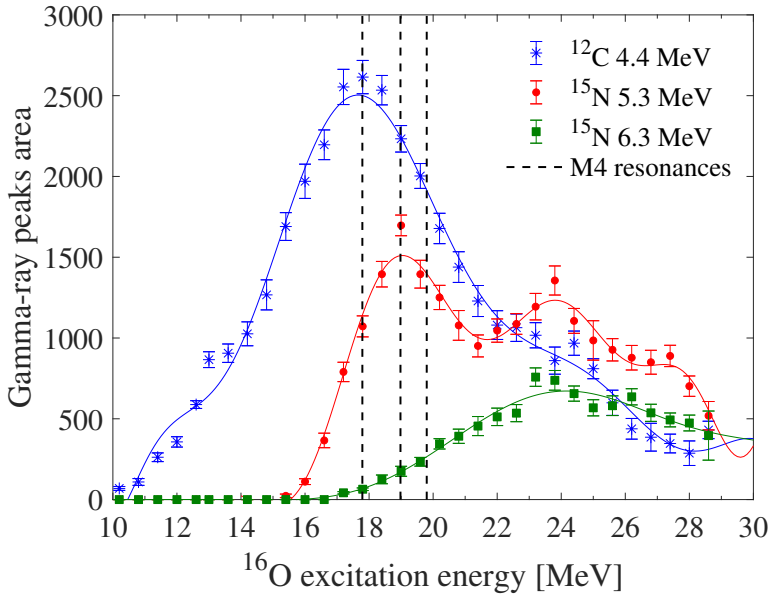

Figure 12.17: Area of the gamma-ray peaks of interest as a function of ^{16}O excitation energy (star, circle and square symbols), considering $LaBr_3$(Ce) data only. A 600-keV binning in excitation energy has been considered. The dashed vertical lines indicate the position of the three M4 resonances of interest. The solid lines are polynomial fits of the experimental data meant to display the overall trends.

The analysis approach consisted in a scanning of the area of the gamma-ray peaks of interest for the decay of the M4 resonances, namely ^{12}C 4439-keV line and ^{15}N 5269, 6332 and 1885-keV gamma rays (see also Figure 10.10), as a function of the excitation energy. 600-keV-wide gates were set on the excitation energy spectrum without any background subtraction and then projected on the gamma-ray energy axis. For each projection, the area of the peaks of interest was measured, fitting the peak with a Gaussian and a linear background. The results of the area scanning for ^{12}C 4439-keV (blue stars), ^{15}N 5269- (red circles) and 6332-keV (green squares) gamma rays is reported in Figure 12.17. In the plot we marked with dashed vertical lines the position of the three resonances of interest. Solid lines are instead polynomial fits of the three sets of points, whose purpose is just to show the curves' trend.

The plot shows that a sensitivity to decay channels of the three M4 states can be achieved with this kind of approach. ^{15}N 5269-keV curve presents a maximum around the energy of the second resonance (18.98 MeV), which can be associated to its decay towards the $5/2^+_1$ state in ^{15}N. The ^{12}C 4439-keV curve features a broad structure with a maximum around the energy of the first M4 resonance (17.79 MeV). This behaviour can be associated to the decay of the first resonance towards the ^{12}C first excited state, but contributions from the other resonances are not excluded due to the very broad peak structure. The ^{15}N 6322-keV curve is instead rather featureless in the region of the resonances.

To confirm these qualitative observations, we proceeded by fitting the experimental points with specific constraints. Firstly, we considered the ^{15}N 5269-keV dataset. We assumed that only a single M4 resonance, the one at 18.98 MeV, decayed towards the ^{15}N $5/2^+_1$ state, that subsequently emitted the 5269-keV gamma ray. This assumption is based on the width of the peak structure ($\sim$3 MeV), which is fully compatible with the KRATTA energy resolution. An increase of the FWHM up to a factor $\sim$1.5 is expected in the case of additional components. We then fitted the experimental data with two Gaussian functions, one with a fixed centroid at 18.98 MeV and the second one around 23 MeV with no constraints. Since no information was available to define the background, we repeated the fitting procedure considering two extreme limits for the baseline (light-green shaded area), as exemplified in the two panels of Figure 12.18. In the first case (left

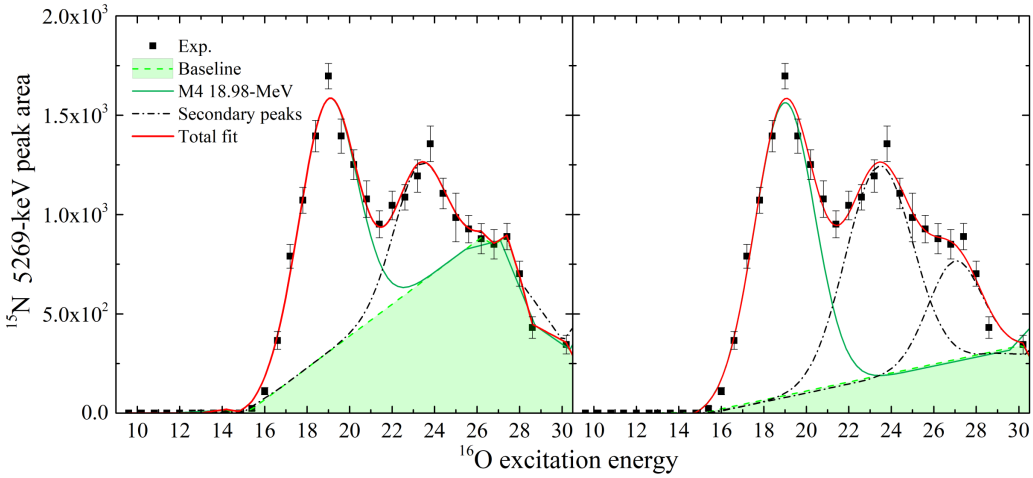

Figure 12.18: Fitting of the experimental ^{15}N 5269-keV gamma-ray peak area as a function of the ^{16}O excitation energy. Two baseline (light-green shaded area) limits have been considered, a much higher one (left) and a much lower one (right). A single M4 resonance with a fixed centroid (18.98 MeV, solid green Gaussian) has been considered decaying toward the excited state emitting the 5269-keV gamma-ray. One (left) or two (right) additional Gaussians (black dash-dot curves) have been introduced to fit the experimental points (black squares). The centroid of the additional Gaussians is kept as a free parameter, as no information is available on their population in previous proton scattering experiments. The total fit is marked by a solid red line.

panel), an interpolated + linear high baseline was chosen. In the second case (right panel), a much lower background was considered, and a third Gaussian at 27 MeV was added to take care of high excitation-energy points. From the two fitting procedures we extracted first of all the area of the 18.98-MeV peak, but also the information on the FWHM. The area and FWHM values extracted with the two background limits were averaged, resulting in: Area(18.98 MeV; ^{15}N 5269 keV) = 4795 $\pm$ 458 $\pm$ 117, FWHM = 3.26 $\pm$ 0.06 $\pm$ 0.08 MeV. The first uncertainty contribution is calculated as the mean standard deviation of the values obtained with the two fitting approaches, the second corresponds to the error propagation on the average calculation, coming from the fit uncertainties. The first error contribution can be identified with the systematic uncertainty deriving from the

Table 12.3: Summary of the fit parameters and results. For every transition of interest for the decay of the M4 triplet in ^{16}O are reported the areas measured for each M4 resonance contribution. The FWHM is also reported: it was measured in the case of the ^{15}N 5269-keV transition and introduced as a fixed parameter in the other cases (see text for details).

M4 E_{exc} [MeV]	^{15}N 5269 keV	
	FWHM [MeV]	Area
17.79	0	0
18.98	3.26 ± 0.06 ± 0.08	4795 ± 458 ± 117
19.80	0	0
M4 E_{exc} [MeV]	**^{15}N 6322 keV**	
	FWHM [MeV]	**Area**
17.79	/	/
18.98	0	0
19.80	3.26 (fixed)	612 ± 92 ± 94
M4 E_{exc} [MeV]	**^{12}C 4439 keV**	
	FWHM [MeV]	**Area**
17.79	3.26 (fixed)	5932 ± 697 ± 139
18.98	0	0
19.80	3.26 (fixed)	1905 ± 954 ± 203

background treatment, while the second is a statistical uncertainty. In the following, for quantities derived from these ones we will propagate the total error, calculated as the root sum square of the two components, including both systematic and statistical uncertainties. Since a single M4 resonance component have been considered on the basis of the peak structure width, in the ^{15}N 5269-keV case, the FWHM information extracted was considered to be the typical resolution at the energy of interest. This parameter was then introduced as fixed in all the other cases. Table 12.3 summarises the parameters of the fit and the results.

Figure 12.19 shows the fit of the experimental data associated to the population of the ^{12}C 2^+_1 state, which decays emitting a 4439-keV gamma ray. Unlike the previous case, this requires a more complex analysis. The main peak associated to the decay of the M4 resonances of interest was fitted considering two components, one from the M4 17.79-MeV resonance and the other from the 19.80-MeV one. The centroid and FWHM has been introduced as fixed parameters in the fit. An additional secondary peak has been considered at 15.42 MeV, as an intense resonance at this energy has been reported in the proton-scattering experiment of Ref. [213] (see also Figure 10.9). Also for this secondary Gaussian, fixed centroid and FWHM parameters were considered. As in the previous case, two separate fits with two opposite baseline limits were performed: in the case of the low background (left panel of Figure 12.19) two additional secondary Gaussians have been considered, around 13 MeV and 23 MeV, with free parameters. In the case of the high-background limit (right panel), only three fixed peaks were set. No

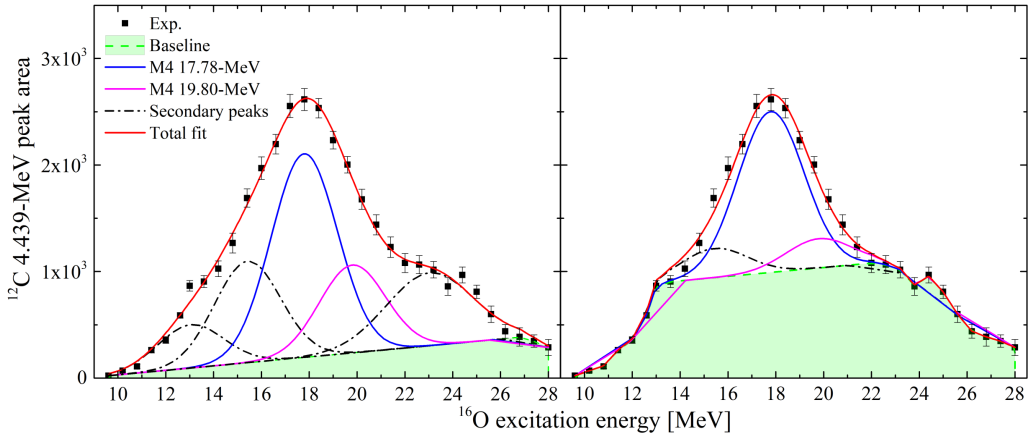

Figure 12.19: Same as Figure 12.18 for the ^{12}C 4439-keV transition. In solid blue and magenta are shown the Gaussian peaks associated to the decay of the M4 17.79-MeV and 19.80-MeV, respectively.

18.98-MeV resonance contribution appeared possible: the fit did not converge by adding a peak at 18.98 MeV and the area of the 18.98-MeV resonance peak resulted as negative in both the cases with a different baseline. The results (summarised in Table 12.3) are the following: Area(17.79 MeV; ^{12}C 4439 keV) = 5932 ± 697 ± 139 and Area(19.80 MeV; ^{12}C 4439 keV) = 1905 ± 954 ± 203.

A similar analysis has been performed for the ^{15}N 6322-keV gamma-ray line, as displayed in Figure 12.20. A small component deriving from the decay of the M4 19.80-MeV resonance has been identified: Area(19.80 MeV; ^{15}N 6322 keV) = 612 ± 92 ± 94 (see Table 12.3 for the results summary).

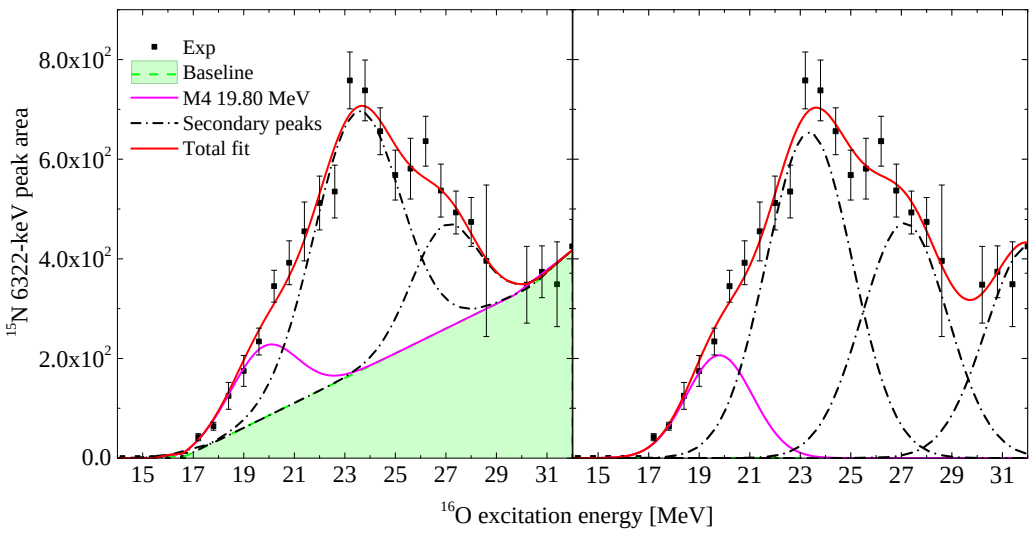

Figure 12.20: Same as Figure 12.18 for the ^{15}N 6332-keV transition. In solid magenta the Gaussian peak of the M4 19.80-MeV resonance.

We note that, in all the three cases presented here, secondary peaks have been introduced, to fit the experimental data outside the region of interest corresponding to the M4 triplet. Except the 15.42-MeV resonance, whose centroid has been introduced as a fixed parameter in the analysis of the ^{12}C 4439-keV experimental data (see Figure 12.19), all the other secondary centroids were kept as free parameters. This is because no other inelastic scattering experiment with either p, e, or π explored the population of resonances above $\sim$ 21 MeV. In addition, we cannot associate our observations to specific excited states in this region, as a large number of resonances is reported in literature from studies with other reaction mechanisms.

Gamma events fraction and decay branchings

The information on the measured areas extracted so far cannot be directly used to deduce the M4 resonances decay branching ratios. To achieve this, one should calculate the fraction of events in which the resonance decay is associated to the population of excited states in daughter nuclei, which emit gamma rays. In fact, not all the possible decay channels are associated to the emission of gamma radiation: the population of daughter nuclei in their ground state is not associated to the emission of gamma rays, and in the present work we could not investigate these decay channels.

The evaluation of the gamma events fraction can be done by comparing the singles spectrum to the coincidence ones. The area of the peak (A_{M4}) associated to the overall population of the three M4 resonances of interest is measured (as they are unresolved) and then the intensity of the peak (I_{M4}) is calculated via Equation (12.5):

$$I_{M4} = \frac{A_{M4}}{(C_b \times T)(1 - DT/100)(\epsilon_\gamma/100)} \tag{12.5}$$

where C_b is the average beam current measured on the beam dump (typically 100-200 pA), T is the time duration ($\sim$ 100 minutes in singles and $\sim$ 1800 minutes in *e016* w2 coincidences), DT the dead time of the acquisition ($\sim$ 70-80 %), and ϵ_γ is the absolute photopeak efficiency (*e.g.*,$\sim$ 0.44 % and $\sim$ 0.40 % at 5269 keV for the four $LaBr_3$(Ce) and PARIS, respectively). Equation (12.5) is valid for both the singles and coincidences, except that in the case of singles the photopeak efficiency should not be taken into account (ϵ_γ = 100 %). In the coincidence measurement, in addition, the total intensity of the populated M4 resonances has been calculated as the sum of the intensities deduced from of the peak areas observed gating on the gamma-ray transitions associated to their decay (^{12}C 4339 keV, ^{15}N 5269 keV and 6332 keV). The same procedure has been repeated considering PARIS and $LaBr_3$(Ce) as independent datasets, and an average value of 56(14) % was deduced for the gamma events fraction. The uncertainty on the scaling factor includes both statistical and systematic contributions, the latter deriving from the background contribution, as similarly explained before in connection with the area scanning process. The extracted scaling factor considers the sum of the three resonances, therefore an additional step is necessary to deduce the gamma fraction for each resonance separately.

Firstly, we considered a total intensity of the three resonances decay in coincidence to gamma rays to be 100 % and we extracted the relative intensity associated to each

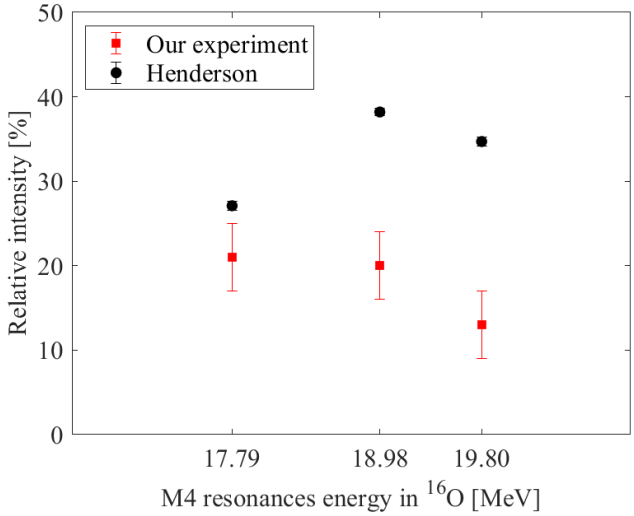

Figure 12.21: Comparison between ^{16}O M4 resonances relative intensities measured in our experiment (red squares) and in Henderson's one (black circles) [213]. In our case, the relative intensity is associated only to events in which the resonances decay to a daughter nucleus that subsequently emits a gamma ray, *i.e.*, 56(14) % of the total intensity, see text for details. The difference between Henderson's values and the ones measured in the present experiment corresponds to the fraction of decays associated to channels in which no gamma ray is emitted (*e.g.*, decays to ground state of daughter nuclei).

resonance, based on the area scanning procedure described above and averaging the $LaBr_3$(Ce) and PARIS results. Secondly, we scaled down each relative intensity on the basis of the overall gamma events fraction (56(14) %): 17.79 MeV → 21(4) %, 18.98 MeV → 20(4) %, 19.80 MeV → 13(4) %. After that, we deduced the total relative intensity of each resonance from the experimental excitation energy spectrum reported in the proton-scattering experiment by Henderson *et al.* in Ref. [213] [1]. Since the experimental conditions (beam energy and scattered-protons detection angle) of Henderson's experiment of Ref. [213] were the same as in the present experiment, we could safely compare our scaled relative intensities to the total extracted ones. The obtained relative intensities are the following: 17.79 MeV → 27.1(5) %, 18.98 MeV → 38.2(4) %, 19.80 MeV → 34.1(5) %. The comparison is presented in Figure 12.21. The present relative intensities represent the gamma-related decay fraction, while the difference between Henderson's relative intensities and the present ones coincides with the fraction of events associated to no emission of gamma rays following the resonance decay.

From the comparison presented in Figure 12.21, we could then extract the absolute decay branchings of the M4 resonances of interest and reconstruct the ^{16}O decay scheme, displayed in Figure 12.22. The results of the branching ratio calculation are reported also in the top part of Table 12.4. In the table, the following notation to define the decay

[1]The original spectrum was reproduced using an extraction tool [232] and then fitted with the OriginPro analysis software [233]

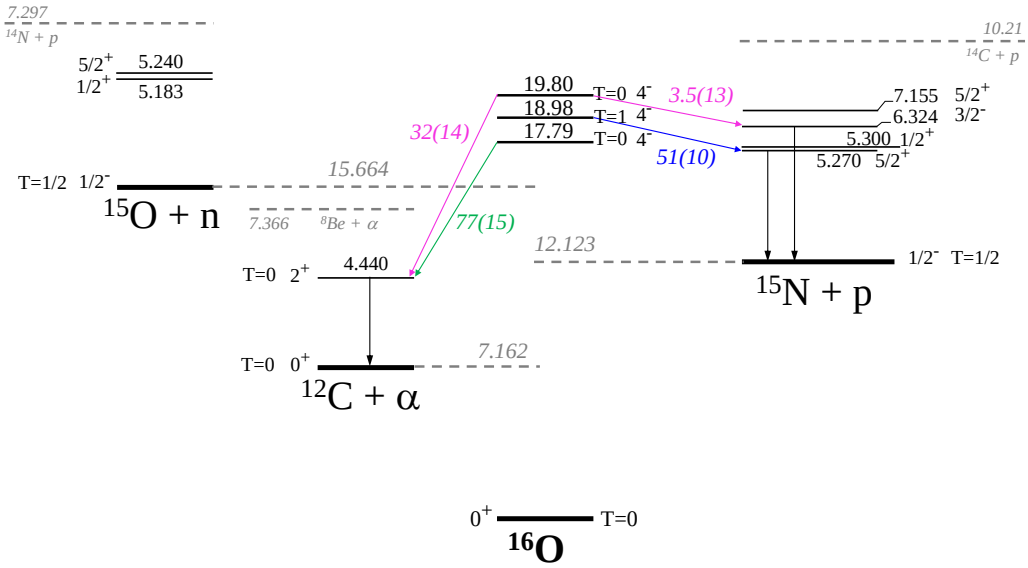

Figure 12.22: ^{16}O M4 states decay scheme. In dashed grey are shown the particle-emission thresholds. All energies are expressed in MeV.

channels is used:

p_0, p_1, p_3: proton-emission decay feeding the $1/2^-_1$ ground state, the $5/2^+_1$ first- and $3/2^-_1$ third-excited states of ^{15}N, respectively;

α_0, α_1: alpha-emission decay feeding the 0^+_1 ground and the 2^+_1 first-excited states of ^{12}C, respectively;

n_0: neutron-emission decay feeding ^{15}O $1/2^-_1$ ground state.

Results discussion

The results obtained are in very good agreement with the previously measured branching ratios measured in the experiment of Ref. [224] (see Section 10.3.2), and reported here for comparison in the bottom part of Table 12.4. In our dataset we could identify all the intense decay channels associated to the emission of gamma rays in the daughter nuclei, but not the less intense ones, namely those reported with $BR < 10\,\%$ in Breuer's work. It is remarkable that even if the triplet of M4 states appeared as unresolved in the excitation energy spectrum, we still reached enough sensitivity through a systematic analysis of the proton-gamma matrix to distinguish between their decay channels and to extract a quantitative information on the decay branching ratios. This study validates the experimental technique, supporting the previous work of the pilot experiment on ^{13}C, realised with a similar method. It also supports the extension of the present method to the investigation of other nuclei such as ^{14}N.

Table 12.4: Comparison between the ^{16}O M4 configurations decay branching ratios (BR) measured in this work and the ones reported in literature in the work of Breuer *et al.* [224]. In our case, no measurement of the branchings for channels in which no gamma ray is emitted was possible. For the decay channels notation, see the text.

			BR (this work) [%]			
E_{exc} [MeV]	p_0	p_1	p_3	α_0	α_1	n_0
17.79	\	0	-	\	77(15)	\
18.98	\	51(10)	0	\	0	\
19.8	\	0	3.5(13)	\	32(14)	\
			BR (Breuer *et al.*) [%]			
Ex [MeV]	p_0	p_1	p_3	α_0	α_1	n_0
17.79	14(<5)	0	-	2.5(<5)	84(10-20)	(2)
18.98	12(<5)	63(5-10)	0	2(<5)	7(<5)	(3)
19.8	8(<5)	9(<5)	11(<5)	2.5(<5)	22(5-10)	(2)

Going deeper into the physical interpretation of the decay scheme obtained, no immediate consideration on spin/parity and isospin of the M4 states of interest and the corresponding final states, populated in the daughter nuclei, can explain the decay scheme. Except those decay channels forbidden by the energy window (*e.g.*, the decay of the 17.79-MeV resonance towards the $3/2^-_1$ third-excited state of ^{15}N), no channel is forbidden by selection rules. In Breuer's work [224], they concentrated mainly on the interpretation of the decay towards the ground state of ^{15}N. This decay of the $(1d_{5/2}1p3/2^{-1})^{4^-}$ resonances has been mainly interpreted in terms of a "nuclear Auger effect" where the hole is promoted from the $p_{3/2}$ to the $p_{1/2}$ shell, while the particle is ejected from the $d_{5/2}$ orbit into the $l = 4$ continuum. This type of decay is however inhibited for the 18-MeV M4 configuration triplet with respect to other T=1 hole states around 13 MeV: they show a weaker overlap with the ^{15}N ground state. In addition, in Breuer's work , the decay from the 4^- T=0 resonance at 19.80 MeV towards the $3/2^-_1$ third-excited state in ^{15}N is justified by the latter having a dominantly $p^{-1}_{3/2}$ hole-state configuration.

In the pion-scattering work of Ref. [63] the authors affirm that the M4 T=1 18.98-MeV state retains nearly equal proton and neutron amplitudes, whereas the lower level (at 17.79 MeV) becomes mostly a proton state and the upper level (at 19.80 MeV) arises mostly as a neutron state, as a result of the isospin mixing of the three M4 resonances. This qualitative interpretation is not exhaustive in assessing the character of the resonances, as it is limited to the proton/neutron character, and does not include more complex (α) features. We cannot directly interpret the decay channels on the basis of this interpretation. In fact, the neutron emission, populating the ground state of ^{15}O is reported as largely suppressed in Breuer's work for all the M4 resonances.

To have a more detailed interpretation of the M4 configurations decay in ^{16}O a theoretical modelling of the resonances wave functions would be necessary. However, standard shell-model calculations are not reliable at such high excitation energies and in general

above the emission thresholds. Gamow Shell Model calculations are not available any time soon for such a heavy system, and in addition such a model cannot predict alpha decay, as it deals with one-particle excitations only. Therefore, for this nucleus we will provide only experimental results.

Nonetheless, ^{16}O has been a valuable test case to validate the proton-gamma coincidence technique to investigate the decay of M4 stretched configurations in light nuclei. It has also confirmed the experimental set-up overall good performance in such kind of studies, in a much more complex case than the previous ^{13}C one. Based on this work, the continuation of the M4 research line has been planned at the Kraków CCB facility.

12.3.2 ^{14}N M4 states decay

For the investigation of M4 states decay in the ^{14}N nucleus, the same technique described before for the oxygen case has been applied. A scanning of the area of the possible gamma-ray peaks associated to the decay of the resonances, as a function of the ^{14}N excitation energy, has been performed. However, only two gamma transitions has been identified with sufficient statistics to be associated to ^{14}N decay, mainly due to the large oxygen contamination. The two identified gamma rays, located at 414 and 718 keV, de-excite ^{10}B (the alpha-emission channel) 1^+_2 third- and 1^+_1 first-excited states, respectively. The area scanning of these two peaks both show an excess of counts around the region at 17 MeV, which could be assigned with the 16.9-MeV M4 resonance. However, the statistics is rather limited, especially in the 414-keV gamma-ray peak, to have quantitative results.

Regarding the other possible gamma rays that should be observed after the M4 resonances decay (see Figure 10.7), some were not observed, others remain uncertain due to the ^{16}O contamination. For example, no information on the deuteron emission decay towards the ^{12}C 4440-keV state can be extracted due to the fact that oxygen itself strongly decays to this state in carbon. For what concerns the proton emission towards ^{13}C, no hint of the 3089-keV gamma ray, de-exciting the $1/2^+_1$ first-excited state, has been observed in an energy region rather clean from other transitions. On the other hand, hints for the presence of a 3684-keV gamma ray were seen, but a very limited statistics prevented a reliable identification of the transition depopulating the $3/2^-_1$ state and no area scanning procedure could be applied. The $5/2^+_1 \rightarrow$ g.s. gamma ray transition would lie instead too close to the ^{12}C 4439-keV first-escape peak to be observed with low statistics. Regarding the alpha-decay channel towards ^{10}B, no 2868-keV gamma ray de-exciting the 2^+_1 3587-keV state was observed, while the $0^+_1 \rightarrow 1^+_1$ 1022-keV transition remained uncertain, since it would appear as unresolved from the 1015-keV ^{27}Al transition, coming from spurious beam interactions with surrounding materials. Finally, the other two gamma-ray transitions depopulating the 1^+_2 together with the 414-keV gamma ray were not observed, as they are expected with nearly 50 % lower intensity [53], and since they have higher energies (1435 keV and 2154 keV), at which the photopeak efficiency drops by roughly 20 % and 35 %, respectively.

The qualitative decay scheme for the ^{14}N 16.9-MeV resonance, which can be deduced from such limited statistics, is summarised in Figure 12.23. With dashed arrow we reported the decay channels that remain uncertain, due to limited statistics or to the

presence of contaminations. Despite the fact that only a qualitative picture could be obtained for this nucleus, there is evidence that we populate the 16.9-MeV M4 resonance in the inelastic proton-scattering reaction. In addition, we demonstrated that we are sensitive to its decay.

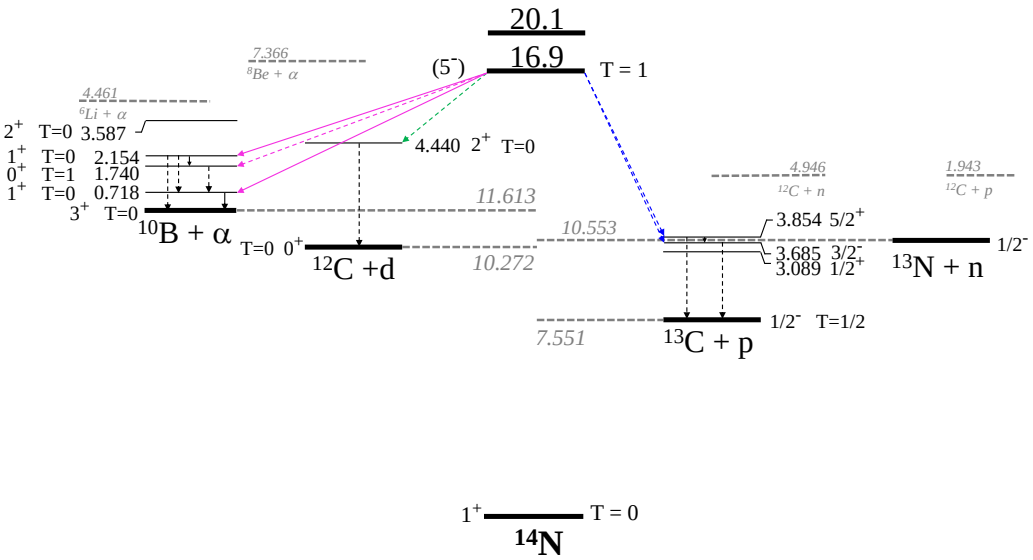

Figure 12.23: Same as Figure 12.22, for the 16.9-MeV M4 resonance in ^{14}N. No quantitative information on the branching ratios is available. The uncertain decay channels or those for which no information is available due to contaminations are reported with dashed arrows.

On the basis of these results, in the near future, a second experiment to investigate ^{14}N has been approved at the Kraków CCB facility. A new lithium amide ($Li^{14}NH_2$) thick target, free of oxygen contamination, will be employed. The proton beam energy and the experimental set-up will be unchanged.

Regarding a possible theoretical interpretation, unlike ^{16}O, ^{14}N could be accessed by recent Gamow Shell Model calculations. Therefore, in the future, we aim at obtaining both experimental and theoretical information on the decay of M4 stretched configurations in this nucleus.

In conclusion, the data analysis of the *e014+e016* experiment has been fully completed, with the entire treatment of the detection sub-systems employed, including the whole statistics. The experimental technique has been validated through the study of a known complex case, ^{16}O, for which the decay of the M4 resonances triplet around 18 MeV has been well reconstructed. The oxygen contamination, however, prevented the full investigation of ^{14}N, for which only a partial qualitative description has been deduced. Further investigation is needed for this nucleus, with a new experiment that will take place in autumn/winter 2021.

Conclusions

The present Thesis work was devoted to an investigation of light neutron-rich nuclei from B to O, with the aim of searching for new observables to validate modern nuclear theoretical models. This study was developed on three levels. In fact, we investigated bound states, near-threshold states and unbound resonances in a number of light systems, within three distinct research lines. In this context, different experimental activities were carried out, related to technical developments of novel instrumentation as well as to extensive data analysis of the experiments designed for these purposes.

Within the first research line, gamma-spectroscopy studies of bound states were carried out in ^{14}C and ^{17,18}N nuclei. These nuclei were populated as a by-product of a large experiment performed at the GANIL facility, employing a deep-inelastic reaction with a ^{18}O beam on a ^{181}Ta target and the AGATA+PARIS+VAMOS multi-array detection system.

A novel Monte Carlo technique, based on the Doppler-Shift-Attenuation Method (DSAM), to determine nuclear-state lifetimes of the order of tens-to-hundreds femtoseconds had to be developed for the purpose of the experiment and it has been presented. The validation of the technique with known lifetimes in ^{17,19}O and ^{17}N is discussed. It is shown that the combined use of a magnetic spectrometer and a γ-ray tracking array (with interaction-point spatial resolution of the order of few millimeters) is crucial for reaching conclusive results. The new DSAM implementation will significantly profit from tracking arrays being upgraded to reach larger angular coverage in the future, and it is expected to become an important tool to investigate exotic neutron-rich nuclei produced with intense radioactive ISOL-type beams.

The new technique has been applied to the case of short-lived states in ^{17}N and ^{14}C. In ^{17}N, we measured the lifetime of the 5515-keV $3/2^-_3$ and 5170-keV $(9/2^+_1)$ states: $\tau(3/2^-_3) < 60$ fs (40 % improvement with respect to the limit reported in literature) and $\tau((9/2^+)_1) = 35^{+110}_{-30}$ fs. We provided also a precise energy measurement for the $(9/2^+)_1$ state ($5174.0^{+1.3}_{-1.8}$ keV), previously reported at lower energy, and of the two de-exciting gamma transitions, namely $2045.0^{+1.2}_{-1.7}$ keV and $2647.8^{+1.4}_{-1.9}$ keV. The results have been compared to large-scale Shell Model calculations. The comparison confirmed the difficulty of the shell-model approach in reproducing positive-parity states in N isotopes, while the lifetime of the $3/2^-_3$ state was predicted in agreement with the experimental limit.

In ^{14}C, we measured the lifetime of the 2^+_1 state, as the reduced transition probability for the $2^+_1 \rightarrow$ g.s. transition presented an apparently anomalous behaviour in the trend of the C isotopic chain. A lifetime $\tau = 65^{+32}_{-29}$ fs was extracted with the novel DSAM implementation, corresponding to B(E2;$2^+_1 \rightarrow 0^+_1$ g.s.)= $0.7^{+0.4}_{-0.3}$ e^{2}fm^4, about five times smaller than the value reported in literature. The new B(E2) value represents a minimum in the reduced transition probability systematics of the C isotopic chain. This new observation is more in line with the typical signature of a shell closure, and can be considered in the future to benchmark *ab initio* theoretical approaches.

To conclude the study of bound states in neutron-rich systems, we illustrated the high-precision gamma spectroscopy of ^{18}N, leading to a complete set of negative-parity states, below the neutron-emission threshold. The level scheme has been reconstructed on the basis of experimental evidences and with the guidance of large-scale SM calculations. Of particular interest was the location of the 1^-_2 excited state in ^{18}N, which has strong impact in nucleosynthesis taking place in stellar environments. The lifetime of one of the newly identified states at 2404.6(13) keV has been measured with the new lifetime-measurement technique: $\tau = 160^{+740}_{-100}$ fs. The large-scale SM calculations reasonably reproduced the experimental data. Selective variations of two-body cross-shell and inter-shell matrix elements were introduced to improve the ^{18}N level ordering description. This modification simultaneously reproduced the ground and first-excited state in ^{16}N, for the first time. The work further confirmed the power of cutting-edge detection systems, such as the AGATA and GRETINA tracking arrays coupled to ancillary detectors, in performing complete spectroscopy of hard-to-reach nuclei lying on the neutron-rich side of the stability valley. All in all, this part of the Thesis work shows how gamma spectroscopy of bound states in light neutron-rich nuclei can be used to provide key observables sensitive to the properties of the nuclear interaction, which are essential to improve and benchmark the most advanced theory approaches.

The second research activity was dedicated to the investigation of electromagnetic decays from unbound states close to particle-emission thresholds in light systems. In the context of this research line, we presented the technical development of the GALILEO TRacking Array for Light Charged particle Ejectiles (GALTRACE), a pixel-type silicon telescope detector array, for the detection of light reaction residues (p,d,t,α), designed as an ancillary for γ-ray spectrometers, namely GALILEO and also AGATA in the next future. The characteristics of the GALTACE array were presented and its performance was demonstrated in an in-beam three-days test experiment, realised at LNL in July 2019, which assessed the capabilities of the array in discriminating between different charged particles, employing pulse-shape analysis techniques. Some technical and mechanical issues were recognised during the experiment, therefore an upgraded version of GALTRACE was realised and additional tests were performed in view of the employment of the array in its full configuration (four telescopes) in a longer experimental campaign.

In particular, the upgraded GALTRACE array was employed, coupled to GALILEO, in the search for a particular near-threshold state in ^{11}B. The existence of a possible resonance just above the proton-separation energy in ^{11}B, which could explain the rare beta-delayed proton emission decay of ^{11}Be, has been addressed by a new experimental approach, namely by detecting its possible γ decay towards lower-lying bound states.

An experiment has been carried out in February/March 2021 at LNL, with the aim of populating ^{11}B in a ^{6}Li(^{6}Li, p)^{11}B fusion/evaporation reaction. SMEC theoretical calculations predicted a rather weak γ branch with respect to the dominating proton emission ($\sim 3 \times 10^{-3}$). Therefore, the detection of a γ transition depopulating the resonance of interest is difficult to accomplish. Particle-gamma coincidence techniques were employed to enhance, first of all, the selectivity to the reaction channel of interest, secondly, to reconstruct the reaction kinematics, and lastly, to reach a better event-by-event γ-ray Doppler-shift correction.

No clear indication for the presence of a γ-ray transition at ~ 9.3 MeV, depopulating the resonance, arose from the analysis. A limit for the existence of such a gamma transition was therefore inferred: we excluded the existence of a peak with a confidence level of about 99 %, under the assumption of a γ branching ratio of 3×10^{-3} (as predicted by SMEC calculations) and a cross section for the population of the state of interest of ~ 150 µb, *i.e.*, similar to the nearby states.

The result of this experiment is expected to provide a strong constrain for theoretical models: in the future a more detailed and direct comparison with theory predictions will be performed. Moreover, the experimental technique developed in this context will serve as a reliable basis to extend this kind of studies to near-threshold states in other light systems.

The third research activity was devoted to the investigation of M4 stretched unbound-states decay in ^{14}N and ^{16}O. In particular, we were interested in the M4 resonances located at 16.9 and 20.1 MeV in ^{14}N and in the triplet of M4 stretched states at 17.79, 18.98 and 19.80 MeV in ^{16}O. The nuclei of interest were populated in a proton inelastic-scattering reaction, in an experiment realised at the Kraków CCB facility, in Poland. The experiment was part of a new research program, whose goal is to shed light on the decay of stretched M4 resonances in light $1p$-shell nuclei, and the experiment described in this Thesis was the second one carried out within the program. The first pilot experiment successfully investigated the decay of the 21.47-MeV M4 resonance in ^{13}C. A significant number of distinct decay branches have been identified, and a comparison of the observations with calculations carried out in the framework of the Gamow Shell Model, which enables calculations of states embedded in the continuum, showed a very good overall agreement.

In the experiment presented in this work, a proton beam of 135 MeV impinged on a thick Li^{14}NH$_2$ target, which was subsequently discovered to be heavily polluted with ^{16}O. The inelastically scattered protons were measured in the KRATTA triple-telescope detector array, while gamma rays were detected in four large-volume $LaBr_3$(Ce) scintillators and in two 9-fold phoswich clusters of the PARIS spectrometer. A detailed description of detectors calibrations and data processing has been reported. We then presented the reaction products identification, crucial to identify the daughter nuclei associated to the decay of unbound states in ^{14}N and ^{16}O.

At the end of the preliminary data processing, a proton-gamma coincidence matrix was produced, from the analysis of which a reconstruction of the decay scheme of the M4 resonances of interest could be achieved. In particular, in the case of ^{16}O, the results are well in agreement with previous experimental data. Therefore, the investigation of ^{16}O has been a valuable test case to validate the experimental technique to study M4

resonances decay in light nuclei. It has also confirmed the validity of the results of the pilot experiment and assessed the overall good performance of the experimental set-up. The physical interpretation of the results is still ongoing and would largely profit from theoretical calculations, that are not available at the moment.

Regarding ^{14}N, only a qualitative picture has emerged from the analysis, due, on the one hand, to the presence of strong contaminants (mostly ^{16}O) in the target and, on the other hand, to the lack of statistics. A new measurement with a target devoid of oxygen contamination is planned for autumn/winter 2021. In this latter case, GSM calculations can be performed to predict the features of the resonances of interest, and a comparison with experimental data would be crucial to further test this newly developed theoretical model.

In conclusion, a number of light systems has been investigated in the present work, focusing on bound states and unbound resonances, passing through the study of states in the vicinity of particle-emission thresholds. Experimental information on different observables has been collected using a combination of gamma- and particle-spectroscopy studies, which allowed to benchmark and stimulate further developments of modern nuclear theoretical models. This will pave the way to future experimental works, exploiting the novel techniques developed in this Thesis.

Appendices

Appendix A

Simulation code and lifetime analysis user manual

In this appendix, we will report a step-by-step description of the procedure to follow to perform tens-to-hundreds femtoseconds nuclear excited-states lifetime measurements with highly-dissipative mechanisms. The present documentation has been prepared to guide the reader in the use of the code developed in the context of the novel technique described in Section 5.2. Explicit instructions and commands to use the existing simulation and analysis codes will be given. The codes have been developed by M. Ciemała from the Kraków IFJ PAN for the experiment number *e676* at GANIL in the AGATA+PARIS+VAMOS campaign in July 2017 (see Chapter 4).

A.1 Prerequisites

To perform the lifetime-measurement analysis, some prerequisites are needed:

1. background-subtracted experimental velocity distribution of the emitting ion after the target, gated on a specific gamma-ray line (see *e.g.*, Figure 5.7);
2. background-subtracted gamma-ray energy spectrum in the region of the peak of interest, eventually divided in two or more sub-spectra gated on θ_{rel}, *i.e.*, the relative angle between the ion and gamma-ray directions (see Figure 5.13);
3. experimental angular distribution of the reaction products, gated on the gamma-ray line of interest (see Figure 5.9);
4. code to generate the events;
5. AGATA simulation software package [153] with proper geometry files and input macros;
6. Analysis scripts (part of the AGATA simulation package) and a program to calculate the χ^2;
7. Analysis software, like Excel [234] or Origin [233].

A.2 First step: output velocity simulation

The first step in the simulation procedure is the output velocity simulation: a very detailed schematic flow chart summarising this step has been already reported in Figure 5.8 in

```
level: ground_state 0.0

level: excited_state1 1906.8 7.600
        decay: ground_state 100 1

level: excited_state2 3129.0 191.
        decay: excited_state1    100 1

level: excited_state3 5170. 0.020
        decay: excited_state2    100 1

level: exciter 100000 0.1
             decay: excited_state3 100 10000
```

Figure A.1: `example.decay` example code. For each defined level, the energy in keV, the lifetime in femtoseconds and the decay scheme (final state, branch and transition ID number) are given.

Section 5.2.1. This step is performed exploiting the event-generation code, which requires four input files: the experimental angular distribution of the reaction products gated on the gamma-ray transition of interest, in `.txt` format, the `example.setup`, `example.decay`, and `input.beta` files.

The angular distribution (angle and normalised counts), gated on the gamma ray of interest, should be produced with 0.4 °/ch binning and then copied into the `190theta.txt` file. Only the region from 38.6° to 51.8° should be considered. These parameters (file name, binning and angular range) can be modified in the code, but are now fixed for simplicity. The `example.setup` file contains the number of events simulated, the information about the target (*e.g.*, A, Z and thickness), about the incoming beam and about the outgoing ejectiles. The `example.decay` input file defines the decay scheme that the user needs to simulate, as reported for example in Figure A.1, where a possible gamma-ray cascade in ^{17}N is reported. In this file, the user shall define an exciter level, from which the state of interest (*i.e.*, `excited_state3` in Figure A.1) will be subsequently populated, and the other excited states involved in the cascade, each with its energy, lifetime and decay properties. More than one decay state can be inserted in the decay pattern, each with its branching and transition identification number. The energy and the lifetime of the exciter state are artificial keywords, inserted to be consistent with the other levels. They simplify the input-file reading, but they are not used in the simulation. The same concerns the transition ID number from the exciter level, which is a randomly chosen number.

As schematically exemplified in Figure 5.8 and extensively discussed in Section 5.2.1, the objective of the output velocity simulation is the extraction of the total kinetic energy losses (TKEL) distribution (see also Figure 5.10) to be passed to the full event generation. In order to extract this distribution, an iterative procedure is required. In the first iteration, we consider the direct population of the state of interest (TKEL = E_0^*, with

probability equal to 1) and we produce a simulated velocity distribution, imposing this condition by modifying the `input.beta` file and writing into it the TKEL in MeV and the probability. For this step, 10^5 events are sufficient. We then run the event generation code by launching the following command:

```
./event_generator ./example.setup name_for_output | tee output_for_distr
```

The code will produce two output files, the first contains the generated events, while the second stores the velocity and angular distribution. The velocity distribution cannot be compared with the experimental one yet: before doing so, it has to be smeared to take into account the VAMOS++ ToF response. The smearing procedure is performed copying the file containing the distribution in the `dist` sub-directory (see next Section for the working directory structure) and then launching the command:

```
./hist_smear.out output_for_distr > histo_with_distribution.txt
```

This will produce not only the simulated velocity distribution in `.txt` format, but also a `.root` file containing the velocity histogram. In the `hist_smear.C` code one can modify the binning of the output velocity distribution, by changing the number of bins in the histogram and the parameters for writing out the distribution to file. After any modification, the code needs to be re-compiled with the `make` command.

After producing this first velocity profile, one has to compare it to the experimental velocity distribution, using for example either the Excel or the Origin software. If the state of interest is populated only directly, *i.e.*, there is a single Gaussian velocity component associated to the direct population of the state, the velocity simulation can be stopped here. Otherwise, the procedure should continue with another iteration, considering an increased TKEL in the `input.beta` file. Velocity distributions associated to higher TKEL in steps of around 2 MeV should be produced and then subtracted from the experimental velocity distribution with an appropriated scaling factor. This process should be repeated until the sum of the scaled simulated velocity distributions, subtracted from the experimental one, gives a difference comparable to 0.

Summarising, the user should produce a number of simulated velocity distributions associated with different TKEL with probability equal to 1 and combine them with appropriate scaling factors, until the experimental velocity is being reproduced. The scaling factors are then converted in percentage values and reported in the `input.beta` file with their corresponding TKEL, as shown in Figure A.2 in the case of the 2779-keV state in ^{19}O (see discussion connected to Figure 5.10).

The probabilities should sum up to 1 and up to six steps are admitted in the present version of the code. The possible values for the TKEL span from the excitation energy of the state of interest to the sum of the particle-emission thresholds of both the projectile-like nucleus considered and its partner produced in the reaction. For example, in the ^{18}O + ^{181}Ta $\rightarrow$ ^{17}N + ^{182}W reaction, the maximum TKEL is 12 980 keV ($TKEL_{max}$ = $S_n(^{17}N)+S_p(^{182}W)$ = 5885 keV + 7095 keV [53]). Before proceeding to the next step, it is advisable to check that the total simulated velocity distribution coincides with the one obtained by summing the different components separately.

```
2.779          0.71
5.0            0.06
7.0            0.1
9.0            0.05
11.0           0.05
13.0           0.03
```

Figure A.2: `input.beta` example code. In the file, the total kinetic energy losses (TKEL) steps required to fully reproduce an experimental velocity profile, expressed in MeV, with the corresponding probabilities are defined. Up to six steps are admitted in the present version of the code. In this specific example, are reported the TKEL for the simulation of the velocity profile associated to the population of the $7/2^+$ excited state in ^{19}O at 2779 keV.

A.3 Second step: full event generation

After simulating the output velocity, the user can proceed with the full event generation. At this point, one has to choose the range and step in energy and lifetime to be simulated. For example, a 10-MeV region around the possible gamma-ray energy, with steps of 1-2 MeV and lifetimes from 5 to 200 fs in steps of 5-10 fs, can be simulated. The process is quite time consuming, therefore it is advisable to start with a reasonable number of steps and eventually increase them later. In addition, when the statistics in the gamma-ray energy spectra is limited, going down to 1 fs steps in lifetime is not advisable, since the uncertainty will be much larger in any case.

This step requires a number of folders to be created in the working directory, corresponding to the gamma-ray energies that have to be simulated. Figure A.3 schematically shows the structure of the working directory. In each folder there should be a set of copies of the `example.decay` file, each with the corresponding excitation energy and lifetime of the state of interest. It is useful to name each file with the value of the lifetime. For example, to simulate a gamma-ray energy of 2041 keV in a range of ±2 keV with steps of 1 keV and lifetimes from 10 to 150 fs in steps of 10 fs, five folders are needed, one for each energy (*i.e.*, `2039keV`, `2040keV`, `2041keV`, `2042keV` and `2043keV`). In each directory there will be fifteen copies of the `example.decay` file, each named after the value of the lifetime (*i.e.*, `10`, `20`, `30`,..., `150`). In each file, the excitation energy of the state of interest is modified accordingly to which folder they belong to. The `example.decay` file reported in Figure A.1, which describes a gamma cascade in ^{17}N where a 2041 keV gamma transition de-excites a state at 5170 keV with a lifetime $\tau = 20$ fs, populating another excited state at 3129 keV, would be inside the `2041keV` directory and would have the file name `20`. It is advisable to create also a set of directories where the output files will be moved after the simulation, for example called `2041keV_input`; the "input" term derives from the fact that the files in these directories will be used as input to the AGATA simulation package, that we will introduce in the next section.

For this step, we usually simulate 4×10^6 events (defined in `example.setup` first line) and we launch the code in a loop with the following script:

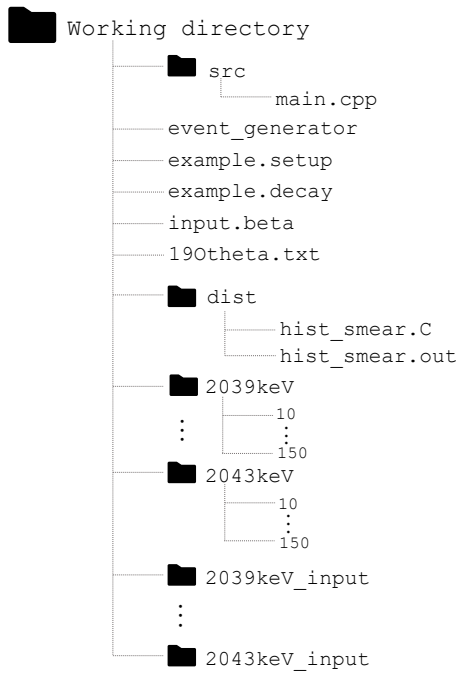

Figure A.3: Structure of the working directory for the event-simulation step. See text for details.

```
for i in {start_lifetime..end_lifetime..lifetime_step};
do cp /PATH_TO_FILE/$i example.decay;
./event_generator ./example.setup out_energy_$i;
mv out_energy_$i /PATH_TO_OUTPUT_FOLDER/.; done
```

The command can be launched in parallel for each energy that has to be simulated. To speed up the calculations, the line number 607 in the `main.cpp` event generator source code should be commented, in order to suppress the printing out of the velocity. The code has to be compiled again with `make`, after commenting the line.

A.4 Third step: AGATA gamma-ray simulation

The third step in the lifetime-measurement process involves the AGATA gamma-ray energy spectra simulation, performed with the GEANT4 AGATA simulation software [153]. We will not discuss here how to install an updated version of the code, but how to use it for the purpose of the present analysis. The code can be called from any location and will produce as output a file called `GammaEvents.0000`, containing non-tracked, non-Doppler-corrected gamma-ray events. These events have to be analysed afterwards with specific analysis codes (given in the same simulation package) to track and Doppler-shift correct the spectra.

The AGATA simulation code requires as input specific geometry input files that depend on the experimental configuration. The necessary input files (for example files

named `aeuler`, `aclust`, `aevent`, `asolid`) should be copied in the folder where the code is called.

The simulation code can be used in two different ways: the first option is to call the program and then pass the commands from command line inside the simulation environment; the second option, that will be discussed here, consists in running the program passing pre-written macros.

In Figure A.4, an example of input macro is shown: the macro defines the specific input geometry file and it enables the list-mode option for saving the output. Here, the `agata8T4D_mod.mac` macro is associated to the geometry of the present experiment, with 8 triple clusters and 4 double clusters. The input macro also specifies the maximum dimension of the output file (4 Gb), it provides the location of the input file, which corresponds to the files produced in the previous step with the event generator, and finally starts the simulation with a fixed number of events (4×10^6 in the present case). For completeness, we report in Figure A.5 also the `agata8T4D_mod.mac`, that is used here mainly to define the specific geometry of the experiment. The commands used in the macro are extensively described in the code user manual [235].

```
/control/execute /PATH_TO_MACRO/agata8T4D_mod.mac
/Agata/file/enableLM
/Agata/file/fileSize 4096
/Agata/generator/emitter/eventFile /PATH_TO_FILE/file
/Agata/run/beamOn 4000000
```

Figure A.4: Example of AGATA simulation code input macro.

The general command to launch the code is:

```
./PATH/Agata -noQT -Ext -b macroname.mac
```

where the `-noQT` option inhibits the opening of a graphical interface, the `-Ext` option is used to pass an external input file and the `-b` option is needed to run the program with a macro. In the present case the best option is to run the program in a loop with a script similar to the following:

```
for i in {start_lifetime..end_lifetime..lifetime_step};
do rm file; ln -s /PATH_TO_INPUT_FILE/out_energy_$i ./file;
/PATH_TO_SIMULATION_CODE/Agata -Ext -noQT -b run.mac;
mv GammaEvents.0000 result_energy_$i;
mv result_energy_$i /PATH_TO_AGATA_RESULTS_FOLDER/.; done
```

At the end of the simulation, the user should check that the number of crystals simulated corresponds to the one present in the experiment, included the missing detectors. For example, in the *e676* experiment 32 detectors were present (31 fully working), but there was a number of missing detectors (associated to non-consecutive numbering, see for example Figure 5.1), that brought the total number of considered crystals to 45. This difference should be fixed at the end of the simulation, before proceeding with the

```
/Agata/file/info/outputMask 11100110
#/Agata/detector/enableAncillary
/Agata/detector/traslateArray 0. 0. 0.
/Agata/detector/solidFile /PATH/A180/A180solid.list
/Agata/detector/angleFile /PATH/A180/A180eulerE676.list
/Agata/detector/wallsFile /PATH/A180/A180wallsS2p.list
/Agata/detector/clustFile /PATH/A180/A180clustS2p.list
/Agata/detector/sliceFile /PATH/A180/A180slice.list
/Agata/detector/enableCapsules
/Agata/detector/wallThickness 4.0
#/Agata/detector/chamberRadius 230.0
#/Agata/detector/chamberMaterial Aluminium
#/Agata/detector/pipeRadius 60.0
#/Agata/detector/targetMaterial Lead
#/Agata/detector/targetSize 62.25 62.25 500.0
/Agata/detector/rotateArray 0. -33.9 0.
/Agata/detector/targetPosition 0 0 0
/Agata/detector/update
#/Agata/generator/recoil/beta 10
#/Agata/generator/gamma/energy 1408.
#/Agata/generator/direction 0 0 1.0
```

Figure A.5: Additional macro to define the experimental geometry. The lines which comes after the # symbol are commented, but are kept to show some other possible commands that can be included in the macro.

analysis codes. In each output file this number should be changed with the following command:

```
sed -i '/SUMMARY 235.008 329.202 OLD# 3 6 6 6 6 6 6/c\SUMMARY 235.008
            329.202 NEW# 3 6 6 6 6 6 6' Simulation_output
```

Pay attention to the other numbers in the line that should remain the same.

At this point, the output files can be passed to the analysis code that will perform tracking and Doppler-shift correction on the γ-ray energy spectra, with the following command:

```
/PATH_TO_ANALYSIS_CODE/analyse.sh filename
```

The code will produce a `filename_output` file, with four columns of data containing the relative angle between the ion and gamma ray (θ_{rel}) in degrees, the Doppler-corrected energy in keV, the beta relativistic parameter and the ID of the detector that fired.

A.5 Fourth step: χ^2 calculation

In the last step of the process, we are ready to calculate the χ^2 for each (E_γ,τ) combination. To do so, the user has to create a text file for each simulated energy, containing the path to all the output files (one for each lifetime). The user has to provide the background-subtracted experimental gamma-ray energy spectra gated on the desired relative-angle ranges (*e.g.*, 120-140°, 140-160°, 160-180°): `.txt` files should contain the counts and the errorbar associated to each bin. The uncertainties are calculated as the square root of the sum of the counts in each bin before the background subtraction, and the counts associated to the background. The `hist.C` ROOT macro, which is used to calculate the χ^2 values, has to be modified accordingly, in order to correctly read the files containing the experimental spectra, to define the angular ranges and the bins that have to be compared. It is advisable to restrict the comparison to the peak region only, excluding the background regions on the sides, that can lead to poor results, because of the background fluctuations that the simulation cannot fully reproduce. The user shall also manually modify the lines number 392, 396 and 399: in these lines a parameter scales the detectors energy resolution (σ) as a function of $\sqrt{E_\gamma}$. This parameter is equal to 1 at $E_\gamma = 2200$ keV, while for example, for a gamma ray at 5515 keV, the parameter increases to 1.6. Then, the following command will compare the simulated and experimental energy spectra in the region of interest and calculate the χ^2 values:

```
for i in ‘cat file_energy‘; do ./hist.out $i >> results_energy; done
```

The program will write into the `results_energy` file a series of numbers divided into columns. The first column corresponds to the total χ^2 and each line is associated with a different lifetime value. The other columns contain the partial χ^2 corresponding to the angular ranges in which the gamma-ray spectrum has been divided.

The final step consists in producing a two-dimensional (τ,E_γ) χ^2 surface, using for example the Origin software. To produce the surface, the user shall insert two additional columns in the `results_energy` files, the first with the associated energy (equal for all the lines in the same file) and the second with the lifetime values. Then, copying the first three columns of these files (E_γ [x], τ [y], χ^2_{tot} [z]) in an Origin workbook and plotting the data with a "Contour-Color fill" option, the map will be ready (see Figure 5.13(d)). At first, the map will not be smooth, since only discrete points have been simulated. To make the map appear smoother, enable the smoothing option, adjusting the number of points and the smoothing parameter, until reaching the desired aspect. Pay attention to the smoothing out feature: it can significantly change the final result introducing fake minima or cancelling out the real ones. The best option is to compare the original and smoothed maps to check that the results are not affected by the process, but only the appearance of the graph is modified.

Appendix B

Gamma spectroscopy summary

In the present Appendix, we will summarise the spectroscopic information associated to the nuclei populated in the GANIL experiment of Part II, in the deep-inelastic ^{18}O+^{181}Ta reaction (see Figure 4.1). In Tables from B.1 to B.23 are listed: the γ-ray energies (E_γ), the spin/parity of the initial and final states ($J_i^\pi \rightarrow J_f^\pi$), the radiation multipolarity (M_γ) and the depopulated state lifetime (τ), expressed in femtoseconds, corresponding to the gamma transitions observed experimentally. From our experimental data we deduced, in particular, the gamma-ray energies for those transitions de-exciting long-lived states (lifetime $\tau \gtrsim 400$ fs), and short-lived states ($\tau \lesssim 400$ fs) feeded from higher-lying long-lived ones. For the transitions depopulating short-lived states (without feeding) we could not extract the gamma ray energy, as these lines appear shifted towards lower energies, due to the short lifetime. In few cases of long lived-states (see Table B.13), we could not measure the energy of the de-exciting transitions due to the limited statistics. In ^{14,16}C (see Tables B.6 and B.8), ^{17,18}N (see Tables B.13 and B.14), ^{17,19,20}O (see Tables B.17, B.19 and B.20) we measured also the lifetimes of a number of excited states, employing a new implementation of the Doppler-Shift Attenuation Method (DSAM), introduced in Section 5.2. All the gamma rays reported are known, except in the case of ^{18}N and ^{19}N. In ^{18}N (Table B.14) we identified eight new gamma transitions (see Section 5.4), while in ^{19}N (Table B.15) a new transition at 2489.7(8) keV has been measured. Missing information is reported in the Tables with a question mark.

In the following Tables, in black is reported the information taken from the database [53], while in blue are reported the values measured in our dataset.

Table B.1: ^{11}B summary.

^{11}B			
$\mathbf{E_\gamma}$ **[keV]**	$\mathbf{J_i^\pi \rightarrow J_f^\pi}$	$\mathbf{M_\gamma}$	$\boldsymbol{\tau}$ **[fs]**
2124.473(27)	$1/2_1^- \rightarrow 3/2_1^-$ (g.s.)	M1	8.1(3)
4444.03(8)	$5/2_1^- \rightarrow 3/2_1^-$ (g.s.)	M1+E2	1.7(1)

Table B.2: ^{12}B summary.

^{12}B			
E_γ [keV]	$J^\pi_i \rightarrow J^\pi_f$	M_γ	τ [fs]
953.10(60)	$2^+_1 \rightarrow 1^+_1$ (g.s.)	M1	260(40)
1667.54(60)	$1^-_1 \rightarrow 2^+_1$	E1	<50
1673.52(60)	$2^-_1 \rightarrow 1^+_1$ (g.s.)	E1	<50

Table B.3: ^{13}B summary.

^{13}B			
E_γ [keV]	$J^\pi_i \rightarrow J^\pi_f$	M_γ	τ [fs]
3690(2)	$?^+ \rightarrow 3/2^-_1$ (g.s.)	[E1]	$55(20)\times10^3$
4131	$?\rightarrow 3/2^-_1$ (g.s.)	?	<30

Table B.4: ^{12}C summary.

^{12}C			
E_γ [keV]	$J^\pi_i \rightarrow J^\pi_f$	M_γ	τ [fs]
4438.91(31)	$2^+_1 \rightarrow 0^+_1$ (g.s.)	E2	88(5)

Table B.5: ^{13}C summary.

^{13}C			
E_γ [keV]	$J^\pi_i \rightarrow J^\pi_f$	M_γ	τ [fs]
3089.049(20)	$1/2^+_1 \rightarrow 1/2^-_1$ (g.s.)	[E1]	1.54(14)
3683.921(23)	$3/2^-_1 \rightarrow 1/2^-_1$ (g.s.)	[M1+E2]	1.59(13)
3853.0(4)	$5/2^+_1 \rightarrow 1/2^-_1$ (g.s.)	[M2+E3]	$12.41(20)\times10^3$

Table B.6: ^{14}C summary.

^{14}C				
E_γ [keV]	$J^\pi_i \rightarrow J^\pi_f$	M_γ	τ [fs]	Notes
6092.4(2)	$1^-_1 \rightarrow 0^+_1$ (g.s.)	[E1]	<10	-
6726.8(8)	$3^-_1 \rightarrow 0^+_1$ (g.s.)	[E3]	$95(12)\times10^3$	-
7009.5(8)	$2^+_1 \rightarrow 0^+_1$ (g.s.)	[E2]	65^{+32}_{-29}	See Section 5.3.2

Table B.7: ^{15}C summary.

^{15}C			
E_γ [keV]	$J_i^\pi \rightarrow J_f^\pi$	M_γ	τ [fs]
739.92(17)	$5/2_1^+ \rightarrow 1/2_1^+$ + (g.s.)	[E2]	$3.77(10) \times 10^6$

Table B.8: ^{16}C summary.

^{16}C				
E_γ [keV]	$J_i^\pi \rightarrow J_f^\pi$	M_γ	τ [fs]	Notes
1759.3(2)	$2_1^+ \rightarrow 0_1^+$ (g.s.)	E2	$11.4^{+1.2}_{-1.9} \times 10^3$	-
2217(2)	$2_2^+ \rightarrow 2_1^+$	?	<180	See Section 3.1 and Ref. [52]
2317(5)	$3_1^{(+)} \rightarrow 2_1^+$	?	$<4.0 \times 10^3$	-
2374(3)	$4_1^+ \rightarrow 2_1^+$	?	$<4.0 \times 10^3$	-

Table B.9: ^{17}C summary.

^{17}C			
E_γ [keV]	$J_i^\pi \rightarrow J_f^\pi$	M_γ	τ [fs]
330.2(2)	$5/2_1^+ \rightarrow 3/2_1^+$ (g.s.)	?	$15.1(24) \times 10^3$

Table B.10: ^{14}N summary.

^{14}N			
E_γ [keV]	$J_i^\pi \rightarrow J_f^\pi$	M_γ	τ [fs]
2312.593(11)	$0_1^+ \rightarrow 1^+$ (g.s.)	[M1]	98(4)
1635.20(20)	$1_1^+ \rightarrow 1^+$ (g.s.)	[M1]	6.9(26)

Table B.11: ^{15}N summary.

^{15}N			
E_γ [keV]	$J_i^\pi \rightarrow J_f^\pi$	M_γ	τ [fs]
1884.77(2)	$5/2_2^+ \rightarrow 5/2_1^+$	[M1(+E2)]	17(9)
2296.8(10)	$7/2_1^+ \rightarrow 5/2_1^+$	[M1+E2]	12^{+12}_{-6}
5269.161(14)	$5/2_1^+ \rightarrow 1/2^-$(g.s.)	[M2+E3]	2.58(14)
5297.817(14)	$1/2_1^+ \rightarrow 1/2^-$(g.s.)	[E1]	25(7)
6322.35(2)	$3/2_1^- \rightarrow 1/2^-$(g.s.)	[M1+E2]	0.211(12)

Table B.12: ^{16}N summary.

^{16}N			
E_γ [keV]	$J_i^\pi \rightarrow J_f^\pi$	M_γ	τ [fs]
276.45(11)	$1_1^- \rightarrow 0_1^-$	[M1]	$5.63(12) \times 10^3$
297.79(11)	$3_1^+ \rightarrow 2_1^-$ (g.s.)	[M1]	$131.7(19) \times 10^3$

Table B.13: ^{17}N summary.

^{17}N				
E_γ [keV]	$J_i^\pi \rightarrow J_f^\pi$	M_γ	τ [fs]	Notes
475.7(3)	$1/2_1^+ \rightarrow 3/2_1^-$	[E1]	$12(2) \times 10^3$	Low statistics
499.7(2)	$(7/2, 9/2)_{(?)}^- \rightarrow 7/2_1^-$	[M1]	$12(2) \times 10^3$	-
532.66(13)	$5/2_1^- \rightarrow 3/2_1^-$	[M1]	$11.0(20) \times 10^3$	-
619.81(12)	$5/2_1^+ \rightarrow 5/2_1^-$	[E1]	$33.0(30) \times 10^3$	
676.4(5)	$5/2_1^+ \rightarrow 1/2_1^+$	[E2]	$33.0(30) \times 10^3$	Low statistics
1152.21(20)	$5/2_1^- \rightarrow 3/2_1^-$	[E1]	$33.0(30) \times 10^3$	-
1222.6(3)	$7/2_1^- \rightarrow 5/2_1^-$	[M1]	$276(81) \times 10^3$	-
1373.94(16)	$3/2_1^- \rightarrow 1/2^-$ (g.s.)	[M1]	92(35)	Feeding long-lived
1722.6(4)	$(7/2, 9/2)_{(?)}^- \rightarrow 5/2_1^-$	[E2]	$12.0(20) \times 10^3$	-
1766(3)	$(1/2, 3/2)_{(?)}^+ \rightarrow 3/2_1^($+)	?	< 120	-
1850.2(2)	$1/2_1^+ \rightarrow 1/2^-$ (g.s.)	[E1]	$(40^{+20}_{-9}) \times 10^3$	-
1906.6(2)	$5/2_1^- \rightarrow 1/2^-$ (g.s.)	[E2]	$11.0(20) \times 10^3$	-
1999.1(20)	$(3/2, 5/2)_{(?)}^- \rightarrow 5/2_1^-$	[M1]	52(22)	-
$2045.0^{+1.2}_{-1.7}$	$(9/2^+)_1 \rightarrow 7/2_1^-$	?	35^{+110}_{-30}	See Section 5.3.1
2508(3)	$(3/2, 5/2)_{(?)}^- \rightarrow 5/2_1^-$	?	< 61	
2526.6(4)	$5/2_1^+ \rightarrow 1/2^-$ (g.s.)	[M2]	$33.0(30) \times 10^3$	-
$2647.8^{+1.4}_{-1.9}$	$(9/2^+)_1 \rightarrow 5/2_1^+$	?	35^{+110}_{-30}	See Section 5.3.1
2835(3)	$5/2_1^+ \rightarrow 3/2_1^-$	?	< 71	-
3203.6(13)	$3/2_2^- \rightarrow 1/2^-$ (g.s.)	[M1]	< 30	Feeding long-lived
3865(3)	$(1/2, 3/2)_{(?)}^+ \rightarrow 5/2_1^-$	?	< 120	-
$4141.0^{+0.7}_{-3.5}$	$3/2_{(?)}^- \rightarrow 3/2_1^-$	?	<60	See Section 5.3.1
4398(3)	$(1/2, 3/2)_{(?)}^+ \rightarrow 3/2_1^-$	?	< 120	-
$5515.0^{+1.7}_{-3.5}$	$3/2_{(?)}^- \rightarrow 1/2^-$ (g.s.)	?	<60	See Section 5.3.1

Table B.14: ^{18}N summary. See Section 5.4 for details.

^{18}N			
E_γ [keV]	$J_i^\pi \rightarrow J_f^\pi$	M_γ	τ [fs]
114.6(1)	$2_1^- \rightarrow 1^-$ (g.s.)	?	$0.40(11) \times 10^6$
154.6(3)	$3_1^- \rightarrow 2_1^-$	?	?
472.7(2)	$(2_2^-) \rightarrow (2_2^-)$	?	?
627(1)	$3_1^- \rightarrow 2_1^-$	?	?
1091(1)	$(1_2^-) \rightarrow 2_1^-$	?	?
1147(1)	$(0_1^-) \rightarrow 1_1^-$ (g.s.)	?	?
1205(1)	$(1_2^-) \rightarrow 1_1^-$ (g.s.)	?	?
1566(1)	$(3_3^-) \rightarrow 3_1^-$	?	?
1663.0(8)	$(4_1^-) \rightarrow 3_1^-$	?	160^{+740}_{-100}
1721.0(11)	$(3_3^-) \rightarrow (2_2^-)$	?	?
2073.4(8)	$(3_2^-) \rightarrow 2_1^-$	?	?
2301.0(8)	$(2_3^-) \rightarrow 2_1^-$	?	?
2416(2)	$(2_3^-) \rightarrow 1_1^-$ (g.s.)	?	?

Table B.15: ^{19}N summary.

^{19}N				
E_γ [keV]	$J_i^\pi \rightarrow J_f^\pi$	M_γ	τ [fs]	Notes
532(2)	$(5/2_1^-) \rightarrow (3/2_1^-)$	?	?	-
1141(3)	$(3/2_1^-) \rightarrow (1/2^-)$(g.s.)	?	?	-
1494(6)	$(7/2_1^-) \rightarrow (5/2_1^-)$	?	?	-
1681(5)	$(5/2_1^-) \rightarrow (1/2^-)$(g.s.)	?	?	-
2489.7(8)	?	?	?	New line. See Ref. [167]

Table B.16: ^{16}O summary.

^{16}O			
E_γ [keV]	$J_i^\pi \rightarrow J_f^\pi$	M_γ	τ [fs]
6129.3(6)	$3_1^- \rightarrow 0^+$ (g.s.)	[E3]	$18.4(5) \times 10^3$
6915.5(6)	$2_1^+ \rightarrow 0^+$ (g.s.)	[E2]	4.70(13)
7115.15(14)	$1_1^- \rightarrow 0^+$ (g.s.)	[E1]	8.3(5)

Table B.17: ^{17}O summary.

^{17}O				
E_γ [keV]	$J_i^\pi \rightarrow J_f^\pi$	M_γ	τ [fs]	Notes
869.87(13)	$1/2_1^+ \rightarrow 5/2^+$(g.s.)	[E2]	$259(3) \times 10^3$	-
$2184.3^{+0.3}_{-0.2}$	$1/2_1^- \rightarrow 1/2_1^+$	[E1]	159^{+40}_{-30}	See Section 5.2
3842.3(4)	$5/2_1^- \rightarrow 5/2^+$(g.s.)	[E1]	≤ 26	-

Table B.18: ^{18}O summary.

^{18}O			
E_γ [keV]	$J_i^\pi \rightarrow J_f^\pi$	M_γ	τ [fs]
1572.07(18)	$4_1^+ \rightarrow 2_1^+$	E2	$24.8(12) \times 10^3$
1651.90(19)	$0_2^+ \rightarrow 2_1^+$	E2	$1.38(16) \times 10^3$
1938.2(2)	$2_2^+ \rightarrow 2_1^+$	M1	26.5(29)
1982.34(21)	$2_1^+ \rightarrow 0^+$ (g.s.)	E2	$2.80(7) \times 10^3$
3114.5(6)	$3_1^- \rightarrow 2_1^+$	E1	62(25)
3271.7(4)	$2_3^+ \rightarrow 2_1^+$	M1+E2	10.1(5)
3548.06(16)	$2_1^- \rightarrow 2_1^+$	E1	< 17
3919.60(22)	$2_2^+ \rightarrow 0^+$ (g.s.)	E2	26.5(29)
4422(?)	$3_2^- \rightarrow 2_1^+$	E1	30(14)
5254(?)	$2_3^+ \rightarrow 0^+$ (g.s.)	E2	10.1(5)

Table B.19: ^{19}O summary.

^{19}O				
E_γ [keV]	$J_i^\pi \rightarrow J_f^\pi$	M_γ	τ [fs]	Notes
1375.50(17)	$1/2_1^+ \rightarrow 3/2_1^+$	M1	$1.27(17) \times 10^3$	-
2370.6(3)	$9/2_1^+ \rightarrow 5/2^+$ (g.s.)	E2	$> 2.4 \times 10^3$	-
$2779^{+1.0}_{-0.8}$	$7/2_1^+ \rightarrow 5/2^+$(g.s.)	M1+E2	140^{+50}_{-40}	See Sec. 5.2 and Ref. [82]
3057.4(5)	$5/2_1^+ \rightarrow 3/2_1^+$	?	$> 0.7 \times 10^3$	-
3138.48(18)	$(1/2, 3/2^-) \rightarrow 3/2_1^+$	?	?	-
3849.49(15)	$3/2^-_{1(?)} \rightarrow 3/2_1^+$	E1	?	-
3945.1(4)	$3/2^-_{1(?)} \rightarrow 5/2^+$(g.s.)	E1	?	-

Table B.20: ^{20}O summary.

^{20}O				
E_γ [keV]	$J_i^\pi \rightarrow J_f^\pi$	M_γ	τ [fs]	Notes
1673.56(18)	$2_1^+ \rightarrow 0^+$ (g.s.)	E2	$10.5(4) \times 10^3$	-
1897.0(9)	$4_1^+ \rightarrow 2_1^+$	?	?	-
2394.6(10)	$2_2^+ \rightarrow 2_1^+$	?	150^{+80}_{-30}	See Section 3.1 and Ref. [52]
3562(7)	$2_3^+ \rightarrow 2_1^+$	?	?	-
3923(11)	$(3_1^-) \rightarrow 2_1^+$	?	?	-
4069.4(23)	$2_2^+ \rightarrow 0^+$ (g.s.)	?	?	-

Table B.21: ^{19}F summary.

^{19}F			
E_γ [keV]	$J_i^\pi \rightarrow J_f^\pi$	M_γ	τ [fs]
1356.9	$\frac{3}{2}^+_1 \rightarrow \frac{5}{2}^+_1$	M1	5.0(30)
2582.7	$\frac{9}{2}^+_1 \rightarrow \frac{5}{2}^+_1$	E2	280(30)

Table B.22: ^{20}F summary.

^{20}F				
E_γ [keV]	$J_i^\pi \rightarrow J_f^\pi$	M_γ	τ [fs]	Notes
167.69(13)	$4_1^+ \rightarrow 3_1^+$	[M1]	$79(6) \times 10^3$	-
657.26(13)	$3_1^+ \rightarrow 2^+$ (g.s.)	[M1+E2]	440(30)	Feeding long-lived
823.76(15)	$4_1^+ \rightarrow 2^+$ (g.s.)	[E2]	$79(6) \times 10^3$	-
1001.7(12)	$5_1^+ \rightarrow 4_1^+$	?	≤ 65	-
1311.0(3)	$2_1^- \rightarrow 2^+$ (g.s.)	[E1]	$1.88(9) \times 10^3$	-

Table B.23: ^{21}F summary.

^{21}F			
E_γ [keV]	$J_i^\pi \rightarrow J_f^\pi$	M_γ	τ [fs]
1754.74(8)	$(7/2^+, 9/2^+) \rightarrow 5/2^+$ (g.s.)	?	3.5(4)

Appendix C

GALTRACE test and new mechanics

This appendix is devoted to the description of the tests of the GALTRACE array (see Chapter 7), performed in preparation to the experiment realised in February/March 2021 to study the case of ^{11}B (see Chapter 8). A new mechanical design will be also presented.

To solve the mechanical issues related to the installation of the GALTRACE set-up, encountered in the commissioning experiment described in Section 7.2, a new 3D-printed ring was produced. The ring, which can host up to four telescopes, is separated in two parts, that can be screwed together once the detectors are mounted. Each telescope is individually pre-installed on a new specifically-designed 3D-printed frame, as shown in Figure C.1. The new frames host not only the telescope, but also the four preamplifier boards: one is placed on the same side of the frame with the detectors, while the other three boards are mounted on the other side of the frame. Dedicated holes in the frame allow the cables to pass to the other side. The preamplifiers remain now inside the ring, unlike in the previous configuration reported in Figure 7.3.

Another important feature of the new mechanics is that the detectors are protected from accidental impacts by a dedicated part of the frame and the wire bonding is shielded. The installation of absorbers is also simplified by additional custom-made 3D-printed plastic supports, which can be fitted on the screws that hold the telescope. The detectors can still be mounted in the forward and backward configurations (with respect to the beam line) from ∼45° to ∼135°, at the same distance ($\gtrsim$5 cm) from the target. With the updated configuration, new custom cables had to be realised to connect the detectors to the preamplifiers and the latter to the flange, through which the signals are transported outside the vacuum chamber. The installation is now faster and easier, with a reduced risk of damaging the detectors.

After the commissioning experiment described in Section 7.2, particular attention was paid to test the detectors, both ΔE and E layers, to prepare the full GALTRACE configuration with four telescopes. First of all, for the available detectors already glued and bonded to their PCB, we checked with a microscope that the wire-bonding was still intact. Those with damaged bonding or accidentally unglued from the board were sent in for repair. Some new silicons were also sent to be installed on the PCB. All the channels of the preamplifiers were tested to check if any of them needed to be repaired.

Then, we moved on to test the static characteristic (current I vs. voltage V curve) of each detector, to find the best working point. As the detectors are inverse biased, we

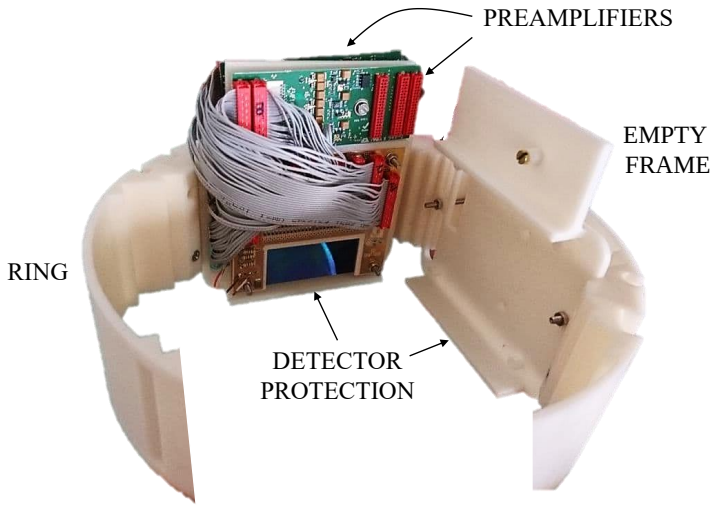

Figure C.1: The new GALTRACE ring and detector supports, with a complete telescope installed on its frame, together with the four preamplifier boards (one visible, three in the back of the frame). The custom cables connect the telescope to the preamplifiers. On the right, an empty frame is visible.

expect to observe the current increasing as a function of the applied voltage up to the point at which the detector is fully depleted: at this point the current saturates. As the applied voltage exceeds a certain threshold, the current abruptly increases causing an avalanche breakdown. The best working point is associated to the voltage at which the current saturates. Figure C.2 shows the I vs. V curves for the four couples of ΔE-E detectors chosen for the full GALTRACE configuration. The thin layers saturate between ~25 and 45 V, while the thick layers are depleted above ~300 V. The breakdown point has been avoided in order to protect the detectors from damaging.

The tests were performed in the first place inside a dedicated vacuum chamber, with the same read-out electronics used during the experiment. A different power supply module was used, the Caen N1470, usually employed to bias germanium detectors, which need high voltages of the order of thousands of volts. When the new mechanical infrastructure (ring and frames) and connecting cables were completed, the same tests were repeated with the GALTRACE telescopes directly installed in the GALILEO scattering chamber, to assure the same conditions expected during an experiment.

The preliminary tests in the dedicated vacuum chamber were repeated few times with different temperature conditions (~ 20 °C-30 °C), as the temperature in the laboratory environment fluctuated significantly during the day. Higher currents were observed when the room temperature was nearly ~ 30 % higher, without significant anomalies in the current trends. Figure C.3 displays the differences in the currents observed for two detectors, one thin and one thick, repeating the characterisation in the evening (warm, ~ 30 °C) and the following morning (cold, ~ 20 °C). The thick detector at the voltage of 500 V reaches the breakdown point when the temperature is warmer. The

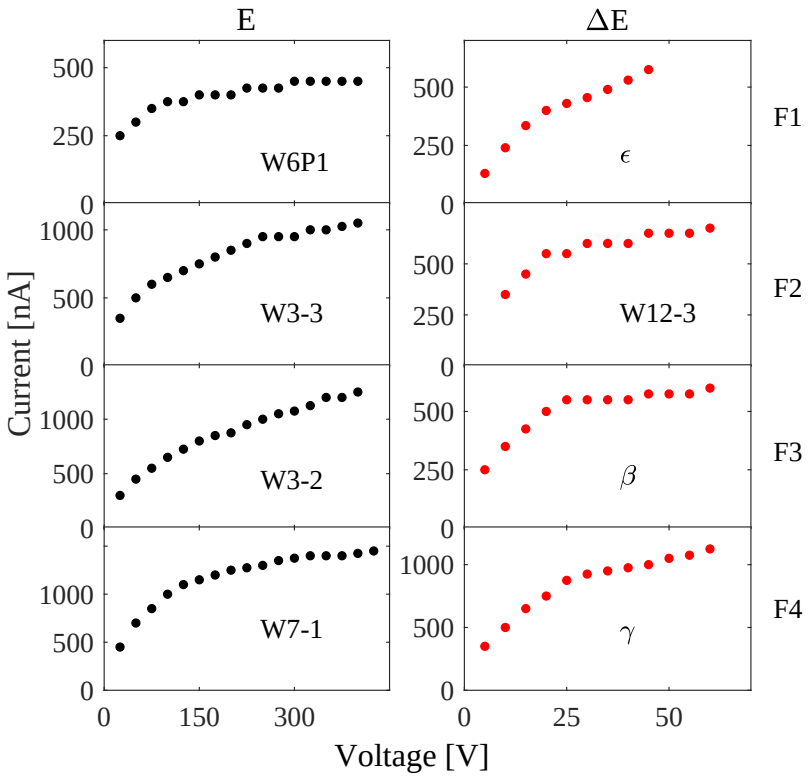

Figure C.2: I vs. V static characterisation of the full GALTRACE configuration detectors. Four ΔE-E couples are shown, with the detector identification string reported in each box (*i.e.*, W6P1, ϵ, W3-3, W12-3, W3-2, β, W7-1, and γ). On the right, we reported the frame number on which the telescopes were mounted. The frame numbers are associated to a specific position in the ring to respect the lookup table of the array, which is essential to guarantee one to one correlation between digitisers channels and detectors pads.

same characterisation was repeated ramping up and down the voltage, with negligible differences.

Among the tested detectors, two E layers were found to behave in an unexpected way, with a very high current, linearly increasing as a function of the voltage and exceeding the maximum 2 µA threshold supported by the power supply module. These two detectors (β E and ϵ E) could not be repaired.

After the static characterisation of the detectors and the definition of the working point, we continued by acquiring the energy spectra of a triple alpha source (^{241}Am + ^{244}Cm + ^{239}Pu). Figure C.4 reports a photograph of a ΔE-E couple inside the vacuum chamber with two triple-alpha sources, ready to be tested. The signal from the common electrode on the ohmic side (back) was considered as trigger.

During the tests we observed that some detectors had a saturated back signal baseline, as if the channel were short-circuited. We found out that this anomalous behaviour was caused by a defect in the decoupling capacitors mounted on the detectors PCBs. These

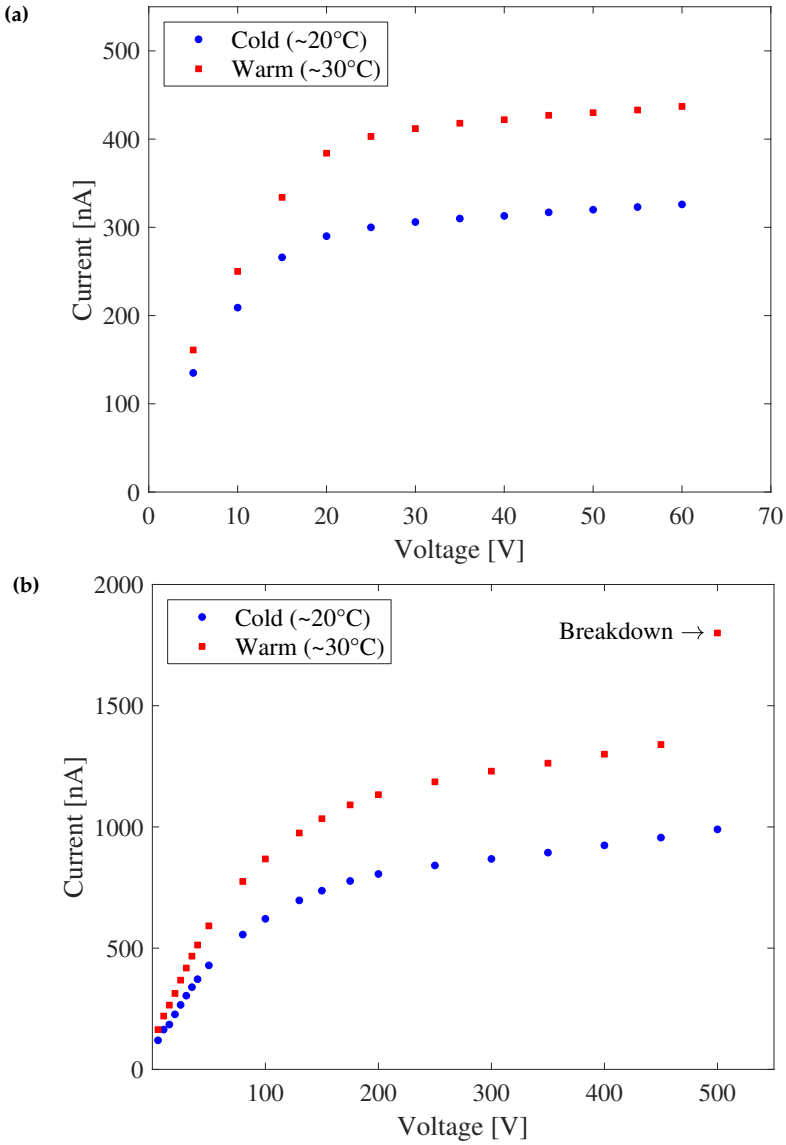

Figure C.3: I vs. V characterisation of the $\beta\,\Delta$E (a) and W7-1 E (b) detectors in two different temperature conditions, namely $\sim 20\,^{\circ}$C and $\sim 30\,^{\circ}$C.

capacitors were glued to the board before being soldered, and the glue acted as a parallel resistance, injecting current in the back preamplifier channel. Removing the glue and changing the capacitors solved the issue.

As an example, the Figures C.5 and C.6 display the acquired α spectra for the first 30 pixels of the W12-3 ΔE detector and the W3-3 E layer, respectively. The W12-3 ΔE layer presented a very good resolution, thanks to which the secondary peaks of the alpha source were clearly visible. Only one pad in sixty was missing and the pixel no. 5 had a

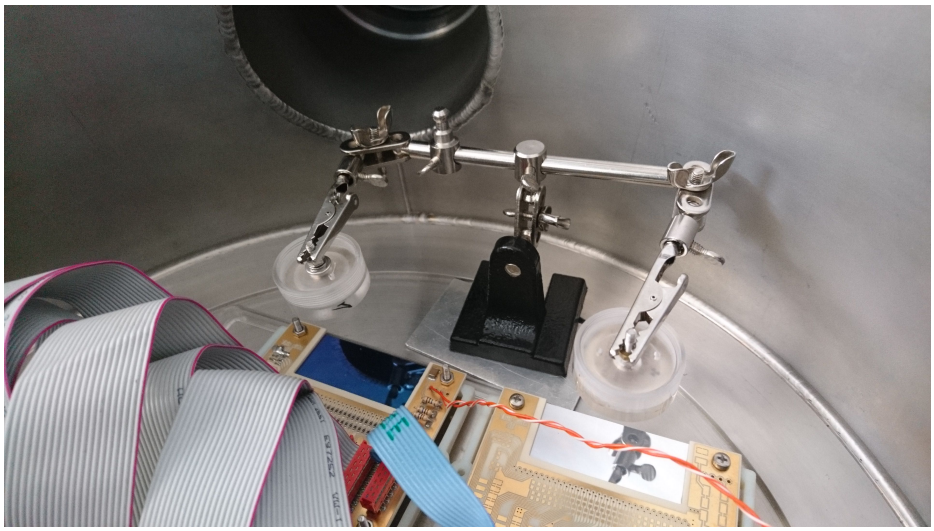

Figure C.4: Inside of the dedicated vacuum chamber, with two detectors (one ΔE, left, and one E, right) to be tested with two triple alpha sources.

worse resolution. Among the ΔE detectors chosen for the full GALTRACE configuration (see Figure C.2), only two pixels in a total of 240 were not working and only a few had a degraded resolution. All the E channels were fully functioning, with the 46-60 channel having a worse resolution with respect to the other ones for the W3-3, W3-2 and W7-1 detectors. The W6P1 silicon had all the four channels working well.

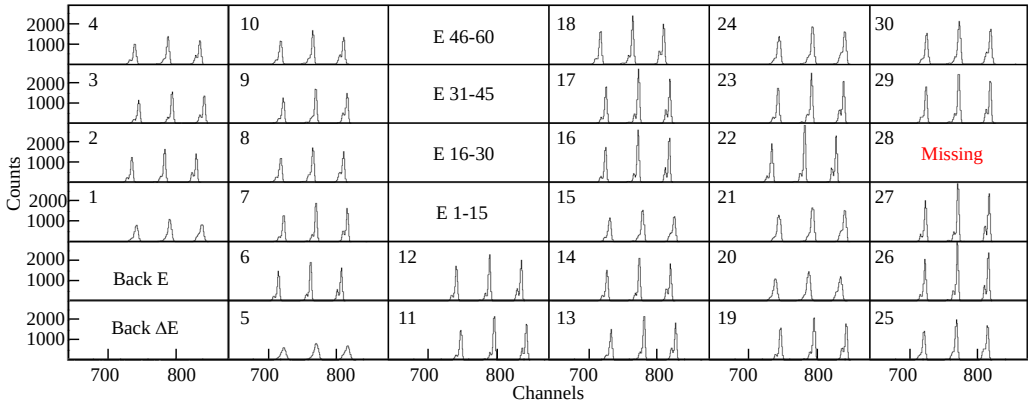

Figure C.5: Alpha spectra of the first 30 pixels of the W12-3 ΔE detector. One channel (no. 28) is missing and one (no. 5) has a worse resolution. All the other pixels have a very good resolution, which permits to discriminate the secondary peaks of the alpha source.

The detectors time stability was also checked during the tests: the detectors were left switched on during the night and the alpha spectra were acquired for more than 12 hours to verify that no fluctuations in the energy gain were present. The detectors turned out

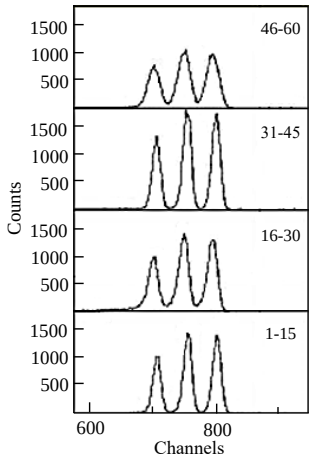

Figure C.6: Alpha spectra of the four channels of the W3-3 E detector. The 46-60 channel has a resolution about 1.5 times worse than the other channels.

to be stable during the long acquisition.

Bibliography

[1] G.G. Adamian, N.V. Antonenko, A. Diaz-Torres, and S. Heinz. "How to extend the chart of nuclides?" *Eur. Phys. J. A*, **56** (2020) 47.

[2] *Creative Commons Attribution 4.0 International License*. Creative Commons. URL: https://creativecommons.org/licenses/by/4.0/legalcode (visited on 07/06/2021).

[3] W. Nazarewicz. *Building the microscopic nuclear energy density functional*. 2014. URL: https://www.slideserve.com/dolf/unedf-building-the-microscopic-nuclear-energy-density-functional (visited on 10/03/2021).

[4] M. Goeppert Mayer. *Phys. Rev.*, **78** (1950) 16.

[5] O. Haxel, J. H. D. Jensen, and H. E. Suess. *Phys. Rev.*, **75** (1949) 1766.

[6] M. Goeppert Mayer. *Phys. Rev.*, **75** (1949) 1969.

[7] C. Yuan *et al.*, *Phys. Rev. C*, **85** (2012) 064324.

[8] C. Mahaux and H.A. Weidenmüller. *Shell Model Approach to Nuclear Reactions*. North-Holland, 1969.

[9] W. Iskra, M. Müller, and I. Rotter. *Phys. Rev. C*, **51** (1995) 1842.

[10] J. Okołowicz, M. Płoszajczak, and I. Rotter. *Phys. Rep.*, **374** (2003) 271.

[11] N. Michel, W. Nazarewicz, M. Płoszajczak, and T. Vertse. *J. Phys. G*, **36** (2008) 013101.

[12] K. Bennaceur, F. Nowacki, J. Okołowicz, and M. Płoszajczak. *J. Phys. G: Nucl. Part. Phys.*, **24** (1998) 1631.

[13] H. W. Barz, I. Rotter, and J. Hōhn. *Nucl. Phys. A*, **275** (1977) 111.

[14] J.-P. Ebran, E. Khan, T. Nikšić, and D. Vretenar. *Nature*, **487** (2012) 341.

[15] M. Freer *et al.*, *Rev. Mod. Phys.*, **90** (2018) 035004.

[16] W. von Oertzen, M. Freer, and Y. Kanada-En'yo. *Phys. Rep.*, **432** (2006) 43.

[17] M. Freer. *Nature*, **487** (2012) 309.

[18] M. Freer. *Scholarpedia*, **5** (2010) 9652.

[19] K. Ikeda, N. Takigawa, and H. Horiuchi. *Prog. Theor. Phys. Suppl.*, **464** (1968) Extra No.

[20] W. von Oertzen. *Phys. At. Nucl.*, **66** (2002) 169.

[21] C. Beck. *J. Phys. Conf. Ser.*, **436** (2013) 012014.

[22] M. Freer *et al.*, *Phys. Rev. Lett.*, *82* (1999) 1383.

[23] P. Descouvemont. *J. Phys. G: Nucl. Part. Phys.*, **35** (2007) 014006.

[24] H. Hergert. *Front. Phys.*, **8** (2020) 379.

[25] P. Navrátil *et al.*, *Phys. Scr.*, **91** (2016) 053002.

[26] R. Machleidt and F. Sammarruca. *Phys. Scr.*, **91** (2016) 083007.

[27] S. Weinberg. *Nucl. Phys. B*, **363** (1991) 3.

[28] B. R. Barrett, P. Navrátil, and J. P. Vary. *Prog. Part. Nucl. Phys.*, **69** (2013) 131.

[29] A. Tichai, R. Roth, and T. Duguet. *Front. Phys.*, **8** (2020) 164.

[30] F. Wegner. *Ann. Phys.*, **3** (1994) 77.

[31] S.D. Glazek and K.G. Wilson. *Phys. Rev. D*, **48** (1993) 5863.

[32] K. Tsukiyama, S.K. Bogner, and A. Schwenk. *Phys. Rev. Lett.*, **106** (2011) 222502.

[33] S.R. Stroberg, H. Hergert, S.K. Bogner, and J.D. Holt. *Annu. Rev. Nucl. Part. Sci.*, **69** (2019) 307.

[34] G. Hagen *et al.*, *Rep. Prog. Phys.*, **77** (2014) 096302.

[35] K. Hebeler, J.D. Holt, J. Menéndez, and A. Schwenk. *Annual Review of Nuclear and Particle Science*, **65** (2015) 457.

[36] T. Otsuka *et al.*, *Phys. Rev. Lett.*, **105** (2010) 032501.

[37] M. Thoennessen. *Rep. Prog. Phys.*, **76** (2013) 056301.

[38] D. S. Ahn *et al.*, *Phys. Rev. Lett.*, **123** (2019) 212501.

[39] T. Nakamura, H. Sakurai, and H. Watanabe. *Prog. Part. Nucl. Phys.*, **97** (2017) 53.

[40] O. Tarasov *et al.*, *Phys. Lett. B*, **409** (1997) 64.

[41] M. Fauerbach *et al.*, *Phys. Rev. C*, **53** (1996) 647.

[42] D. Guillemaud-Mueller *et al.*, *Phys. Rev. C*, **41** (1990) 937.

[43] S. Quaglioni. "Light and unbound nuclei". *Eur. Phys. J. Plus*, **133** (2018) 385. DOI: https://doi.org/10.1140/epjp/i2018-12238-0.

[44] C Forssén, R.Roth, and P. Navrátil. *J. Phys. G: Nucl. Part. Phys.*, **40** (2013) 055105.

[45] J. D. Holt, J. Menéndez, and A. Schwenk. *Eur. Phys. J. A*, **49** (2013) 39.

[46] M. Terasawa *et al.*, *Astrophys. J.*, **562(1)** (2001) 470.

[47] H. Herndl *et al.*, *Phys. Rev. C*, **60** (1999) 064614.

[48] T. Rauscher *et al.*, *Astrophys. J.*, **429** (1994) 499.

[49] C. Broggini *et al.*, *Riv. Nuovo Cim.*, **42** (2019) 103.

[50] J. J. Cowan *et al.*, *Rev. Mod. Phys.*, **93** (2021) 015002.

[51] M. Mumpower, R. Surman, G. McLaughlin, and A. Aprahamian. *Prog. Part. Nucl. Phys.*, **86** (2016) 86.

[52] M. Ciemała *et al.*, *Phys. Rev. C*, **101** (2020) 021303(R).

[53] Brookhaven National Laboratory. *National Nuclear Data Center*. URL: `https://www.nndc.bnl.gov`.

[54] F. Hoyle. *Astrophys. J., Suppl.*, **1** (1954) 121.

[55] M. Freer and H.O.Y. Fynbo. *Prog. Part. Nucl. Phys.*, **78** (2014) 1.

[56] J. Okołowicz, M. Płoszajczak, and W. Nazarewicz. *Prog. Theor. Phys. Suppl.*, **196** (2012) 230.

[57] J. Okołowicz, W. Nazarewicz, and M. Płoszajczak. *Fortschr. Phys.*, **61** (2013) 66.

[58] T. Kibédi *et al.*, *Phys. Rev. Lett.*, 125 (2020) 182701.

[59] N. Michel, W. Nazarewicz, M. Płoszajczak, and K. Bennaceur. *Phys. Rev. Lett.*, **89** (2002) 042502.

[60] S. Raman, L.W. Fagg, and R.S. Hicks. "Giant Magnetic Resonances". *Electric and Magnetic Giant Resonances in Nuclei*. Ed. by J. Speth. World Scientific Publishing Company, 1991. Chap. IV pp. 355–533.

[61] L. Zamick. *Phys. Rev. C*, **29** (1984) 667.

[62] A. Amusa and R. D. Lawson. *Phys. Rev. Lett.*, **51** (1983) 103.

[63] D.B. Holtkamp *et al.*, "Isospin Mixing of 4^- Particle-Hole States in ^{16}O". *Phys. Rev. Lett.*, **45** (1980) 420.

[64] S. Paschalis *et al.*, *Nucl. Instrum. Methods Phys. Res. A*, **709** (2013) 44.

[65] M. Assié *et al.*, 2021. arXiv: `2104.10707 [physics.ins-det]`.

[66] D. Testov *et al.*, *Eur. Phys. J. A*, **55** (2019) 47.

[67] M. Labiche *et al.*, *Nucl. Instrum. Methods Phys. Res. A*, **614** (2010) 439.

[68] S. Pullanhiotan *et al.*, *Nucl. Instrum. Methods Phys. Res. A*, **593** (2008) 343.

[69] M. Rejmund *et al.*, "Performance of the improved larger acceptance spectrometer: VAMOS++". *Nucl. Instrum. Methods Phys. Res. A*, **646** (2011) 184.

[70] A.M. Stefanini *et al.*, *LNL Annual Report*, **LNL-INFN (Rep)-160/00** (1999) 159.

[71] Ö. Skeppstedt *et al.*, *Nucl. Instrum. Methods Phys. Res. A*, **421** (1999) 531.

[72] T. Hüyük *et al.*, *Eur. Phys. J. A*, **52** (2016) 55.

[73] Glenn F. Knoll. *Radiation detection and measurement*. Fourth edition. Wiley, 2010.

[74] H. Morinaga and T. Yamazaki. *In-beam gamma-ray spectroscopy*. North-Holland publishing company, 1976.

[75] A. Bohr and B. Mottelson. *Nuclear structure*. Vol. I: Single-particle motion. World scientific, 1998.

[76] Kenneth S. Krane. *Introductory nuclear physics*. Third edition. Wiley, 1987.

[77] A.E. Blaugrund. *Nucl. Phys.*, **88** (1966) 501.

[78] P.J. Nonal and J.F. Sharpey-Schafer. *Rep. Prog. Phys.*, **42** (1979) 1.

[79] S. Akkoyun *et al.*, "AGATA—Advanced GAmma Tracking Array". *Nucl. Instrum. Methods Phys. Res.*, **668** (2012) 26.

[80] E. Clément *et al.*, *Nucl. Instrum. Methods Phys. Res.*, **855** (2017) 1.

[81] W. Korten *et al.*, *Eur. Phys. J. A*, **56** (2020) 137.

[82] M. Ciemała *et al.*, "Accessing tens-to-hundreds femtoseconds nuclear state lifetimes with low-energy binary heavy-ion reactions". *Eur. Phys. J. A*, **57** (2021) 156.

[83] M. Petri *et al.*, *Phys. Rev. C*, **86** (2012) 044329.

[84] A. O. Nier. *Phys. Rev.*, **77** (1950) 789.

[85] P. Maris *et al.*, *Phys. Rev. Lett.*, **106** (2011) 202502.

[86] H. Crannell *et al.*, *Kakuriken Kenkyu Hokoku: Int. Conf. on Nuclear Structure Studies Using Electron Scattering and Photoreaction*, **5** (1972) 375.

[87] M. Thoennessen. *Rep. Prog. Phys.*, **76** (2013) 056301.

[88] D. Guillemaud-Mueller *et al.*, *Phys. Lett. B*, **41** (1990) 937.

[89] M. Fauerbach *et al.*, *Phys. Rev. C*, **53** (1996) 647.

[90] O.B. Tarasov *et al.*, *Phys. Rev. C*, **409** (1997) 64.

[91] H. Sakurai *et al.*, *Phys. Lett. B*, **448** (1999) 180.

[92] T. Nakamura, H. Sakurai, and H. Watanabe. *Prog. Part. Nucl. Phys.*, **97** (2017) 53.

[93] D. S. Ahn *et al.*, *Phys. Rev. Lett.*, **123** (2019) 212501.

[94] A. Matta *et al.*, tech. rep. Geneva: CERN, 2013. URL: `http://cds.cern.ch/record/1551744/files/INTC-P-377.pdf?version=1` (visited on 09/08/2021).

[95] E. K. Warburton and B. A. Brown. *Phys. Rev. C*, **46** (1992) 923.

[96] F.C. Barker. *Aust. J. Phys.*, **37** (1984) 17.

[97] A. Matta *et al.*, tech. rep. Geneva: CERN, 2019. URL: `http://cds.cern.ch/record/2676313` (visited on 08/02/2021).

[98] A. Saxena and P.C. Srivastava. *Prog. Theor. Exp. Phys.*, **2019** (2019) 073D02.

[99] G. Putt *et al.*, *Nuc. Phys. A*, **399** (1983) 190.

[100] M. Pravikoff *et al.*, *Nuc. Phys. A*, **528** (1991) 225.

[101] M. Wiedeking *et al.*, *Phys. Rev. C*, **77** (2008) 054305.

[102] C. R. Hoffmann *et al.*, *Phys. Rev. C*, **88** (2013) 044317.

[103] G. Audi *et al.*, *Chin. Phys. C*, **36** (2012) 1287.

[104] P. Doleschall and I. Borbély. *Phys. Rev. C*, **62** (2000) 054004.

[105] P. Doleschall, I. Borbély, Z. Papp, and W. Plessas. *Phys. Rev. C*, **67** (2003) 064005.

[106] D. R. Entem and R. Machleidt. *Phys. Rev. C*, **68** (2003) 041001(R).

[107] R. Machleidt and D.R. Entem. *Phys. Rep.*, **503** (2011) 1.

[108] R. Machleidt. *Phys. Rev. C*, **63** (2001) 024001.

[109] V.I. Zagrebaev, B. Fornal, S. Leoni, and W. Greiner. "Formation of light exotic nuclei in low-energy multinucleon transfer reactions". *Phys. Rev. C*, **89** (2014) 054608.

[110] G. J. Balster *et al.*, *Nucl. Phys. A*, **468** (1987) 131.

[111] A. Maj *et al.*, *Acta Phys. Pol. B*, **40** (2009) 565.

[112] A. Giaz *et al.*, *Nucl. Instrum. Methods Phys. Res. A*, **729** (2013) 910.

[113] G. Gosta *et al.*, *Nucl. Instrum. Methods Phys. Res. A*, **879** (2018) 92.

[114] H. Savajols and VAMOS collaboration. *Nucl. Phys. A*, **654** (1999) 1027c.

[115] *AGATA web site*. URL: `https://www.agata.org/` (visited on 06/08/2021).

[116] A. Bracco, G. Duchêne, Zs. Podolyák, and P.Reiter. *Prog. Part. Nucl. Phys.* (2021) 103887.

[117] *GANIL web site*. URL: `https://www.ganil-spiral2.eu/press/` (visited on 09/09/2021).

[118] *Attribution 3.0 Unported License*. Creative Commons. URL: `https://creativecommons.org/licenses/by/3.0/legalcode` (visited on 10/06/2021).

[119] A. Wiens *et al.*, *Nucl. Instrum. Methods Phys. Res. A*, **618** (2010) 223.

[120] B. Bruyneel, B. Birkenbach, and P. Reiter. *Eur. Phys. J. A*, **52** (2016) 70.

[121] B. De Canditiis and G. Duchêne. *Eur. Phys. J. A*, **59** (2020) 276.

[122] H.J. Li *et al.*, *Eur. Phys. J. A*, **54** (2018) 198.

[123] A. Lopez-Martens *et al.*, *Nucl. Instrum. Methods Phys. Res. A*, **533** (2004) 454.

[124] J. Van der Marel and B. Cederwall. *Nucl. Instrum. Methods Phys. Res. A*, **437** (1999) 538.

[125] X. Grave *et al.*, *14th IEEE-NPSS Real Time Conference, 2005.* 2005. DOI: `10.1109/RTC.2005.1547454`.

[126] F. Camera and A. Maj. *PARIS White Book*. Henryk Niewodniczański Institute of Nuclear Physics, 2021. ISBN: 978-83-63542-22-1.

[127] Saint-Gobain Crystals. *Phoswich Detectors For High Energy Backgrounds*. URL: `https://www.crystals.saint-gobain.com/sites/imdf.crystals.com/files/documents/phoswich-data-sheet.pdf` (visited on 06/09/2021).

[128] A. Mentana. "Experimental study of Isospin symmetry in N=Z nuclei". PhD thesis. Università degli Studi di Milano, 2017.

[129] Saint-Gobain Crystals. *Lanthanum Bromide and Enhanced Lanthanum Bromide*. URL: `https://www.crystals.saint-gobain.com/sites/imdf.crystals.com/files/documents/lanthanum-material-data-sheet.pdf` (visited on 06/10/2021).

[130] Saint-Gobain Crystals. *NaI(Tl) and Polyscin NaI(Tl) Sodium Iodide Scintillation Material*. URL: https://www.crystals.saint-gobain.com/sites/imdf.crystals.com/files/documents/sodium-iodide-material-data-sheet_0.pdf (visited on 06/10/2021).

[131] R.Billnert *et al.*, *Nucl. Instrum. Methods Phys. Res. A*, **647** (2001) 94.

[132] Berkeley Nucleonics Corp. *Cerium Bromide*. URL: https://www.berkeleynucleonics.com/cerium-bromide (visited on 06/10/2021).

[133] G. Gupta *et al.*, *Proceedings of the DAE Symp. on Nucl. Phys.* Vol. 62. 2017 1004.

[134] E. Bouquerel *et al.*, *Proc. of International Particle Accelerator Conference IPAC2017, Copenhagen, Denmark 2017*. JACoW, 2017 4522.

[135] C. Boiano *et al.*, *2015 IEEE Nuclear Science Symposium and Medical Imaging Conference (NSS/MIC)*. 2015. DOI: 10.1109/NSSMIC.2015.7581805.

[136] S. Ziliani. "Lifetime measurements of excited states in neutron-rich C and O isotopes: a stringent test of the three body forces with the AGATA-PARIS-VAMOS setup". Master's thesis. Università degli Studi di Milano, 2018. URL: http://www.infn.it/thesis/thesis_dettaglio.php?tid=13068 (visited on 07/29/2021).

[137] S. Ziliani *et al.*, "Spectroscopy of neutron-rich C, O and F isotopes with the AGATA+PARIS+VAMOS setup at GANIL". *Acta Phys. Pol. B*, 50 (2019) 625.

[138] M. Ciemała *et al.*, *Acta Phys. Pol. B*, 50 (2019) 615.

[139] B. Bruyneel *et al.*, *Nucl. Instrum. Methods Phys. Res. A*, **608** (2009) 99.

[140] B. Bruyneel. *Cross talk correction for AGATA detectors*. Presentation at the 6th AGATA week. Padova, Italy. 2007.

[141] *AGATA software package*. URL: https://atrium.in2p3.fr/ (visited on 07/14/2021).

[142] A. Lemasson. Private communication.

[143] S. Ziliani *et al.*, "Complete set of bound negative-parity states in the neutron-rich nucleus ^{18}N". *Phys. Rev. C* (2021). Accepted by the journal.

[144] O.B. Tarasov and D. Bazin. *Nucl. Instrum. Methods Phys. Res. B*, **266** (2008) 4657.

[145] W.U. Schröder and J.R. Huizenga. *Treatise on heavy-ion science*. Vol. 2: *Fusion and quasi-fusion phenomena*. Springer, 1985 113–726.

[146] R. Kaufmann and R. Wolfgang. *Phys. Rev.*, **121** (1961) 192.

[147] J. Wilczynski. *Phys. Lett. B*, **47** (1973) 484.

[148] A.V. Karpov and V.V. Saiko. *Phys. Rev. C*, **96** (2017) 024618.

[149] I. Stefan *et al.*, *Phys. Lett. B*, **779** (2018) 456.

[150] J. Ziegler, J. Biersack, and U.U. Littmark. *The Stopping Power and Range of Ions in Solids*. Vol. 1. Pergamon, 1984.

[151] R. Anne ad others. *Nucl. Instrum. Methods Phys. Res. B*, **34** (1988) 295.

[152] H. Geissel ad others. *Nucl. Instrum. Methods Phys. Res. B*, **195** (2002) 3.

[153] M. Labiche *et al.*, *AGATA GEANT4 Simulations for AGATA@GANIL*. URL: http://npg.dl.ac.uk/svn/agata/ (visited on 07/26/2021).

[154] C. Stahl, J. Leske, M. Lettmann, and N. Pietralla. *Comp. Phys. Commun.*, **214** (2017) 174.

[155] C. Michelagnoli *et al.*, *AIP Conf. Proc.*, **1484** (2012) 281.

[156] F. Hibou, P. Fintz, B. Rastegar, and A. Gallmann. *Nucl. Phys. A*, **171** (1971) 603.

[157] T.K. Alexander, C. Broude, and A.E. Litherland. *Nucl. Phys.*, **53** (1964) 593.

[158] U. Köster. *Eur. Phys. J. A*, **15** (2002) 255.

[159] S. Ziliani *et al.*, "Lifetime analysis of short-lived states in ^{17}N". *Nuovo Cimento C*, **44** (2021) 84.

[160] D.W.O. Rogers. *Nucl. Phys. A*, **226** (1974) 424.

[161] Š.Piskoř and W.Schäferlingová. *Nucl. Phys. A*, **510** (1990) 301.

[162] F. Ajzenberg-Selove. *Nucl. Phys. A*, **523** (1991) 1.

[163] M.J. Throop. *Phys. Rev.*, **179** (1969) 1011.

[164] R. B. Firestone and Zs. Revay. *Phys. Rev. C*, **93** (2016) 054306.

[165] F. Ajzenberg-Selove. *Nucl. Phys. A*, **449** (1986) 1.

[166] S. Ziliani. "Lifetime measurement in the femtoseconds range in neutron-rich light nuclei with the AGATA tracking array". *Nuovo Cimento C*, **43** (2020) 107.

[167] S. Ziliani *et al.*, *Acta Phys. Pol. B*, **51** (2020) 709.

[168] N. Tsunoda *et al.*, *Phys. Rev. C*, **95** (2017) 021304(R).

[169] D. Mengoni *et al.*, *Nucl. Instrum. Methods Phys. Res. A*, **764** (2014) 241.

[170] N. Cieplicka-Oryńczak *et al.*, *Eur. Phys. J. A*, **54** (2018) 209.

[171] A. Goasduff *et al.*, *Nucl. Instrum. Methods Phys. Res. A*, **1015** (2021) 165753.

[172] D. Baye and E.M. Tursonov. *Phys. Lett. B*, **696** (2011) 565.

[173] K. Riisager *et al.*, *Phys. Lett. B*, **732** (2014) 305.

[174] K. Riisager *et al.*, *Eur. Phys. J. A*, **56** (2020) 100.

[175] Y. Ayyad *et al.*, *Phys. Rev. Lett.*, **123** (2019) 082501.

[176] H.O.U. Fynbo *et al.*, 2019. arXiv: 1912.06064 [nucl-ex].

[177] J. Okołowicz, M. Płoszajczak, and W. Nazarewicz. "Convenient Location of a Near-Threshold Proton-Emitting Resonance in ^{11}B". *Phys. Rev. Lett.*, **124** (2020) 042502.

[178] W. Elkamhawy, Z. Yang, H.W. Hammer, and L. Platter. 2020. arXiv: 1909.12206v2 [nucl-th].

[179] M. Płoszajczak and J. Okołowicz. Private communication. 2020.

[180] S. Capra *et al.*, *LNL Annual Report*, **INFN-LNL-258** (2018) 97.

[181] S. Capra *et al.*, *Nucl. Instrum. Methods Phys. Res. A*, **935** (2019) 178.

[182] S. Ziliani *et al.*, *LNL Annual Report 2019*, INFN-LNL Report **259** (2020) 67.

[183] *PIAVE*. URL: https://www.lnl.infn.it/index.php/en/accelerators-3/piave (visited on 06/28/2021).

[184] *ALPI*. URL: https://www.lnl.infn.it/index.php/en/accelerators-3/alpi (visited on 06/28/2021).

[185] D. Bazzacco. *Proc. int. conf. on nuclear structure at high angular 799 momentum*. Vol. Proceedings AECL 10613 **2**. 1992 376.

[186] F.A. Beck. *Prog. Part. Nucl. Phys.*, **28** (1992) 443.

[187] A. Pullia *et al.*, *2012 IEEE Nuclear Science Symposium and Medical Imaging Conference Record (NSS/MIC)*. 2012 819. DOI: 10.1109/NSSMIC.2012.6551218.

[188] D. Barrientos *et al.*, *2012 18th IEEE-NPSS Real Time Conference*. 2012 1. DOI: 10.1109/RTC.2012.6418205.

[189] D. Bazzacco. *The TkT spectrum viewer*. Private communication. 2012.

[190] R. Brun and F. Rademakers. "ROOT - An Object Oriented Data Analysis Framework". *Proceedings AIHENP'96 Workshop, Lausanne, Sep. 1996, Nucl. Instrum. Methods Phys. Res. A*, **389** (1997) 81. See also: https://root.cern/.

[191] O.B. Tarasov and D. Bazin. *Nucl. Instrum. Methods Phys. Res. B*, **266** (2008) 4657.

[192] A. Matta *et al.*, *J. Phys. G: Nucl. Part. Phys.*, **43** (2016) 045113.

[193] K. G. Kibler. "Angular Distributions and Total Cross Sections of Charged Particles from Li^6+Li^6 as a Function of Energy". *Phys. Rev.*, **152** (1966) 932.

[194] *Tandem-XTU*. URL: https://www.lnl.infn.it/index.php/it/acceleratori-2/tandem (visited on 08/31/2021).

[195] Y. Leifels, G. Domogala, R.P. Eule, and H. Freiesleben. *Z. Physik A - Atomic Nuclei*, **335** (1990) 183.

[196] E. Albanese. "Searching for a narrow near-threshold resonance in ^{11}B with gamma-particle coincidences". Master thesis. Università degli Studi di Milano, 2021.

[197] Z. Tang *et al.*, *Phys. Rev. Lett.*, **121** (2018) 022505.

[198] J.R. Taylor. *Introduzione all'analisi degli errori*. Ed. by Zanichelli. Second edition. 2000.

[199] *Progress at LAMPF*. Progress report. Clinton P. Anderson Meson Physics Facility, Los Alamos Scientific Laboratory, University of California, 1981. URL: https://inis.iaea.org/collection/NCLCollectionStore/_Public/12/619/12619284.pdf (visited on 09/12/2021).

[200] B. Zeidman and D. F. Geesaman. *Nucl. Phys. A*, **396** (1983) 419.

[201] R.S. Hicks *et al.*, "M4 excitations in ^{13}C". *Phys. Rev. C*, **34** (1986) 1161.

[202] S.F. Collins *et al.*, "The spectroscopy of ^{13}C by inelastic proton scattering". *Nucl. Phys. A*, **481** (1988) 494.

[203] S.J. Seestrom-Morris *et al.*, "Inelastic Pion Scattering from ^{13}C at 162 MeV". *Phys. Rev. C*, **26** (1982) 594.

[204] K.W. Jones *et al.*, *Phys. Lett. B*, **128** (1983) 281.

[205] D. Dehnhard *et al.*, *Phys. Rev. Lett.*, **43** (1979) 1091.

[206] A.N. Golzov, N.G. Goncharova, and H.R. Kissener. *Nucl. Phys. A*, **462** (1987) 376.

[207] F. Petrovich and W.G. Love. *Nucl. Phys. A*, **354** (1981) 499.

[208] D. B. Holtkamp *et al.*, *Phys. Rev. Lett.*, **47** (1981) 216.

[209] J.C. Bergstrom, R. Neuhausen, and G. Lahm. "Electroexcitation of levels in ^{14}N between 12 and 21 MeV". *Phys. Rev. C*, **29** (1984) 1168.

[210] D. F. Geesaman *et al.*, "Inelastic scattering of 162-MeV pions by ^{14}N". *Phys. Rev. C*, **27** (1983) 1134.

[211] S.J. Seestrom-Morris *et al.*, *Phys. Rev. C*, **31** (1985) 923.

[212] C.E. Hyde-Wright *et al.*, "Electroexcitation of 4^- states in ^{16}O". *Phys. Rev. C*, **35** (1987) 880.

[213] R.S. Henderson *et al.*, "4^- Particle-Hole States in ^{16}O". *Aust. J. Phys.*, **32** (1979) 411. DOI: https://doi.org/10.1071/PH790411.

[214] D. M. Manley *et al.*, *Phys. Rev. C*, **34** (1986) 1214.

[215] C. L. Blilie *et al.*, *Phys. Rev. C*, **30** (1984) 1989.

[216] A. V. Nero, R. S. Ohanian, R. Soneira, and E. G. Adelberger. *Bull. Am. Phys. Soc.*, **19** (1974) 470.

[217] S. Yen *et al.*, *Phys. Lett. B*, **93** (1980) 250.

[218] B.L. Clausen. "Pion scattering to 8^- stretched states in ^{60}Ni". *Ph.D. thesis*. Faculty of the Graduate School of the University of Colorado, 1987.

[219] R. A. Lindgren *et al.*, *Phys. Rev. Lett.*, **47** (1981) 1266.

[220] N. Michel, W. Nazarewicz, M. Płoszajczak, and K. Bennaceur. *Phys. Rev. Lett.*, **89** (2002) 042502.

[221] Y. Jaganathen *et al.*, *Phys. Rev. C*, **96** (2017) 054316.

[222] N. Cieplicka-Oryńczak *et al.*, *Acta Phys. Pol. B Proc. Suppl.*, **13** (2020) 389.

[223] J. Łukasik *et al.*, "KRATTA, a versatile triple telescope array for charged reaction products". *Nucl. Instrum. Methods Phys. Res. A*, **709** (2013) 120.

[224] H. Breuer *et al.*, "Charged particle decay of hole states in ^{16}O". *Phys. Lett. B*, **96** (1980) 35.

[225] *Cyclotron Centre Bronowice*. URL: https://ccb.ifj.edu.pl/en.o_nas.html (visited on 06/15/2021).

[226] *Cyclotron Proteus C-235*. URL: https://ccb.ifj.edu.pl/en.cyklotron_proteus_c_235.html (visited on 06/15/2021).

[227] *Micron Semiconductor Ltd W1*. URL: http://www.micronsemiconductor.co.uk/product/w1/ (visited on 06/18/2021).

[228] C. Boiano, A. Guglielmetti, and S. Riboldi. *2012 IEEE Nuclear Science Symposium and Medical Imaging Conference Record (NSS/MIC)*. 2012 865. DOI: 10.1109/NSSMIC.2012.6551228.

[229] CAEN S.p.A. *V1730*. URL: https://www.caen.it/products/v1730/ (visited on 08/19/2021).

[230] CAEN S.p.A. *DPP-PSD*. URL: https://www.caen.it/products/dpp-psd/ (visited on 08/19/2021).

[231] B.A. Wasilewska. "Badanie rozpadu stanów kolektywnych w reakcjach indukowanych protonami". PhD thesis. Instytut Fizyki Jądrowej Im. Henrika Niewodniczanskiego Polskiej Akademii Naku, 2018.

[232] A. Rohatgi. *WebPlotDigitizer: Version 4.4*. 2021. URL: https://automeris.io/WebPlotDigitizer.

[233] OriginLab Corporation. *Origin(Pro)*. Northampton, MA, USA.

[234] Microsoft Corporation. *Microsoft Excel*. Available from https://office.microsoft.com/excel. 2018.

[235] *AGATA GEANT4 simulation code user manual*. URL: http://agata.pd.infn.it/documents/simulations/docs/agataManual.pdf (visited on 07/28/2021).

List of publications

As of September 2021

The work reported in this thesis was partially published in the following publications:

Peer-reviewed publications

- A. Goasduff, D. Mengoni, F. Recchia, J.J. Valiente-Dobón, R. Menegazzo, G. Benzoni, D. Barrientos, M. Bellato, N. Bez, M. Biasotto, N. Blasi, C. Boiano, A. Boso, S. Bottoni, A. Bracco, S. Brambilla, D. Brugnara, F. Camera, S. Capra, A. Capsoni, P. Cocconi, S. Coelli, M.L. Cortés, F.C.L. Crespi, G. de Angelis, F.J. Egea, C. Fanin, S. Fantinel, A. Gadea, E.R. Gamba, A. Gambalonga, C. Gesmundo, G. Gosta, A. Gottardo, A. Gozzelino, E.T. Gregor, M. Gulmini, J. Ha, K. Hadyńska-Klęk, A. Illana, R. Isocrate, G. Jaworski, P.R. John, S.M. Lenzi, S. Leoni, S. Lunardi, M. Magalini, N. Marchini, B. Million, V. Modamio, A. Nannini, D.R. Napoli, G. Pasqualato, J. Pellumaj, R.M. Pérez-Vidal, S. Pigliapoco, M. Polettini, C. Porzio, A. Pullia, L. Ramina, G. Rampazzo, M. Rampazzo, M. Rebeschini, K. Rezynkina, M. Rocchini, M. Romanato, D. Rosso, A. Saltarelli, M. Scarcioffolo, M. Siciliano, D.A. Testov, D. Tomasella, F. Tomasi, N. Toniolo, C.A. Ur, S. Ventura, F. Veronese, E. Viscione, V. Volpe, O. Wieland, I. Zanon, S. Ziliani, G. Zhang and D. Bazzacco, "The GALILEO γ-ray array at the Legnaro National Laboratories", *Nucl. Instr. Methods Phys. Res. A* **1015**, 165753 (2021), `https://doi.org/10.1016/j.nima.2021.165753`.

- M. Ciemała, S. Ziliani, F. C. L. Crespi, S. Leoni, B. Fornal, A. Maj, P. Bednarczyk, G. Benzoni, A. Bracco, C. Boiano, S. Bottoni, S. Brambilla, M. Bast, M. Beckers, T. Braunroth, F. Camera, N. Cieplicka-Oryńczak, E. Clément, S. Coelli, O. Dorvaux, S. Erturk, G. De France, C. Fransen, A. Goldkuhle, J. Grębosz, M. N. Harakeh, Ł. W. Iskra, B. Jacquot, A. Karpov, M. Kicińska-Habior, Y.-H. Kim, M. Kmiecik, A. Lemasson, S. M. Lenzi, M. Lewitowicz, H. Li, I. Matea, K. Mazurek, C. Michelagnoli, M. Matejska-Minda, B. Million, C. Müller-Gatermann, V. Nanal, P. Napiorkowski, D. R. Napoli, R. Palit, M. Rejmund, Ch. Schmitt, M. Stanoiu, I. Stefan, E. Vardaci, B. Wasilewska, O. Wieland, M. Zięblíński and M. Zielińska, "Accessing tens-to-hundreds femtoseconds nuclear state lifetimes with low-energy binary heavy-ion

reactions", *Eur. Phys. J. A* **57**, 156 (2021), https://doi.org/10.1140/epja/s10050021004516.

- M. Ciemała, S. Ziliani, F. C. L. Crespi, S. Leoni, B. Fornal, A. Maj, P. Bednarczyk, G. Benzoni, A. Bracco, C. Boiano, S. Bottoni, S. Brambilla, M. Bast, M. Beckers, T. Braunroth, F. Camera, N. Cieplicka-Oryńczak, E. Clément, S. Coelli, O. Dorvaux, S. Erturk, G. de France, C. Fransen, A. Goldkuhle, J. Grębosz, M. N. Harakeh, Ł. W. Iskra, B. Jacquot, A. Karpov, M. Kicińska-Habior, Y. Kim, M. Kmiecik, A. Lemasson, S. M. Lenzi, M. Lewitowicz, H. Li, I. Matea, K. Mazurek, C. Michelagnoli, M. Matejska-Minda, B. Million, C. Müller-Gatermann, V. Nanal1, P. Napiorkowski, D. R. Napoli, R. Palit, M. Rejmund, Ch. Schmitt, M. Stanoiu, I. Stefan, E. Vardaci, B. Wasilewska, O. Wieland, M. Zięblíński, M. Zielińska, A. Ataç, D. Barrientos, B. Birkenbach, A. J. Boston, B. Cederwall, L. Charles, J. Collado, D. M. Cullen, P. Désesquelles, C. Domingo-Pardo, J. Dudouet, J. Eberth, V. González, J. Goupil, L. J. Harkness-Brennan, H. Hess, D. S. Judson, A. Jungclaus, W. Korten, M. Labiche, A. Lefevre, R. Menegazzo, D. Mengoni, J. Nyberg, R. M. Perez-Vidal, Zs. Podolyak, A. Pullia, F. Recchia, P. Reiter, F. Saillant, M. D. Salsac, E. Sanchis, O. Stezowski, Ch. Theisen, J. J. Valiente-Dobón, J. D. Holt, J. Menéndez, A. Schwenk and J. Simonis, "Testing *ab initio* nuclear structure in neutron-rich nuclei: Lifetime measurements of second 2^+ state in C 16 and O 20", *Phys. Rev. C* **101(2)**, 021303(R) (2020), https://doi.org/10.1103/PhysRevC.101.021303.

Accepted publications

- S. Ziliani, M. Ciemała, F. C. L. Crespi, S. Leoni, B. Fornal, T. Suzuki, T. Otsuka, A. Maj, P. Bednarczyk, G. Benzoni, A. Bracco, C. Boiano, S. Bottoni, S. Brambilla, M. Bast, M. Beckers, T. Braunroth, F. Camera, N. Cieplicka-Oryńczak, E. Clément, S. Coelli, O. Dorvaux, S. Erturk, G. de France, C. Fransen, A. Goldkuhle, J. Grębosz, M. N. Harakeh, Ł. W. Iskra, B. Jacquot, A. Karpov, M. Kicińska-Habior, Y. Kim, M. Kmiecik, A. Lemasson, S. M. Lenzi, M. Lewitowicz, H. Li, I. Matea, K. Mazurek, C. Michelagnoli, M. Matejska-Minda, B. Million, C. Müller-Gatermann, V. Nanal, P. Napiorkowski, D. R. Napoli, R. Palit, M. Rejmund, Ch. Schmitt, M. Stanoiu, I. Stefan, E. Vardaci, B. Wasilewska, O. Wieland, M. Zięblíński and M. Zielińska, "Complete set of bound negative-parity states in the neutron-rich ^{18}N nucleus", *Phys. Rev. C* – Accepted in September 2021, https://journals.aps.org/prc/accepted/db07eP29QeeEd31910e67c851814355ff12dc281f.

Publications in conference proceedings

- S. Ziliani, M. Ciemała, F. C. L. Crespi, S. Leoni, B. Fornal, A. Maj, P. Bednarczyk, G. Benzoni, A. Bracco, C. Boiano, S. Bottoni, S. Brambilla, M. Bast, M. Beckers, T. Braunroth, F. Camera, N. Cieplicka-Oryńczak, E. Clément, S. Coelli, O. Dorvaux, S. Erturk, G. De France, C. Fransen, A. Goldkuhle, J. Grębosz, M. N. Harakeh, L. W. Iskra, B. Jacquot, A. Karpov, M. Kicińska-Habior, Y. Kim, M. Kmiecik, A. Lemasson, S. M. Lenzi, M. Lewitowicz, H. Li, I. Matea, K. Mazurek, C. Michelagnoli, M. Matejska-Minda, B. Million, C. Müller-Gatermann, V. Nanal, P. Napiorkowski, D.

R. Napoli, R. Palit, M. Rejmund, Ch. Schmitt, M. Stanoiu, I. Stefan, E. Vardaci, B. Wasilewska, O. Wieland, M. Zięblíński, M. Zielińska and AGATA, PARIS, VAMOS Collaborations, "Lifetime analysis of short-lived states in ^{17}N, *Il Nuovo Cimento C* **44(2-3)**, 84 (2021), https://doi.org/10.1393/ncc/i2021-21084-7.

- S. Capra, S. Ziliani, A. Goasduff, S. Leoni, B. Fornal, D. Mengoni, G. Benzoni, I. Zanon, A. Compagnucci, M. Luciani, J. Skowronski, D. Brugnara, N. Cieplicka-Oryńczak, G. Colucci, M. L. Cortes, G. Gosta, A. Gottardo, K. C. Hadynska-Klęk, G. Pasqualato, F. Recchia, M. Siciliano, J. J. Valiente Dobon and A. Pullia, "First in-beam test of the GALTRACE innovative silicon detector array", *Il Nuovo Cimento C* **44(2-3)**, 34 (2021), https://doi.org/10.1393/ncc/i2021-21034-5.

- S. Ziliani, "Lifetime measurement in the femtoseconds range in neutron-rich light nuclei with the AGATA tracking array", *Il Nuovo Cimento C* **43(4-5)**, 107 (2020), https://doi.org/10.1393/ncc/i2020-20107-3.

- N. Cieplicka-Oryńczak, B. Fornal, M. Ciemała, M. Kmiecik, A. Maj, J. Łukasik, P. Pawłowski, B. Sowicki, B. Wasilewska, M. Zięblíński, J. Grębosz, M. Krzysiek, M. Matejska-Minda, K. Mazurek, Y. Jaganathen, S. Leoni, C. Boiano, S. Brambilla, S. Ziliani, S. Bottoni, A. Bracco, F. Camera, Ł.W. Iskra, M.N. Harakeh, C. Clisu, N. Florea, N. Mărginean, R. Mărginean, L. Stan, I. Burducea, D.A. Iancu, M. Sferrazza, M. Płoszajczak and P. Kulessa, "Decay of the stretched M4 resonance in ^{13}C", *Acta Phys. Pol. B, Proceedings Supplement* **13(3)**, 389 (2020), https://doi.org/10.5506/APhysPolBSupp.13.389.

- M. Ciemała, S. Ziliani, F. Crespi, S. Leoni, B. Fornal, A. Maj, P. Bednarczyk, G. Benzoni, A. Bracco, C. Boiano, S. Bottoni, S. Brambilla, M. Bast, M. Beckers, T. Braunroth, F. Camera, N. Cieplicka-Oryńczak, E. Clément, O. Dorvaux, S. Erturk, G. de France, C. Fransen, A. Goldkuhle, J. Grębosz, M.N. Harakeh, Ł.W. Iskra, B. Jacquot, A. Karpov, M. Kicińska-Habior, Y. Kim, M. Kmiecik, A. Lemasson, S.M. Lenzi, M. Lewitowicz, H. Li, I. Matea, K. Mazurek, C. Michelagnoli, M. Matejska-Minda, B. Million, C. Müller-Gatermann, V. Nanal, P. Napiorkowski, D.R. Napoli, R. Palit, M. Rejmund, Ch. Schmitt, M. Stanoiu, I. Stefan, E. Vardaci, B. Wasilewska, O. Wieland, M. Zielińska and M. Zięblíński, "Short-range lifetime measurements for deep-inelastic reaction products: The ^{19}O test case", *Acta Phys. Pol. B* **51(3)**, 699 (2020), https://doi.org/10.5506/APhysPolB.51.699.

- S. Ziliani, M. Ciemała, F. Crespi, S. Leoni, B. Fornal, A. Maj, P. Bednarczyk, G. Benzoni, A. Bracco, C. Boiano, S. Bottoni, S. Brambilla, M. Bast, M. Beckers, T. Braunroth, F. Camera, N. Cieplicka-Oryńczak, E. Clément, O. Dorvaux, S. Erturk, G. de France, C. Fransen, A. Goldkuhle, J. Grębosz, M.N. Harakeh, Ł.W. Iskra, B. Jacquot, A. Karpov, M. Kicińska-Habior, Y. Kim, M. Kmiecik, A. Lemasson, S.M. Lenzi, M. Lewitowicz, H. Li, I. Matea, K. Mazurek, C. Michelagnoli, M. Matejska-Minda, B. Million, C. Müller-Gatermann, V. Nanal, P. Napiorkowski, D.R. Napoli, R. Palit, M. Rejmund, Ch. Schmitt, M. Stanoiu, I. Stefan, E. Vardaci, B. Wasilewska, O. Wieland, M. Zięblíński and M. Zielińska, "Spectroscopy of neutron-rich nitrogen

isotopes with AGATA+PARIS+VAMOS", *Acta Phys. Pol. B* **51(3)**, 709 (2020), https://doi.org/10.5506/APhysPolB.51.709.

- S. Capra, G. Benzoni, A. Compagnucci, J. M. Deltoro, J. Dueñas, A. Goasduff, D. Mengoni, A. Pullia, J. Skowronski, I. Zanon and S. Ziliani, "Validation and Characterization of the GALTRACE Silicon Detector Array Demonstrator", *2019 IEEE Nuclear Science Symposium and Medical Imaging Conference, NSS/MIC 2019*, 9059819 (2019), https://doi.org/10.1109/NSS/MIC42101.2019.9059819.

- M. Ciemała, S. Ziliani, F. Crespi, S. Leoni, B. Fornal, A. Maj, P. Bednarczyk, G. Benzoni, A. Bracco, C. Boiano, S. Bottoni, S. Brambilla, M. Bast, M. Beckers, T. Braunroth, F. Camera, N. Cieplicka-Oryńczak, E. Clément, O. Dorvaux, S. Ertürk, G. De France, A. Goldkuhle, J. Grębosz, M.N. Harakeh, Ł.W. Iskra, B. Jacquot, A. Karpov, M. Kicińska-Habior, Y. Kim, M. Kmiecik, A. Lemasson, H. Li, I. Matea, K. Mazurek, C. Michelagnoli, B. Millon, C. Müller-Gatermann, P. Napiorkowski, V. Nanal, M. Matejska-Minda, M. Rejmund, B. Sowicki, Ch. Schmitt, M. Stanoiu, I. Stefan, B. Wasilewska, M. Zielińska and M. Zięblński, "Determination of lifetimes of excited states in neutron-rich ^{20}O isotope from experiment with the AGATA+PARIS+VAMOS setup", *Acta Phys. Pol. B* **50(3)**, 615 (2019), urlhttps://doi.org/10.5506/APhysPolB.50.615.

- S. Ziliani, M. Ciemała, F. Crespi, S. Leoni, B. Fornal, A. Maj, P. Bednarczyk, G. Benzoni, A. Bracco, C. Boiano, S. Bottoni, S. Brambilla, M. Bast, M. Beckers, T. Braunroth, F. Camera, N. Cieplicka-Oryńczak, E. Clément, O. Dorvaux, S. Ertürk, G. De France, A. Goldkuhle, J. Grębosz, M.N. Harakeh, Ł.W. Iskra, B. Jacquot, M. Kicińska-Habior, Y. Kim, M. Kmiecik, A. Lemasson, H. Li, I. Matea, K. Mazurek, C. Michelagnoli, B. Millon, C. Müller-Gatermann, P. Napiorkowski, V. Nanal, M. Matejska-Minda, M. Rejmund, Ch. Schmitt, M. Stanoiu, I. Stefan, B. Wasilewska and M. Zięblński, "Spectroscopy of neutron-rich C, O, N and F isotopes with the AGATA+PARIS+VAMOS setup at GANIL", *Acta Phys. Pol. B* **50(3)**, 625 (2019), https://doi.org/10.5506/APhysPolB.50.625.

Reports

- S. Ziliani, S. Capra, A. Goasduff, S. Leoni, B. Fornal, D. Mengoni, G. Benzoni, I. Zanon, A. Compagnucci, M. Luciani, J. Skowronski, D. Brugnara, N. Cieplicka-Orynczak, G. Colucci, M. L. Cortés, G. Gosta, A. Gottardo, K. Hadynska-Klęk, G. Pasqualato, F. Recchia, M. Siciliano and J. J. Valiente Dobón, "Preparatory Study of the γ Decay from Near-threshold States in Light Nuclei with the GALILEO+ GALTRACE Setup", *LNL Annual Report 2019, INFN-LNL Report* **259**, ISSN 1828-8561 (2020), http://www.lnl.infn.it/~annrep/read_ar/2019/contributions/pdfs/067_A_63_A058.pdf.